

Electrohydrodynamic instabilities of multi-fluid flows in microfluidic systems

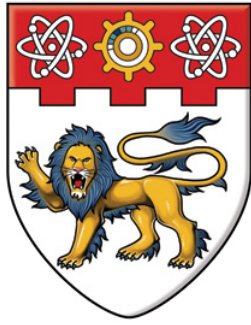
Ding, Zijong

2016

Ding, Z. (2016). Electrohydrodynamic instabilities of multi-fluid flows in microfluidic systems. Doctoral thesis, Nanyang Technological University, Singapore.

<https://hdl.handle.net/10356/69091>

<https://doi.org/10.32657/10356/69091>



NANYANG
TECHNOLOGICAL
UNIVERSITY

**ELECTROHYDRODYNAMIC INSTABILITIES OF
MULTI-FLUID FLOWS
IN MICROFLUIDIC SYSTEMS**

DING ZIJING

**SCHOOL OF MECHANICAL AND AEROSPACE
ENGINEERING**

2016

ELECTROHYDRODYNAMIC INSTABILITIES OF MULTI-FLUID FLOWS IN MICROFLUIDIC SYSTEMS

By

DING ZIJING

School of Mechanical and Aerospace Engineering

A thesis submitted to the
Nanyang Technological University
in partial fulfilment of the requirement for the degree of
Doctor of Philosophy
2016

Acknowledgements

It has been a long journey for me to come to this stage after nearly four years' study in Nanyang Technological University, Singapore. During the journey, I have grown as an independent research scientist. I have been indebted to many people who have helped me during my PhD study.

Firstly, I would like to give my sincere gratitude to my advisor Prof Wong Teck Neng for his continuous guidance and encouragement throughout my research whose advice on this thesis is invaluable. I am very lucky to have the chance of taking the PhD program under his supervision. During my PhD study, Prof Wong provided me with an excellent environment for independent research and has advised me on theoretical modeling and experimental study. I have also greatly benefitted from discussions with him with regards to personal career development. My English has also improved significantly in both spoken and written aspects though my interactions with him.

Secondly, I wish to thank Prof Liu Rong from Chinese Academy of Science. Our collaboration has covered several aspects: linear stability, transition to turbulence and optimization method. During my PhD study, the collaboration with him has significantly advanced our study on thin film dynamics, especially on the coherent solutions in falling liquid films. The collaboration with Prof Liu Rong has been very successful and I am in debt to him from many fruitful discussions. I am also grateful to Prof Duan Fei, Prof Kang Yuejun, Prof Charles Yang and Prof Thomas Gong at Nanyang Technological University for their helpful comments on my research topics. I have also benefitted from the private communications with experts in thin film dynamics and turbulent flows, such as Prof S Kalliadasis and Prof Y Hwang at Imperial College. Discussions with them have significantly advanced my understanding in the research of flow instability.

Finally, I would like to thank my dear wife Yuehua for her great patience, continuous support and endless love, without whom the journey for the PhD would be more tough.

Table of Contents

Acknowledgements	i
Abstract	vi
Nomenclature	viii
1 Introduction	1
1.1 Research Background	1
1.2 Objective and scope	3
1.3 Outline of this thesis	3
2 Literature Review	5
2.1 A Short Introduction to Flow instability	5
2.1.1 Local stability theory	6
2.1.2 Global stability theory	8
2.2 Low dimensional modeling	9
2.3 Electrohydrodynamical instability	15
2.3.1 Some Basics of Electrostatics	15
2.3.2 Perfect Conductors	19
2.3.3 Perfect Dielectrics	23
2.3.4 Leaky Dielectrics	26
2.3.5 Electrolyte solutions	31
3 Dynamics of liquid films on vertical fibers in a radial electric field	37
3.1 Mathematical formulation	37
3.2 Scaling and the asymptotic model	39
3.3 Linear stability analysis	43

3.4	Nonlinear evolution	48
3.5	Coherent solutions: Traveling waves	59
3.6	The fully linearized problem	65
4	Interfacial instability of a core-annular system in the presence of a radial electric field	68
4.1	Non-dimensionalization and base state	71
4.1.1	Base state of the system	73
4.2	Linearized perturbed system	75
4.3	Results and discussion	77
4.3.1	Effects of the electric field	77
4.3.2	Numerical results	83
5	Electrohydrodynamic instability in an annular liquid layer with radial conductivity gradients	97
5.1	Mathematical Formulation	97
5.2	Non-dimensionalization and base state	101
5.2.1	Dimensional base state	101
5.2.2	Nondimensional system	102
5.3	Linear stability analysis	106
5.4	Results and Discussion	109
5.4.1	Limiting case of $a \rightarrow \infty$	109
5.4.2	Finite inner radius a	110
6	Electrohydrodynamic instability of miscible core-annular flows with electric conductivity stratification	129
6.1	Mathematical Formulation	129
6.2	Base state and scalings	134
6.3	Linear stability analysis	137
6.4	Energy analysis	140
6.5	Results and discussion	141
6.5.1	Validation of numerical methods	141
6.5.2	Parametric study	143

7	Conclusions and future work	160
7.1	Conclusions	160
7.1.1	Interfacial instability	160
7.1.2	Electrohydrodynamic mixing	162
7.2	Perspectives of future research	164
7.2.1	Thin film dynamics	164
7.2.2	Electro-Hydrodynamic instability to Chaotic flows	165
7.2.3	Non-Newtonian flows	166
A	Chebyshev collocation method	168
B	Direct numerical simulation: thin films	171
B.1	Periodic domain	171
B.2	non-Periodic domain	173
C	Direct numerical simulation: two-dimensional Rayleigh-Bénard convection	175
	Publications	180

Abstract

In the last decade, the interfacial instability and mixing enhancement in microfluidic flow systems have attracted much attention. The control of interfacial instability is very crucial in multi-phase flow systems, such as the droplet production systems. In microfluidic systems, rapid mixing has been a long-standing challenge for the small Reynolds number in which turbulence will not occur. Previous studies have demonstrated that rapid mixing can be achieved using an electric or magnetic field. In all of these systems, it is rather important to know the instability threshold. This thesis devotes to the discussion of the effects of electric field on the interfacial instability and electro-mixing in an annulus channel.

Based on the evidence that the wave length is often much longer than the mean thickness of a fluid layer, Chapter 3 investigated the linear and nonlinear dynamics of a perfectly conducting liquid film coating on a metal fiber modulated by the gravity effect in the framework of long-wave theory. A radial electric field was imposed between the inner fiber and an outer electrode and the dynamics of the gas phase was neglected. It was found that the electric field can either reinforce or suppress the interfacial instability by manipulating the distance between the outer electrode and the inner fiber. In Chapter 4, the interfacial instability of two coflowing annular liquids in a radial electric field has been discussed when taking into account the dynamics of the outer layer. Unlike the assumption made in Chapter 3 that the liquids were perfectly conducting, the two immiscible liquids in Chapter 4 were leaky-dielectrics. Moreover, in Chapter 4, interfacial instability of two immiscible leaky dielectric fluids was examined in the full range of wave numbers. It was found that in such a system, the interfacial instability can be either caused by the so-called Rayleigh-Plateau mechanism or the viscosity stratification between the two layers. A detailed study of the effects of normal and tangential Maxwell stresses on the two kinds of interfacial instabilities demonstrated that both of them can either stabilize or destabilize the interface, depending on the electrical properties of the two liquids.

However, the two studies in Chapters 3-4 provided evidences that the interfacial instability caused by the Rayleigh-Plateau mechanism can be modulated by the external electric field and thereby control the formation of droplets.

Electro-convection was investigated in Chapters 5-6. Chapter 5 discussed the electrohydrodynamic instability of an annular liquid layer with a radial electrical conductivity gradient which was developed from the imposed radial electric field. Chapter 6 studied the instability in two miscible liquids with an electrical conductivity stratification wherein a uniform axial electric field was imposed. Studies in the two chapters demonstrated that the instability is triggered by the dielectrophoretic effect. Study in Chapter 5 showed that the critical unstable mode in the annular liquid layer could be either stationary or oscillatory, depending on the conductivity gradient. However, in the two-miscible two flows, the critical unstable mode is always oscillatory. Furthermore, results in Chapter 5 indicated that the flow is least stable for a moderate conductivity gradient whereas Chapter 6 demonstrated that the flow is always more unstable for a larger contrast in conductivity. It should also be pointed out that, in Chapter 5, the critical instability could be reinforced by a weak shear flow; while the critical instability is always impeded by the shear flow in Chapter 6.

A summary of the four Chapters 3-6 was made, and perspectives of future works built upon these works have been proposed in Chapter 7.

Nomenclature

Bond number Bo

Capillary number Ca

Channel gap d

Conductivity ratio η

Cylindrical basis $\mathbf{e}_r, \mathbf{e}_\theta, \mathbf{e}_z$

Cylindrical coordinates r, θ, z

Density ρ

Dynamical viscosity μ

Effective diffusivity of electrical conductivity K_{eff}

Electric charge density ρ_e, q_s

Electric displacement \mathbf{D}

Electric field \mathbf{E}

Electric potential ϕ

Electric conductivity σ

Electric current \mathbf{i}

Electric current density \mathbf{J}, \mathbf{J}_e

Electric dipole momentum \mathbf{p}

Electric number Q, Q'

Electrical permittivity ε

Film thickness h

Identity tensor \mathbb{I}

Local flow rate q

Pressure p

Pure imaginary number $i = \sqrt{-1}$

Reynolds number Re

Schmidt number Sc, Sc_e

Small parameter ϵ

Stress tensor $\mathbb{T}^v, \mathbb{T}^M$

Surface normal \boldsymbol{n}

Surface tangential \boldsymbol{t}

Surface tension γ

Temporal eigenvalue ω

Velocity $\boldsymbol{v} = (u, v, w)$

Wavenumber n, k

Weber number We

CHAPTER 1

Introduction

1.1 Research Background

Flow instability in microfluidic systems has attracted much attention in the last decade, such as in ink-jetting, drug-delivery, droplet production and rapid mixing in *MEMS*. In these industrial applications, the interfacial instability phenomenon is widely encountered and the understanding of one such instability is of great importance for precise control the droplet size in ink-jetting and drug-delivery systems. Another long-standing problem in micro-device is that rapid mixing for the flow is always laminar and turbulent mixing does not occur. Previous investigations indicate that applying an external electric or magnetic field is a potential approach to facilitate mixing in conducting liquids. In view of the importance of flow instability in micro-fluidic devices, this thesis is devoted to two basic problems: interfacial instability and electro-convection.

Many pioneering works on the first problem have been devoted to multi-fluid systems, typically, two-fluid flows in a square duct. It has been demonstrated that the interface could be unstable and finite-amplitude traveling waves could be observed. The two-fluid flow is widely encountered in electroosmotic pump systems where an active liquid layer drives the other passive layer. The principle behind the electroosmotic pump system is the electroosmosis phenomenon in conducting liquid layers. Naturally, it would be interesting to ask: "is the interface stable?", "if not, will it rupture and the formation of droplet would be expected to be seen?", "is there any way to suppress the instability in case of the unstable phenomenon

occurs?". Monodisperse droplet formation in jetting systems is also of academic interest. For the production of very fine droplets of sizes down to $20\ \mu m$, the traditional approach using the Rayleigh-Plateau mechanism is not very successful. The traditional approach of adjusting droplet size is to control the flow rate of the jet. In addition, there is an extra problem in very viscous fluids that the breakup of a jet is delayed. Moreover, it seems that for some viscoelastic fluids, the jet may not break up into droplets after a long time. Applying an electric field is successful in accelerating the breakup of a Newtonian jet. The droplet size could also be narrowed down. Indeed, electrified jet is still an active research field. To the best of my knowledge, very limited works have been devoted to non-Newtonian electrified jets despite the fact that in many practical cases the fluids are non-Newtonian, such as in *3D-Bio-Printing* systems.

For mixing enhancement in microfluidic devices, researchers traditionally use long pipes or designed patterned channels to increase the diffusion time. Inducing thermal disturbances is usually not applicable due to the small scale involved. Natural convection will not occur as a result. For conducting liquids, e.g aqueous ionic solutions, an alternative approach is to impose an external magnetic or electric field, which may trigger a circulation flow in the system. It should be noted that the mechanism of magneto- or electro-convection is quite similar to that of the thermal convection, i.e the convection is initiated by a body force. For the successful implementation of an external electric field to enhance mixing in microscale, it is necessary to create a spatial change in the electric properties, such as an abrupt change in electric conductivity or permittivity. To achieve this, one can pump liquids with different ionic concentrations into a channel. There is another approach to trigger electro-convection by ejecting electric charges into the liquid layer from one electrode and collecting them at the other electrode.

A careful look into previous literature indicate that the interfacial instability in multi-layer flows or electroconvection in an electric field was carried out in a planar system, i.e flow

between to parallel electrodes, although there have been a relatively large number of works on electrified jets. Specifically, studies on electro-convection in ionic solutions or aqueous electrolytes in cylindrical channels are very limited. In this thesis, the author is interested in these flows in cylindrical systems for there is a wide application of circular pipe in micro-devices. In addition, circular pipes can avoid the leakage problem in square channels that is widely encountered in experiments. This thesis will investigate the interfacial instability in multi-fluid flows modulated by an electric field and convection initiated by an external electric field in the following four chapters.

1.2 Objective and scope

Many previous studies have concentrated on the square channel flows. The objective of this thesis is to extend the study of electrohydrodynamical instability to other canonical channel flows, annulus channel flows and pipe flow. First, the Rayleigh-Plateau instability distinguishes the annular flow from the planar flow. In this aspect, the thesis will deliver the first study on the influences of electric field on the Plateau-Rayleigh instability in annular flows. Second, this thesis will ‘generalize’ the dielectrophoretic instability which currently exists in the plane-channel flows, e.g plane-Poiseuille flow, to the other canonical flow systems.

The scope of this thesis covers the following two problems:

- (1) Interfacial instability of multi-phase flows in a radial electric field,
- (2) Electro-convection caused by spatial change in electric conductivity.

1.3 Outline of this thesis

The rest of the thesis is organized as follows.

Chapter 2 reviews the state-of-the-art thin films dynamics and some classical models of electrohydrodynamics. Three mathematical models of thin film flow are reviewed and the advantages and shortcomings of these models are commented. For the electrohydrodynamic instability, four typical models are reviewed: perfect conducting liquids, non-conducting liquids, leaky-dielectric liquids and electrolyte solutions. The mathematical description of these four models are laid out along with the four models.

Chapter 3 reports the investigation of a thin liquid film flowing down a vertical fiber in a radial electric field. The linear and nonlinear dynamics of the problem is studied in the framework of the long-wave theory.

Chapter 4 analyses the linear stability of two co-axial leaky dielectric liquids in a radial electric field. This Chapter focuses on the influence of an electric field on the interfacial instability caused by Plateau-Rayleigh mechanism or viscosity stratification.

Chapter 5 presents the study of linear stability of an annular liquid layer with a conductivity gradient in a radial electric field. The effects of geometry, conductivity gradient, shear flow and ionic diffusion on the stationary and oscillatory unstable mode are discussed.

Chapter 6 discusses electro-convection in a conductivity stratified system which is caused by an axial electric field and the instability mechanism is interpreted by an energy analysis.

Chapter 7 summarizes the contents in chapters 3-6 and proposes some prospectives for future works.

CHAPTER 2

Literature Review

2.1 A Short Introduction to Flow instability

Flow instability is widely encountered in our daily lives through occurrences, such as thermal convection and water waves. Many factors can trigger the occurrence of instability in a flow system, such as inertia, surface tension, gravity, centrifugal force and buoyancy [1].

Flow instability is of great interest in fluid mechanics and applied mathematics providing insights in physical mechanisms behind the transitional phenomena. The methodology of flow instability analysis is to investigate how the system responds if it is perturbed by small disturbances. The disturbances can have various forms, for instance, acoustic noise, fluctuation in flow rate and pressure. If the disturbances can absorb energy from the basic flow and grow with time and the system never returns to its original state, then the system is unstable. Otherwise, the system is stable. Perhaps, the most fascinating phenomenon is the transition in a circular pipe which was reported by Reynolds as early as in the nineteenth century. Even though more than one and a half century has past, the transition phenomenon in pipe flow is still an intriguing problem and remains open. Indeed, it was remarked by Richard Feynman that the mechanism of transition was the most difficult problem in classical physics. Many theories have been proposed and have advanced our understanding for this phenomenon. However, none of these theories is complete and successfully addresses this cumbersome problem. For instance, the normal mode analysis of linear stability theory predicts that the flow is always linearly stable even if the Reynolds number is considerably large. The nonmodal analysis sug-

gests that small disturbances can be amplified significantly due to the strong non-normality of the system and it is conjectured that transition will be triggered by the following nonlinear mechanism [2, 3]. However, it predicts that the perturbation energy decays in long time behavior. A group of scientists utilized the dynamical system theory and suggested that other nontrivial solutions of the Navier-Stokes equations exist beyond the classical parabolic profile [4, 5]. Hence, it was conjectured that these solutions were inherently linked to the transition and turbulence at low Reynolds numbers. However, this is still not very successful since it was found that such solutions can exist at a much smaller Reynolds number where no transition has been observed. Therefore, the relevance between these solutions and the transition is questionable. In this thesis, the dynamical system theory approach to the Navier-Stokes equation is not in our scope despite its great importance. Following, advances in linear stability theory will be reviewed in two aspects: (1) local stability; (2) global stability.

2.1.1 Local stability theory

In the past decades, research on flow stability has been focused on parallel laminar flows because of its simplicity, such as plane-Couette flow, plane-Poiseuille flow and Hagen-Poiseuille flow. In these systems, the channel or pipe is assumed to be infinitely long and the velocity profile does not change in its streamwise direction. Indeed, such infinitely long channels or pipes are ‘mathematical’ models which cannot exist in the daily life. However, for a finite but very long channels (length is much larger than the other scales), and the flow is fully developed in the long downstream direction. The flow is laminar if the flow rate is small and turbulence is not triggered. In such a situation, we are interested in the stability of the fully developed velocity profile and such an analysis of stability is the so-called local stability. The standard approach of linear stability analysis is introduced here. Consider a nonlinear system:

$$\frac{\partial F}{\partial t} = \mathcal{L}(F) + \mathcal{N}(F), \quad (2.1)$$

where \mathcal{L} is a linear operator and \mathcal{N} is a nonlinear operator. The system (2.1) admits trivial solutions or equilibrium points in phase space (from the viewpoint of dynamical theory) \bar{F} .

The stability analysis is achieved by introducing small disturbances into the system $F = \bar{F} + F'$ ($|F'| \ll |\bar{F}|$). Hence, the linearized system around the equilibrium point reads:

$$\frac{\partial F'}{\partial t} = \mathcal{L}(F') + \frac{\partial \mathcal{N}}{\partial F}|_{F=\bar{F}} F'. \quad (2.2)$$

Consider the channel flow (e.g. Couette flow, Poiseuille flow) as an example and in a standard way, the disturbance is written as

$$F' = \hat{F}(y) \exp [i(k_x x + k_z z) + \omega t], \quad (2.3)$$

where \hat{F} the amplitude of Fourier mode, (k_x, k_z) wave number, (x, y, z) respectively represents streamwise, wall-normal and spanwise direction. $\omega = \omega_r + i\omega_i$ is the temporal growth rate. When the temporal stability is considered, the wave number k (k_x or k_z) is given and real, while the temporal growth rate ω is often complex and unknown. For the spatial stability, the time frequency ω is given and real, while the spatial wave number is often complex and unknown. The unknown parameters (e.g. ω or k) serve as the eigenvalue of the problem. When the spatial-temporal instability is considered, i.e. the absolute and convective instability, both ω and the wavenumber are complex. In this thesis, the spatial-temporal theory is out of the scope. If the real part of ω is positive, then the disturbances grow with time and the system is unstable. Otherwise, the system is stable $\omega_r < 0$ or neutral $\omega_r = 0$.

Although the local theory has achieved a great success in predicting the stability threshold of Rayleigh-Bénard convection and Taylor-Couette flow, it failed to predict the critical point of Hagen-Poiseuille flow and plane-Couette flow. In addition, the local theory predicts a critical Reynolds number for the plane-Poiseuille flow: $Re = 5772$ which does not agree well with experimental observations. Transition in plane-Poiseuille flow may take place at a Reynolds

number as low as $Re \approx 1000$. This stimulates scientists to apply other theories to interpret the physical mechanism of transition, such as the non-modal theory and nonlinear theory which leads to the doubt of the validation of normal mode analysis.

However, some scientists argued that the normal mode analysis still can be applied to explore the transition mechanism. The inviscid flow theory, such as the Rayleigh inflection point theory, indicates that the flow is unstable if there is an inflection point in the basic flow profile. Motivated by the inviscid theory, Bottaro et al. proposed that, the basic velocity profile is not exactly linear (for plane-Couette flow) since there is always an experimental error [6]. Hence, they conjectured that the distorted velocity profile (the linear profile perturbed by a finite small disturbance) is not linearly stable (see Fig.2.1). Such an idea [7] has been extended to circular

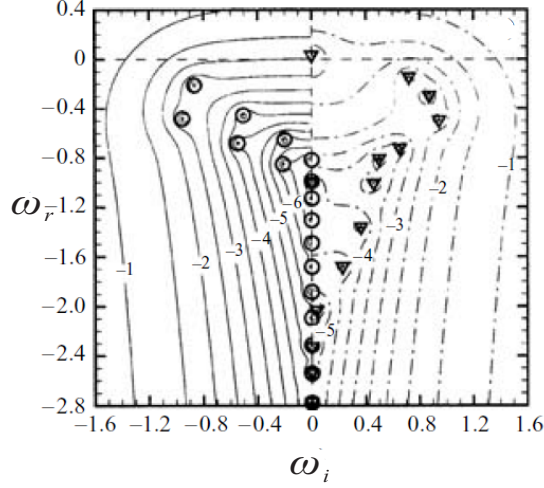


Figure 2.1: Spectra of plane-Couette flow at $Re = 500$, $k = 1.5$ adapted from Ref.[6].

pipe flows.

2.1.2 Global stability theory

In contrast to the local stability theory, the global stability theory is more applicable for real cases in which there is an upstream inlet and a downstream outlet. The base state should

be solved numerically and is much more complex than the base state of a parallel flow (e.g. plane Couette or Poiseuille flow) due to the non-homogeneity of the flow field. The large-scale computation of eigenvalues is the major difficulty in the global theory. Taking the example of a three dimensional problem with spatial grids $N_x \times N_y \times N_z = 50 \times 50 \times 50$, the grid number is on the order 10^5 , and there are four unknowns (i.e. u, v, w, p) at each grid point. If the eigenvalue problem is formulated as

$$\mathcal{A} \mathbf{q} = \omega \mathcal{B} \mathbf{q} \quad (2.4)$$

where $\mathbf{q} = (u, v, w, p)^T$. The size of the matrices \mathcal{A} and \mathcal{B} is about $10^5 \times 10^5$. Therefore, the huge number of eigenvalues is about 10^5 . Since only those eigenvalues close to $\omega = 0$ are concerned, most of these eigenvalues are useless. Moreover, since the data is huge, a numerical strategy for storing data is essential. Thanks to the development of advanced hardware, practical methods have been proposed to deal with this problem in the past few years [8], such as the iterative method. It should be indicated that the global stability of many complex flow systems still remains unexplored. However, although the ‘Global Stability Theory’ is formidable for numerical implementation, it has the same standard steps for stability analysis as the local stability theory.

2.2 Low dimensional modeling

In a microfluidic system, the flow is slow and the Reynolds number is very small, typically $Re < 1$, such that the inertial effect can be ignored. The Navier-Stokes equations can be reduced to the Stokes equations. In many microfluidic systems, the channel width or length is much larger than the channel height. Hence, we can introduce a small parameter into the system $\epsilon = h/L$ where h is the channel height (wall normal direction) and L is a typical length

in the direction perpendicular to the wall-normal direction. In many practical cases, such as multi-phase flow, or droplet production system, the length scale L can be connected to a typical wave length, such as the droplet spacing. Therefore, the system can be asymptotically reduced in power series of the small parameter ϵ . This approach in analyzing the flow systems is called low dimensional modeling.

During the last several decades, such a methodology has been successfully applied for the study of thin liquid films flowing down an inclined plane. There are numerous examples of thin liquid film flow in our daily lives, e.g. rain flowing on glasses and liquid droplets on lotus leaves. In biophysics, an example of liquid film flow is the lung lobe of human beings coated by an ultra thin liquid layer. An even more common phenomenon of thin liquid film flow is tears in human eyes. In industry, the applications of liquid film in coating, cooling systems are widely encountered. In ‘Perspective in Fluid Dynamics’ [9], G.K. Batchelor *et al.* indicated eleven important problems, which were urgent to be solved in fluid mechanics. Among these problems, the dynamics of thin liquid film flow attracted their attention. It should be emphasized here that the thin film flow offers an ideal model for the study of transition to turbulence.

The experimental observation of unstable surface waves in a falling liquid film down an incline was pioneered by the father-son team of Kapitza family [10, 11]. Nonlinear unstable waves were observed in the film flow. Dynamics of the thin film flow can be generally described as follows: a flat film develops at the inlet; as the flat film is not stable, a two-dimensional harmonic wave develops. The two dimensional harmonic wave grows via the nonlinear mechanism which is unstable to the spanwise disturbances. The unstable two dimensional wave develops into three dimensional structures, which exhibits the characteristics of weak turbulence (see Fig.2.2). Theoretical investigation of thin liquid film flow down a plate with inclined angle α was pioneered by Benney [13]. Benney applied the low-dimensional method based on the evidence that the wave length of a typical wave L is much

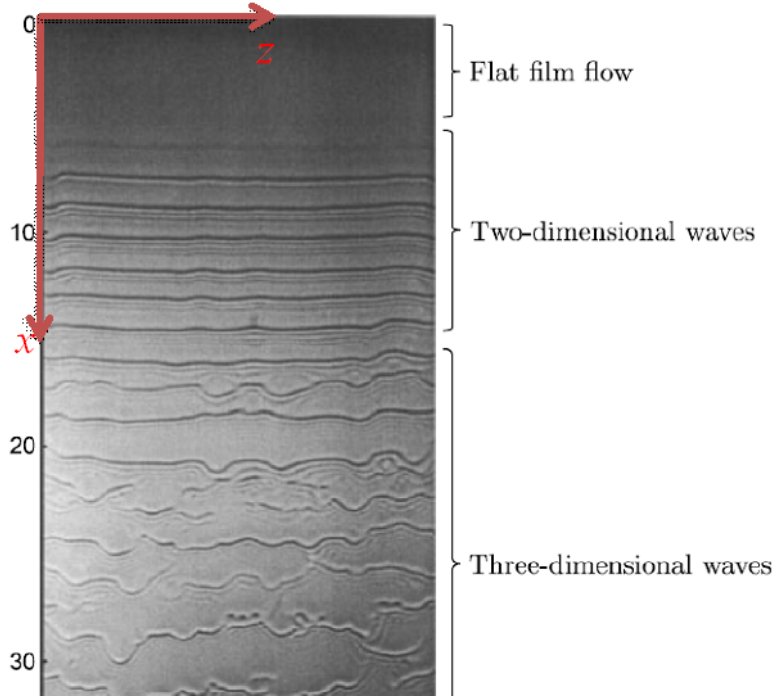


Figure 2.2: Shadow image of waves at $Re = 33$ [12]. One such flow can be often observed in Singapore on raining days from a running liquid film down a slope.

longer than the film mean thickness h_0 wherein the small parameter $\epsilon = h_0/L$ is defined as the film parameter [13]. At the first order approximation, the Benney equation reads:

$$h_t + h^2 h_x + \epsilon \left[\frac{h^3}{6} (-\cot \alpha h_x + \epsilon^2 We h_{xxx}) + \frac{2Re}{5} h^6 h_x \right]_x = 0. \quad (2.5)$$

where h denotes the thickness of the liquid film. However, in Benney's paper [13], he mismatched the order of surface tension γ that the dimensionless Weber number $We = \frac{\gamma}{\rho g h_0^2}$ was assumed to be of order $O(1)$ whence the surface tension term appears in the third order term

which is not appropriate. Hence, It leads to blow-up of solutions in finite time [13]. In the later studies, the Weber number was assumed to have order $O(\epsilon^{-2})$. Thanks to the work of Benney, when a model equation has a similar form as Eq.(2.5), it is referred to as the Benney-type equation. Benney's work has been extended to other systems. For instance, Joo et al. investigated a heated film wherein the evaporating effect was taken into account [14]; Scheid et al. considered the effect of non-uniform heating on the linear and nonlinear dynamics of a falling film by deriving a Benney-type equation [15]; Thiele et al. considered a thin liquid film falling down a porous heated substrate [16]. For a more detailed discussion and application of the Benney-type equation, the readers can refer to the review paper by Oron et al. [17]. The Benney-type equation, generally, is valid when Re is very small, typically $Re = O(1)$. However, when Re is moderate, the Benney-type model usually blows up and gives non-physical solution as indicated by Pumir et al. [18]. This failure is related to the strict slaving of the velocity field to the film thickness h . Although the blow-up phenomenon of Benney equation can be removed by the Padé approximation [19]. However, the regularized equation is in poor agreement with experiments and the data by direct numerical simulation of the full Navier-Stokes equations even though the singularity phenomenon is removed [19].

Shkadov proposed an integral boundary layer (*IBL*) model which introduced one more degree of freedom [20]. In the integral boundary layer model, the Navier-Stokes equations are reduced asymptotically wherein all the second order terms $O(\epsilon^2)$ and higher are neglected (the surface tension term cannot be neglected since the Weber number is assumed to have an order of $O(\epsilon^{-2})$). The streamwise inertia term is of order $O(\epsilon Re)$. The Reynolds number can be assumed to have an order of $O(\epsilon^0) - O(\epsilon^{-1})$, and typically $\epsilon \sim 10^{-2}$. Therefore, the Reynolds number can be up to $Re \sim 10^2$. If $Re \sim O(\epsilon^{-2})$, the full Navier-Stokes equations should be considered because, in the normal momentum equation, the inertia term is of order $O(\epsilon^2 Re)$ which cannot be neglected in this situation. In addition, if $Re \sim O(\epsilon^{-2})$, then $Re \sim 10^4$ provided that $\epsilon = 10^{-2}$. In such a case, the flow is unstable due to the strong viscous shear and

the ‘hard mode’ dominates the instability, i.e. shear mode [21]. In the framework of thin film dynamics, the modeling methodology is valid for the instability of ‘soft mode’, i.e. interfacial mode. The integral boundary layer model solves two coupled equations governing the film thickness h and the local flow rate q :

$$h_t = -q_x, \quad (2.6)$$

$$\delta q_t = h - 3\frac{q}{h^2} - \delta\frac{12qq_x}{5h} + (\delta\frac{6q^2}{5h^2} - \zeta h)h_x + hh_{xxx}. \quad (2.7)$$

Here, $\delta = 3\epsilon Re$ and $\zeta = \epsilon \cot \alpha$ (α is the inclined angle) and $\epsilon^3 We = 1$. Asymptotical expansion of the flow rate equation (2.7) $q = q_0 + \epsilon q_1 + \dots$ does not agree with the Benney equation which implies that if $\alpha \neq \pi/2$, i.e. the plate is moderately inclined, the integral boundary layer model predicts wrong linear stability threshold. The inaccuracy of the integral boundary layer model is due to the assumption of the parabolic velocity profile which causes the error in the prediction of the shear stress at the plate. However, solutions of the integral boundary layer model agree qualitatively with both experimental data and DNS [22]. This method was extended by Kalliadasis to investigate the dynamics of a heated falling film wherein the Marangoni effect on the interfacial instability was discussed [23]. The integral boundary layer model has been extended to study the problem of thin liquid films flowing down vertical cylinders [24, 25].

Motivated by the inconsistency between the integral boundary layer model and Benney equation, Ruyer-Quil and Manneville developed a weighted residual model (R - M model) which addresses the problem successfully [26, 27]. Here, the weighted-residual model is called as the R - M model. The weighted residual model reads:

$$h_t = -q_x, \quad (2.8)$$

$$\delta q_t = -\delta\left(\frac{17qq_x}{7h} - \frac{9q^2h_x}{7h^2}\right) + \frac{5}{6}h(1 - \zeta h_x + h_{xxx}) - \frac{5q}{2h^2}. \quad (2.9)$$

Note that the coefficients in Eq.(2.9) are different from those in Eq.(2.7). To clarify the reason for the difference, reminiscent of the scaled streamwise momentum equation, it writes:

$$3\epsilon Re(u_t + uu_x + vu_y) = -\epsilon p_x + 1 + u_{yy} + O(\epsilon^2). \quad (2.10)$$

The residual of the streamwise equation is written as: $\mathbb{R} = 3\epsilon Re(u_{0,t} + uu_{0,x} + v_0u_{0,y}) - 1 + \epsilon p_x - u_{yy}$. The local flow rate equation (2.7) is obtained by directly integrating the streamwise equation under the assumption of $u \sim (1 - y^2)$. Equation (2.9) is obtained from the Galerkin's method $\int_0^h \mathbb{R} W dy = 0$ to minimize the error of the residual \mathbb{R} where W is the weight function. The weight function for the R - M model Eq.(2.9) is proportional to the velocity profile, whereas the weight function for the integral boundary layer model can be considered as a constant number 1. Asymptotical expansion of Eq.(2.9) recovers Benney's equation Eq.(2.5), which demonstrates the accuracy of the R - M model.

Ruyer-Quil et al. further extended the weighted residual model and revisit the problem of a thin liquid film down a vertical cylinder [28]. The linear stability analysis shows that there is no qualitative difference between the integral boundary layer model and the weighted-residual model when applied to thin liquid films flowing down vertical cylinders. This is due to the fact that the instability is caused by the Rayleigh-Plateau mechanism rather than the fluid inertia. Scheid et al. extended the R - M model to a falling liquid film down a heated inclined plane, wherein the heat convection was neglected by assuming small Prandtl numbers [29]. The comparison between the Benney equation and the weighted residual model as well as the validity of the Benney equation were discussed [29]. Different from the work by Scheid et al. [29], Ruyer-Quil et al. took into account the effect of heat convection and derived three coupled equations governing the film thickness h , the flow rate q and the interface temperature [30]. However, one such study predicts the wrong temperature distribution in the film [30]. Trevelyan et al. further examined the influence of a thicker substrate which was

cooled by the ambient gases on the dynamical behavior of thin liquid films [31]. Trevelyan et al. [31] tried to amend the temperature equation to remove the non-physical results of the temperature equation by using a different weight function. However, their approach was still not very successful [31]. Very recently, Ding and Wong examined the dynamics of a uniformly heated film flowing down a slippery substrate by a weighted-residual model [32]. For more information of the modeling work of thin liquid film flows, the readers can refer to the monograph by Kalliadasis et al. [33].

2.3 Electrohydrodynamical instability

Electrohydrodynamics (EHD) is the study of the relation between the electrodynamics and fluid motion. EHD is also known as EFD (electro-fluid-dynamics) or electrokinetics. EHD covers the following transport mechanisms: electrophoresis, electrokinesis, dielectrophoresis, electroosmosis, and electrorotation. EHD is widely encountered in industrial applications, such as in ink jetting [34] and drug delivery [35]. The study of electrohydrodynamics has a long history. As early as 1882, Lord Rayleigh investigated the equilibrium of conducting liquids in an electric field [36]. In contrast, although “magnetohydrodynamics” (MHD) has a relatively shorter history, it is more commonly known than EHD. The magnetohydrodynamics is of great importance in electricity engineering and theoretical physics, such as in plasma. The original work of MHD was launched by Hannes Alfvén in 1942, for which he received the Nobel Prize in Physics in 1970.

2.3.1 Some Basics of Electrostatics

In this thesis, only electrostatics is considered. The electric field does not change with time or the changing rate of electric field E is very small that the induced magnetic field is negligible.

In the absence of an external magnetic field, the Lorentz force $\mathbf{F} = q_s \mathbf{v} \times \mathbf{B}$ (q_s is the electric charges carried by the fluid parcel) caused by the induced magnetic field is negligible provided that the electric current $\mathbf{J} = \rho_e \mathbf{v}$ (ρ_e is charge density) is not large. The induced magnetic field could not be neglected if the moving speed $|\mathbf{v}|$ of particles approaches the speed of light (see problem 5.16 in the textbook “Introduction to Electrodynamics” by Griffiths [37]). However, such a case does not fall into the scope of this thesis.

In the presence of an electric field, the Maxwell stress is imposed on the liquid particles. For a steady flow, the Maxwell stress is balanced by the viscous stress and pressure which writes in the case:

$$-\nabla p + \nabla \cdot \mathbb{T}^v + \nabla \cdot \mathbb{T}^M = 0. \quad (2.11)$$

In which, $\mathbb{T}^v = \mu(\nabla \mathbf{u} + \nabla \mathbf{u}^T)$ is the viscous stress tensor, and \mathbb{T}^M the Maxwell stress tensor. In the framework of electrostatics, the Maxwell stress tensor is:

$$\mathbb{T}^M = \varepsilon(\mathbf{E}\mathbf{E} - \frac{1}{2}\|\mathbf{E}\|^2\mathbb{I}). \quad (2.12)$$

Here, ε denotes the electric permittivity of the material, \mathbb{I} the identity tensor. Substituting the expression of the Maxwell stress into the stress balance equation (2.11) and taking the operation of divergence, the term $\nabla \cdot \mathbb{T}^M = \mathbf{E}\nabla \cdot (\varepsilon\mathbf{E}) - \frac{1}{2}\|\mathbf{E}\|^2\nabla\varepsilon$. Recall the Gauss’s law:

$$\rho_f = \nabla \cdot \varepsilon\mathbf{E}, \quad (2.13)$$

where ρ_f is the free charge density. Therefore the gradient of Maxwell stress is rewritten as $\rho_f\mathbf{E} - \frac{1}{2}\|\mathbf{E}\|^2\nabla\varepsilon$. Note that the term $\rho_f\mathbf{E}$ is the so-called electric body force. The term $\frac{1}{2}\|\mathbf{E}\|^2\nabla\varepsilon$ is important if the electric permittivity is not uniform in the medium which may be caused by a non-uniform thermal field or the material itself. Here, the dielectrics is assumed to be linear.

The Gauss's law always holds in the form of:

$$\rho_T = \nabla \cdot \varepsilon_0 \mathbf{E}, \quad (2.14)$$

where ρ_T is the total charge density and ε_0 is the vacuum dielectric constant. When an external electric field is imposed on the material, the material is polarized. The polarization of material is related to the strength of the electric field. For many substances, provided \mathbf{E} is not too strong, the polarization is linearly dependent of \mathbf{E} . The dipole moment of manmade materials may depend nonlinearly on \mathbf{E} , especially in modern optical applications. In this thesis, only the linear dielectrics will be considered. For linear dielectrics, the polarization is proportional to the external electric field:

$$\mathbf{p} = \chi_e \varepsilon_0 \mathbf{E}. \quad (2.15)$$

Here, \mathbf{p} is the dipole moment, and χ_e is the electric susceptibility.

The electric charge due to the polarization of substances is related to the dipole moment by

$$\rho_b = -\nabla \cdot \mathbf{p}. \quad (2.16)$$

ρ_b is defined as the bound charge [37].

The total charge ρ_T is the sum of free charge ρ_f and bound charge ρ_b . The free charges can be assumed to be imbedded in the liquids which can move freely or be carried by fluid parcels. In what follows, we will show the assumption that free charges are carried by fluid parcel is important, which simplifies the discussion of the dynamics of flow systems. The bound charges appear in the form of twined electric charges: one positive electric charge with one negative electric charge which are bounded in an electric dipole. Therefore, the Gauss's law can be rewritten as:

$$\nabla \cdot \varepsilon_0 \mathbf{E} = \rho_f + \rho_b = \rho_f - \nabla \cdot \mathbf{p}. \quad (2.17)$$

Furthermore, Eq.(2.13) is modified as:

$$\nabla \cdot \varepsilon_r \varepsilon_0 \mathbf{E} = \rho_f. \quad (2.18)$$

where $\varepsilon_r = 1 + \chi_e$ is the relative permittivity. $\varepsilon_r \varepsilon_0$ is nothing but the electric permittivity of material, i.e. ε . Naturally, the electric displacement \mathbf{D} is defined as:

$$\mathbf{D} = \varepsilon \mathbf{E}. \quad (2.19)$$

Therefore, for linear dielectrics, the Gauss's law has the form of Eq.(2.13).

For electrostatics, the electric field \mathbf{E} is irrotational $\nabla \times \mathbf{E} = 0$. Usually, it is extremely complex to find the solutions of the Gauss equation and the irrotational equation despite their simple expressions. For electrostatics, it is convenient to introduce the electric potential ϕ to solve the problem by simplifying the coupled equations to a one-unknown equation. The electric field is related to the electric potential by:

$$\mathbf{E} = -\nabla \phi. \quad (2.20)$$

In the previous studies of electrohydrodynamics, the liquids are assumed to be perfect conductors, such as mercury; perfect dielectrics, such as oil; leaky dielectrics, such as water. The three models have received many investigations during the last decades. However, these models could not be used to study the dynamics of electrolyte solutions. In the following discussions, review of the three models as well as the electrolyte solution dynamics will be presented.

2.3.2 Perfect Conductors

When a liquid is assumed to be a perfect conductor, the conductivity of the liquid, σ , is infinitely large. Thus, there is no electric charge within the bulk fluid. All the electric charges accumulate at the boundaries of the liquid. Therefore, there is no electric field within the bulk liquid. The electrostatic force should only appear at the boundaries of the liquid. In the previous studies, most of the systems, in which the liquid was assumed to be perfectly conducting, were multi-phase systems, i.e., the liquid contacted with another kind of substance which is not perfectly conducting, for instance air or oil. Especially, the tangential Maxwell stress at the interface should be absent under the assumption of perfectly conducting in the framework of electrostatics because the interface is equipotential and the electric field is perpendicular to the interface. Therefore, the boundary condition of perfect conductors is

$$\phi = \text{constant}. \quad (2.21)$$

Usually, the value of ϕ is given. This condition is of course correct for perfect conductors. Some of the previous works used other conditions for the electric potential at the free surface which seems not consistent with Eq.(2.21) which may confuse the beginners of electrohydrodynamics. It will be shown that these conditions are consistent.

The trend of miniature electric devices stimulate an incredible growth of the study of electrohydrodynamics. One of the most important application is the coating and wetting of solid surfaces. Coating a liquid film has many industrial applications, such as interface protection, heat transfer, micro-lens, growth of insulating film on electric devices, etc.. Some devices may use a liquid droplet as a microlens which is flexible to change its shape compared to the traditional lens. Many approaches have been proposed to control the shape of the liquid drop, for instance: the use of thermocapillary effect [38], or topographical structuring of surfaces [39, 40]. Among all these approaches, the electric field is of particular advantage for the flex-

ibility (electrowetting). A detailed review of electrowetting and its application was provided by Mugele and Baret [41]. It is convenient to simplify the liquid droplet as a perfect conductor, therefore, an electrostatic pressure is imposed on the surface of droplet. The strength of the electrostatic pressure can be controlled by an external electric field. The droplet was considered to be perfectly conducting that the potential at the interface was set to be constant in many of the previous studies [42, 43, 44, 45].

The formation of liquid droplet and surface waves in a perfectly conducting liquid jet or layer in the presence of an electric field have also received much attention. It is interesting to see how the electric field affects the droplet size, surface wave amplitude and surface wave speed. According to the geometry, these previous studies on perfectly conducting liquids can be summarized into two categories. One is the planar flow system and the other is the cylindrical system. For the planar system, it will be interesting to investigate the effect of electric fields on the dynamics of flow system, such as linear stability and transition to turbulence.

The linear stability of a perfectly conducting viscous film falling down an inclined plane was reported by González and Castellanos[46, 47] in a uniform normal electric field. In Ref.[46, 47], a Benney-type equation was derived and the results indicated that the electric field was destabilizing. Their studies demonstrated that the electric field promoted the linear stability as well as the wave speed and amplitude of nonlinear waves [47]. Mukhopadhyay and Dandapat [48] further extended the study [46] to include the effect of fluid inertia. They used an *IBL* model and examined the influence of electric field on the stability [48]. Tseluiko and Papageorgiou [49] performed a direct simulation and revisited the nonlinear dynamics of the system by González and Castellanos [46]. The bifurcation theory approach was employed by Uma and Usha [50] to revisit one such problem via an energy integral model. It should be indicated that the energy integral model is identical to the *R-M* model but the two methods are different in their mathematical methodologies. The authors further extended the study and considered a liquid film flowing down a porous substrate in a normal uniform electric field

[51]. Successively, Uma and Usha investigated the influences of charged surfactants on the dynamical behavior of a contaminated liquid film [52]. The liquid film resting on a horizontal plate under the action of a normal electric field was examined by Tseluiko and Papageorgiou. The linear, the subcritical and supercritical stabilities as well as the nonlinear evolution were documented[53]. It should be noted here that, in Refs.[46, 47, 50, 51, 52], the dimensionless boundary condition for the electric potential at the liquid interface is expressed as:

$$\phi = h - 1. \quad (2.22)$$

It appears that Eq.(2.17) does not agree with the boundary condition Eq.(2.21) as ϕ varies with h . We can decompose the electric field into two parts: the base state $\bar{\phi}$ and the perturbed state ϕ' . The electric potential should be constant at the surface:

$$\phi = \bar{\phi} + \phi' = \text{constant}. \quad (2.23)$$

Taking the basic electric field from Refs.[50, 51] for example, $\bar{\phi} = E_0(h_0 - z)$ where E_0 is the electric field strength of the imposed field and h_0 is the mean thickness of the liquid film. When the surface is perturbed, $\bar{\phi}$ can be written as $E_0(h_0 - h)$. To fulfill Eq.(2.21), the condition for ϕ' :

$$\phi' = \text{constant} - E_0(h_0 - h). \quad (2.24)$$

The constant value is usually chosen to be zero, and $\phi' = E_0(h - h_0)$. Taking the mean thickness of liquid film as the length scale and $E_0 h_0$ as the potential scale, the condition Eq.(2.22) is obtained as described in Refs.[50, 51].

There are two typical cylindrical flows: liquid jet and liquid films flowing down a vertical cylinder. Liquid film flow on a cylinder without an electric field has been investigated extensively in the past decades. Significant advances have been made in the theory of the breakup

of a liquid jet into droplets after the seminal work of Lord Rayleigh [54]. It is of great interests to manipulate the droplet size and breakup time of jets. The influence of an electric field on the breakup of liquid jets was investigated and pioneered by Basset [55]. Basset's analysis showed that electrostatic stresses were stabilizing in the long wave regime while it is destabilizing in the short wave regime. However, Basset's result did not agree with experimental observation. Taylor corrected the error in the analysis of Basset [56]. Saville examined the stability of perfectly conducting Newtonian jets in a radial electric field subjected to infinitesimal axisymmetric and non-axisymmetric disturbances [57]. Results by Saville demonstrated that non-axisymmetric unstable mode can be supported by an external electric field [57]. In the absence of an electric field, the jet is always unstable axisymmetrically. Cloupeau and Prunet-Foch [58] studied droplet formation in a cone-jet flow. The influence of the electric field was found to modify the diameter of the jet as well as the size of droplet. The experimental study of Cloupeau and Prunet-Foch demonstrated that the sinuous mode became the most unstable when the viscosity was high [58] which was called kink instability. Son and Ohba [59] studied the instability of electrohydrodynamic spraying theoretically and experimentally. They found that the axisymmetric mode was dominant when the electric field was not strong; while the most unstable mode shifted to the nonaxisymmetric mode as the electric field increased [59]. Son and Ohba's study showed that the theoretical results compared well with the experimental observation for axisymmetric breakup of the liquid jet; while the value of breakup wavelength from experiment was longer than that from the theoretical analysis for nonaxisymmetric mode [59]. Breakup of perfectly conducting electrified jets was revisited by Collins et al. [60] who analyzed the nonlinear dynamics of jet and numerically simulated the formation of droplet by a one-dimensional model. The one dimensional model was derived using the *WKB* method and one can refer to the work of Eggers [61]. Wang and Papageorgiou [62] considered the a perfectly conducting liquid thread surrounded by an insulating liquid layer in a *DC* electric field, and investigated the influence of the dynamics of the surrounding

layer. Conroy et al. [63] investigated the dynamics of a perfectly conducting liquid thread in an AC electric field but considered an electrostatic problem. The authors have verified that the approximation of electrostatics is valid provided the frequency is not too high [63]. Very recently, Ding et al. investigated a perfectly conducting liquid film falling down a vertical fiber in a radial electric field [64]. The detailed results will be presented in Chapter 3.

2.3.3 Perfect Dielectrics

In perfect dielectrics, there is no free charge and all the charges are bounded in the form of electric dipoles. Perfect dielectric liquid is non-conducting, i.e. insulating. Since there is no free charge in the liquids, the tangential Maxwell force vanishes at the liquid interface. However, the normal Maxwell force at the interface can be nonzero due to the mismatch of electric permittivities of different liquids. Here, we show the Maxwell stress at an interface separating two immiscible liquids (see Fig.2.3):

$$\mathbf{n} \cdot (\mathbb{T}_2^M - \mathbb{T}_1^M) \cdot \mathbf{n}, \quad (2.25)$$

where \mathbf{n} is the surface normal and $\mathbb{T}_i^M (i = 1, 2)$ represents the Maxwell stress tensor in liquid “1” and liquid “2” respectively. This term is usually called as electrostatic pressure and nonzero when $\varepsilon_1 \neq \varepsilon_2$.

For the perfect dielectrics model, the continuities of electric potential and electric displacement at the interface give:

$$\phi_1 = \phi_2, \quad \varepsilon_1 \mathbf{E}_1 \cdot \mathbf{n} = \varepsilon_2 \mathbf{E}_2 \cdot \mathbf{n}. \quad (2.26)$$

The boundary condition (2.26) indicates the tangential electric field is continuous while the normal electric field may be discontinuous across the interface. Clearly, the tangential electric force can be expressed as $\mathbf{F}_t = q_s \mathbf{E}_t$ where q_s is the charge density at the interface, \mathbf{E}_t

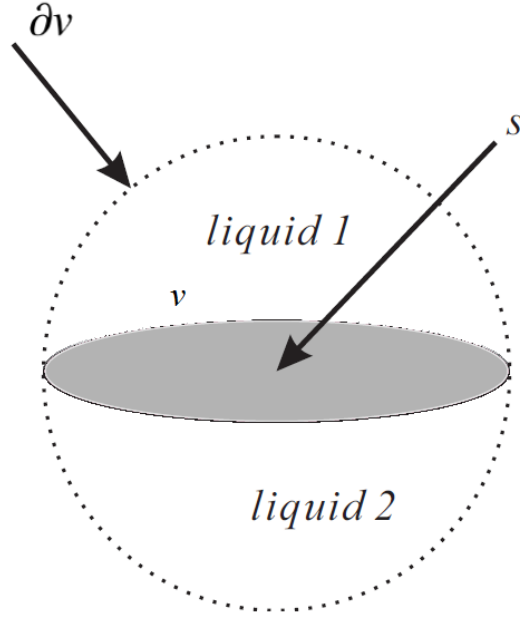


Figure 2.3: A sketch of two immiscible liquids separated by an interface.

is the tangential electric field and \mathbf{t} is the tangential vector. Hence, a common physical phenomenon that the perfect conductor model and perfect dielectrics model share is that there is no tangential Maxwell stress at the interface. The difference is obvious. For the perfect conductor model, free charge exists on the interface, while no free charge exists at the interface for perfect dielectrics model.

The studies of perfect dielectric liquids can be divided into two groups: the planar and cylindrical systems. Since there is no free charge within the bulk fluid regions, these previous studies were all devoted to the interfacial instability in multi-fluid systems. It should be noted that the normal Maxwell stress is balanced by the surface tension. In planar systems, the surface tension is stabilizing the interface. In cylindrical systems, due to the azimuthal curvature, the surface tension is destabilizing the interface. Therefore, in a planar system, if the electrostatic pressure enhances the effect of surface tension, then the electric field sta-

bilizes; otherwise, it destabilizes the interface. However, in a cylindrical system, the effect of electric field on the interfacial instability is opposite. Melcher and Schwarz investigated the effect of a tangential electric field on the linear stability of a sharp interface separating two perfectly dielectric fluids [65]. The authors formulated the problem in the framework of electrodynamics, but an electrostatic field was assumed to facilitate their analysis [65]. The two liquids were assumed to be non-bounded, i.e. there is no solid bounds in their system [65]. This research [65] is of great importance because it established the benchmark model of EHD for the multi-fluid systems. A perfectly non-conducting liquid jet in a radial electric field was investigated by Setiamwan and Heister [66]. The electric field was established by the charged cylindrical surface [66]. The influences of the Maxwell stress on the droplet size through linear stability analysis and numerical simulation were reported previously [66]. The influence of the electric field on the breakup of a planar inviscid liquid sheet was examined by El-Sayed wherein the dynamics of surrounding gases was included [67]. Tilley et al. [68] revisited the problem [67] by the lubrication theory and derived a model equation to study the nonlinear behavior of the liquid sheet, when it was perturbed by small disturbances. The results demonstrated that the electric field can delay the rupture of the liquid sheet [68]. The study [68] was extended by Savettaseranee et al. [69] and the influence of electric field on the rupture of liquid sheet caused by van der Waals forces was examined. Papageorgiou and Vanden-Broeck [70] further examined the nonlinear waves of arbitrary amplitudes and wavelengths in the system [67]. Results showed that the electric field can have a pronounced effect on the shapes and speeds of interfacial waves [70]. It is worthy to note that the results of direct numerical simulation are in excellent agreement with that obtained from the low-dimensional model, when the wavelength is long [70].

Pattern formation in perfectly non-conducting liquid films induced by an electric field was reported by Schäffer et al. [71]. Morariu et al. investigated the hierarchical structure formation and pattern replication in three layered thin non-conducting liquid films. Further works

were carried out by Verma et al. [73] and Wu et al. [74]. Verma et al. numerically and experimentally investigated the pattern formation in the thin film by a lubrication model and considered the influence of homogeneous and heterogeneous electric fields [73]. Wu et al. considered the influences of van der Waals attractions and investigated the pattern formation phenomenon in the system [74]. Tseluiko and Blyth examined the inertial effect on the stability of non-conducting liquid film flow on a wavy substrate by stability analysis of the fully linearized system and a Benney-type equation [75]. Electrowetting by a non-conducting liquid droplet was investigated by Yeo and Chang wherein a lubrication model was proposed to study the dynamics of contact lines which demonstrated that the electric field promoted the spreading speed [76].

2.3.4 Leaky Dielectrics

The leaky dielectric model was first proposed by Taylor in the 1960s based on the evidence that even a small conductivity in the liquid could allow electric charges to accumulate at the interface [77]. Detailed review of the mathematical model of the leaky dielectrics is provided by Saville [78]. The term “leaky” dielectric fluids refer to poorly conducting liquids. Under the assumption of leaky dielectrics [77], free charges only accumulate at the liquid interface; while there is no free electric charge within the bulk region. Therefore, the main distinction between the leaky dielectrics and the perfect dielectrics relies on the presence/absence of the free interfacial charges.

In the framework of electrostatics, the conservation of electric current reads:

$$\frac{d}{dt} \left(\int_v \rho_e dv + \int_s q_s ds \right) + \int_{\partial v} \sigma \mathbf{E} \cdot d\mathbf{S} = 0, \quad (2.27)$$

where the liquid is Ohmic (see the electric current flux $\sigma \mathbf{E}$) and charge diffusion is neglected. The symbol q_s stands for surface charge density, s the interface, and ∂v the boundary of the

small control volume v (See Fig.2.3), σ the electric conductivity.

Applying the divergence theorem, the charge conservative equation is rewritten as:

$$\frac{d}{dt} \int_v \rho_e dv + \int_v \nabla \cdot \sigma \mathbf{E} dv + \frac{d}{dt} \int_s q_s ds - \int_s (\sigma_2 \mathbf{E}_2 - \sigma_1 \mathbf{E}_1) \cdot d\mathbf{s} = 0, \quad (2.28)$$

where $d\mathbf{s} = \mathbf{n} ds$.

Therefore, in the bulk region, the charge conservation equation for incompressible fluids has the differential form

$$\frac{D\rho_e}{Dt} + \nabla \cdot \sigma \mathbf{E} = 0, \quad (2.29)$$

where $\frac{D}{Dt} = \frac{\partial}{\partial t} + \mathbf{u} \cdot \nabla$ is the material derivative.

When it is applied to the interface, the conservation of surface charge writes [78]:

$$\frac{\partial q_s}{\partial t} + \nabla_s \cdot q_s \mathbf{u}_s + q_s (\nabla \cdot \mathbf{n})(\mathbf{u} \cdot \mathbf{n}) = (\sigma_2 \mathbf{E}_2 - \sigma_1 \mathbf{E}_1) \cdot \mathbf{n}, \quad (2.30)$$

where $\nabla_s = \nabla - \mathbf{n}(\mathbf{n} \cdot \nabla)$ is the surface gradient operator, and $\mathbf{u}_s = \mathbf{u} - (\mathbf{u} \cdot \mathbf{n})\mathbf{n}$ is the surface velocity. The interface is assumed to be a material surface.

In many previous studies, the surface charge conservation law Eq.(2.30) is usually expressed as:

$$\frac{\partial q_s}{\partial t} + \nabla_s \cdot q_s \mathbf{u} = (\sigma_2 \mathbf{E}_2 - \sigma_1 \mathbf{E}_1) \cdot \mathbf{n}. \quad (2.31)$$

Here, it is necessary to comment on the conservative equation of the surface charges Eq.(2.31).

First, the temporal derivative $\frac{d}{dt} ds = \nabla \cdot \mathbf{u} ds - \mathbf{n}(\mathbf{n} \cdot \nabla) \cdot \mathbf{u} ds$. Denoting $\nabla_n = \mathbf{n}(\mathbf{n} \cdot \nabla)$, it gives $\frac{d}{dt} ds = \nabla_s \cdot \mathbf{u} ds$. The problem now is how to evaluate the derivative $\frac{dq_s}{dt}$. If $q_s = q_s(x, y, t)$ that the surface is single-valued with respect to the (x, y) plane, then $\frac{dq_s}{dt} = \frac{\partial q_s}{\partial t} + \mathbf{u} \frac{\partial q_s}{\partial x} + \mathbf{v} \frac{\partial q_s}{\partial y} = \frac{\partial q_s}{\partial t} + \mathbf{u} \cdot \nabla q_s$ where u or v respectively represents the velocity in x or y direction. From this point of view, the conservative condition Eq.(2.31) may be not exact or correct. However, in

many cases, the interfacial wave is long, the difference does not come into play in linear or nonlinear up to $O(\epsilon^2)$ analysis [79].

Since the leaky dielectric fluids is considered, there is no net charge density in the bulk region and the electric potential follows the solution of Laplace's equation:

$$\nabla^2 \phi = 0. \quad (2.32)$$

At the boundary, continuity of electric potential and the Gauss's law give

$$\phi_1 = \phi_2, \quad \varepsilon_1 \mathbf{E}_1 \cdot \mathbf{n} - \varepsilon_2 \mathbf{E}_2 \cdot \mathbf{n} = q_s. \quad (2.33)$$

It is clear that the tangential electric field is continuous across the interface.

The leaky dielectric model has received numerous investigations after the pioneering work of Taylor [77]. In the following context, studies of EHD of leaky dielectric fluids in a planar flow system and a cylindrical flow system are reviewed. The interfacial instabilities of leaky dielectric fluids subjected to tangential and normal electric fields were respectively studied by Melcher and Schwarz [65] and Melcher and Smith [80] (Melcher and Schwarz's model is valid to study the electrodynamics of leaky dielectric liquids.). Experimental study by Ozen et al. [81] demonstrated that the size of a droplet in a two-immiscible-liquid system can be controlled by altering the strength of the electric field. Abdella and Rasmussen [82] investigated the instability of two unbounded superposed fluids in a normal electric field. Results of the linear stability analysis showed that the instability is significantly affected by the electric field which can be characterized by the conductivity ratio between the two liquids. Long-wave stability of two initially stationary superposed immiscible leaky dielectric liquids was investigated by Shankar and Sharma by a lubrication model [83]. This model [83] was then extended to a pressure-driven flow system [84]. It was found that the electric field either sta-

bilized or destabilized the system which was dependent on the electric properties of the two liquids [83, 84]. Li et al. [85] extended the problem to the regime of a large flow rate. Different from the work of Ozen et al. [84], the charge relaxation time was assumed to be far smaller than the viscous relaxation time [85]. The stability criterion proposed by Ozen et al. [84] was invalid in the presence of tangential Maxwell stress [85]. A detailed study on the linear stability was conducted to demonstrate that the tangential Maxwell stress significantly affects the unstable mode caused by viscosity stratification [85]. Instead of the normal electric field, Uguz and Aubry [86] considered a tangential electric field and revisited the electrohydrodynamic instability in two immiscible dielectric liquids. Detailed comparisons on the tangential and normal electric field's influence on the interfacial instability were reported [86].

Artana et al. [87] analyzed the dynamics and stability of a leaky dielectric liquid jet surrounded by a non-conducting gas. The influences of injection velocity and surface tension on the linear stability were discussed [87]. Burcham and Saville [88] investigated the instability of leaky dielectric liquid bridge surrounded by dielectric gas in an axial electric field. Li et al. [89] investigated the temporal instability of a two-coaxial liquid jet surrounded by perfect dielectric gases under the influence of a radial electric field. Fluids in the core liquid cylinder was assumed to be perfect dielectrics, and fluids in the annulus cylinder were assumed to be leaky dielectrics. The instability of the liquid jets was discussed theoretically and numerically. The results were found that the liquid viscosity had a negligible effect on the cutoff wave number [89]. However, the electric field significantly affects the cut-off wave number. López-Herrera et al. [90] investigated the instability of two co-axial fluids in a cylindrical duct. The interface was assumed to be uniformly charged initially [90]. This model [90] was extended by Wang to a leaky dielectric thread surrounded by insulating annular fluids in which the long-wave dynamics was examined [91].

Recently, Wray et al. [92, 93] studied a leaky-dielectric liquid film falling down a vertical cylinder driven by gravity. The liquid film was surrounded by leaky-dielectric gases.

However, the dynamics of the gas phase was neglected and a one-sided asymptotic model was proposed. The influence of a radial electric field on the interfacial stability was studied by a Benney-type model. Wray et al. [94] further extended their study and examined the interfacial dynamics subjected to non-axisymmetric disturbances. It was reported that the non-axisymmetric mode could be supported by the electric field [94]. It is noteworthy that all these studies of perfectly conducting films [64] or poorly conducting films [92, 93, 94] were all restricted in the small flow rate regime. No investigation has been devoted to the moderate flow rate or high flow rate regimes. It is noted that, in these studies [64, 92, 93, 94], the Laplace equation was reduced asymptotically. This may be inappropriate when the gap between the liquid interface and the outer electrode is large.

In the pressure driven two-fluid core-annular flow system, the interface may be unstable due to the azimuthal curvature and viscosity stratification. The former is well-known as Plateau-Rayleigh instability (capillary instability); while the latter is interface wave instability caused by a jump in viscosity across the interface. The core annular flow system is of potential applications, such as in pumping crude oil through pipelines by using a less viscous liquid for lubrication where a stable liquid-liquid interface is required. The instability of two immiscible core-annular liquid layers in a pipe was pioneered by Joseph and his coworkers [95, 96] who found that, the stratification of viscosity either destabilizes or stabilizes the system. Selvam et al. extended the study to consider the instability of miscible core-annular flows with viscosity stratification [97]. In these studies [95, 96, 97], the inner liquid layer acts as the core while Dijkstra investigated two annular liquid layers surrounding a thin wire core in a pipe [98]. The instabilities due to capillary, viscosity stratification and viscous shearing were investigated [98]. Dijkstra found that the inserted core played an important role in determining the unstable mode due to the changes in the velocity profile. In addition, the mathematical singular point at the centerline $r = 0$ is removed by the inserted core. The flow system is unstable which can either be in capillary mode (Plateau-Rayleigh instability) or interface wave mode

(caused by viscosity stratification) from small to moderate Reynolds number [98]. The capillary mode could be impeded by the mean shear flow, i.e. as the Reynolds number increases, the capillary mode can be completely stable. When the Reynolds number is very large, the system may be unstable due to viscous shear [98]. Here, it is worth mentioning that even for a single layer flow in such an annulus channel, the flow could be linearly unstable due to the viscous shear which is significantly different from the canonical pipe flow. In Refs.[90, 91], the inner liquid layer was injected into the pipe with a uniformly charged surface. Such a method introduces an electric field in the outer liquid layer while there is no electric field within the inner layer. In the core-annular flow system [98], a radial electric field can be imposed between the inserted thin metal wire and the outer electrode which is more convenient. Recently, Ding et al. extended the study [98] to consider the effect of a radial electric field [99]. The results demonstrated that the capillary mode and the interface wave mode could be completely stabilized by the electric field [99]. Detailed results will be presented in Chapter 4.

2.3.5 Electrolyte solutions

In industrial applications, mixing of different liquids in a microfluidic system is very important. The Reynolds number Re is small in microfluidics, typically $Re \ll 1$. The flow is laminar and mixing due to turbulence will not occur. The use of an electric field has been a successful approach for enhanced mixing [100]. In microfluidics, the application of electrohydrodynamic mixing is based on gradients of electric conductivity since the mechanical techniques are not suited to obtaining mixing for the requirement of prohibitive amounts of power. Electric conductivity can be developed due to a superimposed electric field. The local ionic concentration, pH value, and conductivity gradients develop along the axis of the imposed electric field and the local conductivity could vary by more than an order of magnitude over a length of 1 mm [101]. Obviously, the electric conductivity σ of electrolyte liquids is a function of the

concentration of local ions which is the major distinction of electrolyte liquids. It is different from the previous models introduced in this thesis: for perfect conducting liquids, electric conductivity $\sigma \rightarrow \infty$; for non-conducting liquids, $\sigma = 0$; for poorly-conducting liquids, σ is small but constant. The pioneering work on the dynamics of electrolyte solutions was formulated by Hoburg and Melcher [102] and Hoburg [103]. For more information, the readers can refer to the monograph by Melcher (Ref.[104]) in which detailed mathematics and physics on electro-hydrodynamics were documented. In Refs.[102, 103], the conductivity profile is governed by convection equation, in which, the diffusion of conductivity is neglected provided that the time scale for diffusion of ions is much longer compared to the viscous response time. Baygents and Baldessari [101] dropped the assumption of long time diffusion of ions [102, 103], and adopted the diffusion of ions. It was indicated by them that the diffusion term is critical in determining a correct stability threshold. Baygents and Baldessari proposed that the occurrence of instability was triggered by the dielectrophoretic effect [101]. They found that the lower conductivity boundary had a strong stabilizing effect when the conductivity gradient was large [101]. It should be noted that the assumption of exchange of stability made by Baygents and Baldessari [101] was incorrect because the critical unstable mode may be oscillatory. The unstable mode may be oscillatory which was indicated by Chang et al. [105]. In their analysis [105], Chang et al. considered the influence of a parabolic base flow. While the instability mechanism can be analogue to the classical Rayleigh-Bénard instability in a heated fluid layer, the physical mechanism is much more complex. For instance, in a single heated fluid layer where one imposes a shear flow, the critical unstable mode is always dominated by the longitudinal mode, which is independent of the shear flow [107, 108], while the critical unstable mode in the liquid layer with an electric conductivity gradient depends on the shear flow heavily. Chang et al. found that when the Reynolds number was slightly increased from zero, the instability was enhanced since the shear flow enhanced the dielectrophoretic effect and the transverse mode (zero spanwise wave number) became critical

rather than the longitudinal model (zero streamwise wave number) [105]. However, as the Reynolds number increased further, the longitudinal mode became critical, and the critical mode was independent of the shear flow. Chang et al. reported in their paper that the critical unstable mode was oscillatory when the conductivity gradient was small, but it switched to the stationary mode as the conductivity gradient increased [105]. Ruo et al. extended the model [101] to a rotating system and found that the rotation stabilized the flow, while the electric field destabilized the flow [106]. Recently, Ding and Wong investigated the instability of an annular liquid layer with electric conductivity gradients. Their results showed that the critical unstable mode depended on the geometry of the duct and the critical unstable mode may be either stationary or oscillatory [109]. Detailed results and discussion will be presented in Chapter 5.

Unlike the studies of Baygents and Baldessari [101], Chang et al. [105], Ruo et al. [106] and Ding and Wong [109], in which the electro-convection was triggered due to a spatial gradient in the electric conductivity, Lin et al. [100] considered two miscible flows with an electric conductivity stratification. To achieve such a conductivity stratification flow in experiments, Lin et al. [100] used two electrolytes with different ionic concentrations (see Fig.2.4). The liquids were pumped into the channel using a syringe pump. A Couette flow arose from a tangential electric field due to the electro-osmosis phenomenon after removing the pressure gradient. The electro-osmosis phenomenon was treated as a slippery boundary condition and the slip velocity was related to the zeta potential in the electric double layer. However, the electro-osmosis flow was rather weak. They investigated the linear stability by assuming a quasi-steady base flow and verified their results via a direct numerical simulation. A depth-averaged model was proposed by Storey et al. [111] to investigate the electrohydrodynamical instability in a square pipe. Although the depth-averaged model simplified the problem to a two-dimensional flow, it showed good agreement with the three-dimensional results [111]. The convective and absolute electrokinetic instability with a conductivity stratification was

extended by Chen et al. [110]. Chen et al. used aqueous electrolytes of 10:1 conductivity ratio and applied a streamwise electric field [110]. The two-dimensional instability was studied via a thin-layer assumption that the channel width was much larger than the channel depth. Santos and Storey extended the studies to a flow with streamwise conductivity gradients and investigated the linear instability as well as the nonlinear evolution [112]. Notably, in these studies (Baygents and Baldessari[101]; Chang et al. [105]; Ruo et al. [106]) adopted non-slippery conditions, while in other studies (Lin et al. [100]; Chen et al. [110]; Storey et al. [111]; Santos and Storey [112]) considered a slippery boundary condition. The latter focused on the stability of electro-osmosis flow.

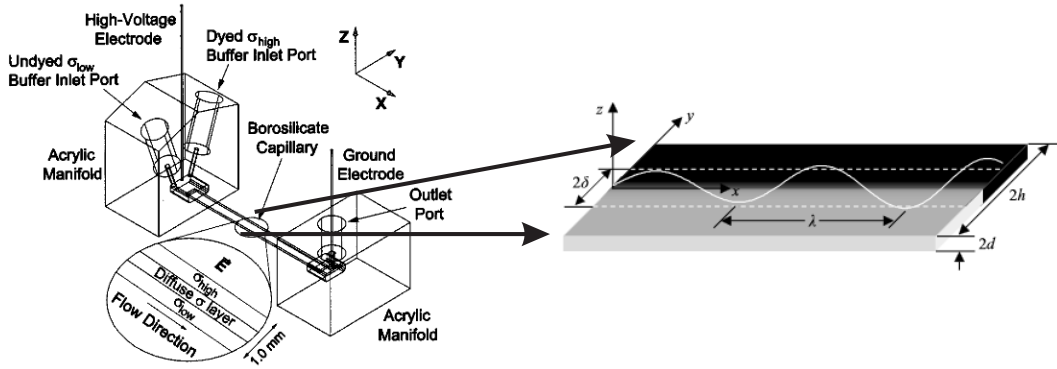


Figure 2.4: Experimental setup of two miscible liquids in electrokinetic flow [100].

The electro-osmotic flow is conceptually explained by Figure 2.5. The electric field induced by free ions is very weak and the ions follows the Boltzmann distribution. In a narrow boundary layer, the charge density is non-zero, while in the main bulk region the liquid is electrically neutral. This boundary layer is the so-called electro-double layer (EDL). In the presence of a tangential electric field, the bulk liquids would slip on the boundary, and therefore a plug flow is formed (see Figure 2.5). The electroosmosis has a potential application in microfluidic systems, such as electro-pump. Many studies of the stability of electro-osmotic flows have been carried out.

The first study of the influence of EDL on the stability of thin inviscid planar electrolyte

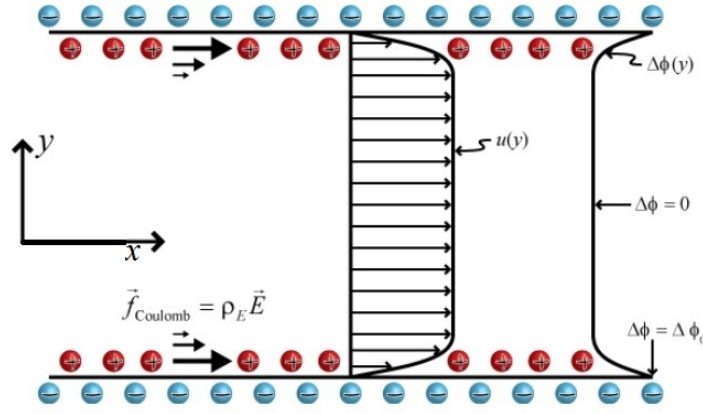


Figure 2.5: Electroosmotic flow arises from an external tangential electric field. From <http://www.kirbyresearch.com/index.cfm/wrap/textbook/microfluidicsnanofluidicsch6.html>.

films was carried out by Felderhof [113]. Two different unstable modes were discussed by Felderhof [113]: the stretching mode and squeezing mode. The EDL was found to destabilize the stretching mode, but stabilize the squeezing mode [113]. Extension work was investigated with considering the viscous effect [114]. Georgiou et al. [115] investigated the stability of an annular electrolyte film and discussed two cases: double layer repulsion and attraction. Double layer repulsion was stabilizing while attraction was destabilizing [115]. Conroy et al. [116] investigated the stability of two co-axial electrolyte liquids in a pipe. They formulated the problem in a more general way. The Nernst-Planck equation was used to describe the motion of ions [116]. The model was then extended by Conroy et al. [116] to study the dynamics of a fouled interface by charged surfactants [117]. It is worth mentioning that, these studies (Felderhof [113], Georgiou et al. [115], Conroy et al. [116, 117]) were all concentrated on the interfacial instability. In the previous studies, the investigation of the stability of multi-layered electrolyte flow has remained very limited although it has received much attention now (see the review paper by Lin [118]). Recently, Ding and Wong [119] investigated the instability of two miscible fluids in a circular pipe with an electric conductivity stratification subjected to an axial electric field. This study will be presented in Chapter 6.

There are other approaches to induce convection in liquid layers beyond the above reviewed

approaches. For instance, using a thermal field coupled with an electric field which is useful in a micro-gravity environment [120, 121, 122]. Another approach could be injecting charges into the fluid layers such that the electric body force can initiate a circulation flow [123]. This method is very useful in the study of dynamics of a nematic layer in an electric field [123]. However, these studies has remained very limited to this date, especially for multi-fluid systems.

CHAPTER 3

Dynamics of liquid films on vertical fibers in a radial electric field

3.1 Mathematical formulation

A perfectly conducting Newtonian liquid film flowing down a vertical fiber is shown in Figure 3.1. The annular flow system is enclosed in a co-axial cylindrical electrode. A high voltage is applied at the outer electrode, while the metal fiber is grounded. Liquids that flow down the fiber under gravity are surrounded by a dielectric gas. The radii of fiber and electrode are $r = a$ and $r = b$, respectively.

In this Chapter, the axisymmetric problem is considered. The cylindrical coordinates (r, z) are chosen. The motion of liquids is governed by the continuity equation and the momentum equation as below,

$$\nabla \cdot \mathbf{u} = 0, \quad (3.1)$$

$$\rho \frac{D\mathbf{u}}{Dt} = -\nabla p + \mu \nabla^2 \mathbf{u} + \rho \mathbf{g}, \quad (3.2)$$

where $\mathbf{u} = u\mathbf{e}_r + w\mathbf{e}_z$ is the velocity. $\frac{D}{Dt} = \frac{\partial}{\partial t} + u\frac{\partial}{\partial r} + w\frac{\partial}{\partial z}$ is the material derivative operator. ρ is the density of the liquid and μ is the dynamic viscosity. \mathbf{g} denotes the gravitational acceleration. The surrounding dielectric gas is assumed to be inviscid whose dynamics is neglected.

Since the electrostatics is considered, the electric potential ϕ in the dielectric gas follows the

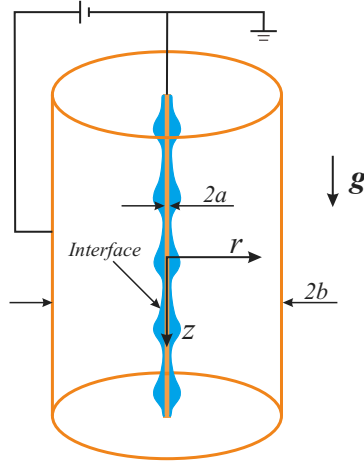


Figure 3.1: Geometry of the system.

solution of Laplace's equation:

$$\nabla^2 \phi = 0. \quad (3.3)$$

On the surface of the fiber $r = a$, there are no-slip and no-penetration conditions,

$$u = w = 0. \quad (3.4)$$

Since the electric potential at the interface $r = a + h(z, t)$ is equipotential under the assumption of perfectly conducting liquids, therefore

$$\phi = 0. \quad (3.5)$$

A high electric potential is imposed at the outer electrode,

$$\phi = \phi_0. \quad (3.6)$$

At the liquid ring's interface $r = a + h(z, t)$, the stress balance condition is expressed as:

$$(\mathbb{T}_l - \mathbb{T}_g) \cdot \mathbf{n} = -\gamma(\nabla \cdot \mathbf{n})\mathbf{n}, \quad (3.7)$$

where \mathbb{T}_l or \mathbb{T}_g is the stress tensor in the liquid phase and gas phase respectively, and $\mathbb{T}_i = -p_i\mathbb{I} + \mathbb{T}_i^v + \mathbb{T}_i^M$ ($i = l, g$). p_i ($i = l, g$) represents the pressure in the liquid or gas phase. $\mathbb{T}^v = \mu[\nabla \mathbf{u} + (\nabla \mathbf{u})^T]$ is the Newtonian stress tensor which is zero in the gas phase. In the liquid phase, the Maxwell stress is absent under the assumption of a perfectly conducting liquid film. In the gas phase, because the electrostatics is considered, the Maxwell stress $\mathbb{T}^M = \varepsilon[\mathbf{E}\mathbf{E} - \frac{1}{2}(\mathbf{E} \cdot \mathbf{E})\mathbb{I}]$. \mathbb{I} is the identity tensor and ε is the electric permittivity of the gas. γ represents the surface tension. \mathbf{n} denotes the surface normal.

Finally, the system is closed by the kinematic condition of interface,

$$h_t + wh_z = u. \quad (3.8)$$

3.2 Scaling and the asymptotic model

The aim of this Chapter is to solve the above equations (3.1)-(3.8) in the long-wavelength limit. It assumes that the radius of the fluid ring $\mathcal{R} = a + h_0$ (h_0 is the initial thickness of the liquid) is much smaller than its characteristic length \mathcal{L} in the axial direction. Craster and Matar took the length scale \mathcal{L} to be related to the capillary length: $\mathcal{L} = \gamma/\rho g \mathcal{R}$, so that the dimensionless equations would not rely on the fluid thickness being small relative to the fiber radius, but small relative to a dynamic length scale [124]. The equations (3.1)-(3.8) are non-dimensionalized by adopting the following scales: $r = \mathcal{R}r'$, $z = \mathcal{L}z'$, $p - p_g = \rho g \mathcal{L} p'$, $\phi = \phi_0$, $w = Ww'$, $u = \epsilon W u'$, $t = \mathcal{L}/W t'$ where $W = \rho \mathcal{R}^2 g / \mu$ is the velocity scale and $\epsilon = \mathcal{R}/\mathcal{L}$.

After dropping the primes of the dimensionless variables, the dimensionless forms of the governing equations (3.1)-(3.3) become

$$r^{-1}(ru)_r + w_z = 0, \quad (3.9)$$

$$\epsilon^4 Re \frac{Du}{Dt} = -p_r + \epsilon^2(u_{rr} + \epsilon^2 u_{zz} + \frac{1}{r}u_r - \frac{u}{r^2}), \quad (3.10)$$

$$\epsilon^2 Re \frac{Dw}{Dt} = 1 - p_z + (w_{rr} + \epsilon^2 w_{zz} + \frac{1}{r}w_r), \quad (3.11)$$

$$\phi_{rr} + \frac{1}{r}\phi_r + \epsilon^2 \phi_{zz} = 0, \quad (3.12)$$

where $Re = \frac{\rho W \mathcal{L}}{\mu}$ is the Reynolds number. Here, the gap between the liquid interface and the outer electrode is assumed to be much smaller than the characteristic length \mathcal{L} [62].

The dimensionless boundary conditions at $r = \alpha$ are,

$$u = w = 0. \quad (3.13)$$

The dimensionless radius is $\alpha = \frac{a}{\mathcal{R}} < 1$. When α is small, the liquid layer is relatively thicker than the fiber. When $a \rightarrow 1$, the liquid film is thin compared to the fiber radius.

At the interface $r = \alpha + h(z, t)$, the dimensionless stress balance conditions are

$$(\epsilon^2 u_z + w_r)(1 - \epsilon^2 h_z^2) + 2\epsilon^2 h_z(u_r - w_z) = 0, \quad (3.14)$$

$$-p - \frac{2\epsilon^2[(w_r + \epsilon^2 u_z)h_z - u_r - \epsilon^2 w_z h_z^2]}{1 + \epsilon^2 h_z^2} - \frac{\epsilon \mathcal{E}[\frac{1}{2}(\phi_r^2 - \epsilon^2 \phi_z^2)(1 - \epsilon^2 h_z^2) - 2\epsilon^2 \phi_r \phi_z h_z]}{1 + \epsilon^2 h_z^2} = \epsilon(2H\mathcal{S}), \quad (3.15)$$

where $2H = -\frac{1}{(h+\alpha)(1+\epsilon^2 h_z^2)^{1/2}} + \frac{\epsilon^2 h_{zz}}{(1+\epsilon^2 h_z^2)^{3/2}}$ is the curvature. $\mathcal{E} = \frac{\varepsilon(\phi_0)^2}{\rho g \mathcal{R}^3}$ is the electric Weber number. $\mathcal{S} = \frac{\gamma}{\rho g \mathcal{R}^2}$ is the dimensionless surface tension. \mathcal{E} is assumed to have an order of $O(\epsilon^{-1})$. The dimensionless surface tension number \mathcal{S} can be connected to a Bond number

$Bo = 1/\mathcal{S} = \frac{\rho g \mathcal{R}^2}{\gamma}$. The Bond number $Bo = \mathcal{R}/\mathcal{L} = \epsilon$ naturally measures the ratio of length scales. In experiments, Bo is typically small (~ 0.3 or so) [124]. We follow the work of Craster and Matar [124] and fix the dimensionless surface tension at $\mathcal{S} = \epsilon^{-1}$ in the following discussions.

For the electric field, boundary conditions are,

$$\phi|_{r=\alpha+h(z,t)} = 0, \quad \phi|_{r=\beta} = 1. \quad (3.16)$$

The dimensionless radius of the outer electrode $\beta = b/\mathcal{R} > 1$. When $\beta \gg 1$, the outer electrode is moved far way from the liquid film.

The dimensionless kinematic condition of the free interface is written in the conservative form,

$$h_t + \frac{1}{\alpha + h} \left(\int_{\alpha}^{\alpha+h} r w dr \right)_z = 0. \quad (3.17)$$

For the leading order problem of ϵ , the velocity profile is described by

$$1 - p_z + w_{rr} + \frac{1}{r} w_r = 0, \quad (3.18)$$

$$w|_{r=\alpha} = 0, \quad w_r|_{r=\alpha+h(z,t)} = 0. \quad (3.19)$$

Therefore, the velocity profile yields,

$$w = \frac{p_z - 1}{4} [(r^2 - \alpha^2) - 2(\alpha + h)^2 \ln(r/\alpha)]. \quad (3.20)$$

Moreover, the normal stress balance condition is reduced as:

$$p = -\frac{E_b}{2} \phi_r^2 + \frac{1}{\alpha + h} - \epsilon^2 h_{zz}, \quad (3.21)$$

where ϵ is absorbed into E_b , i.e., $E_b = \epsilon \mathcal{E}$. Now, the modified dimensionless electric Weber number E_b is assumed to be $O(1)$. The simplification of the curvature in Eq.(3.21) is suggested by Craster and Matar [124]. Inclusion of the term h_{zz} is reflected by the linear stability analysis, which is vital to ensure the correct high-wavenumber cutoff occurs [124, 125].

The leading order governing equation of the electric potential ϕ writes

$$\phi_{rr} + \frac{1}{r}\phi_r = 0. \quad (3.22)$$

The solution of the leading order approximation of the electric potential obtained is:

$$\phi = 1 - \frac{\ln(r/\beta)}{\ln[(\alpha + h)/\beta]}. \quad (3.23)$$

Therefore, in Eq.(3.21), the electrostatic force is given by $F = \phi_r^2 = (\alpha + h)^{-2}[\ln((\alpha + h)/\beta)]^{-2}$. This electrostatic force F describes the attraction between the liquid interface and the outer electrode.

Substituting the velocity w into the kinematic equation Eq.(3.17), the evolution equation of the interfacial shape $h(z, t)$ is,

$$h_t + (\alpha + h)^{-1}q_z = 0, \quad (3.24)$$

with

$$q = -\frac{p_z - 1}{4}[(\alpha + h)^4 \ln(\frac{\alpha + h}{\alpha}) - \frac{h(2\alpha + h)(2\alpha^2 + 6\alpha h + 3h^2)}{4}].$$

The pressure gradient p_z can be calculated by differentiating Eq.(3.21) with respect to z . Turning off the electric field, the evolution equation (3.24) recovers the form in Ref.[124].

3.3 Linear stability analysis

The initial unperturbed state of the system (3.24) is:

$$\bar{h} = 1 - \alpha, \quad \bar{q} = \frac{1}{4}[-\ln(\alpha) - \frac{(1 - \alpha^2)(3 - \alpha^2)}{4}]. \quad (3.25)$$

The linear stability analysis is implemented by perturbing the base state Eq.(3.25) with an infinitesimal harmonic disturbance

$$h = 1 - \alpha + \hat{h}e^{ikz + \lambda t}, \quad (3.26)$$

where \hat{h} is the amplitude of the disturbance, k the wavenumber, $\lambda = \lambda_r + i\lambda_i$ the complex temporal growth rate. Here λ is used as the eigenvalue of the re-scaled system. It can be connected to the eigenvalue ω by $\omega = \epsilon\lambda$ where ω serves as the eigenvalue of the fully linearized system.

After linearizing, the dispersive relation obtained is

$$\lambda_r = \frac{k^2}{16} \left[\frac{E_b(1 - \ln\beta)}{(\ln\beta)^3} + (1 - \epsilon^2 k^2) \right] [-4 \ln \alpha - (1 - \alpha^2)(3 - \alpha^2)], \quad (3.27)$$

$$\lambda_i = \frac{k}{2} (2 \ln \alpha + 1 - \alpha^2). \quad (3.28)$$

The dispersive relation is identical to that obtained by Craster and Matar [124] when the electric field is turned off, i.e. $E_b = 0$. The imaginary part of the eigenvalue, λ_i is independent of the electric field. Therefore, the electric field has no influence on the linear wave speed, but it is questionable as to whether the electric field affects the nonlinear wave speed. Detailed discussion will be presented in Section 3.5. As aforementioned, the eigenvalue λ can be connected to ω by $\omega = \epsilon\lambda$, and the wavenumber k can be connected to κ by $\kappa = \epsilon k$ [124]. Here, ω and κ are the eigenvalue and wavenumber of the fully linearized system in Section

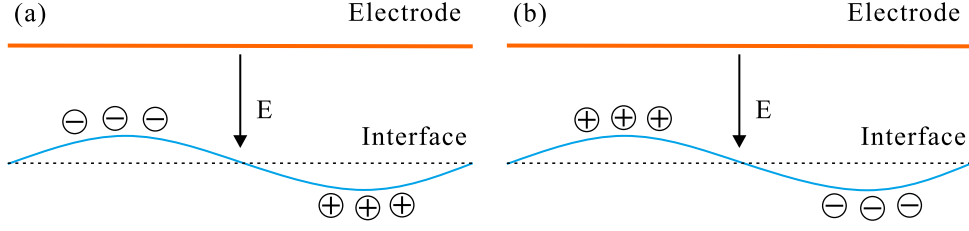


Figure 3.2: The physical mechanism of interfacial instability. “Plus/Minus” symbols stand for positive/negative disturbance charges. (a) $\beta < e$; (b) $\beta > e$.

3.6. Recall that $\mathcal{E} = E_b/\epsilon$, $\mathcal{S} = 1/\epsilon$. The small parameter ϵ can be eliminated from Eq.(3.27) and the dispersive relation is restated as:

$$\omega_r = \frac{\kappa^2}{16} \left[\frac{\mathcal{E}(1 - \ln \beta)}{(\ln \beta)^3} + \mathcal{S}(1 - \kappa^2) \right] [-4 \ln \alpha - (1 - \alpha^2)(3 - \alpha^2)], \quad (3.29)$$

$$\omega_i = \frac{\kappa}{2} (2 \ln \alpha + 1 - \alpha^2). \quad (3.30)$$

It is interesting to see that the influence of electric field on the linear stability is dependent of the dimensionless radius β . When κ is very small, i.e. in the long-wave range, if $\beta < e$, the electric field is destabilizing. When $\beta > e$, the electric field is stabilizing. Additionally, when $\beta = e$, the electric field has no influence on the long-wave stability. The same conclusion can be obtained from Eq.(3.55) in Section 3.6. In order to explain the physical mechanism clearly, let us refer to Figure 3.2. The perturbed electric force $\bar{E}q_s'$ is responsible for the interfacial instability. $q_s' = -\frac{\epsilon(1-\ln(\beta))}{\ln(\beta)^2}H + O(H^2)$ is the perturbed surface charge density, where H measures the deformation of the interface. The linear stability analysis assumes that H is small such that the terms of order $O(H^2)$ and higher can be neglected. \bar{E} is the electric strength at the basic state. Note that the base electric field's always acts in the opposite direction of r . When $\beta < e$, in the elevated region of the interface $q_s' < 0$; while $q_s' > 0$ in the depressed region of the interface. Hence, the electric force will enhance the deformation of the interface. For $\beta > e$, in the elevated region of the interface $q_s' > 0$; while $q_s' < 0$ in the depressed region of the interface. Hence, the electric force will impede the deformation of

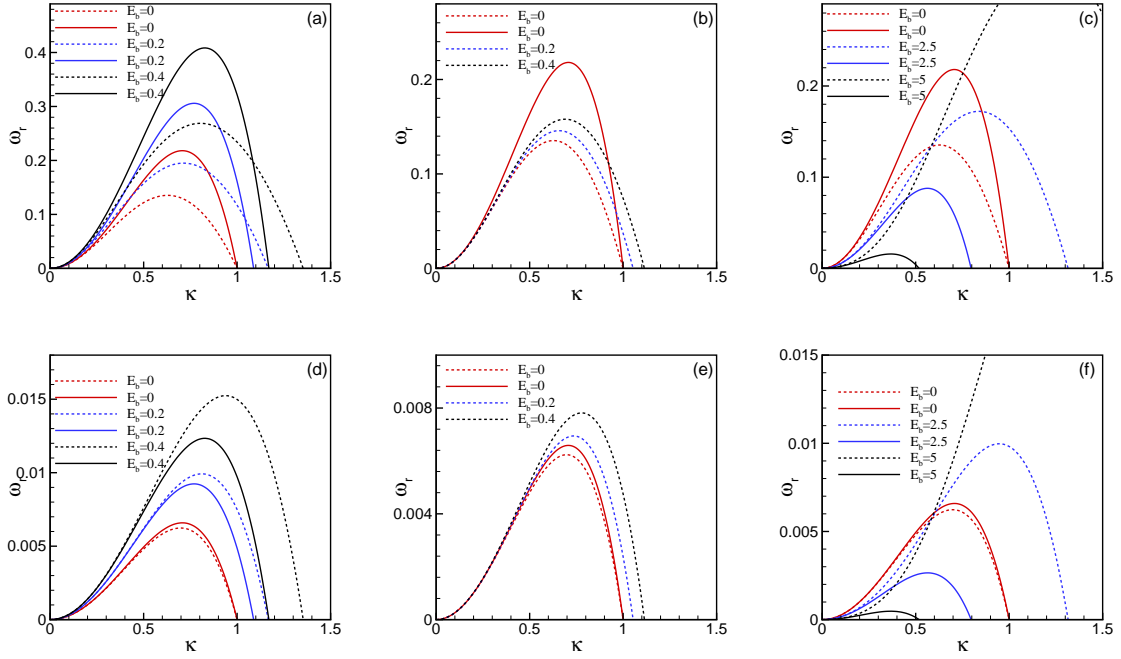


Figure 3.3: The real growth rate ω_r versus the wavenumber κ . Solid lines are obtained by the asymptotic model. Dashed lines are obtained by the fully linearized problem. (a-c) The dependent parameters are $\alpha = 0.25$, $\epsilon = 0.2$, $\beta = 2, e, 5$. (d-f) The dependent parameters are $\alpha = 0.75$, $\epsilon = 0.2$, $\beta = 2, e, 5$.

the interface. For $\beta = e$, however, the perturbed charge density $q_s' = 0$. Thereby, the electric field has a negligible influence on the linear stability of the interface.

The numerical results of the fully linearized problem and the dispersive relation Eq.(3.29) are shown in Figure 3.3. In the calculation of the fully linearized problem, the Reynolds number is set to be very small so as to study the instability of the Stokes flow [127]. Two different values of the fiber radius α and three typical values of the outer electrode radius β are investigated. The influence of α is clear when one compares Figure 3.3(a-c) with 3.3(d-f) that a smaller α is describing a larger real growth rate ω_r . This phenomenon is caused by the surface tension effect as explained in the work of Ding et al. [25, 126] who reported the stability of a liquid film falling down a porous cylinder and indicated that the smaller radius of the cylinder was the more unstable system. Results in Figure 3.3 show that the asymptotic

model does not compare well with the fully linearized problem when α is small. However, in the long-wave range, inspection of the plot reveals that the prediction of asymptotic model agrees well with the fully linearized problem. Craster and Matar [124] reported that the linear stability result of their asymptotic model compared well with the result of the Stokes flow when $\alpha \geq 0.4$; while the agreement deteriorated when α was small. Here, it was observed that, when $\alpha > 0.4$, results of the asymptotic model agree well with that of the fully linearized problem when $E_b = 0$. The agreement, however, deteriorates for large E_b values as shown in Figure 3.3(c,f). This is due to the asymptotic deduction of the Laplace's equation (3.12). In addition, when $\beta = e$, the results by the fully linearized problem show that the electric field has a negligible influence on the long-wave mode, but destabilizes the short wave mode. When $\beta = 5 > e$, the electric field tends to stabilize the long-wave mode, while it destabilizes the short-wave mode as shown in Figure 3.3(c,f). Therefore, it can be concluded here that the asymptotic model is valid in the long wave range.

Equation (3.29) shows that if

$$\mathcal{S}(1 - \kappa^2) + [\mathcal{E}(1 - \ln\beta)]/[(\ln\beta)]^3 \leq 0, \quad (3.31)$$

the long-wave instability can be completely impeded by the electric field. A sufficient condition that the system is stable in the long wave range can be defined as

$$\mathcal{S} + [\mathcal{E}(1 - \ln\beta)]/[(\ln\beta)]^3 \leq 0. \quad (3.32)$$

The maximum real growth rate ω_m of the real growth rate ω_r in Eq.(3.29) can be defined as

$$\omega_m = \frac{[\mathcal{S} + \mathcal{E}(1 - \ln\beta)/(\ln\beta)^3]^2}{64\mathcal{S}}[-4 \ln \alpha - (1 - \alpha^2)(3 - \alpha^2)], \quad (3.33)$$

which occurs at $\kappa_m = \frac{\sqrt{1 + [\mathcal{E}(1 - \ln\beta)]/[\mathcal{S}(\ln\beta)^3]}}{\sqrt{2}}$ and κ_m is defined as the wavenumber of the most

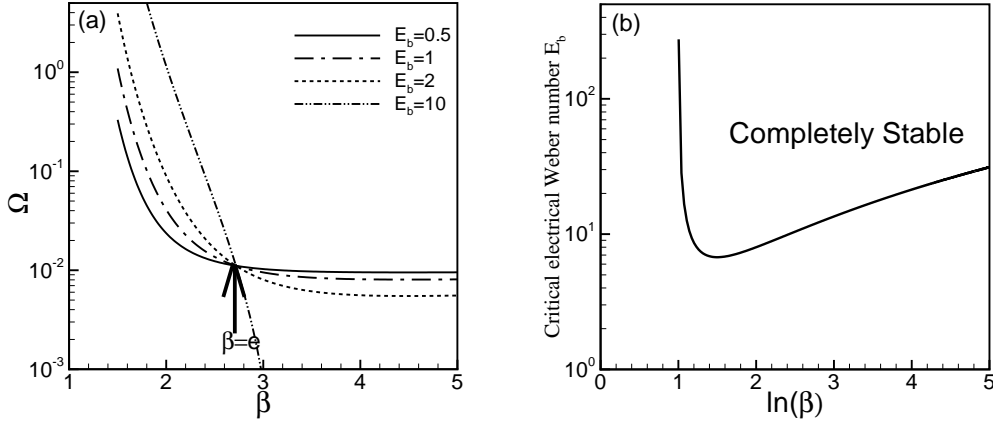


Figure 3.4: (a) $\Omega = \epsilon\omega_m$ versus the radius β predicted by the asymptotic model. (b) The electric Weber number E_b versus the dimensionless radius β predicted by the asymptotic model.

unstable mode [124].

The cut-off wavenumber κ_c corresponding to zero real growth rate is obtained as:

$$\kappa_c = \sqrt{1 + [\mathcal{E}(1 - \ln\beta)]/[\mathcal{S}(\ln\beta)^3]}. \quad (3.34)$$

It is obvious that the cut-off wave number varies with the strength of electric field. Both the wavenumbers, κ_m and κ_c are short waves and strictly lie outside the range of validity of the long-wave model. Note that, the wavenumber κ_m and κ_c should be positive and real, which requires $\mathcal{S} + [\mathcal{E}(1 - \ln\beta)]/[(\ln\beta)^3] > 0$. When $\mathcal{S} + [\mathcal{E}(1 - \ln\beta)]/[(\ln\beta)^3] \leq 0$, the maximum real growth rate $\omega_m = 0$ occurs at $\kappa = 0$ and there is no cut-off wavenumber.

When the outer electrode is very close to the liquid interface, i.e. $\beta \rightarrow 1$, the maximum real growth rate becomes very large as shown in Figure 3.4(a). It indicates that, when $\beta \rightarrow 1$, no matter how small the electric potential difference is, the interfacial instability is enhanced due to the strong attraction between the outer cylinder and the liquid interface. When $\beta \rightarrow \infty$, the electric field $\mathbf{E} = -\nabla\phi$ vanishes, therefore, the electric field has no influence when β is sufficiently large. This conclusion is useful to explain that a larger β is a more stable system.

The analysis agrees with that of a perfectly conducting liquid jet [62], which implies that the solid fiber does not change the influence of the electric field on the linear stability of the interface.

From Eq.(3.32), a critical electric Weber number $E_{b,cr} = \frac{(\ln \beta)^3}{\ln \beta - 1}$ can be found as shown in Figure 3.4(b). Above the value of the critical electric Weber number, the long-wave instability can be completely impeded. In addition, the smallest value of the critical electric Weber number $\min(E_{b,cr}) = \frac{27}{4}$ occurring at $\beta = e^{3/2}$ is found, which is the most economic when we are using an external electric field to impede the long-wave interfacial instability.

3.4 Nonlinear evolution

This section presents the study of the interface subject to a finite-amplitude harmonic disturbance so as to examine the electric field's effect on the nonlinear behavior of the liquid film. The evolution equation Eq.(3.24) is rewritten in the conservative form as

$$s_t + (2q)_z = 0, \quad (3.35)$$

with

$$q = -\frac{p_z - 1}{4} \left[s^2 \left(\frac{1}{2} \ln s - \ln \alpha \right) - \frac{\alpha^4 - 4\alpha^2 s + 3s^2}{4} \right],$$

where $s = (\alpha + h)^2$ is proportional to the area of a cross section. The pressure p is modified as

$$p = -\frac{E_b}{2} s^{-1} \left[\frac{1}{2} \ln s - \ln \beta \right]^{-2} + \frac{1}{\sqrt{s}} - \epsilon^2 (\sqrt{s})_{zz}.$$

The following initial condition is considered that a single harmonic wave is imposed on the interface,

$$s(z, 0) = \left(1 + 0.01 \cos\left(\frac{2\pi z}{L}\right) \right)^2. \quad (3.36)$$

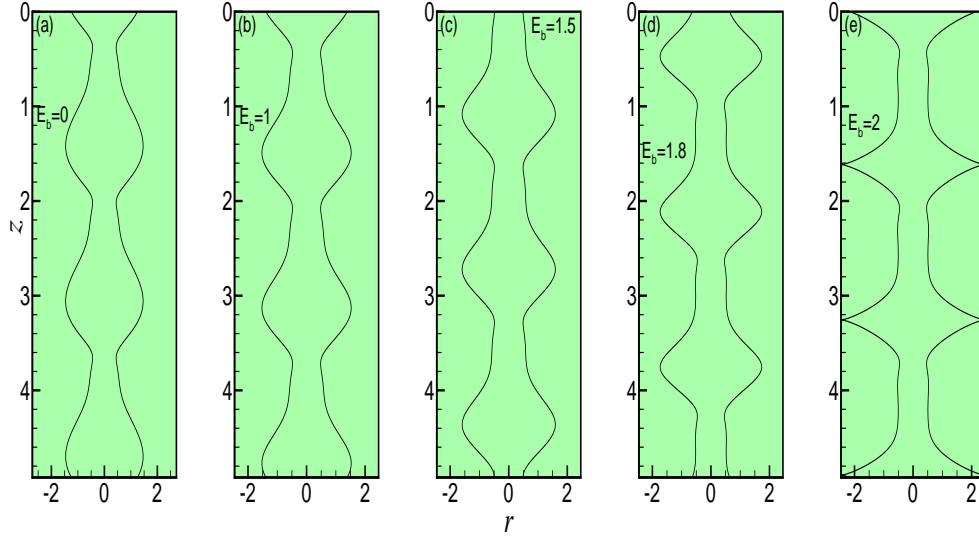


Figure 3.5: (a-d) The periodically extended interfacial shape at instant time $t = 100$. (e) The periodic extended interfacial shape at instant time $t = 9.10$. The other dependent parameters are $\alpha = 0.28$, $\beta = e^{0.9}$, $\epsilon = 0.23$, $L = 1.64$.

Periodical boundary conditions are considered to simulate the nonlinear evolution of the interface. The computational domain is $z = [0, L]$ where L is the non-dimensional length of the domain. The wavenumber $k = \frac{2\pi}{L}$. Section 3.3 indicated that the asymptotic model is valid in the long-wave range, therefore $\kappa = \epsilon k$ should be small, i.e. L/ϵ should be large. Craster and Matar [124] proposed that, in spite of the poor agreement in the linear stability analysis between the asymptotic model and the Stokes flow when α is small, the asymptotic model can still be used to study long-wave dynamics of the film. Their numerical study was in excellent agreement with experimental observations [124]. This Section follows the previous work by Craster and Matar [124], and investigates three typical values of $\alpha = 0.26, 0.28, 0.32$ and $\epsilon = 0.29, 0.23, 0.178$ which are close to the experimental values of α and ϵ by Kliakhandler et al. [127].

Before performing the numerical study, the value of \sqrt{s} should be bounded in (α, β) . When the interface touches the fiber's surface or the outer electrode, the computation is terminated.

The solution is approximated by the Fourier series:

$$s(z, t) = \sum_{-N/2}^{N/2} \hat{s}_n(t) \exp(2in\pi/Lz), \quad (3.37)$$

where \hat{s}_n is the time-dependent coefficient and N is the number of Fourier modes. In the present study, 128 to 512 Fourier modes are enough to provide sufficient accuracy. An implicit Gear's method in time is implemented and the relative error is set less than 10^{-6} .

Figure 3.5 displays the interfacial shape of the liquid film at instant time for $\beta = e^{0.9}$. According to the linear stability analysis, the electric field is destabilizing in this case. The values of ϵ and α are fixed at $\epsilon = 0.23$ and $\alpha = 0.28$. The computational length is chosen to be at $L = 1.64$, and thus the wavenumber $\kappa \approx 0.88$. The wavenumber strictly lies outside the range of validity of the long-wave model. However, the flow pattern in Figure 3.5(a) is similar to the flow regime “b” in the experimental observation [127]. Craster and Matar [124] used the asymptotic model to investigate the dynamics of such close-spacing droplets and found that this was not in agreement with the experimental observation. However, they still used the asymptotic model to examine the dynamics of such a flow pattern in order to give a complete study of the asymptotic model [124]. Similarly, it is informative to show, how the electric field affects the solution of close-spacing droplets. The results here are also given for completeness, because it is interesting to investigate the electric field's influence on the three typical flow regimes. It is observed that, the liquid droplet becomes steeper as E_b increases. When electric Weber is increased to $E_b = 2$, the liquid interface becomes singular and touches the outer electrode at $t \approx 9.10$ as shown in Figure 3.5(e). The maximum value of the liquid film's radius, r_{max} is plotted against the evolution time t in Figure 3.6(a). It is observed that the system can evolve to a steady state after a long time when E_b is less than a certain value. Moreover, the height of the liquid film is promoted by the electric field as shown in Figure 3.6(a). In addition, the growth rate of r_{max} is larger for a larger E_b which demonstrates that

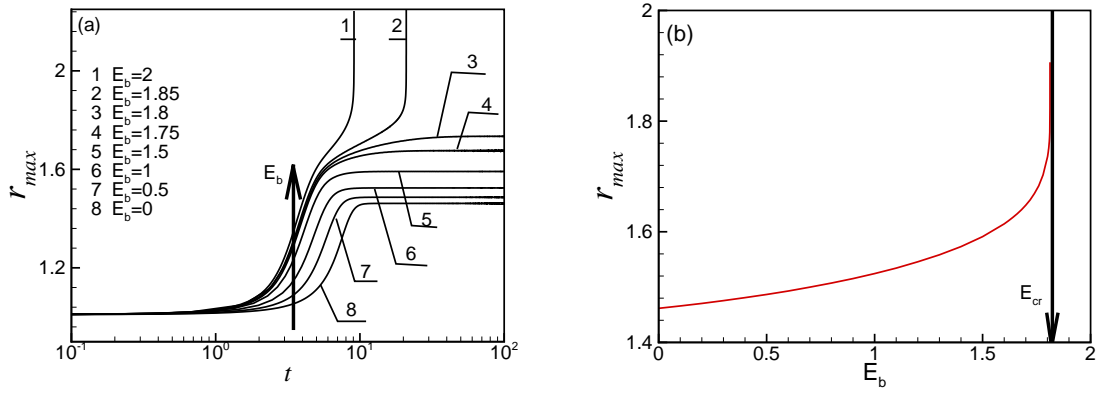


Figure 3.6: (a) The maximum radius r_{max} versus the evolution time t . (b) The maximum radius r_{max} versus the electric Weber number. The other dependent parameters are $\alpha = 0.28$, $\beta = e^{0.9}$, $\epsilon = 0.23$, $L = 1.64$.

the instability is enhanced by the electric field. In order to search for the critical value of E_b whereas the liquid film finally touches the outer electrode rather than evolves to a steady state, the numerical simulation is utilized. r_{max} is plotted against E_b in Figure 3.6(b), in which the critical value of E_b is indicated by $E_{cr} \approx 1.81$. Figure 3.6(b) also shows that the height of the liquid film increases as E_b increases, indicating the electric field is destabilizing. Results in Figure 3.5 and Figure 3.6 demonstrate that the nonlinear study agrees well with the linear stability analysis that the electric field enhances the instability when $\beta < e$.

The nonlinear behavior of the liquid film for $\beta = e$ is of particular interest since the linear stability analysis indicates that the electric field has no influence on the long-wave instability. In fact, the liquid film is unstable due to the Plateau-Rayleigh mechanism even when the electric field is switched off. When the liquid film evolves to a new saturated state due to the capillary instability, the gap between the film's crest and the electrode should be smaller than e . Therefore, in the presence of an electric field, the nonlinear behavior of the interface should be affected significantly. To study the problem, the conditions $\alpha = 0.26$, $\epsilon = 0.29$ and $L = 5.8$ are chosen. It should be noted that the numerical simulation result relies on the initial condition and we cannot obtain a similar result as that in Ref.[127] observed in

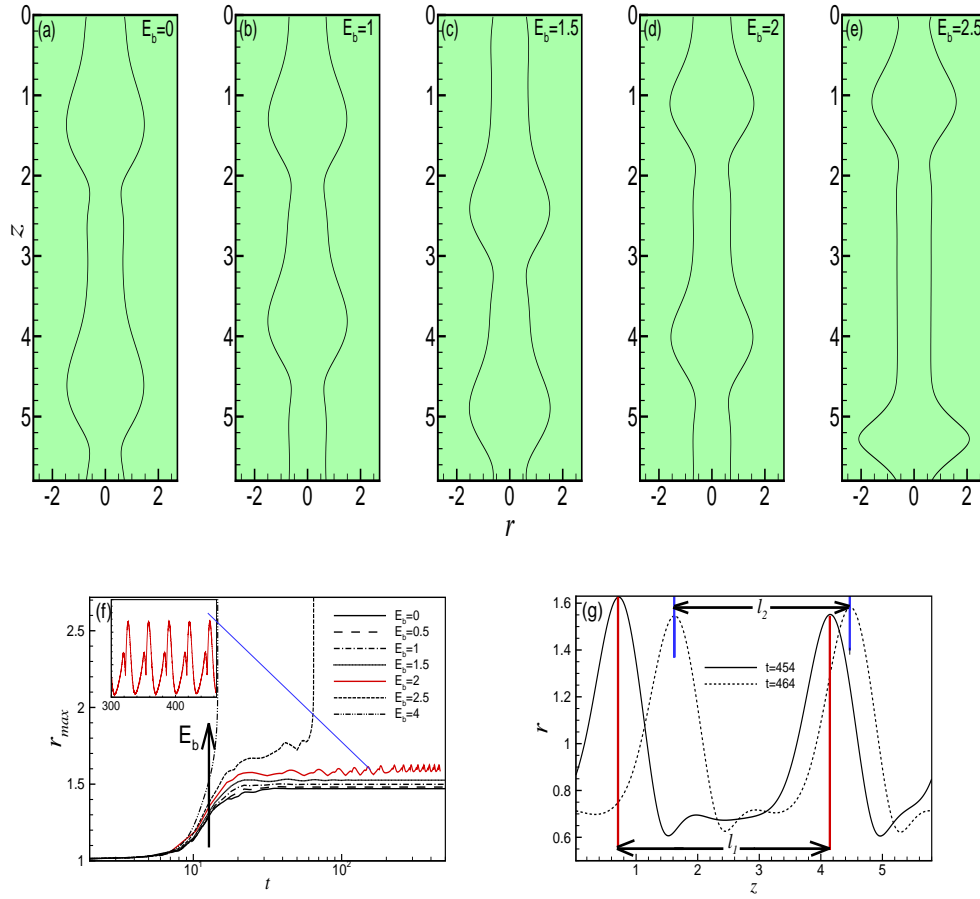


Figure 3.7: (a-e) The interfacial shape. (a-d) are plotted at $t = 500$; (e) is plotted at $t = 64.60$. The other dependent parameters are $\alpha = 0.26$, $\beta = e$, $\epsilon = 0.29$, $L = 5.8$, $\kappa \approx 0.31$. (f) The maximum radius of the liquid ring r_{max} versus the evolution time t . (g) The comparison of the interfacial shapes for $E_b = 2$ at different instant time.

the flow regime “b”. However, the study in this Section can provide insights to explain the effect of electric field on the nonlinear dynamics of the liquid film. Figure 3.7(a) illustrates the interfacial shape for $E_b = 0$. The influence of the electric field on the interfacial shape is shown in Figure 3.7(b-e). An interesting phenomenon observed is that the amplitude of the liquid film starts to oscillate when the electric field is increased to a certain value, for instance $E_b = 2$. Figure 3.7(f) shows the evolution of r_{max} with time t . It demonstrates that the wave amplitude can be either time-independent or time-dependent, when the liquid film evolves to a saturated state. The oscillation in the wave amplitude indicates that the state of the film is not steady. To illustrate this phenomenon, the interface shape at different times is plotted in Figure 3.7(g). The comparison of interfacial wave shape shows that the distance between the wave crests l_1, l_2 as well as the heights of the wave crests are different at the two different times. A further increase in the strength of the electric field will cause the liquid film to touch the outer electrode, for instance $E_b = 2.5, 4$.

When $E_b = 2.5$, the liquid film touches the outer electrode at $t \approx 64.717$. The simulation of this process is presented in Figure 3.8(a-c). To ensure the numerical accuracy, 512 Fourier modes have been utilized and the time accuracy for the Gear’s method is set less than 10^{-8} . It is observed that the interface becomes singular in a quite short time as seen in Figure 3.8(a-c). The electrostatic force is shown in Figure 3.8(d). The attraction between the electrode and the liquid interface becomes very large at the crest of the lower droplet, which squeezes the droplet into the singular shape. This phenomenon could also be observed in an electrified jet or thread [62, 91]. Results in Figure 3.7 and Figure 3.8 indicate that, the electric field is destabilizing in the nonlinear regime, but it does not contradict with the linear theory. In Figure 3.7(f), the electric field almost does not affect the evolution of r_{max} in a short time, which implies that the growth rate of the harmonic wave is almost the same. It indicates that, when the deformation of the interface is small, the prediction of linear stability analysis is correct.

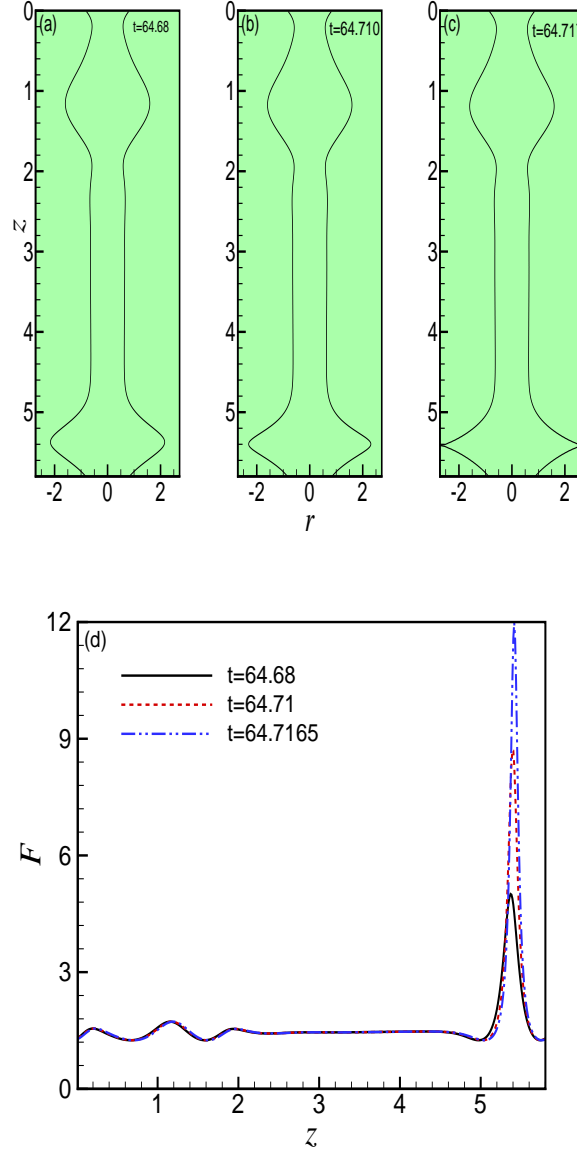


Figure 3.8: (a-c) The interfacial shape at different instant time for $E_b = 2.5$. (d) The distribution of electrostatic force F at the liquid interface. The other dependent parameters are from figure 3.7.

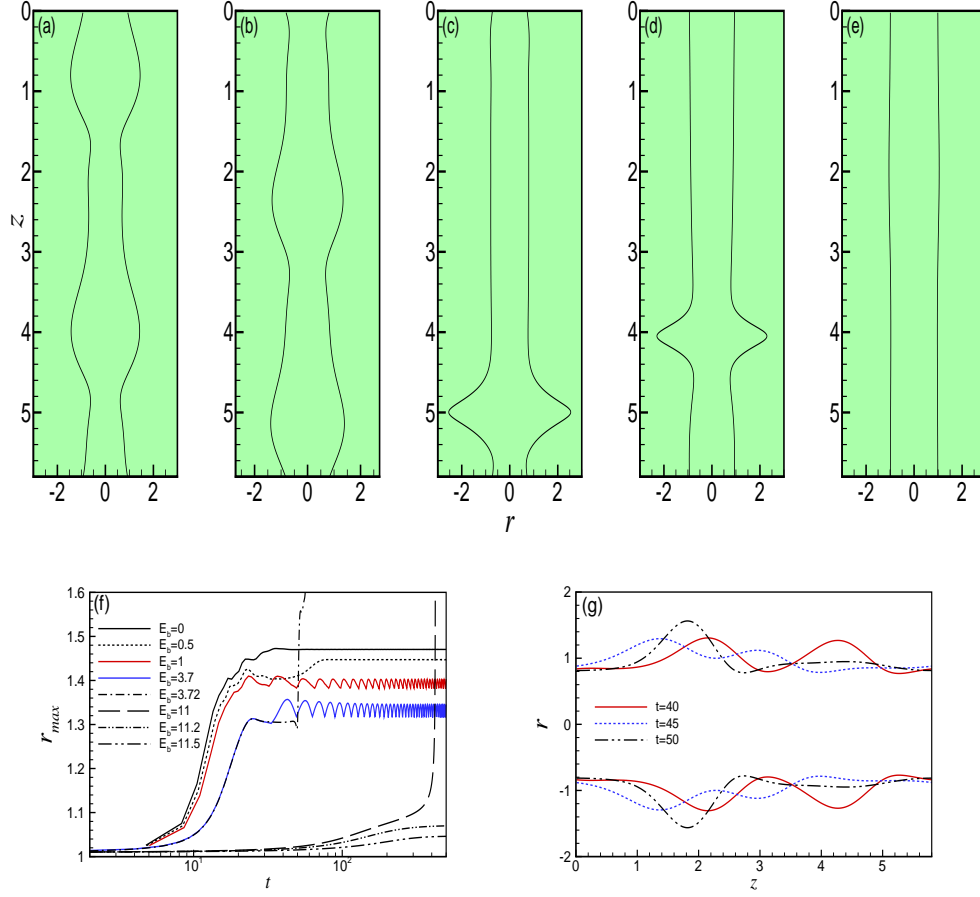


Figure 3.9: (a-e) The interfacial shape. (a) $E_b = 0.5$, $t = 500$; (b) $E_b = 2$, $t = 500$; (c) $E_b = 3.72$, $t = 61.83$; (d) $E_b = 11$, $t = 423.28$; (e) $E_b = 11.5$, $t = 500$. (f) The maximum radius of the liquid ring r_{max} versus the evolution time t . (g) The comparison of the interfacial shapes for $E_b = 3.72$ at different instant time. The other dependent parameters are $\alpha = 0.26$, $\beta = e^{1.1}$, $\epsilon = 0.29$, $L = 5.8$, $\kappa \approx 0.31$.

When the radius β is increased to $e^{1.1}$, and other parameters used in Figure 3.7 are fixed, the electric field's influence on the nonlinear behavior of the interface becomes more complex. The linear stability analysis indicates that the electric field plays a stabilizing role when $\beta > e$. When the nonlinear mechanism becomes important, the electric field can enhance the instability. Clearly, Figure 3.9(a-e) shows the flow pattern can be changed by the electric field. Figure 3.9(f) shows that, when E_b is slightly increased, r_{max} decreases and the liquid film evolves to a steady state. r_{max} starts to oscillate when E_b is further increased, for instance $E_b = 1, 2, 3.7$. The transient simulation shows that when $E_b < 3.719$, r_{max} becomes smaller with increasing the value of E_b . However, the oscillation in the amplitude is promoted by the electric field. As the liquid film is not steady, the coalescence event may happen when E_b is further increased. The maximum height of the film will increase due to the coalescence of the droplets. As a result, the gap between the wave crest and the outer electrode becomes smaller. Thereby, the outer electrode may attract and attach the interface to its surface. This mechanism can be understood by referring to Figure 3.9(g), in which, the coalescence of droplets is shown. Numerical simulation has found out that, when $3.719 < E_b < 11.125$, the electric field can attract the liquid film to the outer electrode due to the droplet coalescence. When $E_b > 11.125$, no rupture phenomenon is observed by numerical study and the wave becomes steady after quite a long time ($t > 10^4$). This is due to the electrostatic force which suppresses the deformation of the interface. The wave amplitude is so small that the electric field could not attract the interface to the outer electrode. The liquid film becomes completely stable when $E_b > \frac{(\ln \beta)^3(1-\kappa^2)}{\ln \beta - 1} \approx 12$, which agrees with the linear stability analysis. Aside from that, Figure 3.9(f) shows that the growth rate of r_{max} is smaller for a larger E_b for short time behavior, which agrees with the linear stability analysis.

Now, it is of interest to study the case: $\beta = e^{3/2}$. For the chosen value of β , the electric field is stabilizing according to the linear stability analysis. In this case, the values $\alpha = 0.32$, $\epsilon = 0.178$ and $L = 5$ are chosen. Study from Ref.[124] suggests that a similar flow pattern as

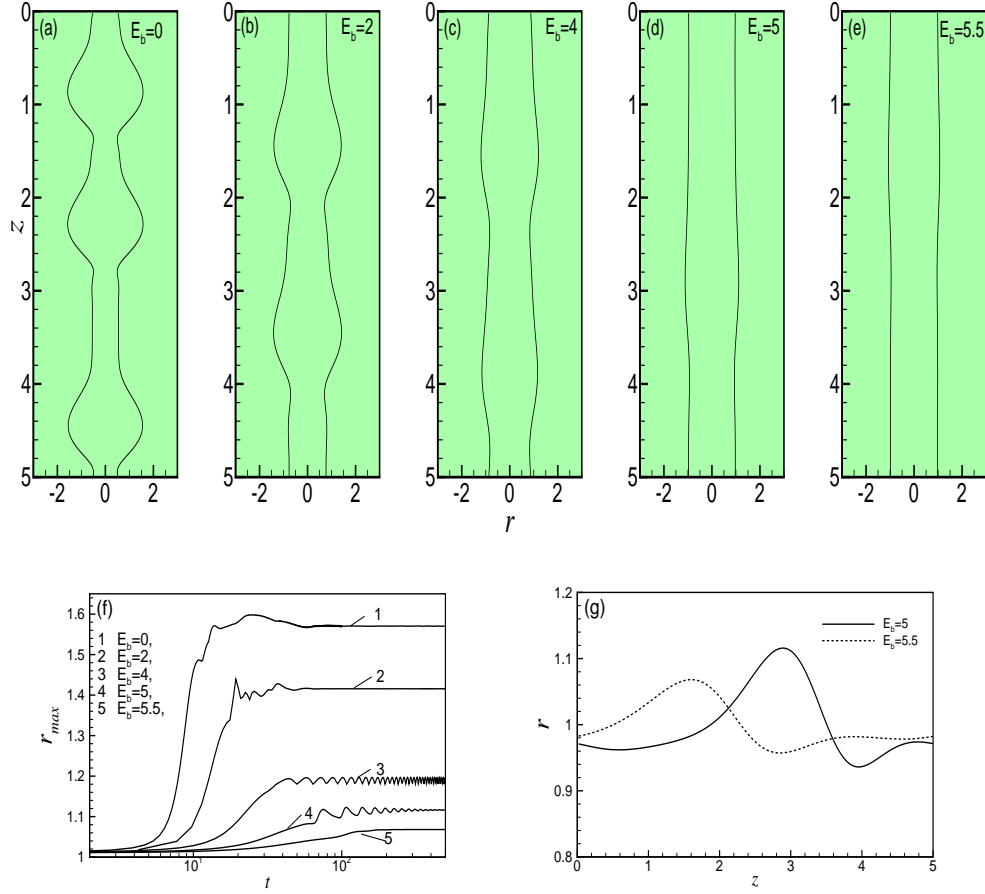


Figure 3.10: (a-e) The interfacial shape at $t = 500$. The other dependent parameters are $\alpha = 0.32$, $\beta = e^{3/2}$, $\epsilon = 0.178$, $L = 5$, $\kappa \approx 0.226$. (f) The maximum radius of the liquid ring r_{max} versus the evolution time t . (g) The comparison of the interfacial shapes for $E_b = 5, 5.5$.

flow regime “c” in the literature [127] may be found by transient simulation for a very small ϵ . Meanwhile, the initial condition of the transient simulation was chosen by a traveling wave solution perturbed by pseudo-random noise [124]. Moreover, 1024 Fourier modes were used for the numerical simulation [124] which was time-consuming. This Section focuses on the influence of electric field on the stability of the annular liquid film. For convenience, $L = 5$ is chosen and the initial condition Eq.(3.36) is used to explain the influence of electric field. The interfacial shape without the external electric field is shown in Figure 3.10(a). When the electric field is turned on, the interfacial wave pattern changes as E_b increases as seen in Figure 3.10(b-e). Figure 3.10(g) shows the comparison of the shape of steady wave for $E_b = 5$, and 5.5. A clearer figure is shown in Figure 3.10(f) that r_{max} becomes smaller as E_b increases. This phenomenon indicates that the electric field is stabilizing. When the electric field is turned on, the permanent wave can also be time-dependent (for instance $E_b = 4$) or time-independent (for instance $E_b = 5$). In this study: $\beta = e^{3/2}$, the singular phenomenon for any electric Weber number $E_b > 0$ is not observed, which indicates that moving the electrode further from the liquid ring can avoid the singular event that may occur in the system.

Finally, the transient simulation with a large $L = 20$ is performed so as to understand the complex dynamics of the film. This study is carried out to investigate the response of the liquid film subject to the finite-amplitude wave in a long computational domain. 512 Fourier modes have been utilized to resolve the problem. The radius of the electrode is fixed at $\beta = e^{3/2}$. The film has evolved to a steady state for $E_b = 1$ as shown in Figure 3.11(a) while it does not become steady for $E_b = 2.5$ as shown in Figure 3.11(b) (Note that, here the spatial axis is z/ϵ rather than z). In fact, for $E_b = 2.5$, no steady state was observed for quite a long time, $t = 5000$. The film is oscillating due to the competition between coalescence of droplet and transition to smaller scales [124]. To illustrate the phenomenon, the space-time diagram of the liquid film is shown in Figure 3.11(b) where the crossing of lines indicates the coalescence of droplets.

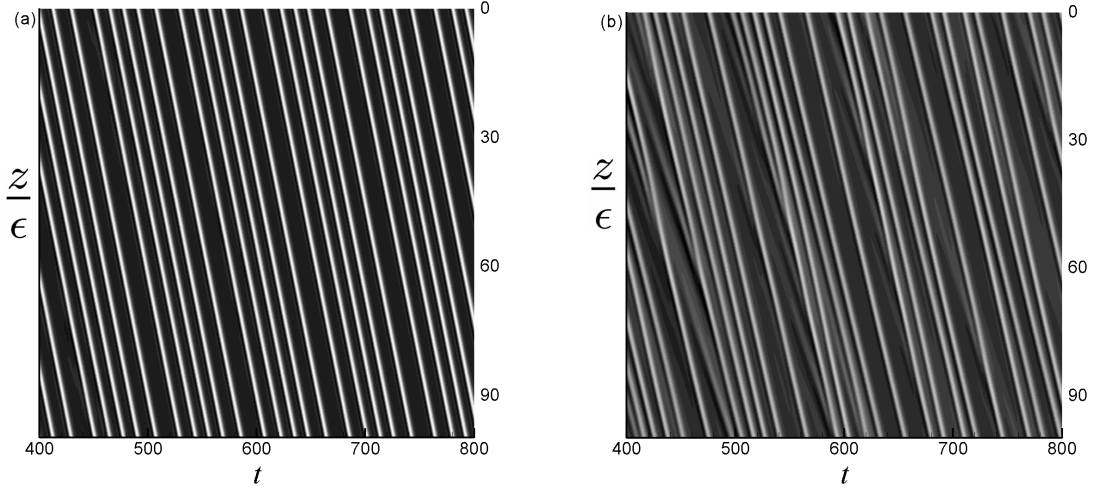


Figure 3.11: Space-time diagram illustrating the dynamics of liquid film, in which the light and dark shading indicate elevated and depressed regions, respectively. (a) $E_b = 1$, (b) $E_b = 2.5$. The dependent parameters are $\alpha = 0.6$, $\epsilon = 0.2$, $\beta = e^{1.5}$, $L = 20$, $\kappa \approx 0.0628$.

3.5 Coherent solutions: Traveling waves

In Section 3.4, the direct simulation of the asymptotic model has been implemented to study the electric field's influence on the nonlinear behavior of the liquid film. However, the study could not answer the question: how does the electric field influence the traveling speed of the steady waves? In this section, coherent solutions in form of traveling waves, i.e., stationary solutions of Eq.(3.35) in a frame of reference moving downstream at a constant speed c are sought by introducing the following transformation:

$$\zeta = z - ct. \quad (3.38)$$

Eq.(3.35) is then transformed to:

$$-cs_\zeta + (2q)_\zeta = 0, \quad (3.39)$$

The unknown variable is set to $s = s(\zeta)$. For a given L (the computational length as defined in

Section 3.4), this is a nonlinear eigenvalue problem where s and c are to be determined. The computational length L also corresponds to the droplet-droplet spacing for a single droplet solution.

Here, the flow rate m in the moving frame is defined as

$$m = - \int_{\alpha}^{\alpha+h(\zeta)} r[w(\zeta) - c]dr. \quad (3.40)$$

The solution of s can be approximated by the Fourier series,

$$s(\zeta) = \sum_{-N/2}^{N/2} \hat{s} e^{2in\pi/L\zeta} \quad (3.41)$$

Since the wave speed c as well as s are unknown, one more condition is needed to fix c . Following Craster and Matar's work, the constraint on the fluid mass is imposed [124]

$$\frac{1}{L} \int_0^L s d\zeta = 1. \quad (3.42)$$

For the convergence of Newton iteration, a reasonable guess for the wave speed and profile should be provided. This can be provided by numerical simulation of the evolution equation of a short computational domain (edge-tracking method). The initial guess can also be given by the information at the supercritical bifurcation point of the evolution equation. A continuation method is used to track the solution branch as parameter changes.

It should be indicated that the traveling wave transformation Eq.(3.38) is only valid when a traveling wave solution exists. The numerical simulation has indicated that the liquid film may become singular in the presence of an electric field. Therefore, in this situation, there is no steady traveling wave and the solution can not be found.

First, the case: $\alpha = 0.3262$, $\epsilon = 0.178$, $L = 8.185$ in the work [124] is revisited. The

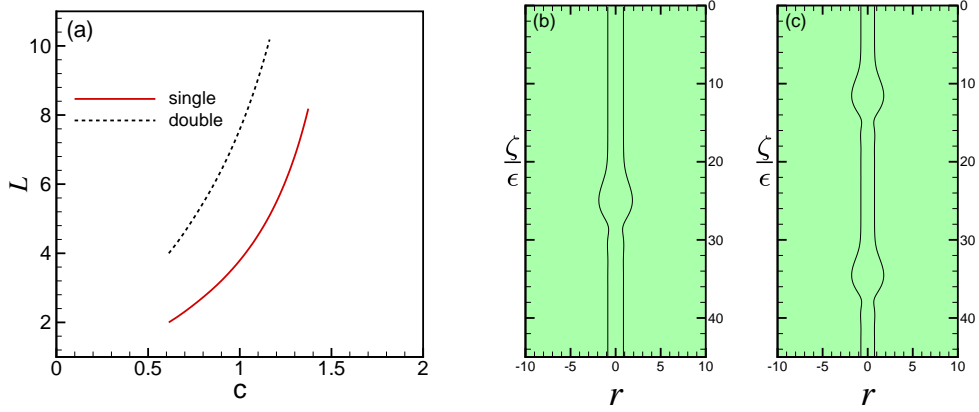


Figure 3.12: (a) The wave speed c versus the length L . (b) The interfacial shape for a single droplet. $c = 1.37$, $L = 8.185$. (c) The interfacial shape for two droplets. $c = 1.04$, $L = 8.185$, $\alpha = 0.3262$, $\epsilon = 0.178$. “single/double” means there is(are) one/two droplet(s) in the computational domain.

solution is tracked by the length L . Clearly, a larger L describes a larger wave speed. Figure 3.12 demonstrates that the asymptotic equation (3.39) exhibits non-uniqueness of solutions. For a given spatial interval, there could be one or two droplets as seen in Figure 3.12(b,c). Our numerical study gives the wave speed $c = 1.37$ at $L = 8.185$ for a single bead which compares well with the result of Craster and Matar ($c = 1.36$ at $L = 8.185$ for a single bead [124]). This agreement confirms the validity of our numerical method. Here, ‘our numerical method’ refers to the numerical method developed by the author of this thesis.

Second, the influence of electric field on these kinds of solutions in Figure 3.12(b,c) is examined. The electric Weber number is fixed at $E_b = 0.1$ while the radius of the electrode β is varied. Results are shown in Figure 3.13. When $\beta < e$, for instance $\beta = e^{0.9}, e^{0.95}$, the traveling wave solution is not found when L exceeds a critical value. When $\beta > e$, the solution does exist. It is noted that, when $\beta < e$, the electric field promotes the wave speed. When $\beta > e$, the wave speed becomes smaller as β increases.

The influence of the electric field on the traveling waves for $\alpha = 0.28$, $\epsilon = 0.23$, $L = 1.64$ is examined by the asymptotic model. The result of numerical simulation in Figure 3.5(a)

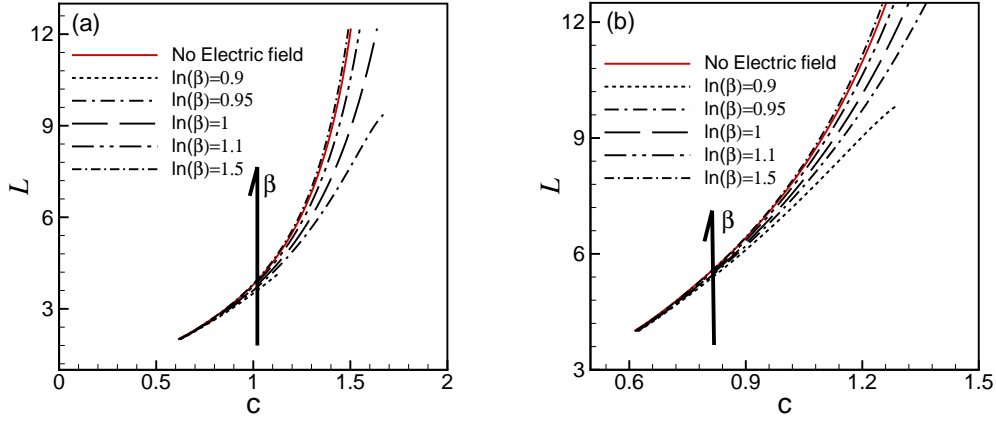
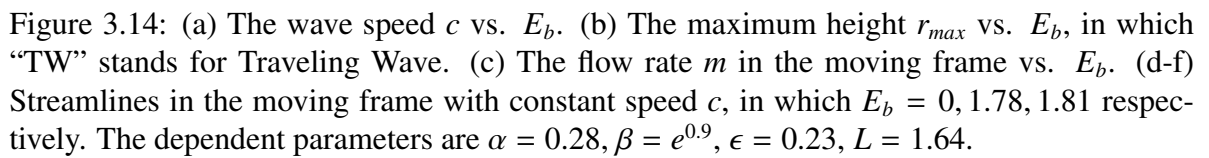


Figure 3.13: (a) The wave speed c vs. the length L for a single droplet case. (b) The wave speed c vs. the length L for two droplets case. The dependent parameters are $E_b = 0.1$, $\alpha = 0.3262$, $\epsilon = 0.178$.

without periodical extension (a single droplet in the computational domain) is chosen as the initial guess of the wave profile. The results are shown in Figure 3.14. The solution agrees with the numerical simulation as seen in Figure 3.14(b). The critical electric Weber number E_{cr} , above which there is no steady traveling waves, $E_{cr} \approx 1.81$ is re-obtained by the traveling wave study. It is interesting to note that although the height of the wave always increases as E_b increases, the wave speed c starts to decrease at $E_b \approx 1.78$ as observed in Figure 3.14(a). The physical mechanism underlying this phenomenon should be the electric field's enhancement on the circulation flow in the wave crest (see Figure 3.14(d-f)). The flow rate m increases as E_b increases till $E_b \approx 1.78$, indicating that the electric field enhances the flow, therefore, a larger c . However, the circulation in the wave crest may retard the flow as $E_b > 1.78$, therefore causing the flow rate m to become smaller. Thereby, the wave speed may become smaller due to the decrease of flow rate.

The electric field's influence on the traveling waves for $\alpha = 0.2551$, $\epsilon = 0.2915$ and $L = 5.81$ (α , ϵ and L are the experimental values of flow regime “a” [127]) is investigated here. For non-zero E_b , the solution is tracked by parameter E_b . The wave speed for $E_b = 0$ is $c = 1.21$,



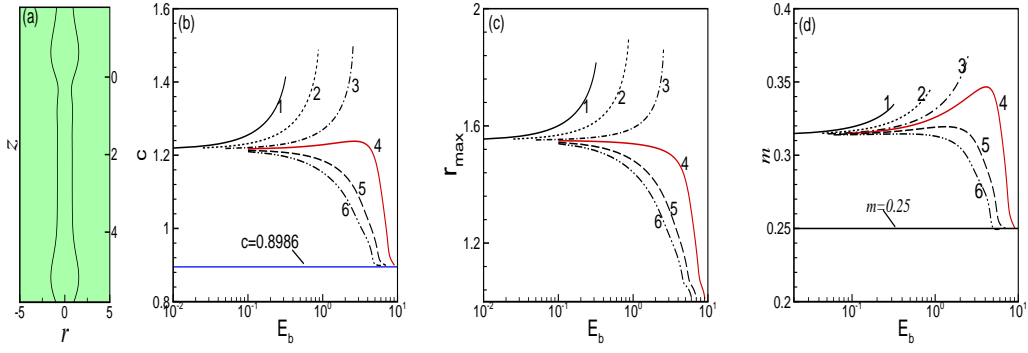


Figure 3.15: (a) The wave profile for $E_b = 0$. (b) The wave speed c vs. the electric Weber number E_b . (c) The maximum height r_{max} vs. the electric Weber number E_b . (d) The flow rate m vs. E_b . The marked lines “1” $\ln(\beta) = 0.9$; “2” $\ln(\beta) = 1$; “3” $\ln(\beta) = 1.1$; “4” $\ln(\beta) = 1.15$; “5” $\ln(\beta) = 1.25$; “6” $\ln(\beta) = 1.5$. The other dependent parameters are $\alpha = 0.2551$, $\epsilon = 0.2915$, $L = 5.81$.

which agrees well with Craster and Matar’s study (Ref.[124] gave $c = 1.195$). Influences of the electric field on the wave speed c and the maximum height r_{max} as well as the flow rate m are shown in Figure 3.15(b-d). Numerical results indicate that (c, r_{max}, m) increase with E_b when $\ln\beta < 1.1$. When $\ln\beta = 1.15$, an interesting phenomenon observed is that, although r_{max} decreases with E_b , c and m reach to their maximum values after that they start to decrease. This phenomenon implies that the electric field enhances the flow and promotes the wave speed. When $\ln\beta > 1.2$, c and r_{max} are observed to decrease as E_b increases. It is found that for $\ln\beta = 1.15, 1.25, 1.5$, $r_{max} \rightarrow 1$, $c \rightarrow 0.8986$, $m \rightarrow 0.25$ as E_b increases to $E_b \approx 9.1, 7, 6$ respectively. The constant value $c = 0.8986$ is nothing but the linear wave speed $c_l = -\frac{\omega_i}{\kappa} = -\frac{1}{2}(2\ln\alpha + 1 - \alpha^2)$. The flow rate $m = 0.25$ is the basic flow rate in the moving frame with the constant speed c_l : $m = c_l(1 - \alpha^2) - \bar{q}$. The critical electric Weber number $E_b = \frac{(\ln\beta)^3(1-\kappa^2)}{\ln\beta-1}$ predicted by the linear stability theory gives $E_b \approx 9.13, 7.03, 6.07$ for the three cases: $\ln\beta = 1.15, 1.25, 1.5$, which agrees with the study of the traveling waves.

3.6 The fully linearized problem

Here, the fully linearized system is carried out so as to verify the validity of the asymptotic model Eq.(3.24). The system is non-dimensionalized by using the length scale $\mathcal{R} = a + h_0$, and pressure scale $\rho g \mathcal{R}$, velocity scale $\rho \mathcal{R}^2 g / \mu$, time scale $\mu / \rho \mathcal{R} g$ and electric potential scale $\phi = \Delta \phi = \phi_0$.

The velocity field \mathbf{u} , pressure p , the electric potential ϕ as well as the interface h are perturbed by infinitesimal harmonic disturbances as:

$$[u, w, p, \phi, h] = [\bar{u}, \bar{w}, \bar{p}, \bar{\phi}, \bar{h}] + [\hat{u}, \hat{w}, \hat{p}, \hat{\phi}, \hat{h}] \exp(ikz + \omega t), \quad (3.43)$$

where $\bar{u}, \bar{w}, \bar{p}, \bar{\phi}, \bar{h}$ refer to the base state and $\hat{u}, \hat{w}, \hat{p}, \hat{\phi}, \hat{h}$ are the Fourier amplitudes of the disturbances. κ is the disturbance wavenumber, and ω is the complex temporal growth rate.

The governing equations of the perturbed system are:

$$D\hat{u} + \frac{\hat{u}}{r} + ik\hat{w} = 0, \quad (3.44)$$

$$\omega \mathcal{R} \hat{u} = -D\hat{p} + (D^2 + \frac{D}{r} - \kappa^2)\hat{u} - \frac{\hat{u}}{r^2} - ik\mathcal{R}\bar{w}\hat{u}, \quad (3.45)$$

$$\omega \mathcal{R} \hat{w} = -ik\hat{p} + (D^2 + \frac{D}{r} - \kappa^2)\hat{w} - \mathcal{R}(ik\bar{w}\hat{w} + \bar{w}_r\hat{u}), \quad (3.46)$$

$$(D^2 + \frac{D}{r} - \kappa^2)\hat{\phi} = 0, \quad (3.47)$$

in which $D = \frac{d}{dr}$. $\mathcal{R} = \frac{\rho^2 g \mathcal{R}^3}{\mu^2}$ can be connected to the Reynolds number by $\mathcal{R} = \epsilon Re$.

The linearized boundary conditions at $r = \alpha$ are

$$\hat{u} = \hat{w} = 0. \quad (3.48)$$

At the liquid interface, the boundary conditions are projected to $r = 1$ by Taylor's expansion,

$$i\kappa\hat{u} + \mathcal{D}\hat{w} + \mathcal{D}^2\bar{w}\hat{h} = 0, \quad (3.49)$$

$$\hat{p} + 2(ik\mathcal{D}\bar{w}\hat{h} - \mathcal{D}\hat{u}) + \mathcal{E}\mathcal{D}\bar{\phi}(\mathcal{D}^2\bar{\phi}\hat{h} + \mathcal{D}\hat{\phi}) = \mathcal{S}(\kappa^2 - 1)\hat{h}, \quad (3.50)$$

$$\hat{\phi} + \mathcal{D}\bar{\phi}\hat{h} = 0, \quad (3.51)$$

$$\omega\hat{h} + i\kappa\bar{w}\hat{h} = \hat{u}. \quad (3.52)$$

Here, the electric Weber number \mathcal{E} and dimensionless surface tension \mathcal{S} can be connected to the modified dimensionless parameters by $\mathcal{E} = E_b/\epsilon$, $\mathcal{S} = 1/\epsilon$.

At the outer electrode $r = \beta$, the boundary condition for the perturbed electric potential is

$$\hat{\phi} = 0. \quad (3.53)$$

The perturbed electric potential is obtained as follows

$$\hat{\phi} = \frac{\hat{h}}{\ln\beta} \frac{I_0(\kappa r)K_0(k\beta) - I_0(\kappa\beta)K_0(\kappa r)}{I_0(\kappa\beta)K_0(\kappa) - I_0(\kappa)K_0(\kappa\beta)}, \quad (3.54)$$

where I_0 and K_0 are the zero order modified Bessel functions.

In the linearized normal stress balance condition (3.50), the electric force term reads

$$\frac{\mathcal{E}}{(\ln\beta)^2} [-1 + \kappa \frac{I_1(\kappa)K_0(\kappa\beta) + I_0(\kappa\beta)K_1(\kappa)}{I_0(\kappa\beta)K_0(\kappa) - I_0(\kappa)K_0(\kappa\beta)}] \hat{h}, \quad (3.55)$$

where I_1 and K_1 are the first order modified Bessel functions. In the long-wave range, $\kappa \rightarrow 0$, the asymptotic electric force term writes

$$\frac{\mathcal{E}(1 - \ln\beta)}{(\ln\beta)^3} \hat{h} + O(\kappa^2). \quad (3.56)$$

The above fully linearized problem is solved by a Chebyshev collocation method.

CHAPTER 4

Interfacial instability of a core-annular system in the presence of a radial electric field

Chapter 3 discussed the interfacial stability of core-annular flows in a radial electric field. The model derived Eq.(3.24) is valid only in the long-wave regime. Specifically, Eq.(3.24) is not able to capture the dynamics of the short waves when an electric field is applied (see Figure 3.3(c,f)). In addition, the dynamics of the outer fluid layer is neglected. This Chapter considers a two-layer flow system as shown in Figure 4.1 and examines the influences of the dynamics of the outer layer. Different from the assumption of perfect conducting liquids of the inner layer and non-conducting gases of the outer layer in Chapter 3, the two immiscible liquids are considered to be leaky dielectrics in this Chapter. Furthermore, it is assumed that the two-fluid system is bound by two concentric cylindrical electrodes. A constant pressure gradient is imposed in the axial direction. The outer electrode with the inner radius $r = b$ is grounded, while the inner electrode with the radius $r = a$ is imposed with a high electric potential. Both liquids are Newtonian with a constant density ρ_i , dynamic viscosity μ_i , dielectric permittivity $\varepsilon_0 \varepsilon_i$ (ε_0 the vacuum electric permittivity), electric conductivity σ_i , where $i = 1, 2$ represents the outer layer and the inner layer respectively. In this chapter, the subscript $i = 1, 2$ represents the outer layer and the inner layer for simplicity, respectively.

The two-dimensional hydrodynamic problem is considered, and the gravity is neglected. Flu-

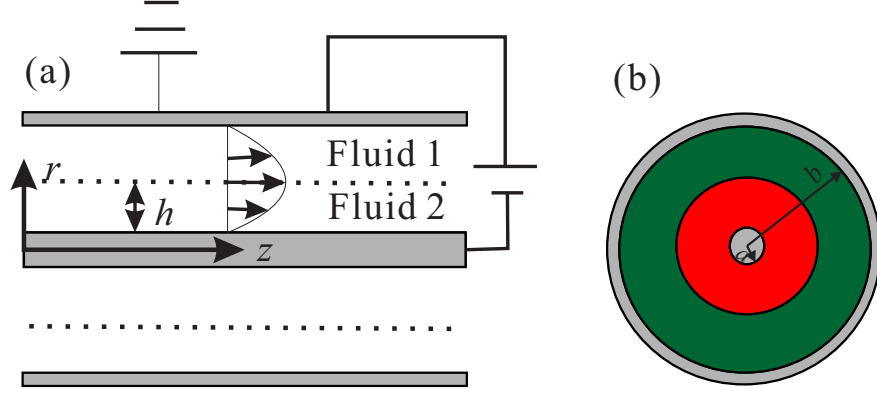


Figure 4.1: Geometry of the two-fluid system. (a) Side-view. (b) Cross-section-view.

ids in each layer are governed by the continuity equation and the momentum equations,

$$\frac{1}{r} \frac{\partial(ru_i)}{\partial r} + \frac{\partial v_i}{\partial z} = 0, \quad (4.1)$$

$$\rho_i \frac{Du_i}{Dt} = -\frac{\partial p_i}{\partial r} + \mu_i (\nabla^2 u_i - \frac{u_i}{r^2}), \quad (4.2)$$

$$\rho_i \frac{Dv_i}{Dt} = -\frac{\partial p_i}{\partial z} + \mu_i \nabla^2 v_i, \quad (4.3)$$

where $(u, v)_i$ the velocity in radial and axial direction respectively, $\frac{D}{Dt} = \frac{\partial}{\partial t} + u_i \frac{\partial}{\partial r} + v_i \frac{\partial}{\partial z}$, and $\nabla^2 = \frac{\partial^2}{\partial r^2} + \frac{1}{r} \frac{\partial}{\partial r} + \frac{\partial^2}{\partial z^2}$.

Since the leaky dielectrics is considered, the electric potential in each layer follows the solution of Laplace's equation,

$$\nabla^2 \phi_i = 0. \quad (4.4)$$

Boundary conditions on the inner surface $r = a$ are,

$$u_2 = v_2 = 0, \quad \phi_2 = \phi_0. \quad (4.5)$$

At $r = b$, boundary conditions are expressed as,

$$u_1 = v_1 = 0, \quad \phi_1 = 0. \quad (4.6)$$

At the liquid-liquid interface, $r = a + h(z, t)$, continuity of the velocity gives,

$$u_2 = u_1, \quad v_2 = v_1. \quad (4.7)$$

The stress is balanced between the two liquid layer by surface tension,

$$(\mathbb{T}_2 - \mathbb{T}_1) \cdot \mathbf{n} = -\gamma(\nabla_s \cdot \mathbf{n})\mathbf{n}, \quad (4.8)$$

where $\mathbb{T}_i = \mathbb{T}_i^v + \mathbb{T}_i^M$ is the stress tensor. \mathbb{T}_i^v stands for the viscous stress tensor and $\mathbb{T}_i^M = \varepsilon_0 \varepsilon_i [\mathbf{E}_i \mathbf{E}_i - \frac{1}{2}(\mathbf{E}_i \cdot \mathbf{E}_i)\mathbb{I}]$ stands for the Maxwell stress tensor and $\mathbf{E}_i = -\nabla \phi_i$. \mathbb{I} is the identity tensor. γ is the surface tension which is constant because the Marangoni effect is neglected in this paper. $\mathbf{n} = \frac{\mathbf{e}_r}{(1+h_z^2)^{\frac{1}{2}}} - \frac{h_z \mathbf{e}_z}{(1+h_z^2)^{\frac{1}{2}}}$ is the surface normal.

Continuity of electric potential at the interface gives

$$\phi_2 = \phi_1. \quad (4.9)$$

For leaky dielectrics, when the ratio of the fluid to electric time scales $\frac{t_F}{t_E} = \frac{h/V_I}{\varepsilon_0/\sigma}$ (V_I is the velocity scale and σ stands for the electric conductivity scale) is very large [85], the conservative equation of interfacial charge (2.31) reduces to,

$$\mathbf{n} \cdot (\sigma_2 \nabla \phi_2 - \sigma_1 \nabla \phi_1) = 0. \quad (4.10)$$

Finally, the system is closed by using the kinematic equation of the liquid-liquid interface,

$$h_t + v_2 h_z - u_2 = 0. \quad (4.11)$$

4.1 Non-dimensionalization and base state

To non-dimensionalize the governing system (4.1)-(4.11), the properties of the inner layer, i.e. ρ_2, μ_2, σ_2 are taken as the property scales; the electric permittivity scale is referred to vacuum permittivity ε_0 ; the length scale refers to the mean depth of the inner layer h_0 ; the velocity scale refers to the moving velocity of interface V_I at the steady state; the time scale is given by h_0/V_I ; the voltage difference between the two cylinders $\Delta\phi = \phi_0 - \phi_g$ (ϕ_g is denoted as the potential of ground, $\phi_g = 0$.) is chosen as the electric potential scale. The relationship between dimensional variables and dimensionless variables (primed) is presented as follows,

$$\left\{ \begin{array}{l} (r, z, h) = (r', z', h')h_0, \\ (u, v)_i = (u', v')_i V_I, \\ (p_1, p_2) = (p'_1, p'_2) \frac{\mu_2 V_I}{h_0}, \quad t = t' \frac{h_0}{V_I}, \\ (\phi_1 - \phi_g) = \phi'_1 \Delta\phi, \quad (\phi_2 - \phi_g) = \phi'_2 \Delta\phi, \\ (\mathbf{E}_1, \mathbf{E}_2) = (\mathbf{E}'_1, \mathbf{E}'_2) \frac{\Delta\phi}{h_0}. \end{array} \right. \quad (4.12)$$

By using these scales, after dropping the primes, the inner layer is governed by the following dimensionless equations,

$$\frac{1}{r} \frac{\partial(ru_2)}{\partial r} + \frac{\partial v_2}{\partial z} = 0, \quad (4.13)$$

$$Re \frac{Du_2}{Dt} = -\frac{\partial p_2}{\partial r} + (\nabla^2 u_2 - \frac{u_2}{r^2}), \quad (4.14)$$

$$Re \frac{Dv_2}{Dt} = -\frac{\partial p_2}{\partial z} + \nabla^2 v_2, \quad (4.15)$$

$$\nabla^2 \phi_2 = 0, \quad (4.16)$$

where $Re = \frac{\rho V_I h_0}{\mu}$ is the Reynolds number.

For the outer layer, the dimensionless governing equations are,

$$\frac{1}{r} \frac{\partial(ru_1)}{\partial r} + \frac{\partial v_1}{\partial z} = 0, \quad (4.17)$$

$$\rho Re \frac{Du_1}{Dt} = -\frac{\partial p_1}{\partial r} + \mu(\nabla^2 u_1 - \frac{u_1}{r^2}), \quad (4.18)$$

$$\rho Re \frac{Dv_1}{Dt} = -\frac{\partial p_1}{\partial z} + \mu \nabla^2 v_1, \quad (4.19)$$

$$\nabla^2 \phi_1 = 0, \quad (4.20)$$

where $\rho = \frac{\rho_1}{\rho_2}$ denotes the density ratio, and $\mu = \frac{\mu_1}{\mu_2}$ denotes the dynamical viscosity ratio.

The dimensionless boundary conditions at $r = a$ are,

$$u_2 = v_2 = 0, \quad \phi_2 = 1. \quad (4.21)$$

At $r = b$, the dimensionless boundary conditions are,

$$u_1 = v_1 = 0, \quad \phi_1 = 0. \quad (4.22)$$

On the interface $r = a + h(z, t)$, after dropping the higher term proportional to $(h_z)^2$, the tangential and normal stress balance conditions are,

$$\begin{aligned} [2u_r h_z + u_z + v_r - 2v_z h_z]_2 - \mu[2u_r h_z + u_z + v_r - 2v_z h_z]_1 \\ + We[\varepsilon_2(E_r^2 h_z + E_r E_z - E_z^2 h_z)_2 - \varepsilon_1(E_r^2 h_z + E_r E_z - E_z^2 h_z)_1] = 0, \end{aligned} \quad (4.23)$$

$$\begin{aligned}
& -p_2 + 2[u_r - (u_z + v_r)h_z]_2 + p_1 - 2\mu[u_r - (u_z + v_r)h_z]_1 \\
& + We[\varepsilon_2(\frac{1}{2}E_r^2 - \frac{1}{2}E_z^2 - 2E_rE_zh_z)_2 - \varepsilon_1(\frac{1}{2}E_r^2 - \frac{1}{2}E_z^2 - 2E_rE_zh_z)_1] = \frac{\kappa}{Ca}, \quad (4.24)
\end{aligned}$$

where $We = \frac{\varepsilon_0 \Delta \phi^2}{\mu_2 V_I h_0}$ denotes the electric Weber number, $\kappa = h_{zz} - \frac{1}{a+h}$ is the curvature. $Ca = \frac{\mu_2 V_I}{\gamma}$ is the capillary number.

The dimensionless continuity of the velocity and voltage potential conditions at the interface hold the same form as Eqs.(4.7) and (4.9),

$$u_2 = u_1, \quad v_2 = v_1, \quad \phi_2 = \phi_1, \quad (4.25)$$

and the dimensionless conservative law of the surface charge is,

$$\mathbf{n} \cdot (\nabla \phi_2 - \sigma \nabla \phi_1) = 0, \quad (4.26)$$

where $\sigma = \frac{\sigma_1}{\sigma_2}$ denotes the electric conductivity ratio.

The dimensionless kinematic condition of Eq.(4.11) holds the same form.

4.1.1 Base state of the system

The flow field and electric field are decoupled at the base state. The base velocity in radial direction vanishes and flow is parallel to the axis, i.e.,

$$\bar{u}_2 = \bar{u}_1 = 0. \quad (4.27)$$

Since the base state of the flow field is assumed to be uniform in z direction and driven by a constant pressure gradient along the axis, then

$$\bar{v}_2 = \frac{C}{4}r^2 + c_1 \ln(r) + c_2, \quad (4.28)$$

$$\bar{v}_1 = \frac{C}{4\mu}r^2 + d_1 \ln(r) + d_2, \quad (4.29)$$

in which,

$$c_1 = \frac{C[(a+1)^2 - \mu(2a+1) - b^2]}{4(\mu \ln \frac{a+1}{a} + \ln \frac{b}{a+1})}, \quad (4.30)$$

$$c_2 = -\frac{C[\mu a^2 \ln \frac{a+1}{a} + a^2 \ln \frac{b}{a+1} + ((a+1)^2 - \mu(2a+1) - b^2) \ln a]}{4(\mu \ln \frac{a+1}{a} + \ln \frac{b}{a+1})}, \quad (4.31)$$

$$d_1 = \frac{C[(a+1)^2 - \mu(2a+1) - b^2]}{4\mu[\mu \ln \frac{a+1}{a} + \ln \frac{b}{a+1}]}, \quad (4.32)$$

$$d_2 = -\frac{C[((a+1)^2 - \mu(2a+1)) \ln b + b^2(\mu \ln \frac{a+1}{a} - \ln(a+1))]}{4\mu[\mu \ln \frac{a+1}{a} + \ln \frac{b}{a+1}]}. \quad (4.33)$$

The coefficient $C = \bar{p}_z$. Since the velocity scale refers to the velocity at the interface, the dimensionless interfacial velocity $V_I = 1$. The pressure gradient is identified as,

$$\frac{\partial \bar{p}}{\partial z} = \frac{4[\mu \ln \frac{a}{a+1} + \ln \frac{a+1}{b}]}{\ln \frac{a}{b} + a^2 \ln \frac{a}{a+1} + a \ln \frac{a^2}{b^2} + b^2 \ln \frac{a+1}{a}}. \quad (4.34)$$

The solution of the voltage potential in the inner and outer layers respectively reads,

$$\bar{\phi}_2 = \frac{\sigma \ln \frac{r}{a+1} + \ln \frac{a+1}{b}}{\sigma \ln \frac{a}{a+1} + \ln \frac{a+1}{b}}, \quad (4.35)$$

$$\bar{\phi}_1 = \frac{\ln \frac{r}{b}}{\sigma \ln \frac{a}{a+1} + \ln \frac{a+1}{b}}. \quad (4.36)$$

When the inner radius is infinitely large, i.e., $a \rightarrow \infty$, the base state reduces the the problem

studied by Ozen et al.[84] as follows,

$$\bar{v}_2 = -\frac{H + \mu}{H(1 + H)}y^2 + \frac{H^2 + 2H + \mu}{H(1 + H)}y, \quad (4.37)$$

$$\bar{v}_1 = -\frac{H + \mu}{\mu H(1 + H)}y^2 + \frac{H^2 + 2H + \mu}{\mu H(1 + H)}y - \frac{1 - \mu}{\mu}, \quad (4.38)$$

$$\bar{\phi}_2 = \frac{\sigma(1 - y) + H}{\sigma + H}, \quad (4.39)$$

$$\bar{\phi}_1 = \frac{-y + H}{\sigma + H}. \quad (4.40)$$

where $H = b - a - 1$ represents the thickness of the outer layer, and $y = r - a$ represents the wall-normal direction. Shifting the origin to the interface, the same velocity and electric potential expressions as Ozen et al.'s [84] can be obtained.

4.2 Linearized perturbed system

This section studies the linear stability of the core-annular flow so as to provide insights on the linear dynamics of the system. Infinitesimal disturbances are introduced to perturb the system. In a standard way, the normal mode analysis is considered. The normal mode analysis is achieved by decomposing F into $F = \bar{F}(r) + \hat{F}(r) \exp(ikz + \omega t)$, where \bar{F} refers to the base state, and \hat{F} the infinitesimal amplitude of a harmonic disturbance with the wave number k and temporal growth rate ω . The complex temporal growth rate $\omega = \omega_r + i\omega_i$, where the real part ω_r is defined as the effective growth rate.

For the inner layer, the perturbed system is governed by,

$$D\hat{u}_2 + \frac{\hat{u}_2}{r} + ik\hat{v}_2 = 0, \quad (4.41)$$

$$Re\omega\hat{u}_2 = -ikRe\bar{v}_2\hat{u}_2 - D\hat{p}_2 + (\mathcal{L}\hat{u}_2 - \frac{\hat{u}_2}{r^2}), \quad (4.42)$$

$$Re\omega\hat{v}_2 = -ReD\bar{v}_2\hat{u}_2 - ikRe\bar{v}_2\hat{v}_2 - ik\hat{p}_2 + \mathcal{L}\hat{v}_2, \quad (4.43)$$

$$\mathcal{L}\hat{\phi}_2 = 0, \quad (4.44)$$

where $D = \frac{d}{dr}$, $\mathcal{L} = D^2 + \frac{1}{r}D - k^2$.

For the outer layer, the perturbed governing system is,

$$D\hat{u}_1 + \frac{\hat{u}_1}{r} + ik\hat{v}_1 = 0, \quad (4.45)$$

$$\rho Re\omega\hat{u}_1 = -ik\rho Re\bar{v}_1\hat{u}_1 - D\hat{p}_1 + \mu(\mathcal{L}\hat{u}_1 - \frac{\hat{u}_1}{r^2}), \quad (4.46)$$

$$\rho Re\omega\hat{v}_1 = -\rho ReD\bar{v}_1\hat{u}_1 - ik\rho Re\bar{v}_1\hat{v}_1 - ik\hat{p}_1 + \mu\mathcal{L}\hat{v}_1, \quad (4.47)$$

$$\mathcal{L}\hat{\phi}_1 = 0. \quad (4.48)$$

Boundary conditions at $r = a$ for the perturbed system are,

$$\hat{u}_2 = \hat{v}_2 = \hat{\phi}_2 = 0. \quad (4.49)$$

At $r = b$, the boundary conditions of the perturbed system are,

$$\hat{u}_1 = \hat{v}_1 = \hat{\phi}_1 = 0. \quad (4.50)$$

The boundary conditions at the liquid-liquid interface $r = a + h$ are projected to $r = a + 1$ by using the Taylor's expansion. The interface is perturbed to $h = 1 + \hat{\eta} \exp(ikz + \omega t)$, where $\hat{\eta}$ measures the deformation of the interface. After dropping the higher order terms, the conditions of perturbed velocities read,

$$\hat{u}_2 = \hat{u}_1, \quad \hat{v}_2 + D\bar{v}_2\hat{\eta} = \hat{v}_1 + D\bar{v}_1\hat{\eta}. \quad (4.51)$$

The voltage potential conditions of the perturbed system at the interface are,

$$\hat{\phi}_2 + D\bar{\phi}_2\hat{\eta} = \hat{\phi}_1 + D\bar{\phi}_1\hat{\eta}, \quad D\hat{\phi}_2 + D^2\bar{\phi}_2\hat{\eta} = \sigma(D\hat{\phi}_1 + D^2\bar{\phi}_1\hat{\eta}), \quad (4.52)$$

and note that $D\bar{\phi}_2 = \sigma D\bar{\phi}_1$, and $D^2\bar{\phi}_2 = \sigma D^2\bar{\phi}_1$.

The perturbed stress balance condition in the tangential and normal direction, respectively, reads,

$$\begin{aligned} [ik\hat{u} + D\hat{v} + D^2\bar{v}\hat{\eta}]_2 - \mu[ik\hat{u} + D\hat{v} + D^2\bar{v}\hat{\eta}]_1 \\ + We[\varepsilon_2 D\bar{\phi}_2(ikD\bar{\phi}_2\hat{\eta} + ik\hat{\phi}_2) - \varepsilon_1 D\bar{\phi}_1(ikD\bar{\phi}_1\hat{\eta} + ik\hat{\phi}_1)] = 0, \end{aligned} \quad (4.53)$$

$$\begin{aligned} -\hat{p}_2 + 2[D\hat{u} - ikD\bar{v}\hat{\eta}]_2 + \hat{p}_1 - 2\mu[D\hat{u} - ikD\bar{v}\hat{\eta}]_1 \\ + We[\varepsilon_2 D\bar{\phi}_2(D^2\bar{\phi}_2\hat{\eta} + D\hat{\phi}_2) - \varepsilon_1 D\bar{\phi}_1(D^2\bar{\phi}_1\hat{\eta} + D\hat{\phi}_1)] = \frac{1}{Ca}[\frac{\hat{\eta}}{(a+1)^2} - k^2\hat{\eta}]. \end{aligned} \quad (4.54)$$

The perturbed kinematic condition is,

$$\omega\hat{\eta} + ik\bar{v}_2\hat{\eta} - \hat{u}_2 = 0. \quad (4.55)$$

4.3 Results and discussion

4.3.1 Effects of the electric field

This Section discusses the influences of electric field on instability of the interface theoretically. The governing equation of the perturbed electric field can be solved by Bessel's function,

$$\hat{\phi}_1 = e_1 I_0(kr) + e_2 J_0(kr), \quad \hat{\phi}_2 = e_3 I_0(kr) + e_4 J_0(kr), \quad (4.56)$$

in which I_0 , J_0 are modified Bessel's functions of order zero, and $I'_0 = kI_1$, $J'_0 = -kJ_1$ where I_1 , J_1 are modified Bessel's functions of order one. Using the boundary conditions, the coefficients are determined as follows,

$$e_1 = \frac{1}{\mathcal{P}} \frac{1 - \sigma}{(a+1)[\sigma \ln \frac{a}{a+1} + \ln \frac{a+1}{b}]} \hat{\eta}, \quad (4.57)$$

$$e_2 = -I_0(kb)/J_0(kb)e_1, \quad (4.58)$$

$$e_3 = Qe_1, \quad (4.59)$$

$$e_4 = -I_0(ka)/J_0(ka)Qe_1, \quad (4.60)$$

with

$$\mathcal{P} = Q \frac{I_0(ka+k)J_0(ka) - J_0(ka+k)I_0(ka)}{J_0(ka)} - \frac{I_0(ka+k)J_0(kb) - J_0(ka+k)I_0(kb)}{J_0(kb)}, \quad (4.61)$$

$$Q = \sigma \frac{J_0(ka) I_1(ka+k)J_0(kb) + J_1(ka+a)I_0(kb)}{J_0(kb) I_1(ka+k)J_0(ka) + J_1(ka+a)I_0(ka)}. \quad (4.62)$$

In the normal stress balance condition Eq.(4.54), the term $[\varepsilon_2 D \bar{\phi}_2 D^2 \bar{\phi}_2 - \varepsilon_1 D \bar{\phi}_1 D^2 \bar{\phi}_1] \hat{\eta}$ is equal to $-\frac{\varepsilon_2 \sigma^2 - \varepsilon_1}{(a+1)^3 [\sigma \ln \frac{a}{a+1} + \ln \frac{a+1}{b}]^2} \hat{\eta}$, and the other term $[\varepsilon_2 D \bar{\phi}_2 D \hat{\phi}_2 - \varepsilon_1 D \bar{\phi}_1 D \hat{\phi}_1] = \frac{\varepsilon_2 \sigma^2 - \varepsilon_1}{(a+1)[\sigma \ln \frac{a}{a+1} + \ln \frac{a+1}{b}]} D \hat{\phi}_1$. According to the solution of the electric field, $D \hat{\phi}_1 = k[I_1(ka+k) + I_0(kb)J_1(ka+k)/J_0(kb)]e_1$ which is modified as,

$$D \hat{\phi}_1 = \frac{k[I_1(ka+k) + I_0(kb)J_1(ka+k)/J_0(kb)]}{\mathcal{P}} \frac{1 - \sigma}{(a+1)[\sigma \ln \frac{a}{a+1} + \ln \frac{a+1}{b}]} \hat{\eta}, \quad (4.63)$$

then, the effect of electric field on the interfacial stability is proportional to,

$$[S \frac{(\varepsilon_2 \sigma^2 - \varepsilon_1)(1 - \sigma)}{(a+1)^2 [\sigma \ln \frac{a}{a+1} + \ln \frac{a+1}{b}]^2} - \frac{\varepsilon_2 \sigma^2 - \varepsilon_1}{(a+1)^3 [\sigma \ln \frac{a}{a+1} + \ln \frac{a+1}{b}]^2}] \hat{\eta}.$$

The parameter $S = \frac{k[I_1(ka+k) + I_0(kb)J_1(ka+k)/J_0(kb)]}{\mathcal{P}}$. The value of S is found to be always positive.

For small to moderate Reynolds numbers, the system is susceptible to the Plateau-Rayleigh instability and interface wave instability[98]. The former is caused by surface tension due to the azimuthal curvature; and the latter is due to viscosity stratification. The capillary and interface wave instabilities are associated with interface deformation. It is noted that, when $\sigma^2 = \varepsilon_1/\varepsilon_2$, the normal Maxwell stress becomes zero at the liquid-liquid interface.

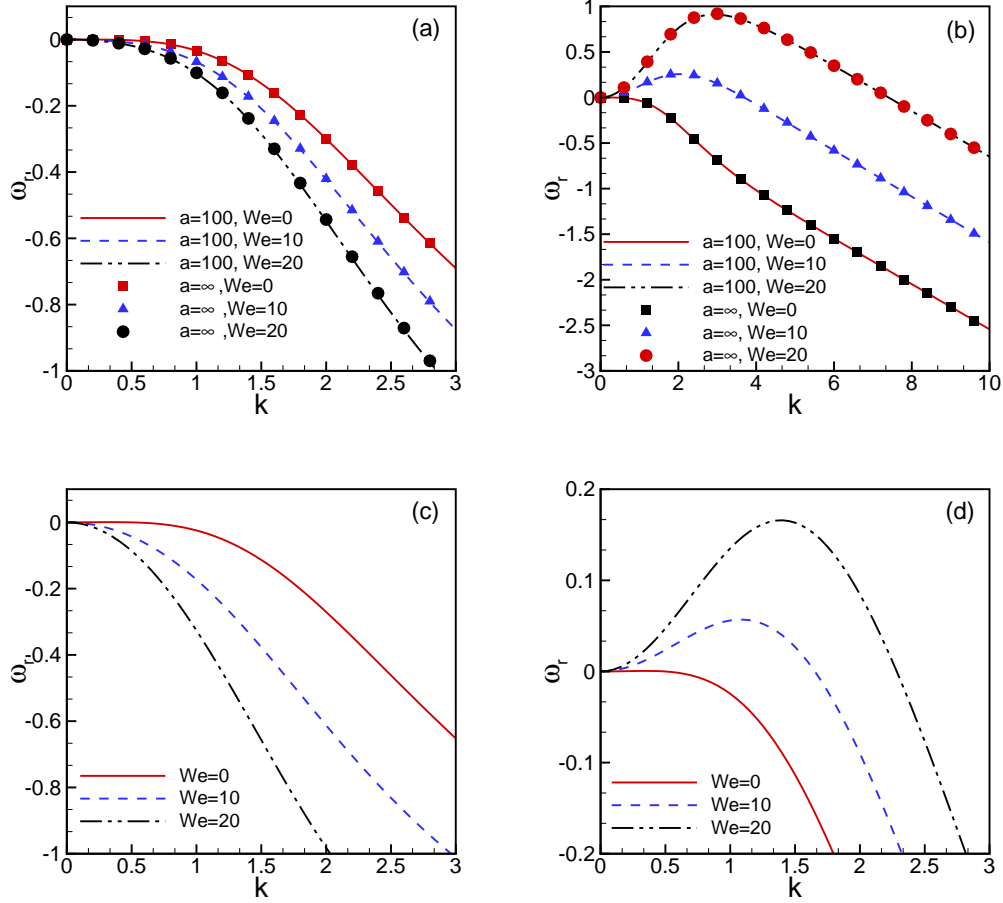


Figure 4.2: (Color online) Effective Growth rate versus disturbance wave number. (a) $\varepsilon_1 = 2$, $\varepsilon_2 = 10$, $\sigma = 0.5$. (b) $\varepsilon_1 = 5$, $\varepsilon_2 = 10$, $\sigma = 0.5$. (c) $\varepsilon_1 = 10$, $\varepsilon_2 = 1$, $\sigma = 1$. (d) $\varepsilon_1 = 5$, $\varepsilon_2 = 10$, $\sigma = 1$. The other parameters $Re = Ca = a = H = \rho = \mu = 1$.

For this two-fluid core-annular system, when

$$\sigma^2 > \varepsilon_1/\varepsilon_2 \quad \text{and} \quad \sigma < 1 - \frac{1}{S(a+1)}, \quad (4.64)$$

or,

$$\sigma^2 < \varepsilon_1/\varepsilon_2 \quad \text{and} \quad \sigma > 1 - \frac{1}{S(a+1)}, \quad (4.65)$$

the electric field impedes the deformation of interface. Otherwise, it enhances the deformation of interface. This two core-annular flow system can be reduced to a bilayer system coflowing between two parallel infinite plates when the inner radius a is infinitely large, i.e., $a \rightarrow \infty$. Eqs.(4.64) and (4.65) agree with the results by Ozen et al.[84] when $a \rightarrow \infty$ and the charge relation time is fast. Ozen et al.[84] proposed that, for the two-fluid layer flowing between two parallel plates in a normal electric field, when $\sigma^2 > \varepsilon_1/\varepsilon_2$ and $\sigma < 1$, or $\sigma^2 < \varepsilon_1/\varepsilon_2$ and $\sigma > 1$, the electric field can stabilize the system. Otherwise, the electric field destabilizes the system. However, the criterion set by Ozen et al.[84] is only valid to explain the normal Maxwell stress's effect which cannot be used to explain the effect of the tangential Maxwell stress[85]. The surface charge induces a tangential Maxwell stress which has an important effect on the stability of the system. Nevertheless, for the core-annular flow system, when the instability is dominated by the capillary force, the theoretical results in Eqs.(4.64) and (4.65) can be referred as a criterion of capillary instability. When the electric properties satisfy Eqs.(4.64) or (4.65), the electric field can impede the capillary instability. Otherwise, the electric field enhances the capillary instability. Furthermore, when the electric properties do not satisfy Eqs.(4.64) or (4.65), the electric field always enhances the deformation of interface.

Since this chapter considers the leaky dielectrics, free charges accumulate at the liquid-liquid interface which induces a tangential Maxwell stress qE_t (q is the surface charge density and E_t is the tangential component of \mathbf{E} at the liquid-liquid interface). Viscous stress at the liquid-liquid interface is balanced by the tangential Maxwell stress. In Eq.(4.53), the linearized

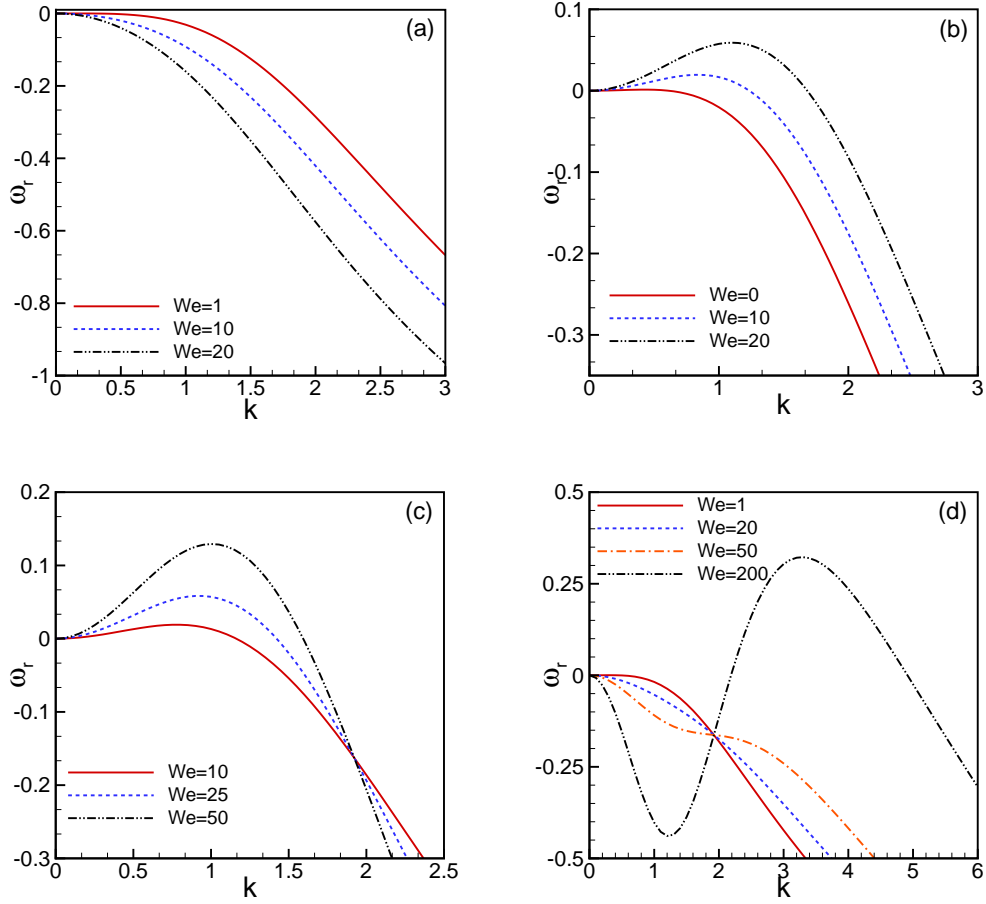


Figure 4.3: (Color online) The tangential Maxwell stress effect on the growth rate. (a) $\epsilon_1 = 2.5$, $\epsilon_2 = 10$, $\sigma = 0.5$, $\mu = 1$; (b) $\epsilon_1 = 10$, $\epsilon_2 = 2.5$, $\sigma = 2$, $\mu = 1$; (c) $\epsilon_1 = 2.5$, $\epsilon_2 = 10$, $\sigma = 0.5$, $\mu = 2$; (d) $\epsilon_1 = 10$, $\epsilon_2 = 2.5$, $\sigma = 2$, $\mu = 2$. The other parameters $Re = Ca = a = H = \rho = 1$.

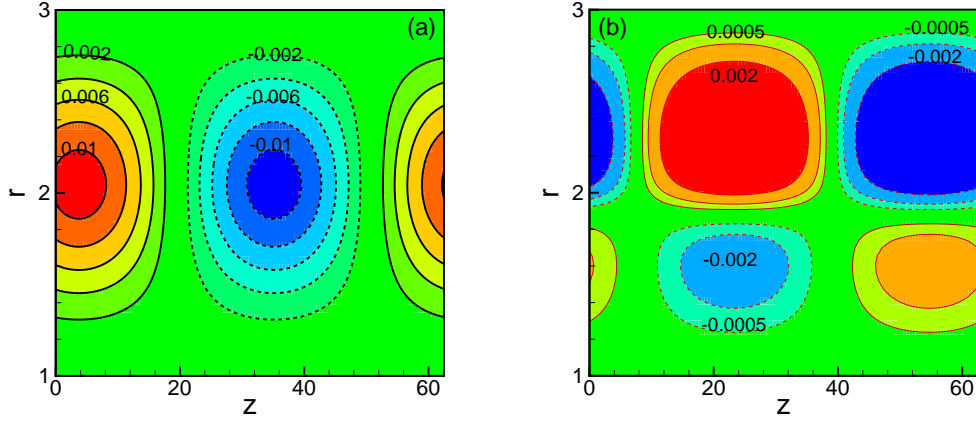


Figure 4.4: (Color online) Perturbed flow field plotted by the streamfunction ψ' . (a) $\varepsilon_1 = 10$, $\varepsilon_2 = 5$, $\sigma = 2$; (b) $\varepsilon_1 = 10$, $\varepsilon_2 = 2.5$, $\sigma = 2$. The other dependent parameters $Re = \rho = Ca = a = H = \mu = 1$, $We = 10$, $k = 0.1$.

tangential Maxwell stress is,

$$ik \frac{(\varepsilon_2 \sigma - \varepsilon_1)}{(a+1)^2 [\sigma \ln \frac{a}{a+1} + \ln \frac{a+1}{b}]^2} (1 + \mathcal{R}(1 - \sigma)) \hat{\eta},$$

in which, $\mathcal{R} = \frac{I_0(ka+k) - I_0(kb)J_0(ka+k)/J_0(kb)}{\rho} < 0$. The tangential Maxwell stress is zero when $\sigma = \varepsilon_1/\varepsilon_2$. In this situation, the two liquids could be viewed as perfectly non-conducting. The influence of the tangential Maxwell stress on the interfacial instabilities (the capillary and interface wave instabilities) is very complex because it is coupled with the viscous stress. Particularly, when $\sigma = \varepsilon_1/\varepsilon_2 = 1$, the electric field has no influences on the system because both the normal and tangential Maxwell stress are zero in the stress balance condition. Numerical examination of influences of the electric field on the interfacial instabilities will be presented in the next section.

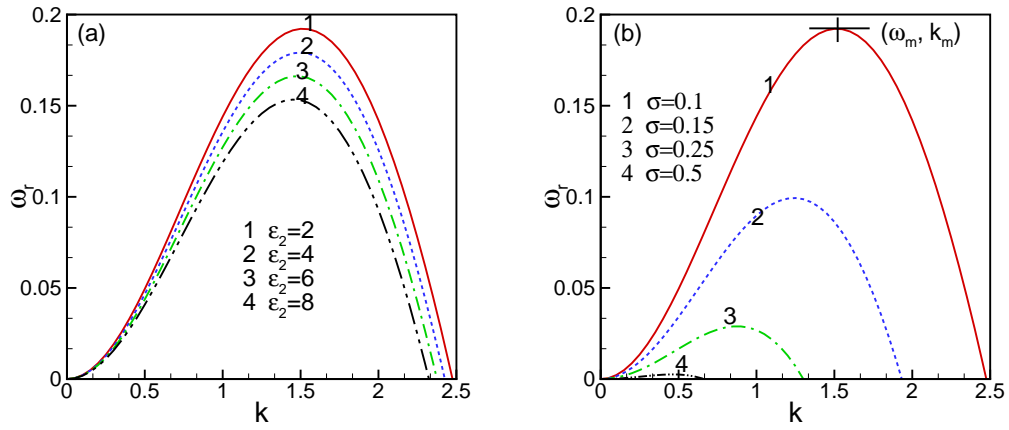


Figure 4.5: (Color online) (a) Electric permittivity on the effective growth rate. The dependent parameters $Re = \rho = Ca = We = a = 1$, $H = 0.5$, $\sigma = \mu = 0.1$. (b) Electric conductivity ratio on the effective growth rate. The dependent parameters $Re = \rho = Ca = We = a = 1$, $H = 0.5$, $\mu = 0.1$, $\epsilon_1 = 1$, $\epsilon_2 = 2$.

4.3.2 Numerical results

This section presents the numerical results of the linear stability analysis. The eigenvalue problem was resolved by the Chebyshev collocation method. The computation domain of each layer was transformed to the Chebyshev domain $[-1, 1]$.

The transformation for the inner layer is,

$$y_2 = 2(r - a) - 1. \quad (4.66)$$

The transformation for the outer layer is,

$$y_1 = 2 \frac{r - (a + 1)}{b - (a + 1)} - 1. \quad (4.67)$$

The solution of the perturbed system is achieved by Chebyshev polynomials,

$$[\hat{u}, \hat{v}, \hat{\phi}]_i = \sum_{j=0}^N [U_j, V_j, \Phi_j]_i T_j, \quad (4.68)$$

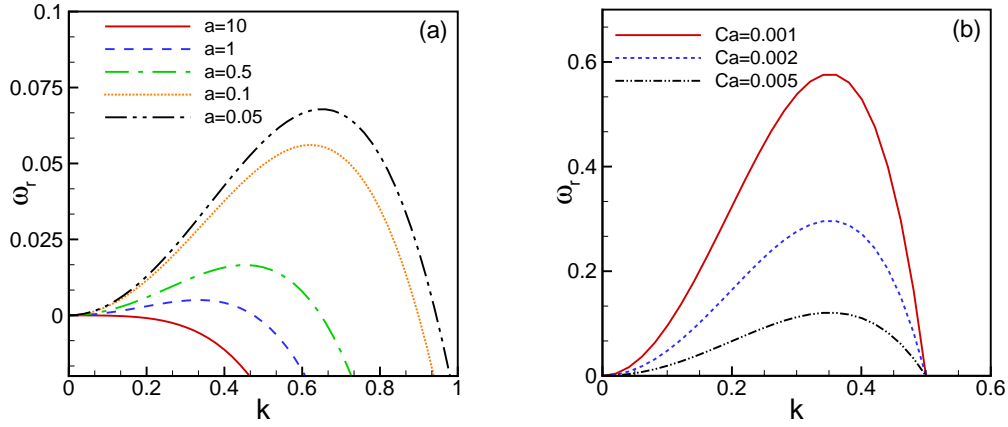


Figure 4.6: (Color online) (a) Inner radius of the duct on the effective growth rate. The dependent parameters are $\varepsilon_1 = 1$, $\varepsilon_2 = 10$, $\sigma = 0.5$, $Ca = 0.1$, $We = a = H = Re = \rho = \mu = 1$. (b) Capillary number Ca on the effective growth rate. The depending parameter $Re = a = H = \rho = \mu = 1$, $We = 0$.

where $T_j = \cos(j \cos^{-1} y)$ with $y \in [-1, 1]$ is the Chebyshev polynomial.

As shown in Figure 4.2(a), when $\sigma^2 > \varepsilon_1/\varepsilon_2$ and $\sigma < 1 - \frac{1}{S(a+1)}$, the electric field impedes the capillary instability. Figure 4.2(b) shows that when the electric field strength increases, i.e., increasing the value of We , the effective growth rate ω_r increases indicating that the electric field is destabilizing when $\sigma^2 < \varepsilon_1/\varepsilon_2$ and $\sigma < 1 - \frac{1}{S(a+1)}$. In Figure 4.2(a,b), we reproduced the results by Ozen et al. [84] at the limiting case $a = \infty$. Figure 4.2(a,b) show that, when a is large, the results agree with the results of a planar system[84]. In Figure 4.2(c), when $\sigma^2 < \varepsilon_1/\varepsilon_2$ and $\sigma > 1 - \frac{1}{S(a+1)}$, the electric field stabilizes the system. In Figure 4.2(d), $\sigma^2 > \varepsilon_1/\varepsilon_2$ and $\sigma > 1 - \frac{1}{S(a+1)}$, the electric field is destabilizing.

To examine the tangential Maxwell stress on the interfacial instability, two typical values of electric conductivity ratio is chosen, $\sigma = 0.5, 2$ and the permittivity ratio $\varepsilon = \varepsilon_1/\varepsilon_2 = \sigma^2$ so that the normal Maxwell stress vanishes in Eq.(4.54). Results in Figure 4.3 illustrate that the effect of tangential Maxwell stress on the instability is strongly influenced by the viscosity ratio. As seen in Figure 4.3(a), for $\sigma^2 = \varepsilon_1/\varepsilon_2 = 0.25$, $\mu = 1$, the electric field is stabilizing; when $\sigma^2 = \varepsilon_1/\varepsilon_2 = 4$, $\mu = 1$, the electric field is destabilizing as shown in Figure 4.3(b).

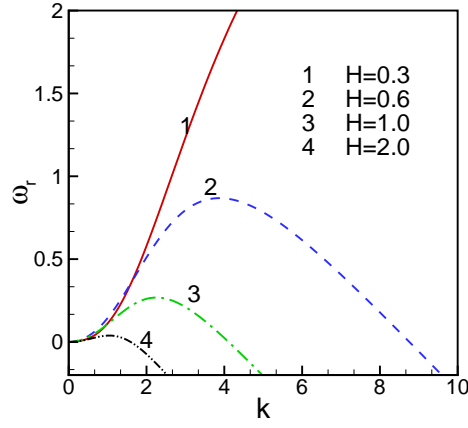


Figure 4.7: (Color online) Thickness ratio on the effective growth rate. The dependent parameters $Re = \rho = \mu = Ca = We = a = 1$, $\varepsilon_1 = 5$, $\varepsilon_2 = 10$, $\sigma = 0.1$.

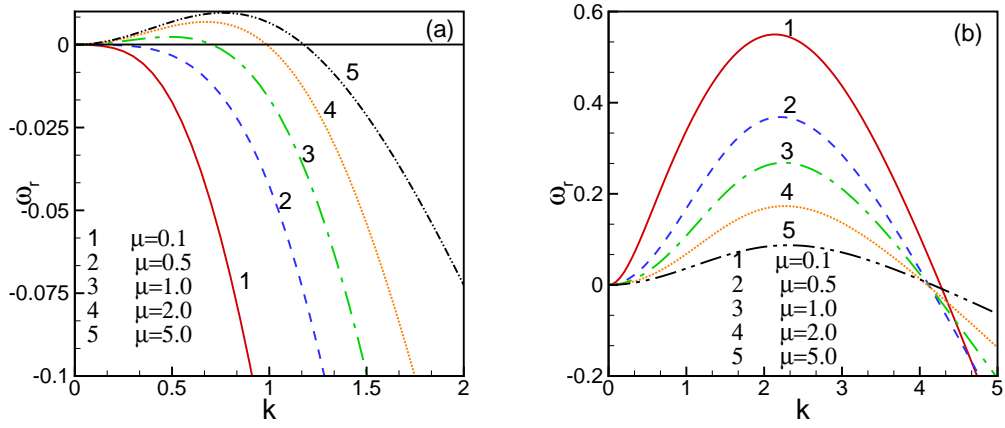


Figure 4.8: (Color online) Viscosity ratio on the effective growth rate. (a) $\varepsilon_1 = 5$, $\varepsilon_2 = 10$, $\sigma = 1$. (b) $\varepsilon_1 = 5$, $\varepsilon_2 = 10$, $\sigma = 0.1$. The other parameters $Re = \rho = Ca = We = 1$, $a = 1$, $b = a + 2$.

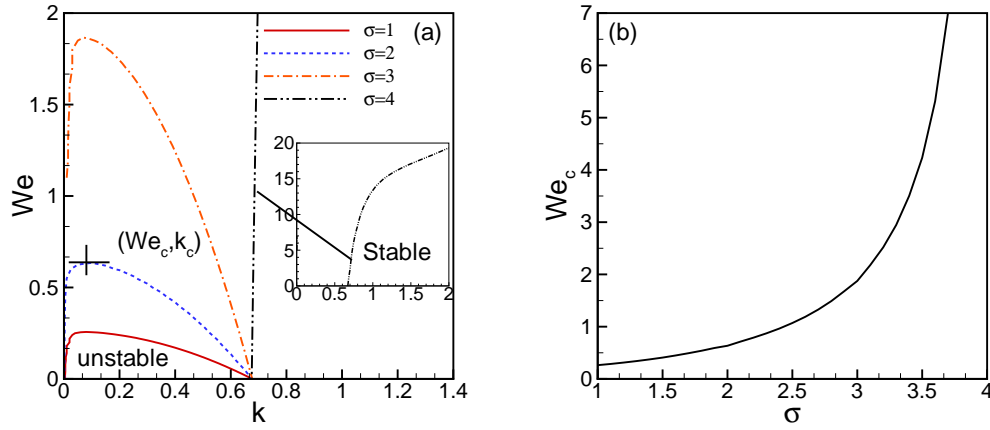


Figure 4.9: (Color online) (a) Marginal stability curve $We - k$. (b) The critical electric Weber number versus the conductivity ratio. The depending parameters are $\varepsilon_1 = 10$, $\varepsilon_2 = 1$, $Re = \rho = Ca = a = H = 1$, $\mu = 5$.

When the viscosity ratio is increased to $\mu = 2$, the electric field's influence on the stability is changed. In Figure 4.3(c), although the input electric properties are the same as those in Figure 4.3(a), the electric field is destabilizing. Furthermore, same input values of electric properties are selected in Figure 4.3(d) as in Figure 4.3(b). The electric field stabilizes the long-wave mode but destabilizes the short wave mode as is seen in Figure 4.3(d).

Both the normal and tangential Maxwell stresses are found to either stabilize or destabilize the interface. To show the effects of normal and tangential Maxwell stress on the perturbed flow field are different, a streamfunction of the perturbed flow field ψ' is defined as follows,

$$u'_i = \frac{1}{r} \frac{\partial \psi'_i}{\partial z}, \quad v'_i = -\frac{1}{r} \frac{\partial \psi'_i}{\partial r}, \quad (4.69)$$

where $(u', v')_i$ is the velocity of the perturbed flow system.

Figure 4.4 illustrates the electric field's influence on flow field in the long-wave range. In Figure 4.4(a), tangential Maxwell stress vanishes for the input electric properties while the normal stress destabilizes the interface. In Figure 4.4(b), the selected values of electric properties are the same as those in Figure 4.3(b) that the tangential Maxwell destabilizes the interface

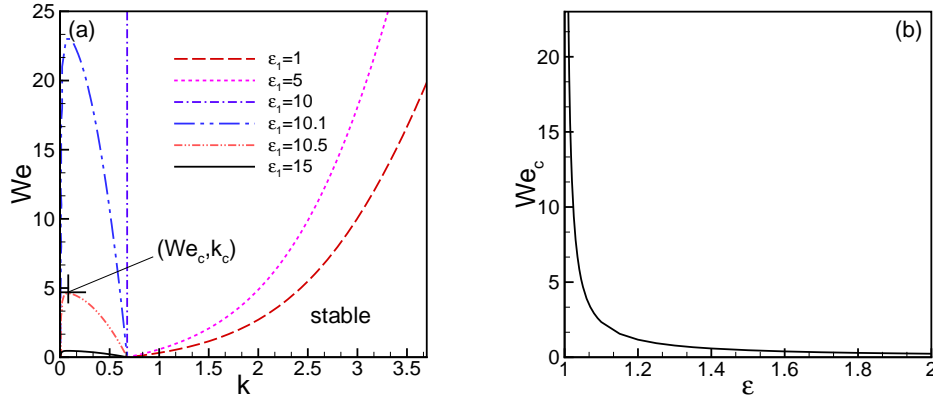


Figure 4.10: (Color online) (a) Marginal stability curve $We - k$. (b) The critical electric Weber number versus the permittivity ratio $\varepsilon = \varepsilon_1/\varepsilon_2$. The depending parameters are $\varepsilon_2 = 10$, $Re = \sigma = \rho = Ca = a = H = 1$, $\mu = 5$.

and the normal Maxwell stress is zero. It can be observed that, the convection cells in Figure 4.4(a) are different from that in Figure 4.4(b). Since in the long-wave range, the instability is dominated by capillary forces. In Figure 4.4(a), convection is due to the deformation of interface caused by the capillary instability and the flow pattern will not change no matter how large the electric field is imposed; while in Figure 4.4(b), the tangential Maxwell stress can induce a circulation flow in each layer and the flow pattern may change with the imposed electric field because its magnitude changes with the imposed strength of electric field. The instability caused by the tangential Maxwell stress is very much like that of Marangoni effect [128].

The effect of the dielectric permittivity on the growth rate is shown in Figure 4.5(a). The permittivity $\varepsilon_1 = 1$ is held fixed. The value of ε_2 is varied to study the influence of permittivity on the dispersive relation. In Figure 4.5(a), the selected parameters give $\sigma^2 < \varepsilon_1/\varepsilon_2$ and $\sigma < 1 - \frac{1}{S(a+1)}$. Thus, the electric field is destabilizing. The effect of the electric field on the interfacial deformation is proportional to $\sigma^2 - \varepsilon_1/\varepsilon_2 < 0$. The value of $|\sigma^2 - \varepsilon_1/\varepsilon_2|$ (the destabilizing effect of the electric field) decreases as ε_2 increases. Therefore, when ε_2 increases, the effective growth rate decreases. Figure 4.5(b) presents the influence of the electric con-

ductivity ratio $\sigma = \sigma_1/\sigma_2$ on the effective growth rate and indicates the growth rate decreases with increasing the conductivity ratio. For the selected parameters, the value of $|\sigma^2 - \varepsilon_1/\varepsilon_2|$ decreases as σ increases. As a result, the enhancement of the electric field on the deformation of interface decreases as σ increases. Therefore, the growth rate decreases as σ increases. Here, (ω_m, k_m) is defined as the effective growth rate and wave number of the most unstable perturbation as shown in Figure 4.5(b). The most unstable perturbation is the major cause of interfacial instabilities, and its wave length characterizes the size of liquid droplets that is formed due to the interface's rupture [81].

Influence of the radius of the inner cylinder on the growth rate is shown in Figure 4.6(a). It should be noted that when $k < \frac{1}{a+1}$, the destabilizing effect of surface tension dominates its stabilizing effect. When $k < \frac{1}{a+1}$, reducing the inner radius a would increase the destabilizing effect [54]. Thus, the system would be more unstable when a becomes smaller. Similar results are shown in Figure 4.6(b), in which, the electric Weber number is fixed at zero so as to investigate the influences of surface tension. Obviously, the capillary force is destabilizing the system in the long wave range due to the azimuthal curvature.

Figure 4.7 shows the influence of thickness of the outer layer H . The growth rate decreases with increasing the thickness of the outer layer. First, the total fluid mass increases when the thickness of the outer liquid layer increases. Second, the electric strength reduces as the radius b increases [90]. Therefore, the effective growth rate decreases with increasing the thickness of the outer layer.

The influences of the viscosity ratio μ is further investigated. Results are shown in Figure 4.8. Figure 4.8(a) shows that the effective growth rate ω_r increases with increasing μ , while in Figure 4.8(b), the effective growth rate ω_r decreases with increasing μ . Results in Figure 4.8 show the viscosity either destabilizes or stabilizes the system. The destabilizing effect is due to viscosity stratification [98]. However, the viscous dissipation of the system increases for a larger μ . As a result, the system becomes more stable as shown in Figure 4.8(b).

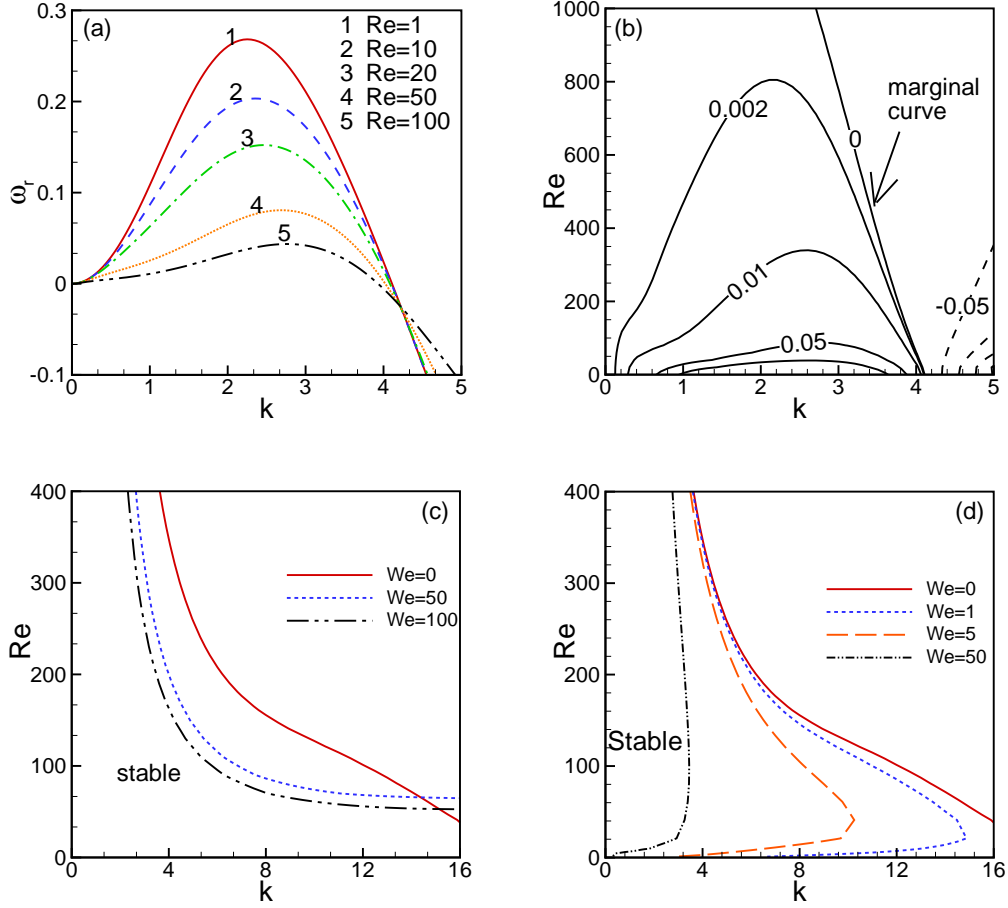


Figure 4.11: (Color online) (a) The Reynolds number Re on the effective growth rate. The dependent parameters $\rho = \mu = Ca = We = a = H = 1$, $\varepsilon_1 = 5$, $\varepsilon_2 = 10$, $\sigma = 0.1$. (b) The contour plot of growth rate in $Re - k$ plane. The dependent parameters are the same as figure 4.11(a). (c) The marginal stability curves for interface wave mode. The dependent parameters $\rho = 1$, $a = 0.1$, $H = 0.1$, $\mu = 0.5$, $J = 0$, $\varepsilon_1 = 10$, $\varepsilon_2 = 2.5$, $\sigma = 2$. (d) The marginal stability curves for interface wave mode. The dependent parameters $\rho = 1$, $a = 0.1$, $H = 0.1$, $\mu = 0.5$, $J = 0$, $\varepsilon_1 = 10$, $\varepsilon_2 = 5$, $\sigma = 2$.

It is of interests to investigate how large the electric field should be imposed, such that it can impede the capillary instability. To study the problem, the marginal curve in $We - k$ plane is plotted in Figure 4.9(a), where the electric properties are chosen that the electric field can impede the capillary instability. The viscosity ratio is $\mu = 5$ and the Reynolds number is fixed at $Re = 1$. The marginal stability curves in Figure 4.9(a) shows that the unstable region enlarges and the critical Weber number We_c increases as the conductivity ratio increases which indicates that a larger electric field should be imposed to stabilize the interface for a larger conductivity ratio. It is obvious that the capillary instability can be stabilized by an external electric field since a stable region exists when We exceeds its critical value. However, when $\sigma = 4$, it is observed that there is no such critical Weber number since the electric field enhances the instability for the input values of electric properties σ , ε_1 and ε_2 . As is seen in Figure 4.9(b), the critical electric Weber number increases with σ and no critical electric Weber number is found by us when $\sigma \approx 3.9$. It is found that there is a critical electric Weber number when $\sigma = 3.7(\sigma^2 > \varepsilon_1/\varepsilon_2)$ and the electric field has a stabilizing effect that can impede the capillary instability, although the normal Maxwell stress enhances the capillary instability($\sigma^2 > \varepsilon_1/\varepsilon_2$). Therefore, it can be concluded that, the stabilizing effect of the electric field is due to the tangential Maxwell stress.

To examine the influence of electric field on the marginal curves, the value of conductivity ratio is fixed, but the permittivity ratio $\varepsilon_1/\varepsilon_2$ is varied. Here, to simplify the discussion, the conductivity ratio is fixed at $\sigma = 1$ and the permittivity $\varepsilon_2 = 10$. The value of ε_1 is varied from $\varepsilon_1 = 1$ to $\varepsilon_1 = 20$. Figure 4.10(a) shows that, when $\varepsilon_1 \leq 10$, there is no critical electric Weber number. The marginal curve does not depend on We when $\varepsilon_1 = 10$ due to the absence of Maxwell stress. The electric field can stabilize the interface with increasing the value of ε_1 . For instance, $\varepsilon_1 = 10.5$, when We is larger than We_c , the capillary instability is completely impeded. As the value of ε_1 increases, the suppression of the electric field on the capillary instability becomes more significant as seen in Figure 4.10(a). This phenomenon agrees with

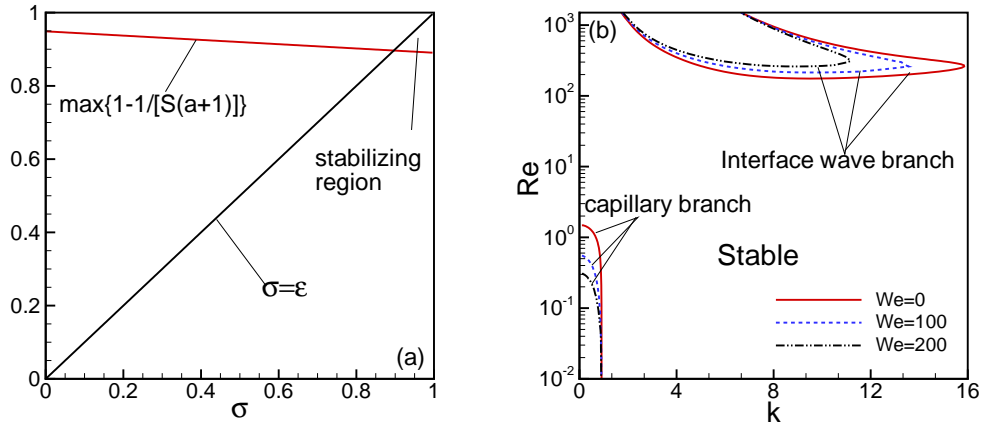


Figure 4.12: (Color online) (a) The conductivity ratio σ versus the maximum value of $1 - \frac{1}{S(a+1)}$ in wavenumber range $[0, 16]$. (b) The marginal stability curves for interface wave mode. The dependent parameters $\rho = 1$, $a = 0.1$, $H = 0.1$, $\mu = 0.5$, $J = 10$, $\varepsilon_1 = 9$, $\varepsilon_2 = 10$, $\sigma = 0.9$.

the analysis in the Section (4.3.1) that the electric field impedes the capillary instability when $\sigma^2 < \varepsilon_1/\varepsilon_2$ and $\sigma > 1 - \frac{1}{S(a+1)}$. In Figure 4.10(b), the critical electric Weber number We_c is plotted against the permittivity ratio $\varepsilon_1/\varepsilon_2$. The critical electric Weber number is observed to decrease with increasing ε .

The influence of Re on the capillary mode is examined and results are shown in Figure 4.11(a,b). It is found that the larger Re the smaller is the growth rate in Figure 4.11(a). The value of Re can be increased through increasing V_I (the velocity at the interface). The interfacial shear effect will be enhanced as Re increases. Dijkstra indicated that the interfacial shear can stabilize the capillary breakup phenomenon [98]. In this system, the effective growth rate decreases with increasing Re , which also indicates that the interfacial shear impedes the capillary instability. To exemplify the influences of Re on the capillary instability, the contour lines of growth rate is plotted in the $Re - k$ plane as shown in figure 4.11(b). First, the wave number k is fixed, for instance, $k = 2.5$. Then, the growth rate decreases as Re increases. The marginal curve corresponding to the zero growth rate in Figure 4.11(b) bends leftward which indicates that the capillary instability is stabilized by interfacial shear.

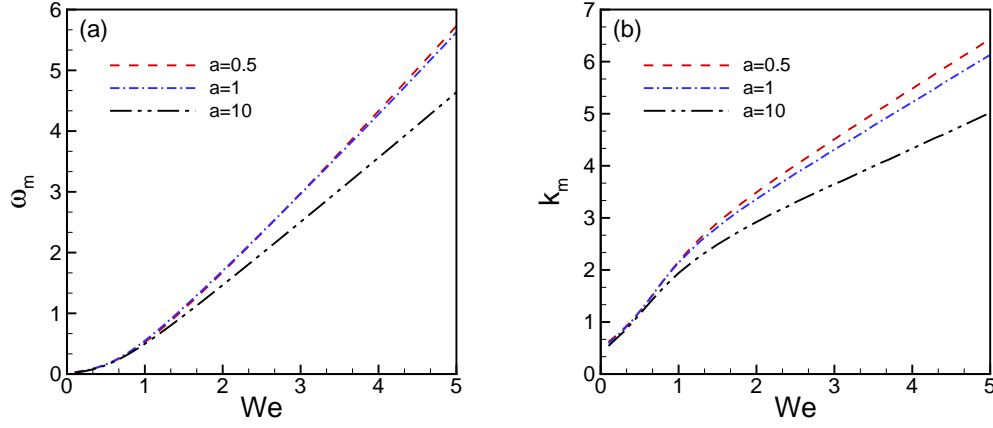


Figure 4.13: (Color online) The electric Weber number on the maximum growth rate and wave number. The dependent parameters $Re = \rho = Ca = \Delta h = 1$, $\mu = \sigma = 0.1$, $\varepsilon_1 = 5$, $\varepsilon_2 = 10$.

The interface may be unstable due to viscosity stratification (interface wave mode) when Re is moderate [98]. Furthermore, the marginal curves are plotted in the $Re - k$ plane to examine the influence of electric field on the interface wave mode due to viscosity stratification across the interface. Results are shown in Figure 4.11(c,d). In order to discuss the influences of electric field on the interface wave mode, the capillary number Ca is replaced by Re/J where $J = \gamma h_0 \rho_2 / \mu_2^2$. The surface tension number J is fixed at zero so that the capillary instability due to the azimuthal curvature vanishes. The input values in Figure 4.11(c) are chosen with the reference from Dijkstra [98], but the values of radii a, b are slightly different. In our case, $a = 0.1$. While in the work of Dijkstra [98], $a \approx 0.11$. When $We = 0$, a similar marginal curve as that by Dijkstra [98] can be reproduced. When $We > 0$, for the selected input values of electric properties in Figure 4.11(c), the normal Maxwell stress is zero. The marginal curve moves leftward as We increases, which indicates that the tangential Maxwell stress enhances the interface wave instability since the stable region in the $Re - k$ plane becomes smaller. In figure 4.11(d), the electric properties are fixed at $\varepsilon_1 = 10$, $\varepsilon_2 = 5$, $\sigma = 2$, so that the tangential component of Maxwell stress is zero in Eq.(4.53). In Figure 4.11(d), it can be observed that the electric field enhances the interface wave mode since the stable region in the $Re - k$ plane

shrinks as We increases. Results in Figure 4.11(d) indicate that the electric field enhances the deformation of the interface ($\sigma^2 > \varepsilon_1/\varepsilon_2$ and $\sigma > 1 - \frac{1}{S(a+1)}$), thus destabilizes the system.

It would be interesting to ask “can the electric field impede the interface wave instability in Figure 4.11(c,d) as well as the capillary instability?” The condition $\sigma = \varepsilon_1/\varepsilon_2$ is considered so that no tangential Maxwell stress is present on the interface. According to Eq.(4.65), the condition that the electric field can stabilize the interface requires:

$$1 - \frac{1}{S(a+1)} < \sigma < \sqrt{\varepsilon_1/\varepsilon_2}, \quad (4.70)$$

and $\sigma = \varepsilon_1/\varepsilon_2$ implies that $\sigma < 1$. When $a \rightarrow \infty$, there is no such condition in Eq.(4.70) that the electric field can impede the interface wave mode when $\sigma = \varepsilon$. The expression of S varies with the wavenumber k , the radii a, b , and the conductivity ratio σ . Here, the radii are fixed at $a = 0.1, b = 1.2$. In the range of wavenumber $k \in [0, 16]$, A sufficient condition for σ that the electric field can impede the interfacial instabilities (capillary and interface wave instabilities) is obtained by modifying Eq.(4.70) as,

$$\max\{1 - \frac{1}{S(a+1)}\} < \sigma < 1. \quad (4.71)$$

Such a range of σ in Eq.(4.71) does exist as shown in Figure 4.12(a) as indicated by “stabilizing region”. In this region, the electric field can stabilize the interfacial instabilities because it impedes the deformation of interface.

Numerical verification of Eq.(4.71) is shown in Figure 4.12(b). The surface tension number in Figure 4.12(b) is fixed at $J = 10$ which changes the topology of the marginal curve of the interface wave branch. The conductivity ratio and permittivity ratio are $\sigma = \varepsilon = 0.9$. The interface wave branch moves upward while the capillary branch moves downward as We increases, demonstrating that the electric field can impede the capillary the interface wave instabilities. Apart from that, Figure 4.12(b) also shows that the interfacial shear can sup-

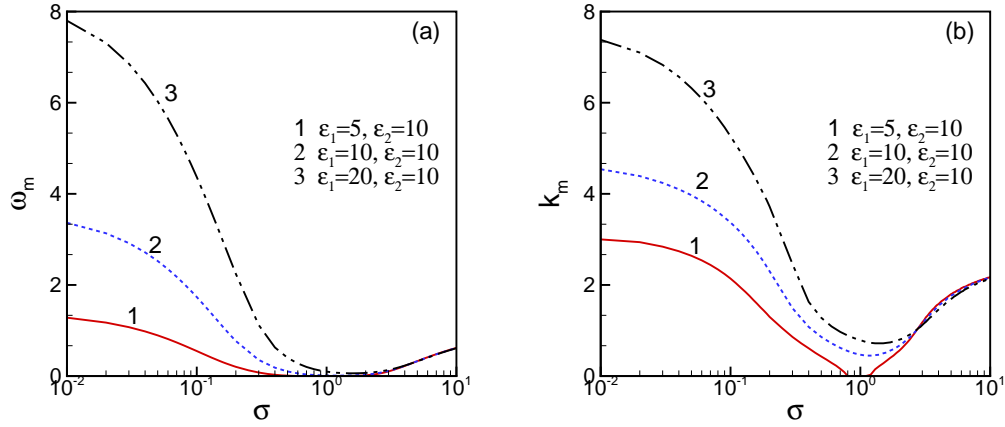


Figure 4.14: (Color online) The electric conductivity ratio on the maximum growth rate and wave number. The dependent parameters $Re = \rho = Ca = H = We = a = 1, \mu = 0.1$.

press the capillary instability. The destabilizing effect of the electric field on the interface is investigated because liquid mixing in micro-scale channels is of particular importance. The Re number is usually very small in micro-scale flow systems, typically $Re = O(1)$. Therefore, in the following discussion, Re is fixed at $Re = 1$.

The electric Weber number We is plotted against ω_m and k_m in Figure 4.13. It is observed that, a larger We is describing a larger ω_m and k_m . It indicates that, when the input parameters $\sigma^2 < \varepsilon_1/\varepsilon_2$ and $\sigma < 1 - \frac{1}{S(a+1)}$, the electric field enhances the deformation of the interface, thus destabilizing the system.

Figure 4.14 shows the conductivity ratio's influence on ω_m and k_m . The magnitude of electric field's effect on the deformation of interface is proportional to $|\sigma^2 - \varepsilon_1/\varepsilon_2|$. When $\sigma < 1 - \frac{1}{S(a+1)}$, and $\sigma^2 < \varepsilon_1/\varepsilon_2$, the interfacial deformation is enhanced by the electric field and the electric field plays a destabilizing role in the system. The value of $|\sigma^2 - \varepsilon_1/\varepsilon_2|$ decreases with increasing σ . As a result, the enhancement of electric field on the interfacial deformation reduces. Therefore, both the maximum growth rate ω_m and maximum wave number k_m decrease. With the increase in σ , the electric field may stabilize the system, i.e. $\omega_m \leq 0$. This can be seen from the stable region for $\varepsilon_1 = 5$ and $\varepsilon_2 = 10$. When $\sigma^2 > \varepsilon_1/\varepsilon_2$ and

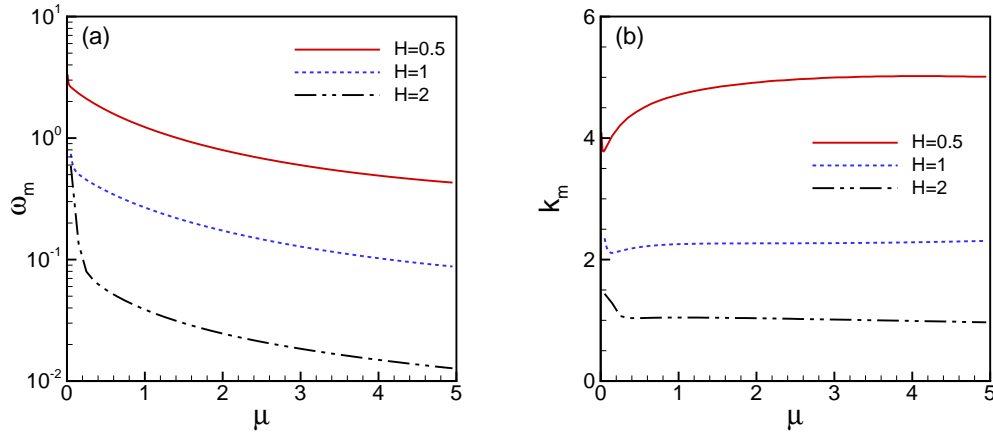


Figure 4.15: (Color online) The viscosity ratio on the maximum growth rate and wave number. The dependent parameters $Re = \rho = Ca = We = a = 1$, $\sigma = 0.1$, $\varepsilon_1 = 5$, $\varepsilon_2 = 10$.

$\sigma > 1 - \frac{1}{S(a+1)}$, the electric field destabilizes the system, and the value of $|\sigma^2 - \varepsilon_1/\varepsilon_2|$ becomes larger as σ increases. As a result, the system becomes more unstable when σ increases.

When σ is small and $\sigma^2 < \varepsilon_1/\varepsilon_2$, ω_m and k_m increases as the value of $\varepsilon = \varepsilon_1/\varepsilon_2$ increases. This is because the value of $|\sigma^2 - \varepsilon|$ increases with increasing ε when $\sigma^2 < \varepsilon$, and the destabilizing effect of the electric field is enhanced. When $\sigma^2 > \varepsilon$ and $\sigma > 1 - \frac{1}{S(a+1)}$, the value of $\sigma^2 - \varepsilon$ reduces with increasing ε . Thus the maximum growth rate decreases. However, because the selected input values of $(\varepsilon_1, \varepsilon_2)$ are chosen that $\sigma^2 \gg \varepsilon$, ε does not have significant influences on the growth rate and wave number when $\sigma^2 > \varepsilon$ and $\sigma > 1 - \frac{1}{S(a+1)}$, although it is found that the maximum growth rate is slightly decreased as shown in Figure 4.14. The influence of viscosity ratio μ on ω_m and k_m are plotted in Figure 4.15. For the selected input parameters, the maximum growth rate ω_m decreases with increasing the viscosity ratio μ due to the viscous dissipation. Influence of viscosity ratio μ on the maximum wave number k_m is not significant when μ is large. It is observed that when μ is very small, k_m decreases initially, then increases. This phenomenon implies that the unstable mode changes. Figure 4.16 shows that the perturbed flow field is stronger in the outer layer when $\mu = 0.1$, while it is stronger in the inner layer when $\mu = 4$.

Results in Figure 4.16 indicate that for small μ , instability is dominated by the outer layer, while for large μ , instability is dominated by the inner layer. Physically, the viscous dissipation effect is associated with the fluid viscosity. The viscous dissipation effect is stronger in the inner layer for small viscosity ratio, while it is stronger in the outer layer for large viscosity ratio. As a result, increasing μ shifts the domination of instability from the outer layer to the inner layer. Apart from that, results in Figure 4.15 show that the larger thickness ratio the smaller are ω_m and k_m .

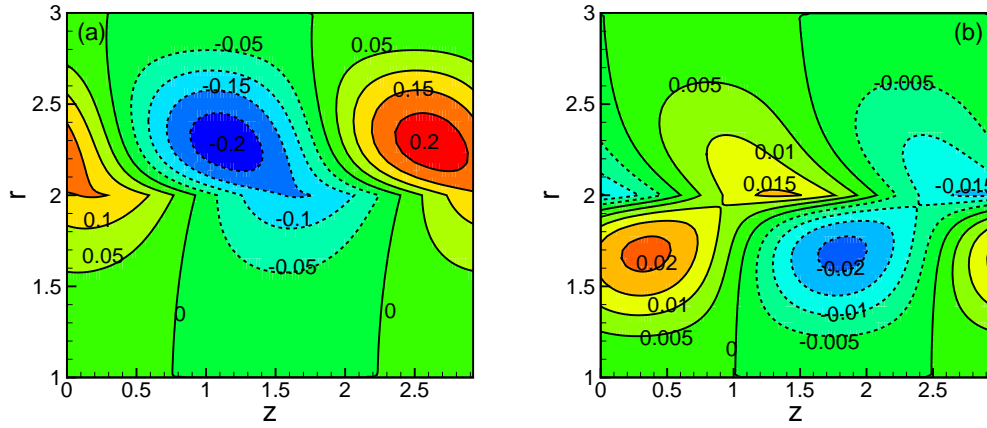


Figure 4.16: (Color online) Perturbed flow field plotted by the streamfunction ψ' . The dependent parameters $Re = \rho = Ca = We = a = H = 1$, $\sigma = 0.1$, $\varepsilon_1 = 5$, $\varepsilon_2 = 10$. (a) $\mu = 0.1$, $k = 2.13$; (b) $\mu = 4$, $k = 2.13$.

CHAPTER 5

Electrohydrodynamic instability in an annular liquid layer with radial conductivity gradients

5.1 Mathematical Formulation

In Chapter 3 and Chapter 4, the interfacial instability of annular liquid layers in a radial electric field has been discussed in which influence of the Maxwell stress at the liquid-liquid or liquid-gas interface on the interfacial dynamics has been examined. This Chapter devotes to electro-convection of an annular liquid layer with an electric conductivity gradient in the radial direction as shown in Figure 5.1. The liquids are eletrolyte solutions and considered to be Newtonian with constant density ρ , kinematical viscosity ν , and dynamical viscosity $\mu = \rho\nu$. An electric field is imposed in the radial direction and a constant pressure gradient is imposed along the axis.

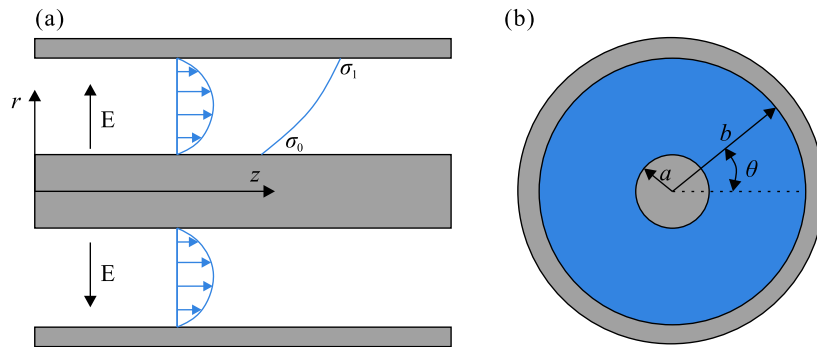


Figure 5.1: Geometry of the system. (a) Side-view. (b) Cross-view.

In this chapter, the three-dimensional hydrodynamical problem is considered. The cylindrical coordinates (r, θ, z) are chosen. Gravity is neglected. Fluids are governed by the continuity equation and the momentum equation,

$$\nabla \cdot \mathbf{v} = 0, \quad (5.1)$$

$$\rho \frac{D\mathbf{v}}{Dt} = -\nabla p + \mu \nabla^2 \mathbf{v} + \mathbf{f}, \quad (5.2)$$

where $\mathbf{v} = u\mathbf{e}_r + v\mathbf{e}_\theta + w\mathbf{e}_z$ is the velocity. $\frac{D}{Dt}$ is the material derivative operator. \mathbf{f} is the electric force which can be related to the Maxwell stress tensor \mathbb{T}^M by,

$$\mathbf{f} = \nabla \cdot \mathbb{T}^M. \quad (5.3)$$

Usually, analysis of Eq.(5.2) is difficult because the electric field is coupled to the free charge density ρ_e according to Maxwell's equations. Moreover, the free charge density is coupled to the flow field. This Chapter assumes that the electric current density \mathbf{J}_e as well as the induced current density $\frac{\partial \varepsilon \mathbf{E}}{\partial t}$ are modest so that the induced magnetic field is negligible. Therefore, the electrostatic problem is considered,

$$\nabla \times \mathbf{E} = 0. \quad (5.4)$$

Hence, the Maxwell stress $\mathbb{T}^M = \varepsilon \mathbf{E} \mathbf{E} - \frac{1}{2} \varepsilon \|\mathbf{E}\|^2 \mathbb{I}$. The parameter ε is the dielectric permittivity and \mathbf{E} is the electric field. The $\|\mathbf{E}\|^2 = \mathbf{E} \cdot \mathbf{E}$ and \mathbb{I} is the identity tensor. Since the charge density is given by the Gauss's law,

$$\rho_e = \nabla \cdot (\varepsilon \mathbf{E}), \quad (5.5)$$

the momentum equation (5.2), now is re-written as,

$$\rho \frac{D\mathbf{v}}{Dt} = -\nabla p + \mu \nabla^2 \mathbf{v} + \rho_e \mathbf{E} - \frac{1}{2} \|\mathbf{E}\|^2 \nabla \varepsilon. \quad (5.6)$$

The term $\frac{1}{2}\|E\|^2\nabla\epsilon$ is ignored and the electric permittivity ϵ is assumed to be constant.

The electrostatics is considered in this Chapter and the electric field E can be related to the gradient of electric potential by

$$E = -\nabla\phi. \quad (5.7)$$

Conservation of electric charge gives,

$$\frac{\partial\rho_e}{\partial t} + \nabla \cdot J_e = 0. \quad (5.8)$$

In this Chapter, the liquid is an Ohmic conductor which neglects the diffusion of the charge.

Then the current density J_e is given by,

$$J_e = \sigma E + \rho_e v, \quad (5.9)$$

where σ is the electric conductivity. Substituting Eq.(5.9) into the current conservative law gives,

$$\frac{D\rho_e}{Dt} + \nabla \cdot (\sigma E) = 0. \quad (5.10)$$

Since the liquid layer is an ionic conductor, the conductivity of which is dependent on the local ionic concentration. The conductivity can be described by the following diffusion equation as proposed by Melcher [104],

$$\frac{D\sigma}{Dt} = K_{eff}\nabla^2\sigma, \quad (5.11)$$

where K_{eff} is an effective diffusivity due to the Brownian motion of the ions [101, 105]. Lin et al. derived a similar equation describing the diffusion of electric conductivity from the species conservation law [100] and the electric conductivity was linearly dependent on the ionic concentration. The effective diffusivity K_{eff} can be related to the diffusive coefficients of species in the work of Lin et al. through a linear combination [100]. Equation (5.11) is valid

if the local electric time is much faster than the fluid time and the time for ion electromigration [101, 105],

$$\frac{\epsilon}{\sigma_0} \ll \frac{d^2}{\nu} \ll \frac{d}{\varpi E_0} \quad \text{and} \quad \frac{d^2}{\varpi k_B T}, \quad (5.12)$$

in which, $k_B T$ is the Boltzmann temperature, ϖ is a characteristic mobility of the charge-carrying solutes and d is the thickness of the liquid. The diffusive term $K_{eff} \nabla^2 \sigma$ is suggested by Baygents and Baldessari [101] who indicated that the diffusion term had a stabilizing effect and was responsible for the existence of a threshold electric field below which the flow was stable. This has also been pointed out in Ref.[100]. In the study of Chang et al. [105], it is implied that when the diffusion term is neglected, the transverse mode is always stable. Hence, the diffusion term is retained and its effect on the stability of the flow will be discussed.

At the inner boundary $r = a$, there are non-slip and non-penetration boundary conditions,

$$u = v = w = 0. \quad (5.13)$$

The electric conductivity at $r = a$ is given,

$$\sigma = \sigma_0. \quad (5.14)$$

At the outer boundary, $r = b$, the non-slip and non-penetration conditions are considered,

$$u = v = w = 0. \quad (5.15)$$

The electric conductivity at $r = b$ is given as well,

$$\sigma = \sigma_1. \quad (5.16)$$

5.2 Non-dimensionalization and base state

5.2.1 Dimensional base state

The velocity in the radial and azimuthal directions vanishes at the base state, i.e. $\bar{u} = \bar{v} = 0$. The flow is parallel to the axis which is driven by a constant pressure gradient $\frac{\partial \bar{p}}{\partial z} = C$. The electric field is parallel to the radial direction at the base state. Therefore, the flow field and the electric field are decoupled. The velocity profile at the base state is:

$$\bar{w} = \frac{C}{4\mu} \left(r^2 - \frac{b^2 \ln(r/a) - a^2 \ln(r/b)}{\ln(b/a)} \right). \quad (5.17)$$

The pressure \bar{p} at the base state is written as $\bar{p} = f(r) + Cz$. The variables with the over bars represent the respective variables at the base state.

Assuming that the shear flow does not disturb the steady conductivity profile, then the conductivity profile at the base state is described by,

$$\bar{\sigma} = \frac{\sigma_1 \ln(r/a) - \sigma_0 \ln(r/b)}{\ln(b/a)}. \quad (5.18)$$

The electric field is obtained from the charge conservation equation (5.10),

$$\bar{E}_r = \frac{aE_0\sigma_0 \ln(b/a)}{r[\sigma_1 \ln(r/a) - \sigma_0 \ln(r/b)]}, \quad (5.19)$$

where E_0 is the electric strength at $r = r_0$. Note that, the per unit length current \mathbf{i} across the fluid layer (the length is along the axial direction) can be defined as $\mathbf{i} = \mathbf{e}_r \int_0^{2\pi} \bar{\sigma} \bar{E}_r r d\theta$. At the base state, $\mathbf{i} = a\sigma_0 E_0 \mathbf{e}_r$ is constant indicating that a constant electric current is applied across the fluid layer. The electric strength at $r = b$ is $E_r = \frac{a\sigma_0}{b\sigma_1} E_0$.

The electric potential at the base state is defined as,

$$\bar{\phi} = \phi_0 - aE_0\sigma_0 \ln(b/a) \frac{\ln[\sigma_1 \ln(r/a) - \sigma_0 \ln(r/b)]}{\sigma_1 - \sigma_0}, \quad (5.20)$$

where ϕ_0 is the reference electric potential.

The charge density $\bar{\rho}_e$ is obtained from the Gauss's law,

$$\bar{\rho}_e = \epsilon \left(\frac{1}{r} \frac{\partial r E_r}{\partial r} \right) = - \frac{\epsilon(\sigma_1 - \sigma_0)aE_0\sigma_0 \ln(b/a)}{r^2[\sigma_1 \ln(r/a) - \sigma_0 \ln(r/b)]^2}. \quad (5.21)$$

5.2.2 Nondimensional system

The nondimensional scales are introduced here: the length scale $d = b - a$, the velocity scale $W = -\frac{Cd^2}{8\mu}$, the time scale d/W , the pressure scale ρW^2 , the electric strength scale E_0 , the conductivity scale $\Delta\sigma = \sigma_1 - \sigma_0$, the charge density scale $\varepsilon \frac{E_0 \Delta\sigma}{d\sigma_0}$. The current density \mathbf{J}_e is scaled by referring to $E_0\sigma_0$ and the non-dimensional \mathbf{J}'_e is expressed as,

$$\mathbf{J}'_e = \frac{\Delta\sigma}{\sigma_0} \sigma' \mathbf{E}' + \mathbf{E}' + \frac{\Delta\sigma}{\sigma_0} \frac{\varepsilon/\sigma_0}{d/W} \rho'_e \mathbf{v}'. \quad (5.22)$$

Naturally, the dimensionless governing equations emerge,

$$\nabla \cdot \mathbf{v} = 0, \quad (5.23)$$

$$\frac{D\mathbf{v}}{Dt} = -\nabla p + \frac{1}{Re} \nabla^2 \mathbf{v} + Q \nabla^2 \phi \nabla \phi, \quad (5.24)$$

$$\frac{D(\nabla^2 \phi)}{Dt} + R_t [(1 + \eta\sigma) \nabla^2 \phi + \eta \nabla \phi \cdot \nabla \sigma] = 0, \quad (5.25)$$

$$\frac{D\sigma}{Dt} = \frac{1}{ReS c_e} \nabla^2 \sigma, \quad (5.26)$$

where the electric charge ρ_e in the momentum equation is eliminated by using the dimension-

less Poisson's equation,

$$\rho_e = -\frac{1}{\eta} \nabla^2 \phi. \quad (5.27)$$

$Re = \frac{Wd}{\nu}$ is the Reynolds number; $Q = \frac{\epsilon E_0^2}{\rho W^2}$ which measures the ratio of electric force to inertia force; $\eta = \frac{\Delta \sigma}{\sigma_0}$ which characterizes the conductivity gradient for a given channel gap d ; $R_t = \frac{d/W}{\epsilon/\sigma_0}$ which measures the ratio of viscous relaxation time to electric relaxation time; $Sc_e = \frac{\nu}{K_{eff}}$ is the Schmidt number. The parameter $R_t = \frac{1}{Re} \frac{d^2 \sigma_0}{\nu \epsilon}$ is usually a large number and has the magnitude of 10^7 provided that $Re = O(1)$, $d = 10^{-3}m$, $\sigma_0 = 10^{-2}S/m$, $\epsilon = 10^{-9}C/(m \cdot V)$, $\nu = 10^{-6}m^2/s$. Hence, the term $\frac{D(\nabla^2 \phi)}{Dt}$ can be neglected[105].

The dimensionless boundary conditions at $r = a$ are

$$u = v = w = 0, \quad (5.28)$$

$$\sigma = 0. \quad (5.29)$$

At $r = b$, the dimensionless boundary conditions write

$$u = v = w = 0, \quad (5.30)$$

$$\sigma = 1. \quad (5.31)$$

The dimensionless base state is defined as follows,

$$\bar{w} = -2[r^2 - \frac{(b^2 - a^2) \ln(r/a) + a^2 \ln(b/a)}{\ln(b/a)}], \quad (5.32)$$

$$\bar{\sigma} = \frac{\ln(r/a)}{\ln(b/a)}, \quad (5.33)$$

$$\bar{E}_r = \frac{a \ln(b/a)}{r[\eta \ln(r/a) + \ln(b/a)]}, \quad (5.34)$$

$$\bar{\phi} = -\frac{a \ln(b/a)}{\eta} \ln[\eta \ln(r/a) + \ln(b/a)], \quad (5.35)$$

$$\bar{\rho}_e = -\frac{a \ln(b/a)}{r^2 [\eta \ln(r/a) + \ln(b/a)]^2}. \quad (5.36)$$

Note that the charge density $\bar{\rho}_e$ is negative, while the base state of the electric field is positive. Therefore, the electric body force $\rho_e \mathbf{E}$ acts in the opposite direction to the radial direction.

When the radius $a \rightarrow \infty$, the base state reduces to the problem studied by Chang et al. [105]:

$$\bar{w}(x) = 4(x - x^2), \quad (5.37)$$

$$\bar{\sigma} = x, \quad (5.38)$$

$$\bar{E}_r = \frac{1}{\eta x + 1}, \quad (5.39)$$

$$\bar{\phi} = -\frac{1}{\eta} \ln(\eta x + 1), \quad (5.40)$$

$$\bar{\rho}_e = -\frac{1}{(\eta x + 1)^2}, \quad (5.41)$$

where $x = r - a$ represents the wall-normal direction.

The base state (5.32)-(5.36) of this system depends on the inner radius a and η . The charge density $\bar{\rho}_e$ and the electric field strength \bar{E}_r are plotted in Figure 5.2. Figure 5.2(b) and Figure 5.2(d) show that the electric-field strength decreases more rapidly for a smaller a . For instance, when $a = 0.1$, $\eta = 10$, E_r decreases from 1 to 0.1 near $r = 0.3$. However, when $a = 10$, $\eta = 10$, the electric-field strength E_r decreases from 1 to 0.1 near $r = 10.8$. The charge density also decreases more rapidly for a smaller a by comparing Figure 5.2(a) with 5.2(c). Furthermore, in Figure 5.2, it implies that for a large conductivity gradient, the portion of the fluid layer where the electric force $\bar{\rho}_e \bar{E}_r$ is appreciable is proximal to the inner surface.

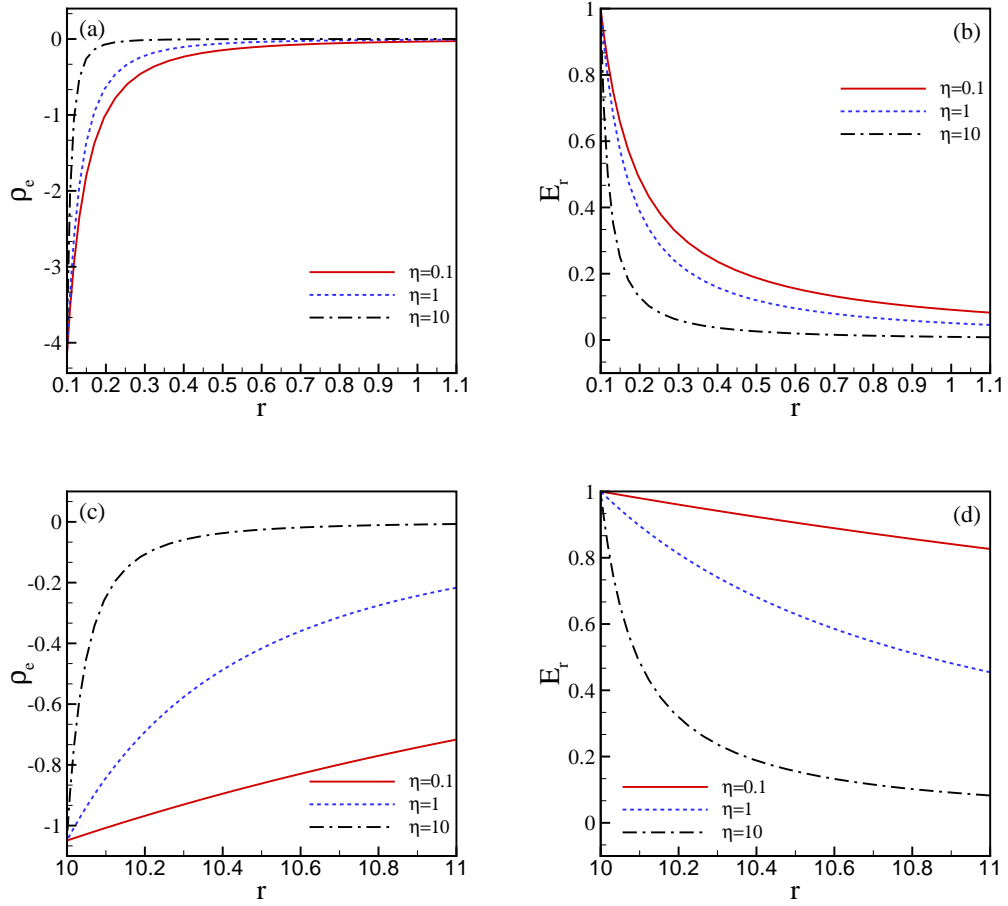


Figure 5.2: (a),(c): the charge density of the base state. (b),(d): the strength of the electric field at the base state. (a),(b) are plotted at the dimensionless radius $a = 0.1$; (c),(d) are plotted at the dimensionless radius $a = 10$.

5.3 Linear stability analysis

Although the analytical base state has been obtained in Sec.5.2, it is not necessary to be stable. To investigate the stability of the flow, the linear stability theory by introducing infinitesimal disturbances into the system is applied,

$$\mathbf{v} = \bar{\mathbf{v}} + \mathbf{v}', \quad p = \bar{p} + p', \quad \phi = \bar{\phi} + \phi', \quad \sigma = \bar{\sigma} + \sigma'. \quad (5.42)$$

The variables $\mathbf{v}' = u'\mathbf{e}_r + v'\mathbf{e}_\theta + w'\mathbf{e}_z$, p' , ϕ' and σ' are the infinitesimal disturbances. On substituting the perturbed variables $(\mathbf{v}, p, \phi, \sigma)$ into the dimensionless governing equations, and after linearizing, the governing equations of the infinitesimal disturbances obtained are:

$$\frac{\partial u'}{\partial r} + \frac{u'}{r} + \frac{1}{r} \frac{\partial v'}{\partial \theta} + \frac{\partial w'}{\partial z} = 0, \quad (5.43)$$

$$\frac{\partial u'}{\partial t} + \bar{w} \frac{\partial u'}{\partial z} = -\frac{\partial p'}{\partial r} + \frac{1}{Re} \left(\nabla^2 u' - \frac{u'}{r^2} - \frac{2}{r^2} \frac{\partial v'}{\partial \theta} \right) + Q \left(\nabla^2 \bar{\phi} \frac{\partial \phi'}{\partial r} + \frac{\partial \bar{\phi}}{\partial r} \nabla^2 \phi' \right), \quad (5.44)$$

$$\frac{\partial v'}{\partial t} + \bar{w} \frac{\partial v'}{\partial z} = -\frac{1}{r} \frac{\partial p'}{\partial \theta} + \frac{1}{Re} \left(\nabla^2 v' - \frac{v'}{r^2} + \frac{2}{r^2} \frac{\partial u'}{\partial \theta} \right) + \frac{Q \nabla^2 \bar{\phi}}{r} \frac{\partial \phi'}{\partial \theta}, \quad (5.45)$$

$$\frac{\partial w'}{\partial t} + \bar{w} \frac{\partial w'}{\partial z} = -\frac{d\bar{w}}{dr} u' - \frac{\partial p'}{\partial z} + \frac{1}{Re} \nabla^2 w' + Q \nabla^2 \bar{\phi} \frac{\partial \phi'}{\partial z}, \quad (5.46)$$

$$\frac{\partial(\nabla^2 \phi')}{\partial t} + \bar{w} \frac{\partial(\nabla^2 \phi')}{\partial z} = -\frac{d(\nabla^2 \bar{\phi})}{dr} u' - R_t [(1 + \eta \bar{\sigma}) \nabla^2 \phi' + \eta (\nabla^2 \bar{\phi} \sigma' + \frac{d\bar{\phi}}{dr} \frac{\partial \sigma'}{\partial r} + \frac{d\bar{\sigma}}{dr} \frac{\partial \phi'}{\partial r})], \quad (5.47)$$

$$\frac{\partial \sigma'}{\partial t} + \bar{w} \frac{\partial \sigma'}{\partial z} = -\frac{d\bar{\sigma}}{dr} u' + \frac{1}{Re S c_e} \nabla^2 \sigma', \quad (5.48)$$

where $\nabla^2 = \frac{\partial^2}{\partial r^2} + \frac{1}{r} \frac{\partial}{\partial r} + \frac{1}{r^2} \frac{\partial^2}{\partial \theta^2} + \frac{\partial^2}{\partial z^2}$ and noting that $\nabla^2 \bar{\phi} = -\eta \bar{\rho}_e$, $\frac{\partial \bar{\phi}}{\partial r} = -\bar{E}_r$.

In a standard way, the normal mode analysis is considered,

$$\begin{pmatrix} \mathbf{v}' \\ p' \\ \phi' \\ \sigma' \end{pmatrix} = \begin{pmatrix} \hat{\mathbf{v}}(r) \\ \hat{p}(r) \\ \hat{\phi}(r) \\ \hat{\sigma}(r) \end{pmatrix} \exp[i(n\theta + kz) + \omega t], \quad (5.49)$$

where k is the streamwise wavenumber, n is the azimuthal wavenumber, $\omega = \omega_r + i\omega_i$ is the complex temporal growth rate whose real part ω_r describes the exponent growth rate of the amplitudes of disturbances, and the hats denote the Fourier amplitudes of disturbances. The normal mode analysis results in the eigenvalue problem of ω .

The velocity and electric conductivity at $r = a, b$ are fixed, thus boundary conditions of the perturbed system at $r = a, b$ are expressed as follows,

$$\hat{u} = \hat{v} = \hat{w} = \hat{\sigma} = 0. \quad (5.50)$$

The radial component of the electric field E_r at the boundary is assumed to be fixed, then the perturbed conditions of electric potential at the inner and outer surface are,

$$\frac{d\hat{\phi}}{dr} = 0. \quad (5.51)$$

A Chebyshev collocation method is implemented to resolve the eigenvalue problem, and the physical domain is transformed to the Chebyshev domain,

$$\zeta = 2\frac{r-a}{b-a} - 1. \quad (5.52)$$

The variables \hat{u} , \hat{v} , \hat{w} , \hat{p} , $\hat{\phi}$, $\hat{\sigma}$ are expanded as

$$\begin{aligned}\hat{u} &= \sum_0^N a_m T_m(\zeta), & \hat{v} &= \sum_0^N b_m T_m(\zeta), & \hat{w} &= \sum_0^N c_m T_m(\zeta), \\ \hat{p} &= \sum_0^N d_m T_m(\zeta), & \hat{\phi} &= \sum_0^N e_m T_m(\zeta), & \hat{\sigma} &= \sum_0^N f_m T_m(\zeta),\end{aligned}\tag{5.53}$$

where $T_m(\zeta)$ denotes the m th Chebyshev polynomial.

When the azimuthal wavenumber $n = 0$ and $a \rightarrow \infty$, the eigenvalue problem reduces to,

$$D\hat{u} + ik\hat{w} = 0,\tag{5.54}$$

$$\omega\hat{u} + ik\bar{w}\hat{u} = -D\hat{p} + \frac{1}{Re}\mathcal{L}\hat{u} + Q[D^2\bar{\phi}D\hat{\phi} + D\bar{\phi}\mathcal{L}\hat{\phi}],\tag{5.55}$$

$$\omega\hat{w} + ik\bar{w}\hat{w} = -D\bar{w}\hat{u} - ik\hat{p} + \frac{1}{Re}\mathcal{L}\hat{w} + ikQD^2\bar{\phi}\hat{\phi},\tag{5.56}$$

$$\omega\mathcal{L}\hat{\phi} + ik\bar{w}\mathcal{L}\hat{\phi} = -D^3\bar{\phi}\hat{u} - R_t[(1 + \eta\bar{\sigma})\mathcal{L}\hat{\phi} + \eta(D^2\bar{\phi}\hat{\sigma} + D\bar{\phi}D\hat{\sigma} + D\bar{\sigma}D\hat{\phi})],\tag{5.57}$$

$$\lambda\hat{\sigma} + ik\bar{w}\hat{\sigma} = -D\bar{\sigma}\hat{u} + \frac{1}{ReSc_e}\mathcal{L}\hat{\sigma},\tag{5.58}$$

where $\mathcal{L} = D^2 - k^2$, $D = \frac{d}{dx}$.

The equations (5.54)-(5.58) are solved with the boundary conditions at $x = 0, 1$,

$$\hat{u} = \hat{w} = \hat{\sigma} = D\hat{\phi} = 0.\tag{5.59}$$

The above system is identical to the two-dimensional problem studied by Chang et al. [105].

5.4 Results and Discussion

This section is organized into two parts. In the first part, the limiting case of an infinitely large inner radius, *i.e.* $a \rightarrow \infty$, is considered. The two dimensional axisymmetric system is investigated by comparing the results with the previous study of Chang et al. [105] to examine the validity of “our numerical method”. The second part deals with the three dimensional instability of the annular flow under the consideration of a finite inner radius a . The parametric studies on the stability characteristics are investigated.

5.4.1 Limiting case of $a \rightarrow \infty$

This section presents the results of the eigenvalue analysis which starts with the case of a sufficiently large radius. Hence, a small parameter can be defined as

$$\delta = \frac{b - a}{a}. \quad (5.60)$$

When $\delta \rightarrow 0$, the problem can be reduced to the problem studied by Chang et al. [105].

The dimensionless parameter Q is related to the Reynolds number Re and electric Schmidt number Sc_e as

$$Q = \frac{Q'}{Re^2 Sc_e}, \quad (5.61)$$

where $Q' = \frac{\epsilon E_0^2}{\mu K_{eff}/d^2}$ represents the scaled electric energy density.

Figure 5.3(a) illustrates the marginal stability curves in the $Q' - k$ plane which reproduces the results by Chang et al. [105]. The critical point (Q'_c, k_c) is compared with their results [105] in Table 5.1. It is found that some of the results in Ref.[105] are inaccurate. When the parameter η exceeds some certain value, the marginal curve presents a bimodal structure[105], for instance $\eta = 50$. However, this bimodal structure can be multi-valued as shown in Figure

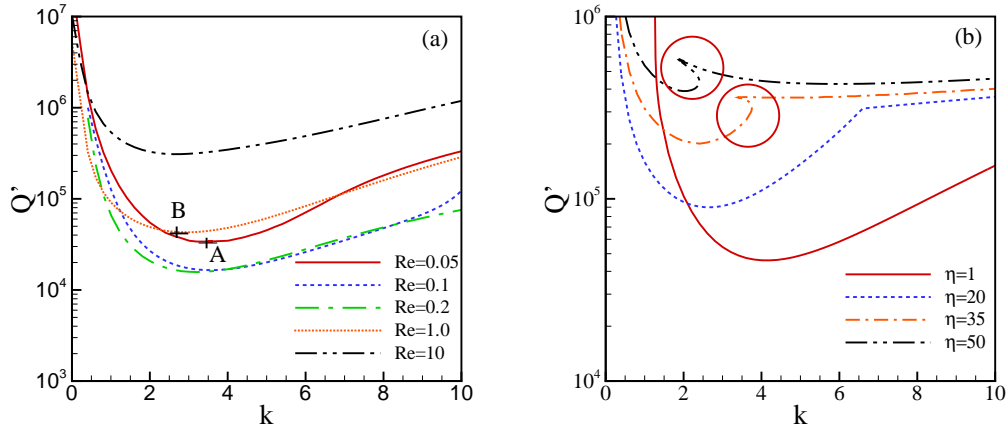


Figure 5.3: Marginal stability curves.(a) $Sc_e = 1000$, $\eta = 10$. (b) $Re = 1$, $Sc_e = 1000$. The parameter $R_t \rightarrow \infty$.

Table 5.1: The leading eigenvalues of the critical stability points A and B in Figure 5.3(a).

	Re	η	k_c	Q'_c	ω
Chang et al.[105]	0.05	10	3.50	3.359×10^4	$0 - 4.937i$
Present work	0.05	10	3.50	3.3589×10^4	$0.0000 - 4.9378i$
Chang et al.[105]	1	10	2.95	4.295×10^4	$0 - 2.850i$
Present work	1	10	2.95	4.2953×10^4	$0.0000 - 2.8503i$

5.3(b) which was overlooked by Chang et al.[105].

5.4.2 Finite inner radius a

This section presents the stability analysis of the annular flow system of a finite radius a . The normal mode analysis is implemented. The influences of a , Re , η and Sc_e on the stability of the system are discussed in this section. The parameter R_t is assumed to be infinitely large.

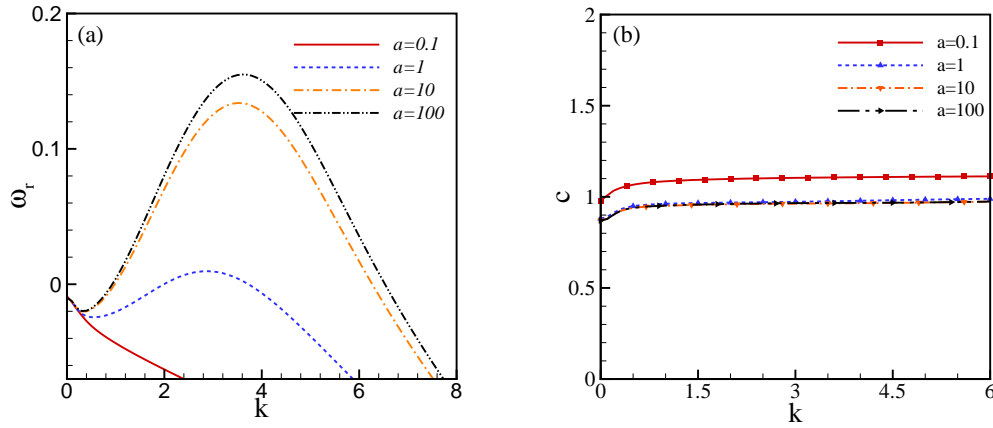


Figure 5.4: (a) Growth rate of the most unstable disturbances ω_r versus wavenumber k , (b) linear wave speed c versus wavenumber k . The depending parameters are $Re = 1$, $Sc_e = 1000$, $Q' = 10^5$, $\eta = 10$, $n = 0$.

Influence of inner radius

First, the influences of the inner radius a on the stability of the transverse unstable mode (the azimuthal wavenumber $n = 0$) are examined by fixing the parameter $Q' = 4.2953 \times 10^4$, $\eta = 10$, $n = 0$, $k = 2.95$, $Re = 1$, $Sc_e = 1000$.

Figure 5.4(a) shows the real part of the eigenvalue, ω_r versus the disturbance wavenumber k , and indicates that the system becomes more unstable for a larger inner radius a . The leading eigenvalue is listed in Table 5.2 which demonstrates that the real part of the growth rate becomes larger as the inner radius a increases. When a is sufficiently large, it reproduces the result showed in Section 5.4.1. The results indicate that, when the system is perturbed by streamwise disturbances, the system can be stabilized by reducing the inner radius a . The physical mechanism is explained here. As explained by Chang et al. [105], the flow instability of this system was mainly dominated by the dielectrophoretic effect, the viscosity and the ionic diffusion. When a fluid parcel with lower electric conductivity moves outwards (in the r direction), it enters in the region of higher electric conductivity. If the diffusion effect is not strong enough, the electric force will drive the fluid parcel continuously. Otherwise, the

Table 5.2: The first leading eigenvalues for $Q' = 4.2953 \times 10^4$, $n = 0$, $k = 2.95$, $Re = 1$, $Sc_e = 1000$, $\eta = 10$.

Inner Radius	$a = 0.1$	$a = 1$	$a = 10$
ω	$-0.0828 - 3.2580i$	$-0.0479 - 2.8960i$	$-0.0078 - 2.8509i$

ionic diffusion will remove the conductivity difference between the flowing fluid parcel and its surroundings, hence, impeding the electrohydrodynamic instability. The dielectrophoretic effect can be characterized by $\bar{\rho}_e \bar{E}_r$ [101, 105]. As the charge density and electric field strength are shown in Figure 5.2, it is clear that the dielectrophoretic effect becomes stronger in the region near the outer surface when the inner radius becomes larger. Therefore, the system becomes more unstable with increasing the inner radius a .

Here, a linear wave speed c in the streamwise direction is defined as $c = -\frac{\omega_i}{k}$. It is observed that the linear wave speed c decreases with increasing a as shown in Figure 5.4(b). Additionally, c initially increases when wavenumber k is small, but it does not change when k is large. Apart from that, when $a \geq 1$, the influence of the inner radius a on the linear wave speed is not significant.

Because a Squire's transformation of this system is not possible, the influences of spanwise disturbances (disturbances in the azimuthal direction) should be studied which may cause the system to be more unstable. Figure 5.5 presents the marginal curves for three typical cases: $a = 0.1, 1, 10$. It is observed that the most unstable azimuthal wavenumber respectively is $n = 1, 5, 35$. The non-zero value of n indicates that the spanwise disturbances make the system to be more unstable. Here, the lowest marginal stability curve in Figure 5.5(a-c) is defined as the global marginal stability curve. Above the global marginal curve, the system is unstable. The comparison of the global marginal stability curves is shown in Figure 5.5(d) which indicates that the system becomes more unstable for a larger inner radius a . When $a = 1, 10$, the global marginal stability curve presents a bimodal structure. The bimodal structure indicates that

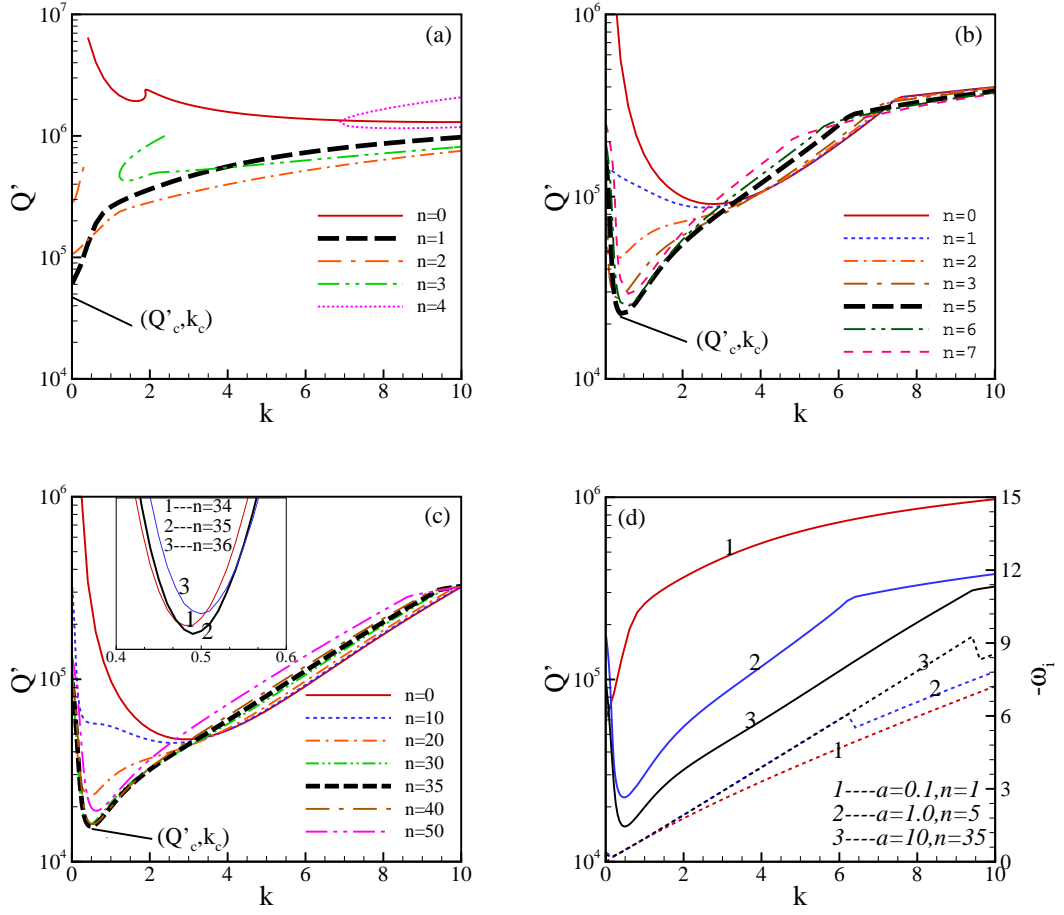


Figure 5.5: (a-c) Marginal stability curves in the $Q' - k$ plane for $a = 0.1, 1, 10$ respectively. (d) Solid lines for the global marginal stability curves and dashed lines for the corresponding frequency $-\omega_i$. The depending parameters are $Re = 1$, $Sc_e = 1000$, $\eta = 10$.

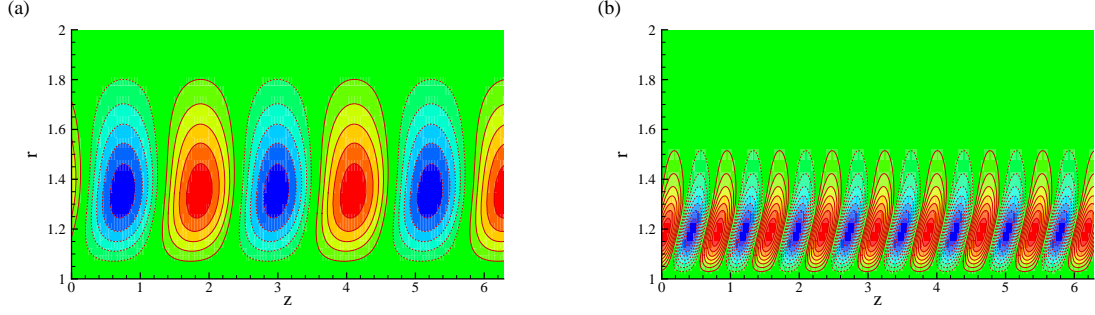


Figure 5.6: Convection cell patterns.(a) $Q' = 9.1090 \times 10^4$, $k = 2.81$; (b) $Q' = 36.3981 \times 10^4$, $k = 8.21$; The other depending parameters are $a = 1$, $Re = 1$, $Sc_e = 1000$, $\eta = 10$, $n = 0$.

there are two different unstable modes. Here, according to the difference in wavenumber, the unstable mode corresponding to a smaller wave number is defined as the long-wave unstable mode, while the mode corresponding to a larger wave number is defined as the short-wave mode. For instance, when $a = 1$ and $n = 0$ (the marginal curve presents a bimodal structure in Figure 5.5(b) for $a = 1$, $n = 0$), for the long-wave unstable mode, the convection cell occupies almost the whole thickness of the fluid layer; while the short-wave unstable mode, the convection cell is almost constrained within the inner half of the channel as shown in Figure 5.6. However, the critical instability is determined by the lower branch of the bimodal structured marginal curve indicating that the long-wave unstable mode dominates the short-wave unstable mode. Figure 5.5(d) shows that the frequency $-\omega_i$ jumps down when $a = 1$, 10 showing that the unstable mode switches from the long-wave mode to the short wave mode as the wavenumber k increases.

When $a = 0.1$, $n = 1$, the critical value of (Q'_c, k_c) is $(6.0898 \times 10^4, 0)$, and the corresponding eigenvalue is $\lambda = 0$ indicating that the unstable mode is stationary. However, for $a = 1, 10$, the critical value of (Q'_c, k_c) , respectively reads $(2.2556 \times 10^4, 0.47)$, $(1.5620 \times 10^4, 0.49)$, and the corresponding eigenvalue is $\omega = 0 - 0.4567i$, $\omega = 0 - 0.4748i$, respectively. The non-zero imaginary parts of eigenvalues for the two cases $a = 1, 10$ indicate that the most unstable modes are given by oblique waves. In addition, the critical streamwise disturbance

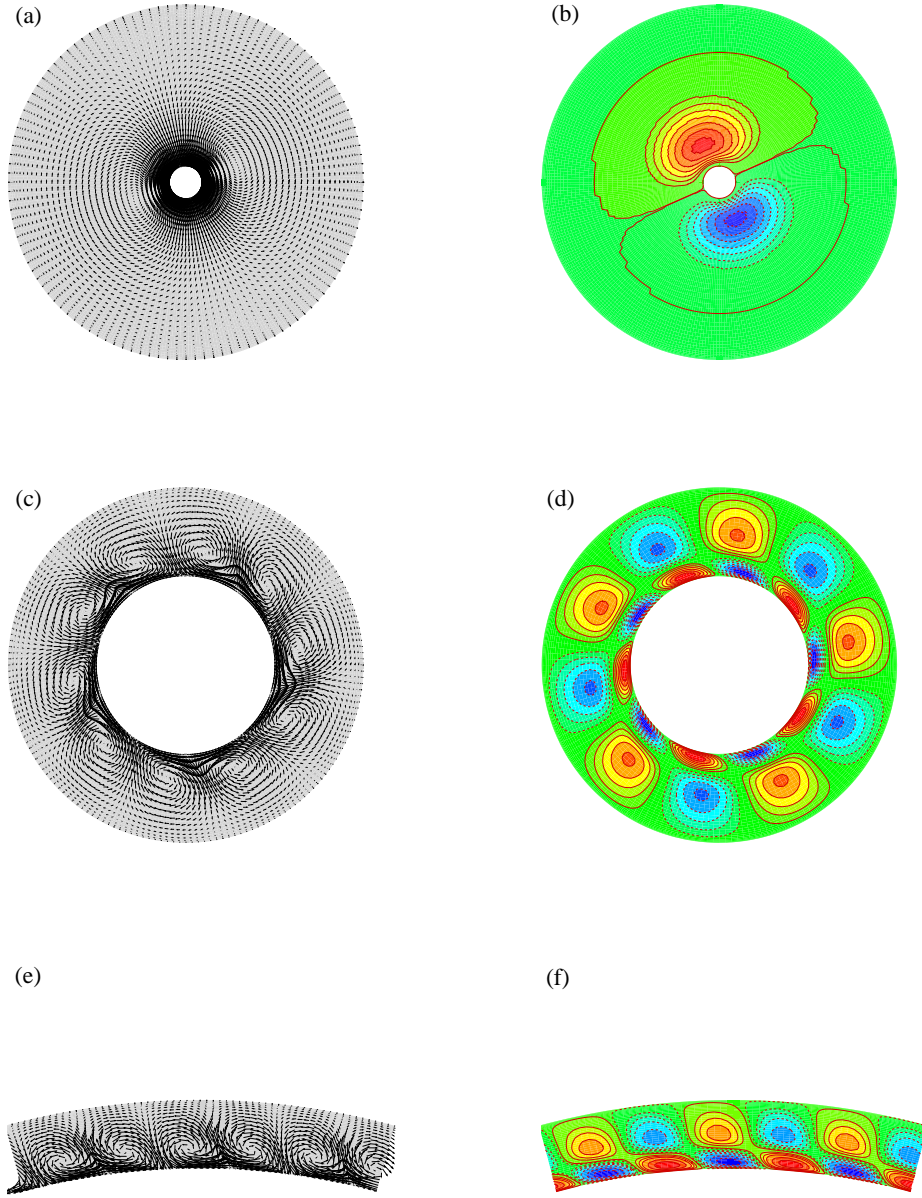


Figure 5.7: The cross section $r - \theta$ view of the flow field. (a,c,e) The velocity components of u' and v' . (b,d,f) The contour plot of velocity component w' . (e,f) $\theta \in [\frac{5\pi}{12}, \frac{7\pi}{12}]$. The depending parameters: (a,b) $(Q'_c, k_c) = (6.0898 \times 10^4, 0)$, $a = 0.1$, $n = 1$; (c,d) $(Q'_c, k_c) = (2.2556 \times 10^4, 0.47)$, $a = 1$, $n = 5$; (e,f) $(Q'_c, k_c) = (1.5620 \times 10^4, 0.49)$, $a = 10$, $n = 35$. The other parameters are $Re = 1$, $Sc_e = 1000$, $\eta = 10$.

wavenumber k is much smaller than the critical azimuthal wave number n . As shown from the above discussion, the instability is triggered by the dielectrophoretic effect. According to the perturbed system, this effect is characterized by the linearized body force $\rho_e \mathbf{E}$, i.e., the radial component force $f_r = \bar{\rho}_e E'_r + \rho'_e \bar{E}_r$, the streamwise component force $f_z = \bar{\rho}_e E'_z = ik\bar{\rho}_e \hat{\phi}$ and the azimuthal component force $f_\theta = \bar{\rho}_e E'_\theta = \frac{in}{r} \bar{\rho}_e \hat{\phi}$. The magnitudes of f_z and f_θ are proportional to k and n/r , respectively. If k is much larger than n/r , the streamwise disturbances dominate the instability. Otherwise, the spanwise disturbances dominate the instability. To illustrate this, the perturbed velocity field is plotted in Figure 5.7. Figure 5.7(a) shows the velocity field (u', v') and Figure 5.7(b) presents the contour lines of the velocity component w' in the $r - \theta$ plane. The velocity field (u', v') as well as the contour lines of w' are not distorted as seen in Figure 5.7(a,b). The result demonstrates that the unstable mode is stationary. In Figure 5.7(b), the magnitude of w' is much smaller than the magnitudes of u' and v' which indicates that the instability is dominated by spanwise disturbances. Figure 5.7(c-f) shows the perturbed flow fields of $a = 1, 10$ in which the velocity fields (u', v') and the contour lines of w' are distorted. One such phenomenon implies that the unstable mode is oscillatory. In addition, in Figure 5.7(d,f), the magnitude of w' is not as small as that in Figure 5.7(b) indicating the most unstable mode is given by three-dimensional oblique wave.

Figure 5.8 illustrates the variations of critical electric field number Q'_c , critical frequency $-\omega_{ic}$ and critical wavenumbers n_c, k_c with the radius a . Obviously, the critical electric field number Q'_c decreases with increasing a . When $a \leq 0.4$, the frequency $-\omega_{ic}$ of the most unstable mode as well as the critical wave number k_c are zero, indicating that the most unstable mode is stationary. It is discovered that the critical wave number n_c increases with increasing a , although for some cases, $a = 0.2, 0.3, 0.4$, the critical wavenumber is the same: $n_c = 4$. This is because the wavenumber n is characterized by the pairs of convection cells in the spanwise direction which is an integer. When $a \rightarrow \infty$, the critical wavenumber $k \approx 0.5$, and $Q'_c \approx 1.5 \times 10^4$.

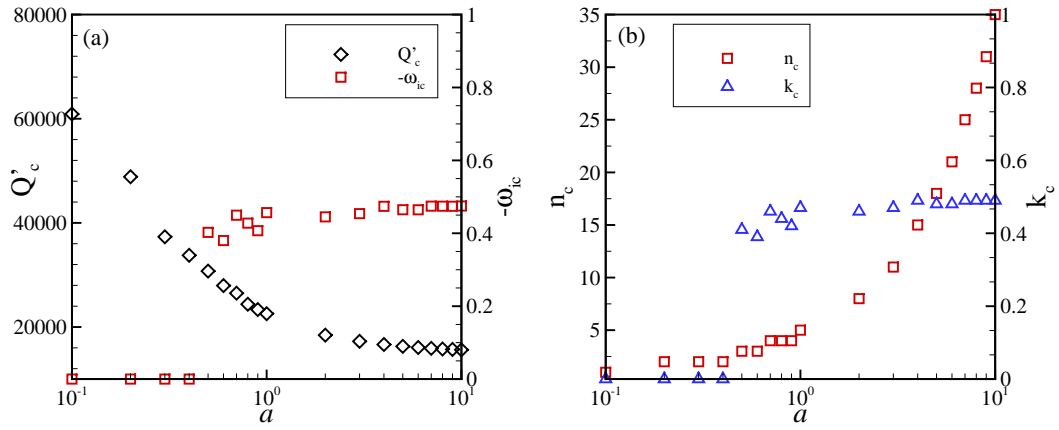


Figure 5.8: (a) The critical electric field number Q'_c and the corresponding frequency $-\omega_i$ versus the radius a . (b) The critical wavenumbers n_c and k_c versus the radius a . The other depending parameters are $Re = 1$, $Sc_e = 1000$, $\eta = 10$.

Influence of electric conductivity gradient

In this section, the influence of the electric conductivity gradient on the stability is investigated. The other dimensionless parameters are held fixed. Figure 5.9(a) illustrates the marginal stability curves for several typical input values of $\eta = 0.1, 1, 10, 100$. For the selected input values of η , when the electric conductivity gradient is small, e.g. $\eta = 0.1, 1$, increasing the value of η enhances the flow instability since the marginal curve dips lower. However, as the value of η further increases, the marginal curve rises gradually, e.g. the marginal stability curves for $\eta = 10, 100$ as shown in Figure 5.9(a). The frequency $-\omega_i$ versus the disturbance wavenumber is shown in Figure 5.9(b). It shows that $-\omega_i$ decreases as the electric conductivity gradient increases. Particularly, it is observed that, for $\eta = 0.1, 1, 10$, the frequency $-\omega_i$ of the critical unstable mode is not zero, which indicates the most unstable mode is oscillatory; while the critical frequency $\omega_i = 0$ for $\eta = 100$, which indicates that the most unstable mode is stationary.

To elucidate the two different unstable modes, the perturbed flow field is plotted in Figure 5.10. Figure 5.10(a,b) shows that the flow field in the $r - \theta$ plane as well as the contour lines

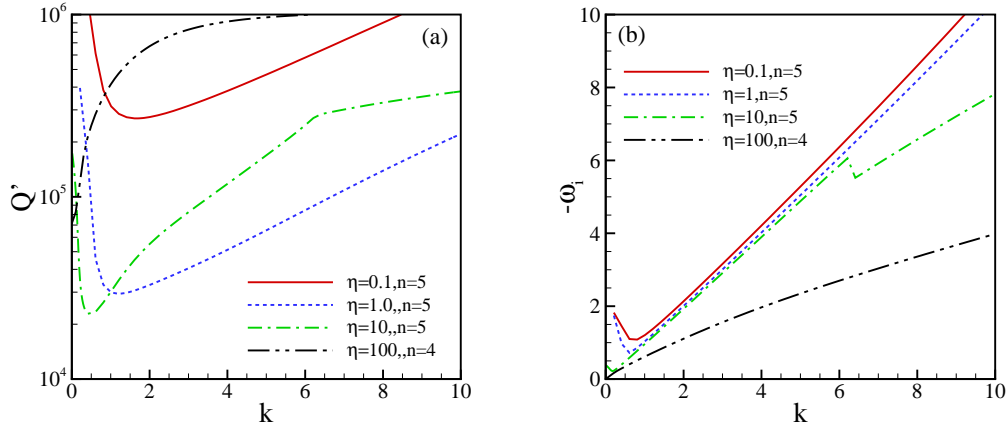


Figure 5.9: (a) Global marginal stability curves and (b) the corresponding frequency $-\omega_i$. The other depending parameters are $a = 1$, $Re = 1$, $Sc_e = 1000$.

of w' are strongly distorted. The flow field in the $r - \theta$ plane is not distorted in Figure 5.10(c). Moreover, the magnitude of w' in Figure 5.10(d) is much smaller than the magnitudes of (u', v') in Figure 5.10(c). Figure 5.10 indicates that increasing the value of η shifts the unstable mode from the oscillatory mode to the stationary mode.

In order to have a full understanding of the influence of electric conductivity gradient on the stability, the critical electric field number Q'_c , critical wavenumbers k_c , n_c and the critical frequency $-\omega_i$ versus the electric conductivity η are investigated. Results are shown in Figure 5.11.

Figure 5.11 shows that the frequency $-\omega_i$, critical wavenumbers n_c and k_c jump at $\eta \approx 17.5$, indicating that the critical unstable mode switches to the stationary mode from the oscillatory mode. The results in Figure 5.11 show that the critical wavenumber k_c decreases gradually as the conductivity gradient increases when $\eta < 17.5$, while the wavenumber n_c jumps from $n = 5$ to $n = 4$ at $\eta \approx 17.5$. The decrease in k_c indicates that the spanwise disturbances become important in destabilizing the system. When the critical unstable mode switches to the stationary mode, the wavenumber $k_c = 0$ which indicates that the spanwise disturbances are the major causes that initiate the electro-convection in this system. Figure 5.11(a) shows that

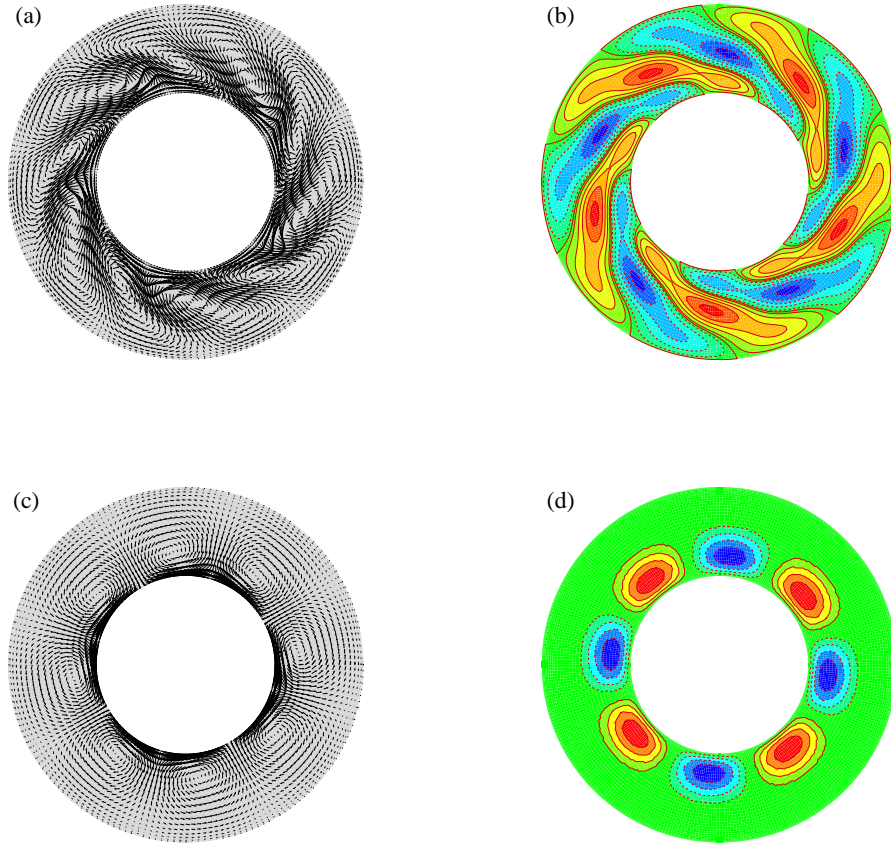


Figure 5.10: The cross section $r - \theta$ view of the flow field. (a,c)The velocity components of u' and v' .(b,d) The contour plot of velocity component w' . The depending parameters: (a,b) $(Q'_c, k_c) = (26.9395 \times 10^4, 1.66)$, $n_c = 5$, $\eta = 0.1$; (c,d) $(Q'_c, k_c) = (7.1410 \times 10^4, 0)$, $n_c = 4$, $\eta = 100$. The other parameters are $a = 1$, $Re = 1$, $Sc_e = 1000$.

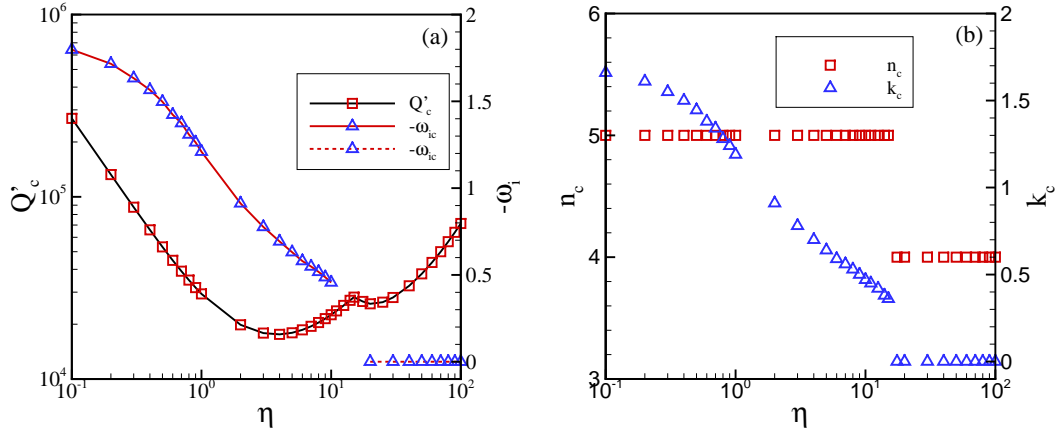


Figure 5.11: (a) The critical electric field number Q'_c and the corresponding frequency $-\omega_i$ versus η . (b) The critical wavenumbers n_c and k_c versus η . The other depending parameters are $a = 1$, $Re = 1$, $Sc_e = 1000$.

the critical electric field number Q'_c decreases gradually till $\eta \approx 4$ which implies that the instability of the oscillatory mode is enhanced. However, as the conductivity gradient increases, Q'_c increases gradually and reaches to a maximum, which reflects that the oscillatory mode is impeded. When the critical unstable mode switches to the stationary mode, the critical electric field number Q'_c decreases to a minimum till $\eta \approx 20$, then it increases gradually as η increases. Such a phenomenon indicates that, the stationary mode can either be enhanced or impeded via increasing the conductivity gradient.

In order to understand the physical mechanism, a limiting case: $\eta \rightarrow 0$ is taken into account. The electric body force term in Eq.(5.24) can be re-written as

$$f = Q \nabla^2 \phi \nabla \phi = -\eta \rho_e Q \nabla \phi. \quad (5.62)$$

When $\eta \rightarrow 0$, the body force $f \rightarrow 0$. Hence, no matter how large the electric field strength is, the system is always stable because the dielectrophoretic effect is absent. Actually, the mechanism can be analogous to the Rayleigh-Bénard convection. If there is no temperature gradient, the heated liquid layer should be always stable. A electric Rayleigh number can be

defined as $Ra_e = Q'\eta$ which approaches zero as $\eta \rightarrow 0$. As a result, the system becomes stable when $\eta \rightarrow 0$.

Furthermore, if a fluid parcel moves outwards under the action of electric field, it enters in the region of higher electric conductivity. When the conductivity gradient is small (the oscillatory mode dominates the instability), the ionic diffusion effect is insignificant. As the electric conductivity gradient is increased, the dielectrophoretic effect will be enhanced since the conductivity difference between the fluid parcel and its surroundings is increased. Consequently, the instability is enhanced. As the conductivity gradient increases, the diffusion effect becomes significant such that the conductivity difference between the fluid parcel and its surroundings will be removed due to diffusion effect. Hence, when the conductivity gradient is large, a stronger electric field is necessary to trigger the occurrence of instability. Moreover, Baygents and Baldessari [101] explained the physics of electrohydrodynamic instability mechanism in a planar system by the base state profile of electric body force. They pointed out that the portion of fluid where the electric body force was significant was close to the lower-conductivity boundary and became increasingly narrow as the conductivity gradient increased [101]. They suggested that the lower boundary produced a strong stabilizing effect when the conductivity gradient was large [101]. Figure 5.2 suggests that the portion where electric body force $\bar{\rho}_e \bar{E}_r$ is significant is very narrow for a large conductivity gradient. It seems that the inner cylinder attracts the electric charge into the thin boundary layer, beyond which there is very few electric charges. As we have discussed in the above section that the convection is initiated by the body force $(f_r, f_\theta, f_z) = (\bar{\rho}_e E'_r + \rho'_e \bar{E}_r, \bar{\rho}_e E'_\theta, \bar{\rho}_e E'_z)$. Outside of the boundary layer, the charge density $\bar{\rho}_e \approx 0$ and $\bar{E}_r \approx 0$ when the conductivity gradient is large. Hence, the body force outside the boundary layer is too small to initiate convection in the system. Note that the electric force is multiplied by the dimensionless parameter Q' . Thus, a higher value of Q' is necessary to trigger the instability of this system.

When the instability is dominated by the stationary mode, the physical mechanism is similar

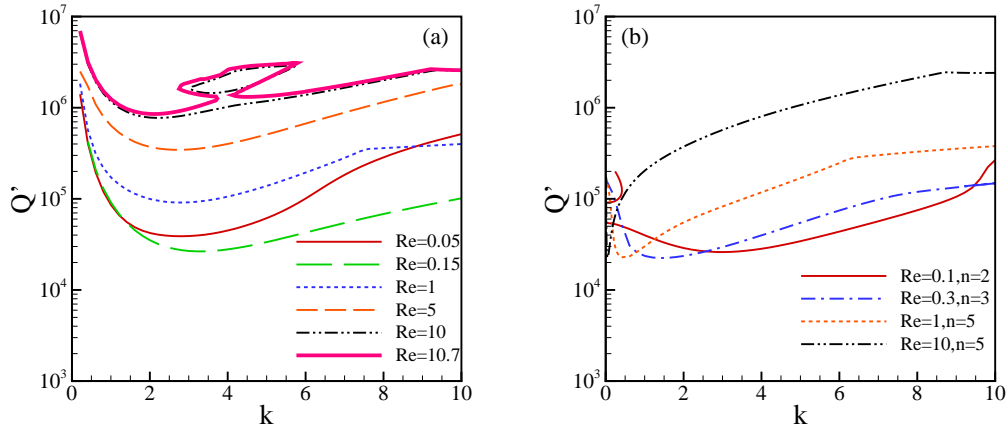


Figure 5.12: (a) Marginal stability curves of the transverse unstable mode, $n = 0$. (b) The global marginal stability curve. The other depending parameters are $a = 1$, $Sc_e = 1000$, $\eta = 10$.

to that of the oscillatory mode. This is very different from the classical Rayleigh-Bénard convection, in which, the larger temperature gradient is the more unstable system.

Influence of Reynolds number

In this section, the influence of the Reynolds number on the stability of this system is discussed by fixing the other dimensionless parameters. First, in Figure 5.12(a), the influence of Re on the stability of transverse unstable mode, i.e., $n = 0$, is shown. When Re is small, the marginal stability curve dips lower gradually till about $Re \approx 0.15$, then it rises rapidly. Results in Figure 5.12(a) indicate that, when Re is small, the instability is enhanced by the shear flow; while when Re is large, the shear flow impedes the instability. The physical mechanism is explained here. When the Reynolds number is small, with increasing Re , the electrohydrodynamic motion will be enhanced. Therefore, the system will be more unstable when the Reynolds number increases. However, as the Reynolds number is increased further, the viscous shear effect and the diffusive effect become significant. Due to the advection of electric conductivity, a conspicuous enhancement of diffusive effect would be caused by

increasing the Reynolds number. Furthermore, the viscous stress is a factor that dissipates energy of the system, which plays a stabilizing role in this system and will also be enhanced as Re increases. However, it should be emphasized that, the inertia would also increase as Re increases which is the major destabilizing effect in high-Reynolds-number shear flows. Because in this system, the Reynolds number is not large $Re \in [0, 10]$ and instability due to “Reynolds stress” will not occur. Once the diffusive effect and viscous dissipation effect are strong, the marginal stability curve will rise when the Reynolds number is increased further. An interesting phenomenon observed is that there may exist a stable looped region lying in the above of the marginal stability curve when Re is increased, for instance, $Re = 10$. This phenomenon is caused by the interactions between the dielectrophoretic effect, viscous effect and ionic diffusive effect. The stable looped region will vanish when Re increases further.

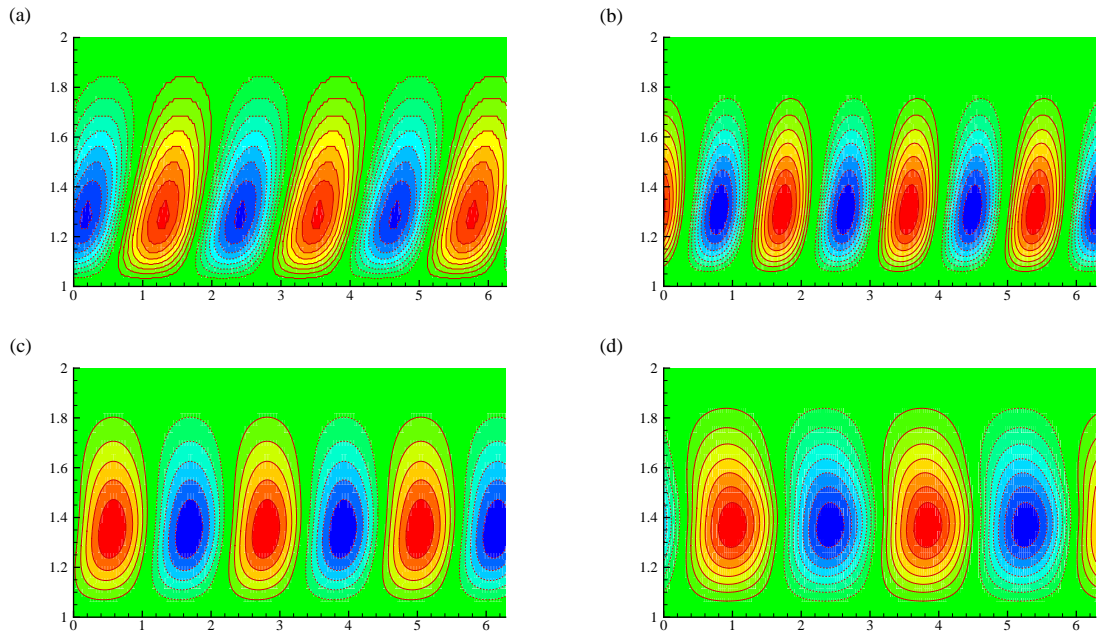


Figure 5.13: Convection cell patterns.(a) $Re = 0.05$, $Q' = 3.8855 \times 10^4$, $k = 2.81$; (b) $Re = 0.1$, $Q' = 2.6883 \times 10^4$, $k = 3.41$; (c) $Re = 1$, $Q' = 9.1090 \times 10^4$, $k = 2.81$; (d) $Re = 10$, $Q' = 77.2105 \times 10^4$, $k = 2.21$. The other depending parameters are $a = 1$, $Sc_e = 1000$, $\eta = 10$.

To illustrate the above discussion, we plot the convection cell patterns of four typical cases at their corresponding critical state with $Re = 0.05, 0.1, 1, 10$ in figure 5.13. As seen in figure 5.13(a), the transverse mode appears to be inclined traveling wave in the streamwise direction. When Re is increased to 0.1, convection near the outer electrode becomes weaker because the diffusive effect near the outer electrode is enhanced by the shear flow. The inclined angle is also reduced if compared with the case $Re = 0.05$. As Re increases further, the inclined angle reduces continuously. When $Re = 10$, the convection cell appears to be distorted which is caused by the imposed shear flow. However, the transverse mode may not be critical because the spanwise disturbances may make the system to be more unstable.

Figure 5.12(b) presents the global marginal stability curve. Comparing figure 5.12(a) and 5.12(b), we observe that the system is more unstable when it is perturbed by three-dimensional disturbances. Moreover, it is observed that the critical point (Q'_c, k_c) moves leftward as the Reynolds number increases. In order to explain the influences of Reynolds number on the stability of the three dimensional problem, the critical electric field number Q'_c , the critical frequency $-\omega_{ic}$, the critical wavenumber n_c and k_c are investigated. The results are shown in figure 5.14.

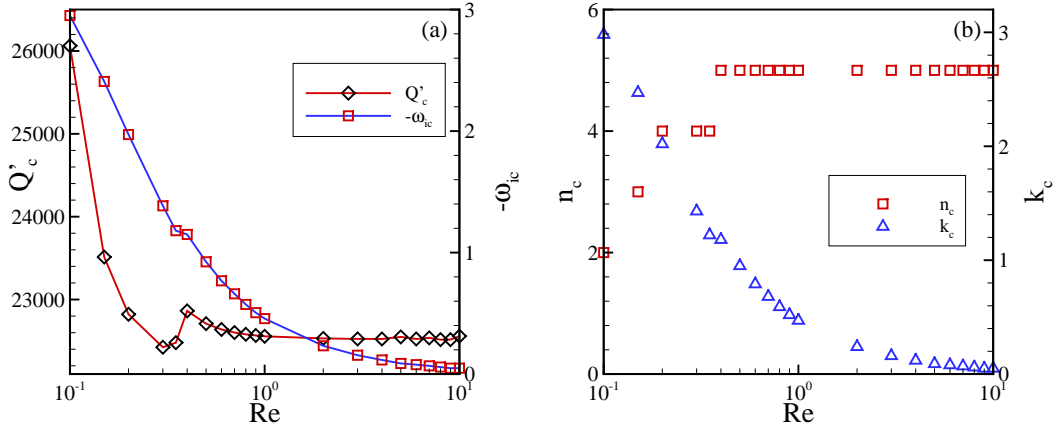


Figure 5.14: (a) The critical electric field number Q'_c and the corresponding frequency $-\omega_i$ versus Re . (b) The critical wavenumbers n_c and k_c versus Re . The other depending parameters are $a = 1$, $Sc_e = 1000$, $\eta = 10$.

Figure 5.14(a) demonstrates that the critical electric field number Q'_c decreases with Re gradually till about $Re \approx 0.3$, then it increases till $Re \approx 0.4$. After that, Q'_c decreases gradually, and when $Re \geq 1$, the influence of Reynolds number on Q'_c is not significant. The critical frequency decreases as Re increases and $\omega_i \approx 0$ at $Re = 10$. In figure 5.14(b), when $Re < 0.3$, the critical wavenumber k_c decreases, while n_c increases. The instability is triggered by the dielectrophoretic force \mathbf{f} . When $k_c > n_c/r$, f_z dominates f_θ , i.e., convection in $r - z$ plane is stronger than that in $r - \theta$ plane. As aforementioned, a slightly increasing in the Reynolds number from zero will enhance the dielectrophoretic effect. Thus, Q'_c decreases with increasing the Reynolds number until it reaches a minimum. As the Reynolds number is increased further, the convection in the $r - z$ plane will be impeded due to the enhancement of diffusive effect, hence Q'_c increases. After Q'_c reaches a maximum, Q'_c gradually decreases as the Reynolds number increases further till about $Re \approx 1$, because the dielectrophoretic effect in θ direction is enhanced. When $Re > 1$, Q'_c is almost independent of the shear flow. It is evident in figure 5.14(b) that n_c/r ($r \in [1, 2]$) is much larger than k_c when $Re > 1$ which indicates

the streamwise wavelength of the disturbance is much longer than its spanwise component, and the convection in $r - \theta$ plane is much stronger than that in $r - z$ plane. When $Re > 1$, although the spanwise disturbance becomes the major cause that destabilizes the system, the long-wave streamwise disturbance would make the system to be more unstable.

Influence of electric Schmidt number

The influence of the electric Schmidt number Sc_e is investigated in this section. Its influence on the marginal stability curve of transverse mode is illustrated in Figure 5.15(a). The marginal stability curve dips lower as Sc_e increases till $Sc_e \approx 150$. It then rises rapidly as Sc_e increases.

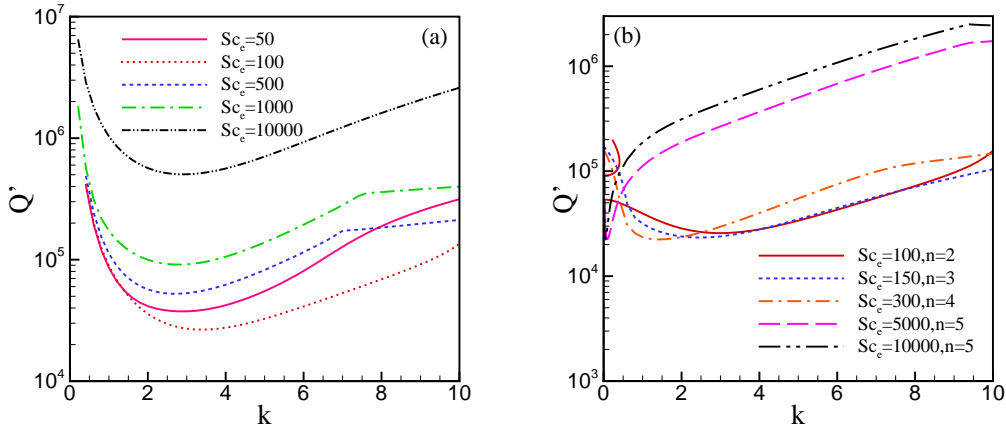


Figure 5.15: (a) Marginal stability curves of the transverse unstable mode, $n = 0$. (b) The global marginal stability curve. The other depending parameters are $a = 1$, $Re = 1$, $\eta = 10$.

Recall the definition of this parameter: $Sc_e = \frac{\nu}{K_{eff}}$. The value of Sc_e can be increased by reducing K_{eff} . Hence, the ionic diffusive effect becomes smaller as Sc_e increases. Therefore, the dielectrophoretic effect is enhanced as Sc_e increases (K_{eff} decreases) and the system becomes more unstable. However, on the other hand, for a large Sc_e , the definition of Sc_e tells that the viscous effect dominates the diffusion effect, and the viscous effect becomes

significant with increasing Sc_e . Since the viscous effect plays a stabilizing role in the system, the fluid layer will be stabilized as Sc_e increases further.

The global marginal stability curve for the three dimensional problem is shown in Figure 5.15(b). Clearly, with increasing the value of Sc_e , the critical wavenumber k_c decreases, which indicates that the streamwise component of the wavelength becomes longer. In order to illustrate the influence of electric Schmidt number on the three-dimensional stability, the critical electric field number Q'_c and the critical frequency $-\omega_{ic}$ are plotted in Figure 5.16(a). Note that the critical wavenumber $n_c \neq 0$ and critical frequency $\omega_{ic} \neq 0$ which indicates that the critical unstable mode was given by three dimensional oblique waves. The critical frequency $-\omega_{ic}$ approaches zero when Sc_e is very large. Additionally, Q'_c decreases with increasing the value of Sc_e till $Sc_e \approx 300$, then it increases with increasing Sc_e till $Sc_e \approx 500$. As Sc_e increases further, Q'_c decreases slightly, then Q'_c seems to be independent of Sc_e . It was reported by Chang et al. [105] that the influence of Sc_e on the longitudinal unstable mode in a planar system was insignificant when $Sc_e \geq 10^3$. Similarly, in this core-annular system, the Q'_c seems to be independent of Sc_e when $Sc_e > 10^3$ because the the spanwise disturbance is the major cause of the flow instability.

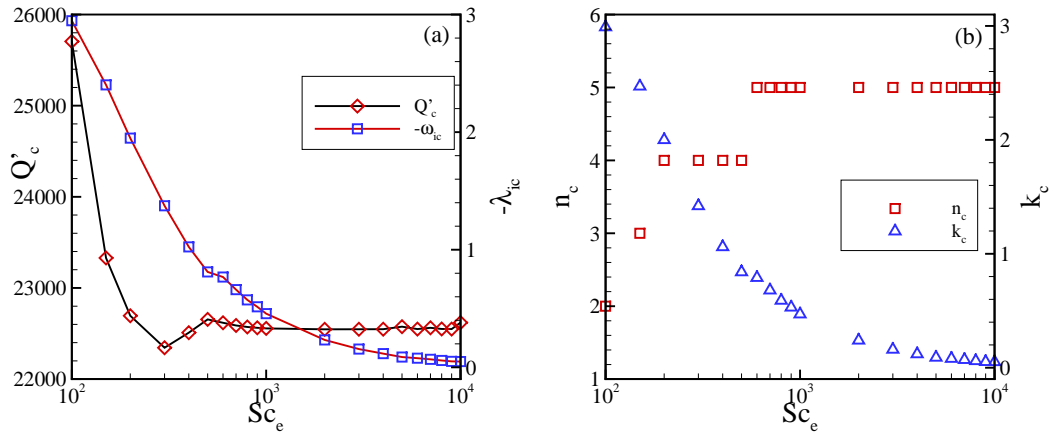


Figure 5.16: (a) The critical electric field number Q'_c and the corresponding frequency $-\lambda_i$ versus SSc_e . (b) The critical wavenumbers n_c and k_c versus SSc_e . The other depending parameters are $a = 1$, $Re = 1$, $\eta = 10$.

CHAPTER 6

Electrohydrodynamic instability of miscible core-annular flows with electric conductivity stratification

6.1 Mathematical Formulation

In Chapter 5, the instability of an annular liquid layer with a conductivity gradient has been discussed. The conductivity gradient is developed due to the applied radial electric field [101]. In many microfluidic systems, rapid mixing in a circular pipe is of particular interest. To enhance the mixing, this Chapter proposes to impose an axial electric field as shown in figure 6.1. The two liquids are miscible dilute aqueous electrolytes. The liquids are Newtonian and the density ρ , kinematic viscosity ν , and dynamic viscosity $\mu = \rho\nu$ of the two liquids are assumed to be the same [100]. There is a sharp change in the ionic concentration where the two liquids meet at $r = a$. Therefore, a sharp change in the electric conductivity occurs at $r = a$. The purpose of this chapter is to investigate how the electric field enhances the mixing in such an electric conductivity stratification system. The two liquids are pumped into the pipe by a constant axial pressure gradient.

The three-dimensional hydrodynamical problem is considered and the cylindrical coordinates (r, θ, z) are chosen. Gravity is neglected. Motion of the liquids is governed by the continuity

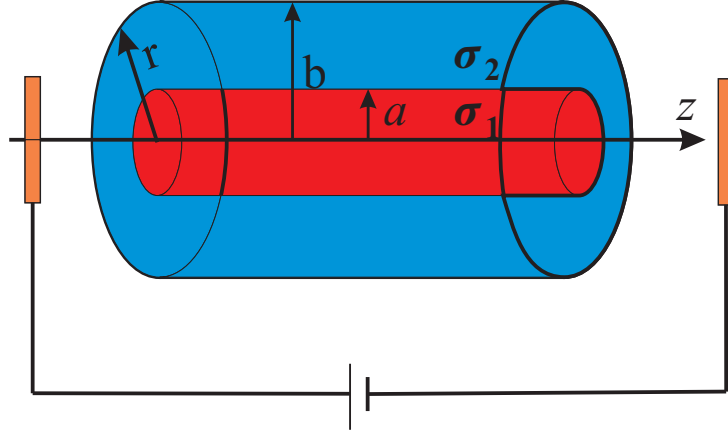


Figure 6.1: Geometry of the system.

equation and the momentum equation,

$$\nabla \cdot \mathbf{v} = 0, \quad (6.1)$$

$$\rho \frac{D\mathbf{v}}{Dt} = -\nabla p + \mu \nabla^2 \mathbf{v} + \mathbf{f}, \quad (6.2)$$

where $\mathbf{v} = u\mathbf{e}_r + v\mathbf{e}_\theta + w\mathbf{e}_z$ is the velocity. $\frac{D}{Dt} = \frac{\partial}{\partial t} + u\frac{\partial}{\partial r} + \frac{v}{r}\frac{\partial}{\partial \theta} + w\frac{\partial}{\partial z}$ is the material derivative operator. \mathbf{f} is the electric force which can be related to the Maxwell stress tensor \mathbb{T}^M by,

$$\mathbf{f} = \nabla \cdot \mathbb{T}^M. \quad (6.3)$$

Usually, analysis of Eq.(6.2) is difficult because the electric field is coupled to the free charge density ρ_e according to Maxwell's equations. Moreover, the free charge density is coupled to the flow field. As aforementioned in Chapter 5, in this Chapter, it is also assumed that the electric current density \mathbf{J}_e as well as the induced current density $\frac{\partial \varepsilon \mathbf{E}}{\partial t}$ are modest, such that the induced magnetic field is negligible and the electrostatic problem can be considered,

$$\nabla \times \mathbf{E} = 0. \quad (6.4)$$

The Maxwell stress $\mathbb{T}^M = \epsilon \mathbf{E} \mathbf{E} - \frac{1}{2} \epsilon \|\mathbf{E}\|^2 \mathbb{I}$. The parameter ϵ is the dielectric permittivity and \mathbf{E} is the electric field. Here, $\|\mathbf{E}\|^2 = \mathbf{E} \cdot \mathbf{E}$ and \mathbb{I} is the identity tensor. The charge density is given by the Gauss's law,

$$\rho_e = \nabla \cdot (\epsilon \mathbf{E}). \quad (6.5)$$

Hence, the momentum equation (6.2), now is written as,

$$\rho \frac{D\mathbf{v}}{Dt} = -\nabla p + \mu \nabla^2 \mathbf{v} + \rho_e \mathbf{E} - \frac{1}{2} \|\mathbf{E}\|^2 \nabla \epsilon. \quad (6.6)$$

In isothermal and the dilute electrolyte solution conditions, the electric permittivity ϵ is approximately that of the solvent [100]. In some non-isothermal conditions, this term $\frac{1}{2} \|\mathbf{E}\|^2 \nabla \epsilon$ is very crucial since there is a gradient of permittivity due to the non-isothermal condition which causes a circulation flow in the system [122]. In this chapter, an isothermal condition and constant electric permittivity are assumed for the dilute electrolyte solutions. Therefore, the term $\frac{1}{2} \|\mathbf{E}\|^2 \nabla \epsilon$ is ignored. In previous studies in Refs.[109, 105], this term $\frac{1}{2} \|\mathbf{E}\|^2 \nabla \epsilon$ was also neglected under the assumptions of dilute electrolyte solution and an isothermal environment.

Because the electrostatics is considered, the electric field \mathbf{E} can be related to the electric potential by

$$\mathbf{E} = -\nabla \phi. \quad (6.7)$$

Hence, the Gauss's law (6.5) is expressed by the following Poisson's equation:

$$\nabla^2 \phi = -\frac{\rho_e}{\epsilon}. \quad (6.8)$$

Conservation of electric charge gives,

$$\frac{\partial \rho_e}{\partial t} + \nabla \cdot \mathbf{J}_e = 0. \quad (6.9)$$

In this Chapter, the electrolyte solution considered is assumed as an Ohmic conductor which neglects the diffusion of the charge. Then the current density \mathbf{J}_e is given by,

$$\mathbf{J}_e = \sigma \mathbf{E} + \rho_e \mathbf{v}, \quad (6.10)$$

where σ is the electric conductivity. Substituting Eq.(6.10) into the current conservative law, we obtain,

$$\frac{D\rho_e}{Dt} + \nabla \cdot (\sigma \mathbf{E}) = 0. \quad (6.11)$$

Because the electrolyte solution is considered to be an ionic conductor, the conductivity depends on the local ion concentration. Accordingly, the conductivity can be described by the following diffusion equation [101, 104, 105],

$$\frac{D\sigma}{Dt} = K_{eff} \nabla^2 \sigma, \quad (6.12)$$

where K_{eff} is an effective diffusivity due to the Brownian motion of the ions. Eq.(6.12) is valid if the local electric time is much faster than the fluid time and the time for ion electromigration,

$$\frac{\epsilon}{\sigma} \ll \frac{b^2}{\nu} \ll \frac{b}{\varpi E} \quad \text{and} \quad \frac{b^2}{\varpi k_B T}, \quad (6.13)$$

in which, $k_B T$ is the Boltzmann temperature, ϖ is a characteristic mobility of the charge-carrying solutes. The conditions imply that the ions are carried by fluid parcel. Typical values of these parameters can be found in Melcher's book [104] and Lin et al.'s work [100]: $\epsilon \approx 10^{-10} \text{C/V}$, $\varpi \approx 10^{-8} \text{m}^2/\text{V} \cdot \text{s}$, kinematic viscosity $\nu \approx 10^{-6} \text{m}^2/\text{s}$, conductivity $\sigma \approx 10^{-4} \text{S/m}$ and strength of a typical electric field $E = O(10^3) \text{V/m}$ and the pipe's radius $b = 10^{-3} \text{m}$. A similar form as Eq.(6.12) was also derived by [100] from the species conservation law if the electromigration was neglected. It was indicated in Chapter 5 that $K_{eff} \nabla^2 \sigma$ was responsible for the existence of a threshold electric field and cannot be neglected.

At the initial time, the electric conductivity in each layer is $\sigma = \sigma_1|_{r < a}, \sigma_2|_{a < r < b}$ ($\sigma_1 \neq \sigma_2$). The subscript $i = 1, 2$ denotes the inner layer and outer layer, respectively. This can be achieved by using two aqueous electrolytes with different ionic concentrations [100, 110].

In this chapter, the non-slip and non-penetration boundary conditions at $r = b$ are applied:

$$u = v = w = 0. \quad (6.14)$$

Here, the basic flow is driven by pressure, and the maximum speed occurring at the center line is around $10^{-4} - 10^{-2} m/s$. Usually, the electroosmosis flow is very weak and the flow velocity can be estimated by Helmholtz-Smoluchowski formula $U_E = -\varepsilon E \zeta / \mu$ where ζ is the zeta potential which is responsible for the electroosmosis flow. This velocity usually has an order of $O(10^{-6}) m/s$ provided $\zeta = -10^{-2} V$, $\varepsilon = 10^{-10} C/V \cdot m$ and $\mu = 10^{-3} kg/m \cdot s$, $E = 10^3 V/m$. Clearly, the electro-osmotic velocity is much weaker than the pressure driven flow. Hence, in what follows, the non-slip and non-penetration boundary conditions in (6.14) are applied that the electro-osmosis phenomenon is neglected. If the electric field is developed due to the electroosmosis and the pressure gradient is removed after the two liquids are pumped into the pipe, the assumption in Eq.(6.14) is not applicable.

There is no flux of the ions at $r = b$, therefore,

$$\frac{\partial \sigma}{\partial r} = 0. \quad (6.15)$$

The circular pipe is non-conducting,

$$\frac{\partial \phi}{\partial r} = 0. \quad (6.16)$$

6.2 Base state and scalings

At the base state, the flow field and the electric field are decoupled because the electrolyte solution is initially neutral, i.e. the net charge density is zero. The flow is driven by a constant pressure gradient $\partial_z \bar{p}$. Therefore, the base velocity profile is

$$\bar{w} = \frac{\partial_z \bar{p}}{4\mu}(r^2 - b^2). \quad (6.17)$$

This Chapter adopts the assumption that the interface between the two liquids has grown diffusively to a finite thickness δ . Moreover, we assume that the diffusion is sufficiently slow to allow us to employ a quasi-steady base state for the linear stability analysis. Provided $\delta \ll 1$, the profile of the conductivity can be approximated by the error function:

$$\bar{\sigma} = \frac{\sigma_1 + \sigma_2}{2} + \frac{\sigma_2 - \sigma_1}{2} \text{erf}\left(\frac{r - a}{\delta}\right). \quad (6.18)$$

Equation (6.18) was used by Selvam et al. [97] in their study to describe the profile of viscosity of a viscosity stratified flow in a circular pipe.

The base electric conductivity profile can also be obtained via solving [100]:

$$\frac{\partial \sigma}{\partial t} = K_{eff} \left(\frac{\partial^2 \sigma}{\partial r^2} + \frac{1}{r} \frac{\partial \sigma}{\partial r} \right). \quad (6.19)$$

In experiments, K_{eff} ranges from $10^{-9} - 10^{-12} m^2/s$.

The charge density ρ_e is zero, and the electric field exists only in the axial direction. This gives the base state of the electric potential:

$$\bar{\phi} = \phi_0 - Ez, \quad (6.20)$$

where E is the imposed electric field's strength, ϕ_0 is the reference electric potential.

Taking the velocity scale $W = -\frac{\partial_z \bar{p} b^2}{4\mu}$, the length scale b , the time scale b/W , the pressure scale ρW^2 , the electric potential scale Eb , the conductivity scale $\sigma_2 - \sigma_1$, we non-dimensionalize the system (6.1)-(6.16):

$$\nabla \cdot \mathbf{v} = 0, \quad (6.21)$$

$$\frac{D\mathbf{v}}{Dt} = -\nabla p + \frac{1}{Re} \nabla^2 \mathbf{v} + \frac{Q}{Re^2 Sc} \nabla^2 \phi \nabla \phi, \quad (6.22)$$

$$\frac{1}{R_t} \frac{D(\nabla^2 \phi)}{Dt} + \nabla \cdot \{[(\eta - 1)\sigma + 1] \nabla \phi\} = 0, \quad (6.23)$$

$$\frac{D\sigma}{Dt} = \frac{1}{Re Sc} \nabla^2 \sigma, \quad (6.24)$$

where $Re = \frac{\rho W b}{\mu}$ is the Reynolds number; $Q = \frac{\varepsilon E^2 b^2}{\mu K_{eff}}$ is the scaled electric energy and is defined as the electric number; $\eta = \frac{\sigma_2}{\sigma_1}$ denotes the conductivity ratio; and $Sc = \frac{\nu}{K_{eff}}$ is the electric Schmidt number. Baygents and Baldessari[101] proposed that $Sc \in [10^3, 10^6]$. In the study by Chang et al.[105], Sc was assumed to vary in $[10^2, 10^5]$. The parameter $R_t = \frac{d/W}{\epsilon/\sigma_1}$ measures the ratio of fluid time to electric time. It is assumed that R_t is very large that the electric time is quite smaller than the fluid time in this thesis. Therefore, Eq.(6.23) can be simplified to:

$$[(\eta - 1)\sigma + 1] \nabla^2 \phi + (\eta - 1) \nabla \sigma \cdot \nabla \phi = 0. \quad (6.25)$$

Dimensionless boundary condition at $r = 1$ are

$$u = v = w = \frac{\partial \sigma}{\partial r} = \frac{\partial \phi}{\partial r} = 0. \quad (6.26)$$

The dimensionless base state is defined as follows:

$$\bar{w} = 1 - r^2, \quad (6.27)$$

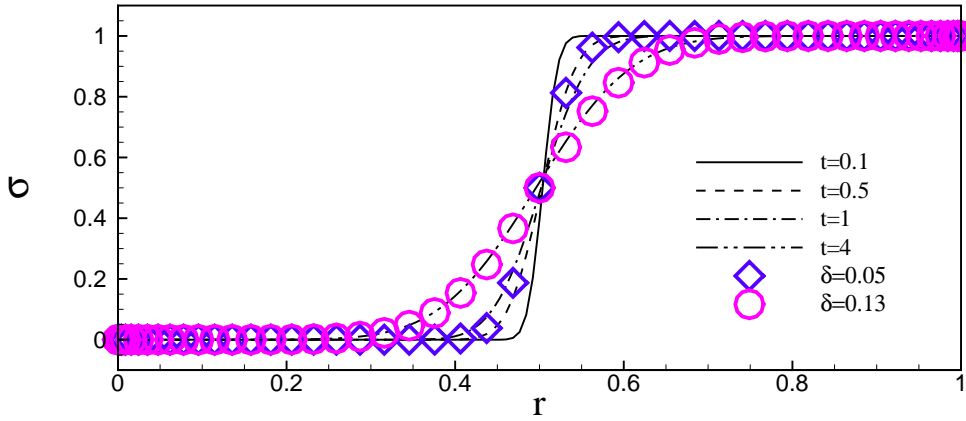


Figure 6.2: The base electric conductivity profile. The lines are obtained by numerical experiments of the dimensionless form of equation (6.19) and the circles and diamonds are obtained from the error function Eq.(6.28). The depending parameters are $a = 0.5$, $ReSc = 1000$.

$$\bar{\sigma} = \frac{1}{2} + \frac{1}{2} \operatorname{erf}\left(\frac{r-a}{\delta}\right), \quad (6.28)$$

$$\bar{\phi} = -z, \quad (6.29)$$

in which a is scaled on the length scale b which falls in the range of $(0, 1)$. Note that $\nabla^2 \bar{\phi} = 0$ and $\frac{\partial \bar{\sigma}}{\partial r} = \frac{1}{\delta \sqrt{\pi}} \exp\left(-\frac{(r-a)^2}{\delta^2}\right)$. In this Chapter, the range of δ is fixed, $\delta \in [0.05, 0.15]$. To verify Eq.(6.28), we assume that the the concentration has a Heaviside profile initially, and the conductivity profile at instant time t is solved numerically by the dimensionless form of Eq.(6.19) and a regular condition is imposed at the centerline $\frac{d\sigma}{dr} = 0$.

The base conductivity profile is shown in Figure 6.2. It is obvious that the electric conductivity profile can be approximated by the error function in Eq.(6.28) via adjusting the value of δ at an instant t . In the following study, Eq.(6.28) will be used as the profile of the electric conductivity at the base state for the convenience in the study of linear stability.

6.3 Linear stability analysis

The linear stability analysis of the flow system is implemented by perturbing the base state with infinitesimal disturbances:

$$[u, v, w, p, \sigma, \phi] = [0, 0, \bar{w}, \bar{p}, \bar{\sigma}, \bar{\phi}] + [u', v', w', p', \sigma', \phi'], \quad (6.30)$$

where the primed variables are the infinitesimal disturbances. In a standard way, the normal mode analysis is considered:

$$[u', v', w', p', \sigma', \phi'] = [\hat{u}, \hat{v}, \hat{w}, \hat{p}, \hat{\sigma}, \hat{\phi}] \exp(i(n\theta + kz) + \omega t), \quad (6.31)$$

in which $[\hat{u}, \hat{v}, \hat{w}, \hat{p}, \hat{\sigma}, \hat{\phi}]$ is the Fourier amplitude, n is the azimuthal wave number, k is the streamwise wave number, ω is the complex temporal growth rate.

Substituting Eq.(6.30) with the normal mode analysis into Eqs. (6.21), (6.22), (6.24), (6.25) and after linearizing, the governing equations of the eigenvalue problem obtained are

$$D\hat{u} + \frac{\hat{u} + in\hat{v}}{r} + ik\hat{w} = 0, \quad (6.32)$$

$$\omega\hat{u} = -D\hat{p} - ik\bar{w}\hat{u} + \frac{1}{Re}(\mathcal{L}\hat{u} - \frac{\hat{u} + 2in\hat{v}}{r^2}) \quad (6.33)$$

$$\omega\hat{v} = -\frac{in\hat{p}}{r} - ik\bar{w}\hat{v} + \frac{1}{Re}(\mathcal{L}\hat{v} - \frac{\hat{v} - 2in\hat{u}}{r^2}) \quad (6.34)$$

$$\omega\hat{w} = -ik\hat{p} - i\alpha\bar{w}\hat{w} - D\bar{w}\hat{u} + \frac{1}{Re}\mathcal{L}\hat{w} - \frac{Q}{PeRe}\mathcal{L}\hat{\phi}, \quad (6.35)$$

$$Pe\omega\hat{\sigma} = -PeD\bar{\sigma}\hat{u} - iPe k\bar{w}\hat{\sigma} + \mathcal{L}\hat{\sigma}, \quad (6.36)$$

$$[(\eta - 1)\bar{\sigma} + 1]\mathcal{L}\hat{\phi} + (\eta - 1)D\bar{\sigma}D\hat{\phi} - ik(\eta - 1)\hat{\sigma} = 0, \quad (6.37)$$

where $\mathcal{L} = D^2 + \frac{1}{r}D - \frac{n^2}{r^2} - k^2$, $D = \frac{d}{dr}$. The Péclet number $Pe = ReSc$. Note that, the value of

Pe cannot be small because diffusion of conductivity is slow.

Boundary conditions at $r = 1$ are

$$\hat{u} = \hat{v} = \hat{w} = D\hat{\sigma} = D\hat{\phi} = 0. \quad (6.38)$$

At the centerline $r = 0$, the singular nature of the cylindrical coordinate system requires special treatment. To deal with the singular point of the system (6.32)-(6.37), we use the fact that velocity vector as well as the other scalar variables have a vanishing azimuthal dependence as they approach the centerline, i.e.

$$\lim_{r=0} \frac{\partial \mathbf{v}'}{\partial \theta} = \lim_{r=0} \frac{\partial p'}{\partial \theta} = \lim_{r=0} \frac{\partial \sigma'}{\partial \theta} = \lim_{r=0} \frac{\partial \phi'}{\partial \theta} = 0, \quad (6.39)$$

where $\mathbf{v}' = u' \mathbf{e}_r + v' \mathbf{e}_\theta + w' \mathbf{e}_z$ is the velocity disturbance.

In the form of Fourier modes, the regular boundary conditions are

$$in\hat{u} - \hat{v} = \hat{u} + in\hat{v} = n\hat{w} = n\hat{p} = n\hat{\sigma} = n\hat{\phi} = 0. \quad (6.40)$$

If $n = 0$, the boundary conditions are

$$\hat{u} = \hat{v} = D\hat{w} = D\hat{p} = D\hat{\sigma} = D\hat{\phi} = 0. \quad (6.41)$$

If $n = 1$, the boundary conditions are

$$D\hat{u} = D\hat{v} = \hat{w} = \hat{p} = \hat{\sigma} = \hat{\phi} = 0. \quad (6.42)$$

The velocity conditions of $n = 1$ agree with the boundary conditions given by Khorrami [129] for a single fluid flow in a circular pipe.

When $n \geq 2$, the boundary conditions are

$$\hat{u} = \hat{v} = \hat{w} = \hat{p} = \hat{\sigma} = \hat{\phi} = 0. \quad (6.43)$$

A Chebyshev collocation method is implemented to solve the eigenvalue problem, and the physical domain is transformed into the Chebyshev domain,

$$\zeta = 2r - 1. \quad (6.44)$$

The variables $\hat{u}, \hat{v}, \hat{w}, \hat{p}, \hat{\sigma}, \hat{\phi}$ are expanded as

$$\begin{aligned} \hat{u} &= \sum_0^N a_m T_m(\zeta), & \hat{v} &= \sum_0^N b_m T_m(\zeta), & \hat{w} &= \sum_0^N c_m T_m(\zeta), \\ \hat{p} &= \sum_0^N d_m T_m(\zeta), & \hat{\sigma} &= \sum_0^N f_m T_m(\zeta), & \hat{\phi} &= \sum_0^N e_m T_m(\zeta), \end{aligned} \quad (6.45)$$

where $T_m(\zeta)$ denotes the m th Chebyshev polynomial.

In order to modify the computation near the interface $r = a$, the Chebyshev collocation points are clustered in the mixing region at $r = a$ using the following stretching function [130]:

$$\xi = \frac{a}{\sinh(f_b r_0)} [\sinh[(r - r_0)] + \sinh(f_b a)], \quad (6.46)$$

where $r_0 = \frac{1}{2f_b} \ln \left[\frac{1 + (\exp(f_b - 1)a)}{1 + (\exp(-f_b) - 1)a} \right]$. The coefficient f_b determines the degree of clustering and $f_b = 6$. The parameter a represents the location of interface around which clustering is desired.

After clustering the Chebyshev collocation points into the diffusion region, it needs to calculate the eigenvalue problem via the clustered grid. Therefore, a transformation on the deriva-

tives between the clustered grid and the Chebyshev grid should be made,

$$\frac{df}{d\xi} = \frac{df}{dr} \frac{dr}{d\xi} = \frac{1}{G'(r)} \frac{df}{dr}, \quad (6.47)$$

where $G(r) = \xi$ and f stands for the variables \hat{u} , \hat{v} , \hat{w} , \hat{p} , $\hat{\sigma}$ or $\hat{\phi}$. Note that the derivative $\frac{df}{dr} = 2 \frac{df}{d\xi}$.

For the second derivative of f , using the chain-rule, the transformation writes

$$\frac{d^2 f}{d\xi^2} = \frac{1}{(G')^2} \frac{d^2 f}{dr^2} - \frac{G''}{(G')^3} \frac{df}{dr}. \quad (6.48)$$

The derivative $\frac{d^2 f}{dr^2} = 4 \frac{d^2 f}{d\xi^2}$. Numerical validation of our method will be made in the following discussion.

6.4 Energy analysis

In order to understand the physical mechanism, the energy analysis is applied [131]. Multiplying the conjugates of the variables \hat{u}^* , \hat{v}^* , \hat{w}^* on the both sides of Eqs.(6.33)-(6.35) and summing these equations after integrating over the cross-sectional area, gives the energy balance equation:

$$\dot{E}_k = I + V + E_e. \quad (6.49)$$

Here, the kinetic energy growth rate is:

$$\dot{E}_k = \omega_r \int_0^1 r(|\hat{u}|^2 + |\hat{v}|^2 + |\hat{w}|^2) dr, \quad (6.50)$$

the work done by the Reynolds stress:

$$I = - \int_0^1 r \text{Re}(\mathbf{D}\bar{\mathbf{w}}\hat{\mathbf{w}}^*\hat{\mathbf{u}})dr, \quad (6.51)$$

and the viscous dissipation:

$$V = -\frac{1}{Re} \int_0^1 r \{ (|\mathbf{D}\hat{\mathbf{u}}|^2 + |\mathbf{D}\hat{\mathbf{v}}|^2 + |\mathbf{D}\hat{\mathbf{w}}|^2) + (\frac{n^2}{r^2} + k^2)(|\hat{\mathbf{u}}|^2 + |\hat{\mathbf{v}}|^2 + |\hat{\mathbf{w}}|^2) + \frac{|\hat{\mathbf{u}}|^2 + |\hat{\mathbf{v}}|^2}{r^2} - 4n \frac{\text{Im}(\hat{\mathbf{u}}^*\hat{\mathbf{v}})}{r^2} \} dr. \quad (6.52)$$

The work done by the electric force:

$$E_e = \frac{Q}{PeRe} \int_0^1 r \text{Re}(\mathbf{D}\hat{\mathbf{w}}^*\mathbf{D}\hat{\phi} + \frac{n^2\hat{\mathbf{w}}^*\phi}{r^2} + k^2\hat{\mathbf{w}}^*\phi)dr. \quad (6.53)$$

Since the magnitude of the eigenfunction is arbitrary, we normalize the eigenfunction by its maximum absolute value. The terms in the energy analysis are re-scaled with respect to the total kinetic energy $\int_0^1 r(|\hat{\mathbf{u}}|^2 + |\hat{\mathbf{v}}|^2 + |\hat{\mathbf{w}}|^2)dr$. For an unstable flow, \dot{E} should be positive. The energy analysis will be applied to interpret the instability mechanism in the following discussions.

6.5 Results and discussion

6.5.1 Validation of numerical methods

First, the validation of “our numerical method” is examined via setting $Q = Pe = 0$, therefore, the electric field is turned off and the ionic advection is absent. Since the parameter $Q = 0$ and Eq.(6.37) does not produce any eigenvalues, the conductivity profile has no in-

	$c(n = 0, k = 1)$	$c(n = 1, k = 0.5)$	$\omega'(n = 1, k = 0)$
SH	$0.93675536 - 0.06374551i$	$0.84646970 - 0.07176332i$	-0.00734099
Present work	$0.93675536 - 0.06374551i$	$0.846469697 - 0.07176332i$	-0.007340985

Table 6.1: The first leading eigenvalues of the system for $Re = 2000$, $Pe = Q = 0$. We have utilized 51 points for the eigenvalue problem and related the eigenvalue to that of **SH** by $\omega' = i\omega$ and $c = \omega'/k$.

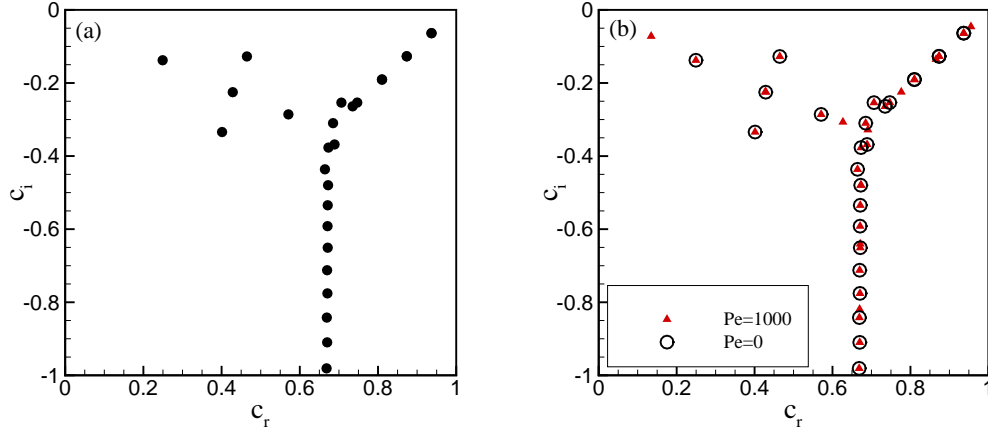


Figure 6.3: Eigenspectra for $Re = 2000$, $n = 0$, $k = 1$. (a) The eigenspectrum for the Hagen-Poiseuille flow which is identical to that by **SH**. (b) The comparison of the conductivity stratified pipe flow (triangle points) and the Hagen-Poiseuille flow (circles). The conductivity ratio $\eta = 2$ and the parameters $Q = 0$, $a = 0.5$, $\delta = 0.05$. It is obvious that when $Pe > 0$, there are some extra eigenvalues as compared to the Hagen-Poiseuille flow. The parameter $c = i\omega/k$.

fluence on the spectrum of the problem and the eigenvalue problem should be identical to a single fluid flowing in a circular pipe. The numerical results are compared with Schmid and Henningson[3] (herein referred as **SH**) for $Re = 2000$. The leading eigenvalue is listed in Table 6.1. Excellent agreement between our numerical results and that of **SH** demonstrates the validity of “our numerical method”.

When $Re \rightarrow 0$, i.e. the inertia of the fluid is negligible, the growth rate is determined by the ionic diffusion equation (6.36). In a viscosity stratified plane-Poiseuille flow[132], the eigenspectrum of the diffusion equation presents a similar structure ‘Y-shape’ as the Orr-

Sommerfeld problem. Hence, the diffusion equation will produce more eigenvalues in the stratified flow than a single fluid flow [132]. Similarly, in the pipe flow with conductivity stratification, the eigenspectrum structure is different from the result of **SH** as demonstrated in figure 6.3. In the following discussion, the base flow in the pipe is considered to be weak and discussion will be concentrated on the instability caused by the electric force in microfluidic channels.

6.5.2 Parametric study

Effect of the conductivity ratio

The influence of the conductivity ratio on the linear stability analysis is of particular interest and will be investigated in this section. Before presenting the numerical study, let us consider the case of two liquids with the same electric conductivity, i.e. $\eta = 1$. The linearized electric current conservation equation (6.37) reduces to,

$$\mathcal{L}\hat{\phi} = 0. \quad (6.54)$$

Hence, in the linearized momentum equation (6.35), the electric force that can trigger the instability is absent. Therefore, the system will be linearly stable. Numerical study also indicates that the eigenvalue ω is not influenced by the electric number Q for $\eta = 1$ and $\omega_r < 0$. A useful conclusion can be inferred here: the system becomes more stable as η increases when $\eta < 1$, while the system becomes more unstable as η increases when $\eta > 1$. To study the influence of the conductivity ratio on the linear stability, the other parameters are fixed: $Re = 1$, $Sc = 1000$, $a = 0.5$ and $\delta = 0.1$. To study the linear stability, 51 collocation points are sufficient to provide satisfying accuracy.

Firstly, consider two typical cases: $\eta = 0.5$, $\eta = 2$. The electric number Q is fixed so as

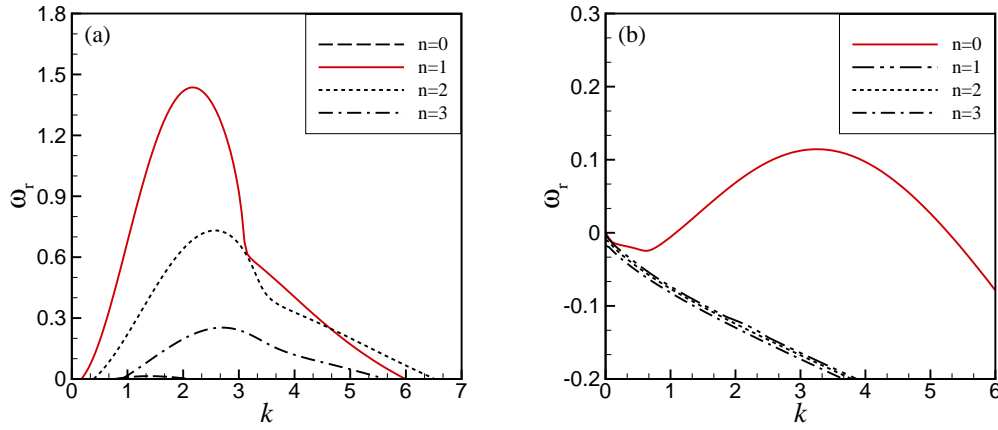


Figure 6.4: The real temporal growth rate ω_r versus the wave number k . (a) $Q = 5 \times 10^4$, $\eta = 0.5$. (b) $Q = 10^4$, $\eta = 2$.

to study the growth rate of the disturbance. Results in Figure 6.4(a) demonstrate that the azimuthal disturbances make the system more unstable. It also implies that the azimuthal wave number n of the critical mode is $n = 1$. Results are different in Figure 6.4(b). It shows that the azimuthal wave number of the most unstable mode is $n = 0$ for $\eta = 2$. These results imply that, the critical unstable mode of the system varies with the conductivity ratio η . To elucidate the critical unstable mode in the system, the marginal curves in the $Q - k$ plane are investigated. Figure 6.5 demonstrates that the wave number n of the critical unstable mode for $\eta = 0.5, 2$ is $n = 1, 0$ respectively. The azimuthal wave number of the critical unstable mode is defined as the critical azimuthal wave number n_c . Here, Q_c is the critical electric number, and k_c is the critical streamwise wave number. The imaginary part of eigenvalue ω for the critical unstable modes in Figure 6.5 is nonzero. It indicates that the critical unstable modes are oscillatory. The perturbed fields of the charge density and the conductivity in the $r - \theta$ plane are shown in Figure 6.6 to illustrate the two different unstable modes. In Figure 6.6(a,b), the unstable mode is defined as the corkscrew mode; while the unstable mode in Figure 6.6(c,d) is defined as the axisymmetric mode. Numerical evaluation of the energy contribution of E_e demonstrates that it is always positive. It demonstrates that the electric force is the main factor

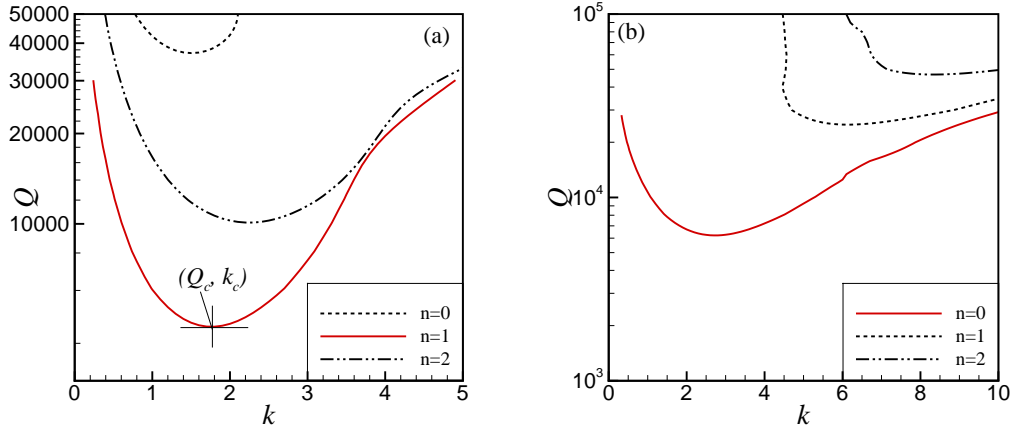


Figure 6.5: The marginal stability curves. (a) $\eta = 0.5$. (b) $\eta = 2$.

that destabilizes the system. The instability is referred to as the dielectrophoretic instability [101, 105] as have been discussed in Chapter 5.

In order to reveal the influence of the conductivity ratio on the critical unstable mode, i.e. in which range of η , the critical unstable mode is the corkscrew mode or the axisymmetric mode, the behavior of (Q_c, n_c, c) versus the value of η is investigated. The wave speed c of the critical mode is defined as

$$c = -\omega_i/\alpha_c. \quad (6.55)$$

Results in Figure 6.7(a) indicate that the system becomes more unstable for a larger contrast in the electric conductivity between the two layers. Similar phenomenon has been observed by Lin et al. [100] of a liquid layer with conductivity stratification in a square channel. Experimental observation and stability analysis suggested that the flow became more unstable for a larger conductivity contrast [100]. However, they focused on the two-dimensional instability and how the conductivity ratio influenced the three-dimensional stability was not investigated [100]. Here, investigation of the three-dimensional instability in Figure 6.7(c) shows that the critical wavenumber n_c jumps from 1 to 0 as the conductivity ratio increases to $\eta = 1$. It indicates that, for the selected input values of other dimensionless parameters, the critical

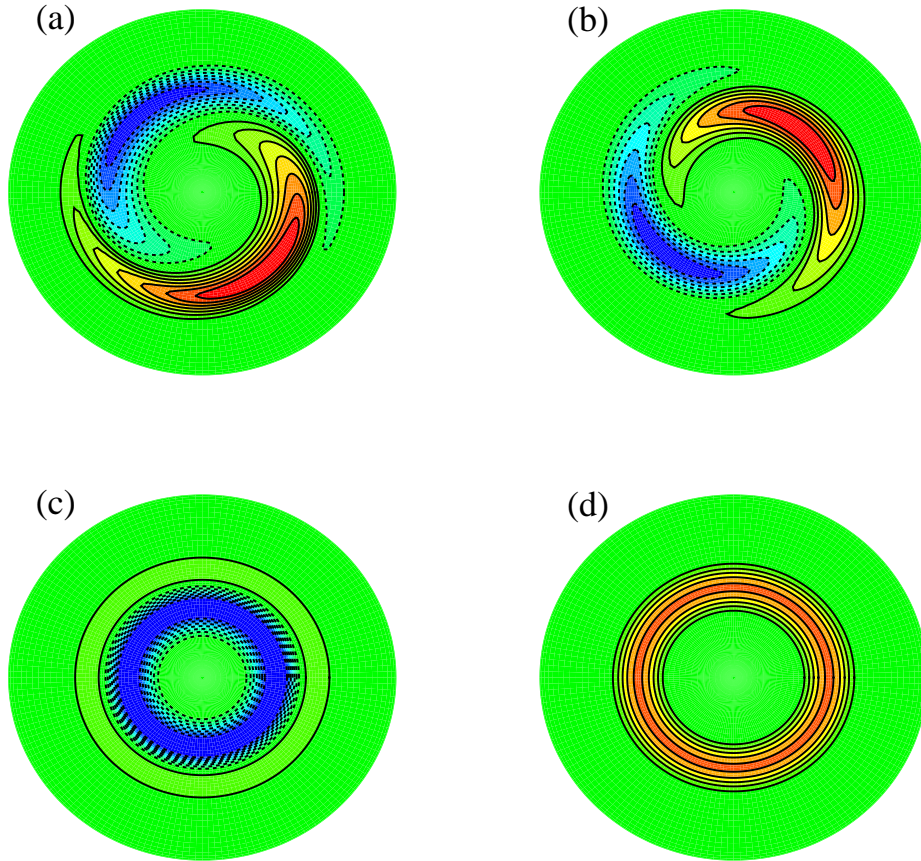


Figure 6.6: (a,b) The perturbed field of the electric charge ρ_e and the perturbed field of the conductivity σ for $\eta = 0.5$, $Q_c = 4505.8$, $n_c = 1$, $k_c = 1.75$ in the $r - \theta$ plane. (c,d) The perturbed field of the electric charge ρ_e and the perturbed field of the conductivity σ for $\eta = 2$, $Q_c = 6197.0$, $n_c = 0$, $k_c = 2.75$ in the $r - \theta$ plane.

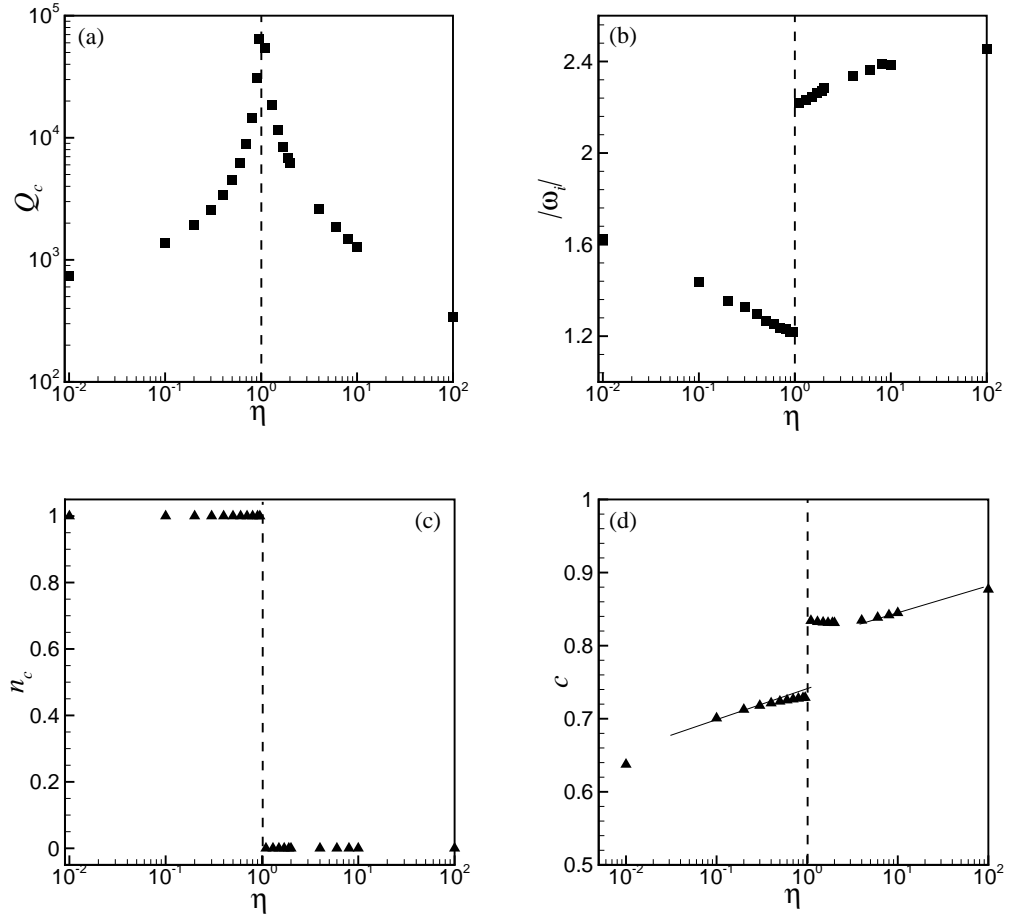


Figure 6.7: (a) The critical electric strength number Q_c vs. η . (b) The critical frequency $|\lambda_i|$ vs. η . (c) The critical wavenumber n_c vs. η . (d) The wave speed of the critical mode c vs. η .

unstable mode is dominated by the corkscrew mode when the inner conductivity is larger; while the axisymmetric mode dominates the instability when the outer conductivity is larger. Moreover, in a square-duct flow system, Lin et al. gave the physical properties of the flow system for a conductivity ratio $\eta = 10$ which are applied to estimate the critical strength of the applied electric field in the current system here [100]. The present results show that, for $\eta = 10$, the critical value electric number $Q_c \approx 10^3$. It gives the critical electric strength $E \approx 2 \times 10^3 \text{ V/m}$ provided that the electric permittivity $\epsilon = 6.9 \times 10^{-10} \text{ C/V} \cdot \text{m}$, the dynamic viscosity $\mu = 10^{-3} \text{ kg/m} \cdot \text{s}$, the effective diffusivity $K_{eff} = 2 \times 10^{-9} \text{ m}^2/\text{s}$ and the pipe radius $b = 10^{-3} \text{ m}$. Hence, it is possible to achieve the electromixing in a circular pipe at small Reynolds flow by an electric field in experiments. Figure 6.7(b) shows that $\omega_i \neq 0$ which demonstrates that the unstable mode is oscillatory. Figure 6.7(d) shows that the critical wave speed c increases with increasing η . Figure 6.7(d) also shows that, when $\eta < 1$, the wave speed is smaller for a larger conductivity contrast; when $\eta > 1$, the wave speed is larger for a larger conductivity contrast. Additionally, the wave speed $c > 0$ indicates that the linear wave propagates to the downstream.

Effect of interface location

This section discusses the influence of the interface location on the linear stability of the system. The other parameters are fixed at $Re = 1$, $Sc = 1000$, $\delta = 0.05$ so as to investigate the dielectrophoretic instability. $\delta = 0.05$ is chosen under the consideration of a sharper interface. Two conductivity ratios $\eta = 0.5, 2$ will be considered in the following discussion. The convergence of “our numerical method” has been examined that $N = 60$ is enough to provide adequate resolution at reasonable computational cost.

Selvam et al. found that the interface location had a significant influence on the critical instability of a viscosity stratified pipe flow and the least unstable mode occurred at approximately 0.6 times the pipe radius [97]. In the present problem of a liquid with conductivity stratifi-

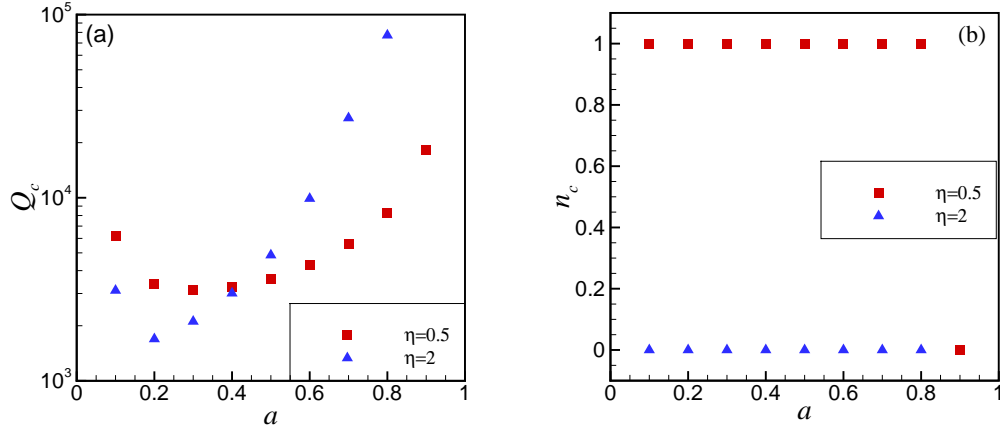


Figure 6.8: (a) The critical electric strength number Q_c vs. a . (b) The critical wavenumber n_c vs. a .

cation, similar phenomenon is observed. However, the instability of the present problem is triggered by the electric field; while in the problem by Selvam et al. [97], the instability is due to the Reynolds stress. If the interfacial location is very near the centerline or the pipe wall, the diffusion of ions will remove soon the conductivity difference. Furthermore, consider a very sharp interface, when $a \rightarrow 0$ or $a \rightarrow 1$, no matter how large the electric field is imposed, the system should be stable due to the homogenous conductivity profile. Hence, it can be concluded that, as the interface is slightly moved away from the centerline, the system becomes more unstable. As the interface approaches the outer boundary, i.e. the pipe wall, the system should become more stable. Therefore, there should be an optimal location of the interface that the flow is least stable. Two typical cases of $\eta = 0.5, 2$ have been investigated numerically and the range of the interface location a is considered to be in $[0.1, 0.9]$. The variation of critical wavenumber n_c and the critical electric number Q_c with the location a is shown in Figure 6.8. Figure 6.8(a) demonstrates that, for $\eta = 0.5, 2$, the system becomes more unstable as a increases from 0.1 till $a \approx 0.3$, $a \approx 0.2$ respectively, while it becomes more stable as a increases further. Additionally, for $\eta = 0.5$, it is observed that the critical unstable mode shifts from the corkscrew mode $n_c = 1$ to the axisymmetric mode $n_c = 0$ as a

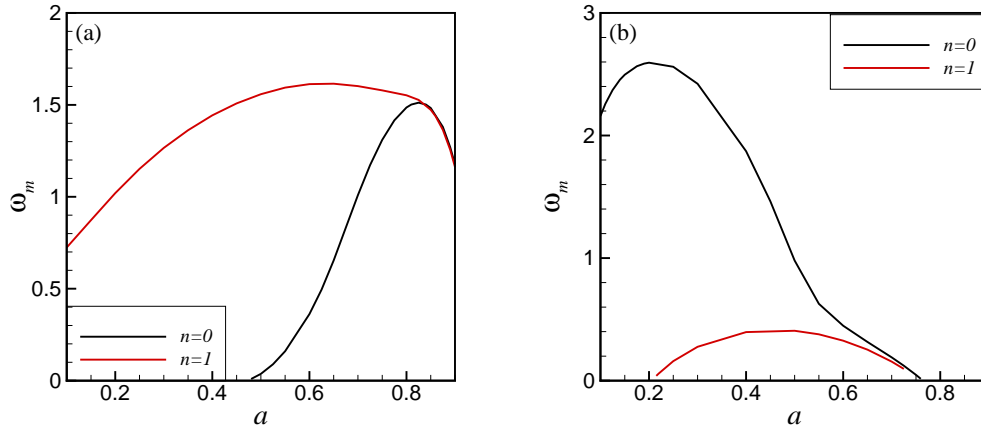


Figure 6.9: The maximum growth rate ω_m vs. a . (a) $Q = 5 \times 10^4$, $\eta = 0.5$. (b) $Q = 5 \times 10^4$, $\eta = 2$.

increases to a critical value $a \approx 0.83$. For $\eta = 2$, the axisymmetric mode always dominates the instability.

It is interesting to investigate the maximum growth rate of the system since the rapid mixing is of particular interests[100]. To investigate the maximum growth rate, the electric number was fixed. The behavior of the maximum growth rate $\omega_m = \max(\text{Re}(\omega))$ versus the interface location a was then scrutinized. The ω_m describes the growth rate of the most unstable mode. The corkscrew mode as well as the axisymmetric mode were investigated as shown in Figure 6.9. Figure 6.9(a) shows that the maximum growth rate occurs at $a \approx 0.6$. The maximum growth rate ω_m versus a were examined by reducing the value of Q and it was found that the peak point in the ω_m – a plane moved leftwards as shown in Figure 6.10(a). It implies that, for a strong electric field, the most unstable mode prefers an intermediate a for $\eta = 0.5$ although the critical unstable mode prefers $a \approx 0.3$. The mechanism is very complex because the electric force destabilizes the flow while the viscous dissipation as well as the ionic diffusion tend to stabilize the system. In order to explain the results, the energy analysis was applied. As the interface location a increases, the viscous dissipation effect becomes weaker till $a \approx 0.6$, after which it becomes stronger as a increases further as shown in Figure 6.10(b). This is the

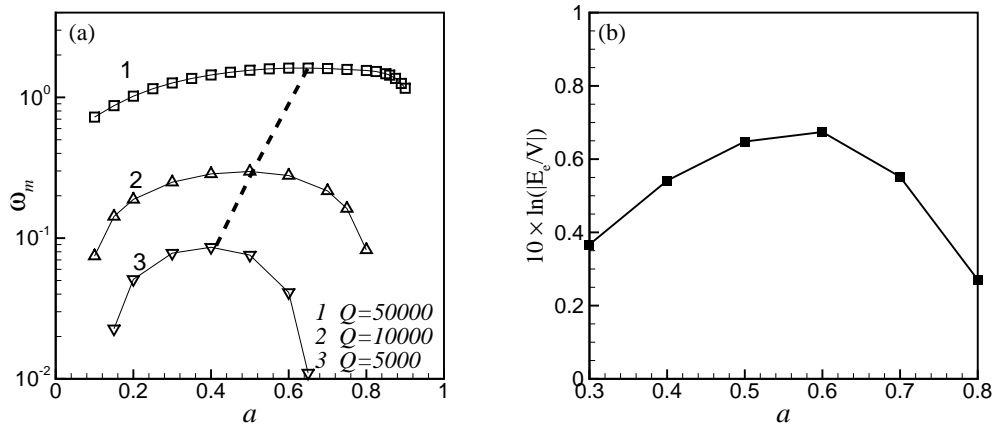


Figure 6.10: (a) The maximum growth rate ω_m of the corkscrew mode $n = 1$ vs. a for different values of input electric number Q . (b) The log ratio between the energy E_e and V , in which, the electric number $Q = 5 \times 10^4$ and the wavenumber k corresponds to the most unstable mode.

reason why for an unstable flow, $Q = 5 \times 10^4$, the maximum growth rate occurs at $a \approx 0.6$. In addition, it is observed that, for $\eta = 0.5$, the maximum growth rate of the axisymmetric mode dominates the corkscrew mode when $a \gtrsim 0.83$ for $Q = 5 \times 10^4$. It indicates that the axisymmetric mode becomes critical when the interface approaches the pipe wall. Figure 6.9(b) demonstrates that the maximum growth rate occurs at $a \approx 0.2$ which indicates that the most unstable mode and the critical unstable mode prefer $a \approx 0.2$. Additionally, for $\eta = 2$, the axisymmetric mode always dominates the corkscrew mode.

Effect of interface thickness

This section investigates of the influence of the interface thickness on the critical instability. The other parameters are fixed: $Re = 1$, $Sc = 1000$, $a = 0.5$. In the above discussions, two values of δ have been selected for discussion. It has been observed that, the system becomes more stable for a larger value of δ . The marginal stable curves for three typical values of δ are shown in Figure 6.11. For a liquid with viscosity stratification, Selvam et al. reported that, for a thicker interface, the flow becomes more stable [97]. They explained that the stabilizing

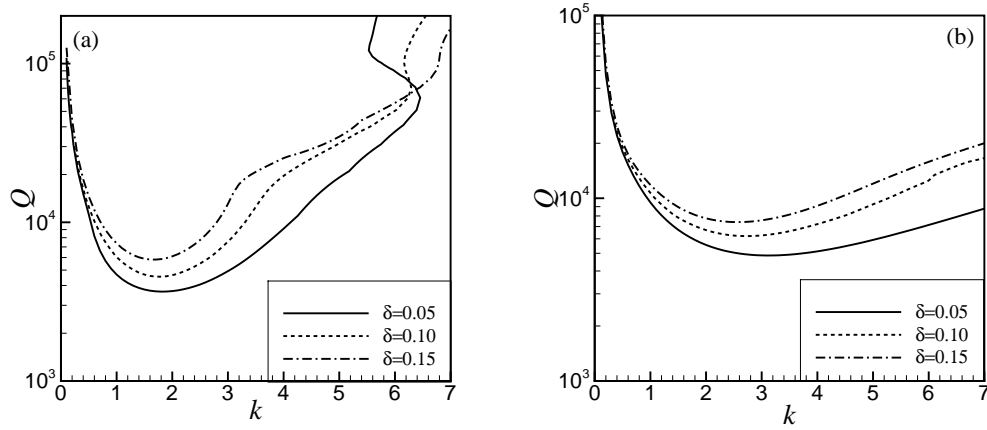


Figure 6.11: The marginal stability curves. (a) $\eta = 0.5$. (b) $\eta = 2$.

effect is due to the diffusion effect and becomes more significant for a thicker interface which dissipates the kinetic energy and inhibits the instability [97]. The study by Chang et al. [105] and discussion in Chapter 5 showed that, the system becomes more stable with reducing the conductivity gradient when the conductivity gradient is small, while the flow becomes more stable as the conductivity gradient increases when the conductivity gradient is large. In the present study, if the conductivity ratio is fixed, the conductivity gradient within the interface becomes smaller as the interface becomes thicker. Current study shows that, the flow becomes more stable as the conductivity gradient decreases which is different from the previous study [105] and Section 5.4 of this thesis. In fact, in the current study, a thicker interface implies that the system undergoes a longer diffusion time. Assuming that the conductivity is uniform in the system due to diffusion for quite a long time, a completely stable flow would be expected. Therefore, the system may become more stable as the interface becomes thicker. Numerical studies demonstrate that, with increasing the interface thickness δ , the marginal curve rises up in the $Q - k$ plane which indicates that the flow becomes more stable as the interface becomes thicker which supports the above analysis. The result is similar to the phenomenon in a viscosity stratified flow [97], but different from the studies by Chang et al. [105]. The difference is due to the flows studied by Chang et al. [105] and that in Chapter 5 are bounded

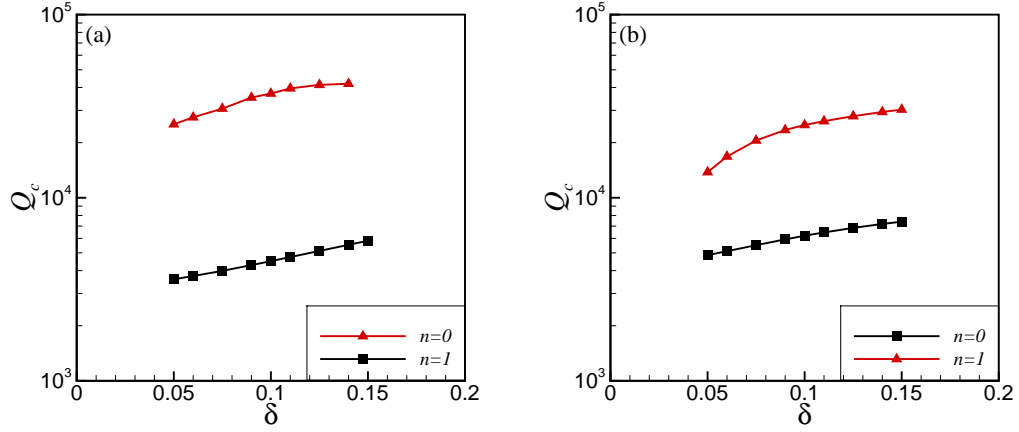


Figure 6.12: The critical electric strength number Q_c vs. δ . (a) $\eta = 0.5$, (b) $\eta = 2$.

by two solid walls. However, in this problem, the flow is only bounded by the outer pipe wall. It was observed that, for the axisymmetric mode, $\eta = 2$, the critical wavenumber k_c becomes smaller as δ increases as seen in Figure 6.11(b). It indicates that, the wavelength of the disturbance becomes longer as δ increases. In order to show the effect of δ on the critical stability, the critical electric number Q_c was plotted against δ in Figure 6.12. Figure 6.12 also demonstrates that the system becomes more stable as δ increases. Additionally, the corkscrew mode dominates the instability for $\eta = 0.5$, and the axisymmetric mode dominates the instability for $\eta = 2$.

Effect of shear flow

This section aims to reveal the influence of the shear flow on the dielectrophoretic instability. The other parameters are fixed at $a = 0.5$, $\delta = 0.1$. Prior to present the numerical study, the electric force term in the linearized axial momentum equation (6.35) is re-considered:

$$-\frac{Q}{RePe}\mathcal{L}\hat{\phi} = \frac{Q}{Re^2Sc}\hat{\rho}_e. \quad (6.56)$$

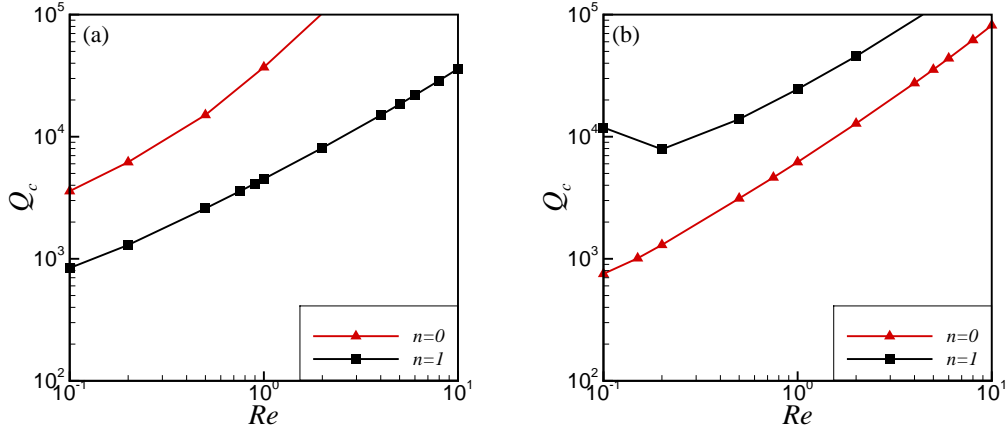


Figure 6.13: The critical electric strength number Q_c vs. Re . (a) $\eta = 0.5$, (b) $\eta = 2$.

The value of Sc is fixed at $Sc = 1000$. Equating $\frac{Q}{Re^2 Sc}$ at two different values of Re , gives:

$$Q_2 = \frac{Re_2^2}{Re_1^2} Q_1. \quad (6.57)$$

This relation reflects the fact that, when the value of $\frac{Q}{Re^2 Sc}$ is fixed, a smaller Re describes a smaller Q . It implies that, when the Reynolds number is small, the system may be more unstable. This Chapter considers a weak shear flow under the consideration of flow in microfluidic channel and proposes that Re has a range of $[0.1, 10]$ provided that the pipe radius is $10^{-3}m$ and kinematic viscosity $\nu = 10^{-6}m^2/s$. The maximum velocity occurring at the center line $r = 0$ can be varied from $10^{-4}m/s$ to $10^{-2}m/s$.

For $\eta = 0.5$, the corkscrew mode dominates the instability; and for $\eta = 2$, the axisymmetric mode dominates the instability. Figure 6.13 illustrates that the critical electric number Q_c increases as Re increases, indicating that the shear flow impedes the electro-convection in the system. Interestingly, the corkscrew mode for $\eta = 2$ can be enhanced by the shear flow as seen in Figure 6.13(b) although it never becomes critical for the selected input values of Re , η and Sc . It is different from the previous study by Chang et al. [105] and section 5.4 of this thesis which show that, the critical instability can either be enhanced or impeded by

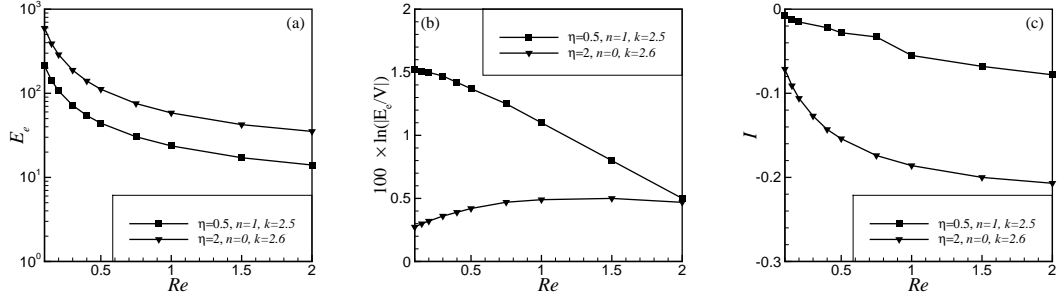


Figure 6.14: (a) Electric energy E_e vs. Re . (b) The log ratio between the electric energy and the viscous dissipation vs. Re . (c) The work of Reynolds stress vs. Re . The electric number $Q = 10^4$.

the shear flow. In the present study, the shear flow always impedes the critical instability. In order to understand the physical mechanism, the value of Q and the wavenumber k were fixed to investigate the energy contributions of the electric force, Reynolds stress and viscous stress. For some Re , the flow is stable, e.g. $Re > 2.5$ for $\eta = 0.5$ and $Re > 2$ for $\eta = 2$. The electric energy becomes smaller as demonstrated in Figure 6.14(a). \dot{E}_k becomes smaller as Re increases and is negative as Re exceeds some critical value which indicates the system becomes stable as Re increases. However, the underlying factor that stabilizes the system is not the reduction in the electric energy. Figure 6.14(b) shows that, as the Reynolds number increases, $\ln(|\frac{E_e}{V}|)$ decreases for $\eta = 0.5$; while $\ln(|\frac{E_e}{V}|)$ increases for $\eta = 2$. It indicates that, the stabilizing mechanisms of the two cases $\eta = 0.5, 2$ are different. The case of $Re = 10$ were examined and result showed that, for $\eta = 0.5$, $\ln(|\frac{E_e}{V}|) < 0$; for $\eta = 2$, $\ln(|\frac{E_e}{V}|) > 0$. It indicates that, for $\eta = 0.5$, the increase of the viscous dissipation is the major factor that stabilizes the flow although the Reynolds stress also plays a stabilizing role as shown in Figure 6.14(c). For $\eta = 2$, because the electric energy always dominates the viscous dissipation, i.e. $E_e > |V|$, the stabilizing factor in the system is due to the Reynolds stress which dissipates the kinetic energy of the perturbation. The results indicate that, the imposed shear flow can impede the dielectrophoretic instability via the dissipation mechanisms of the viscous stress and the Reynolds stress.

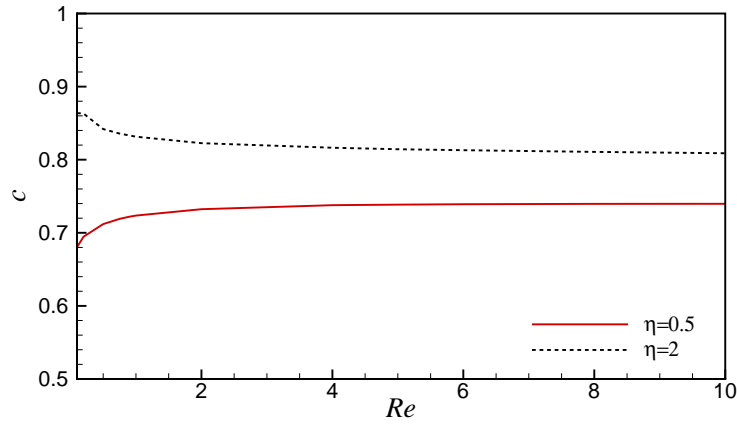


Figure 6.15: The wave speed of the critical unstable mode versus the Reynolds number.

Furthermore, the influence of Re on the wave speed c was investigated as shown in Figure 6.15. It was observed that, for $\eta = 0.5$, the critical wave speed c increases slightly as Re increases initially, then it has a negligible influence on the wave speed. However, the wave speed decreases slightly as Re increases from $Re = 1$ for $\eta = 2$, and then the wave speed seems to be independent on Re . The results by Chang et al. [105] indicated that, the critical frequency of the critical transverse unstable mode $-\omega_i$ was independent of the Reynolds number when $Re > 1$. This implies that the critical wave speed is independent of Re . In this system, it can be observed that the wave speed c is independent of Re for both the two critical unstable modes: corkscrew mode and axisymmetric mode when $Re > 2$.

Effect of ionic diffusion

This section presents a study of the ionic diffusion's influence on the dielectrophoretic instability. The other parameters are fixed: $Re = 1$, $a = 0.5$, $\delta = 0.1$. In the governing equations (6.32)-(6.37), replacing Re by Pe does not change the governing equations which indicates that the effect of ionic diffusion on the flow instability should be similar to that of Re . However, the results should not be the same as shown in the above section, in which, Re is varied

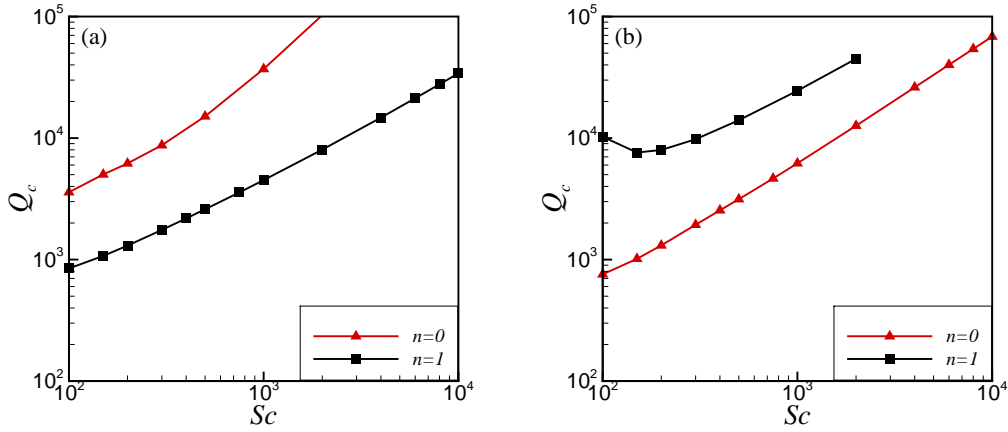


Figure 6.16: The critical electric strength number Q_c vs. Sc . (a) $\eta = 0.5$, (b) $\eta = 2$.

while Sc is fixed. Therefore, it is necessary to investigate the influence of Sc on the stability by fixing the value of Re .

The critical electric number Q_c versus the Schmidt number is shown in Figure 6.16. The corkscrew mode dominates the instability for $\eta = 0.5$ and the axisymmetric mode dominates the instability for $\eta = 2$ as shown in Figure 6.16. The system becomes more stable as Sc increases. Results in figure 6.16 are quite similar to those in Figure 6.13 which demonstrates that the influence of Sc on the flow stability is similar to that of Re .

The instability mechanism is then interpreted by the energy analysis. The critical instability of the system is considered here. The viscous dissipation term V is always negative and plays a stabilizing role. The electric force work $E_e > 0$ which triggers the electro-convection in the system. $\ln(|\frac{E_e}{V}|)$ was calculated and found to increase with Sc initially, then it decreased as Sc increased further as shown in Figure 6.17(a). It indicates that the viscous dissipation effect becomes weaker as Sc increases from $Sc = 100$ while it becomes stronger when Sc is very large. When Sc is not too large, $Sc = O(10^2)$, the Reynolds stress plays a key role in stabilizing the system since its dissipation effect becomes stronger as Sc increases as shown in Figure 6.17(b). As Sc increases further, for $\eta = 0.5$, the dissipation effect by Reynolds

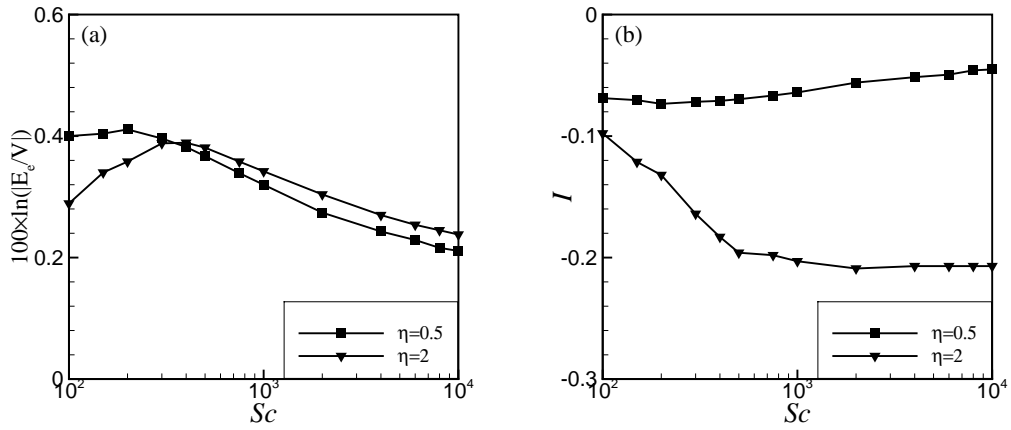


Figure 6.17: (a) The log ratio between the electric energy and the viscous dissipation vs. Sc . (b) The work of Reynolds stress vs. Sc .

stress becomes weaker; while for $\eta = 2$, the Reynolds stress's work reaches a plateau as seen in Figure 6.17(b). Such a phenomenon indicates that, although the Reynolds stress dissipates the kinetic energy, it is not the major factor that causes the system to be more stable when Sc is increased. As shown in Figure 6.17(a), $\ln(|\frac{E_e}{V}|)$ starts to decrease when Sc exceeds a certain value. It indicates that the viscous dissipation increases with Sc and becomes the major stabilizing factor. Moreover, recall the definition of $Sc = \frac{\nu}{K_{eff}}$. It indicates that the viscous effect becomes stronger as the parameter Sc increases. Since viscous dissipation plays a stabilizing role, the system becomes more stable as Sc increases. The effect of Sc on the critical stability in this system is different from the previous study by Chang et al. [105] and what has been discussed in section 5.4 of this thesis. In these studies ([105] and Chapter 5), Sc was found to have a dual effect: with increasing Sc can either enhance or inhibit the critical instability. Present study shows that, for $\eta = 2$, the corkscrew mode can either be enhanced or impeded as Sc increases as seen in Figure 6.16(b). However, the critical unstable mode always becomes stable. For an unstable flow, we observed that, Sc can play a dual role in the system that the growth rate of disturbances can become either larger or smaller as Sc increases which is not shown here since we are only interested in the critical stability of this

system.

CHAPTER 7

Conclusions and future work

7.1 Conclusions

7.1.1 Interfacial instability

Chapter 3 and Chapter 4 discussed the interfacial instability of core-annular flows in a radial electric field. The interface is unstable even without the external electric field which is due to the renowned Plateau-Rayleigh mechanism.

In Chapter 3, an asymptotic model was proposed to study the linear and nonlinear dynamics of a thin liquid film flowing down a vertical fiber whereas the dynamics of its surrounding gas was neglected. The liquid film was assumed to be perfectly conducting. Linear stability analysis of the asymptotic model indicated that, when the ratio between radius of the outer electrode and the initial radius of the liquid film $\beta < e$, the linear instability was enhanced by the electric field; when $\beta = e$, the electric field had a negligible influence on the linear instability; when $\beta > e$, the electric field impeded the linear instability. Nonlinear simulation of the asymptotic model was also studied. When $\beta < e$, the electric field promoted the wave height, which can cause the film to be singular. When $\beta = e$, the nonlinear simulation showed that the electric field enhanced the deformation of the interface. When $\beta \geq e$, the study showed that the permanent wave may be time-dependent or time-independent, depending on the strength of the electric field. For instance, when $\beta = e^{1.1}$, the electric field can lead to the droplet coalescence and cause the liquid film to be singular. In the study of the case $\beta = e^{3/2}$, the singular

phenomenon was not observed for all electrical Weber number, and the maximum height of the wave decreased as the electrical Weber number increased. Investigation on steady traveling waves was further conducted to discuss the influence of electric field on the wave speed. It was found that the wave speed and the wave amplitude can be promoted or decreased by the electric field. Particularly in some situations, the wave speed may increase/decrease while its amplitude decreased/increased as the strength of the external electric field increased.

In Chapter 4, the dynamics of the outer layer was taken into account and the base flow arose due to a constant axial pressure gradient. The two liquids were considered to be leaky dielectrics. Results of the linear stability analysis showed that, depending on the ratios of electrical properties (the electrical permittivity ratio and electrical conductivity ratio between the outer layer and inner layer), the electric field can either stabilize or destabilize the system. Both theoretical analysis and numerical studies were carried out. It was found that an external electric field can completely impede the capillary instability. Linear stability analysis showed that the system can be stabilized by increasing the inner radius of the duct or the thickness of the outer layer. It was found that viscosity had dual effects on the stability of the system. Viscosity stratification may cause instability in the system, while viscous dissipation effect had a stabilizing effect. The Reynolds number on the stability was investigated and it was found that the capillary instability could be suppressed by the interfacial shear. Also, the electric field can either stabilize or destabilize the interface wave instability due to viscosity stratification, which was dependent of the electrical properties. Furthermore, a range of electrical properties was identified that the electric field can suppress the capillary instability as well as the interface wave instability. Further investigations of the input parameters on the effective growth rate and the wave number of the most unstable perturbation were conducted. It was found that the effective growth rate and wave number depended on the strength of the electric field and the electrical permittivities and conductivities. The viscosity ratio's effect on the growth rate and wave number of the most unstable disturbance was investigated. It was

found that, for some selected input parameters, the instability of the system was dominated by the outer layer when the viscosity ratio was small; for large viscosity ratio, instability was dominated by the inner layer.

7.1.2 Electrohydrodynamic mixing

Chapter 5 and Chapter 6 discussed electro-mixing in micro-channels in which the dielectrophoretic instability was investigated in the framework of electrostatics. The three dimensional hydrodynamical problem has been considered for the both problems.

In Chapter 5, an annular liquid layer with radial electrical conductivity gradient in a radial electric field was investigated. A constant pressure gradient was imposed along the axial direction causing a weak shear flow. The critical unstable mode was found to be either oscillatory or stationary depending on the following dimensionless parameters: the dimensionless inner radius a , the electrical conductivity gradient, the Reynolds number Re and the electrical Schmidt number Sc_e .

To illustrate the influence of the radius a on the instability, the other dimensionless parameters were fixed: $\eta = 10$, $Re = 1$ and $Sc_e = 10^3$. It was found that, when the dimensionless radius $a < 0.4$, the major cause of instability was the spanwise disturbance and the critical unstable mode was stationary. When $a > 0.4$, the critical unstable mode was given by three-dimensional oblique waves. Furthermore, it was observed that the system became more unstable as the radius a increased.

The influence of the conductivity gradient on the instability was examined. The other dimensionless parameters were fixed at $a = 1$, $Re = 1$ and $Sc_e = 10^3$. When the conductivity gradient was small, the critical unstable mode was found to be three-dimensional oblique waves. As the conductivity gradient increased, the system became more unstable because the dielectrophoretic effect was enhanced. However, when the conductivity gradient was in-

creased further, the stability of the system was enhanced due to the enhancement of the ionic diffusion effect. Apart from that, the stationary mode became critical when $\eta \geq 20$.

In order to understand the influence of the imposed shear flow, the Reynolds number was varied while the other parameters were fixed: $a = 1$, $\eta = 10$, $Sc_e = 10^3$. It was found that, when $Re < 0.3$, increasing Re would cause the system to be more unstable. The most unstable mode was the three dimensional oblique wave. When $Re > 1$, the critical electric field seemed to be independent of Re because the spanwise disturbances dominated the instability.

The effect of electrical Schmidt number Sc_e on flow instability was investigated by fixing the other parameters at $a = 1$, $\eta = 10$, $Re = 1$. It was found that, the three dimensional system may either be more unstable or more stable as Sc_e increased. When $Sc_e > 10^3$, it was found that the critical electric field seemed not to be influenced by Sc_e .

Chapter 6 investigated the electrohydrodynamic instability of two miscible flows in a micro-pipe with electrical conductivity stratification. An axial electric field was imposed, which can instigate the electro-convection in the system. A weak shear flow arose from an axial pressure gradient. The influences of conductivity ratio, interface location, interface thickness, shear flow and ionic diffusion on the critical stability of the flow were discussed in detail. An energy analysis was carried out to interpret the instability mechanism.

It was found that, the system was more unstable for a larger electrical conductivity contrast. When the electrical conductivity was larger within the inner layer, the critical unstable mode may either be the corkscrew mode or the axisymmetric mode, depending on the interface location. A detailed study showed that the critical unstable mode shifted from the corkscrew mode to the axisymmetric mode as the interface approached the pipe wall. When the electrical conductivity was larger in the outer layer, the critical unstable mode was dominated by the axisymmetric mode. The interface location had a significant influence on the critical unstable mode. The system was more stable when the interface was close to the centerline or the

pipe wall. The flow became more stable as the interface became thicker. The shear flow and ionic diffusion were found to have a stabilizing effect via the dissipation mechanisms of the Reynolds stress and viscous stress.

7.2 Perspectives of future research

7.2.1 Thin film dynamics

In Chapter 3, the dynamics of a thin liquid film in a radial electric field has been investigated by an asymptotic model which is valid for small Reynolds number flow. Indeed, when the thin film is thick, the Reynolds number can be moderate and this asymptotic model cannot be used. To deal with this problem, the author will apply the weighted-residual method and derive a two-equation model to relieve this difficulty. Moreover, the streamwise diffusion may be included as indicated by Ruyer-Quil et al.[28]. Additionally, the asymptotic reduction of the Laplace equation of the electrical potential is not appropriate when the gap between the liquid film and outer electrode is large. Hence, the full Laplace equation should be retained. Furthermore, how the electric field influences the absolute/convective instability is still in question: such as a thin film flowing down an inclined plate or on a vertical cylinder.

Another interesting problem is to investigate the dynamics of liquid films coating on porous cylinders or fibers. For many biological materials, e.g. hair, vessel, textile threads (cotton threads), in microscope, they are not solid and many of them are penetrable. Preliminary studies of such flow systems have been carried by the author and his coworkers. It should be pointed out here: (i) our study applied the Darcy equation to describe the motion of liquids in the porous cylinder and a Beavers-Joseph condition was adapted to the cylindrical system; (ii) the problem has been reduced to a thin film flowing down a vertical fiber with a slippery surface and flow within the porous cylinder was neglected. However, recent experimental

studies by us in the Fluid Mechanics Lab in Nanyang Technological University showed that, the droplet on a porous fiber (a cotton textile thread) is much slender, i.e. smaller height and slower than that flowing down a solid fiber. Such an observation strongly demonstrates that the mathematical formulation in our previous studies[25, 126] is not applicable for the current model in experiments. We will perform further investigation into this problem so as to unveil the underlying mechanism behind such a phenomenon from both theoretical modeling and more accurate experimental design.

There are still many open problems in the research field of thin film dynamics, such as thin film flows at moderate Reynolds numbers on patterned topological surfaces, weak turbulence coupled with multi-fields, e.g thermal field, electro- or magneto- fields, chemical reactions and biological flow systems. More importantly, the application of the weighted-residual model is very limited to a few systems: such as thin film flows with Marangoni effects. One of the author's future research is to extend the methodology of weighted-residual model to these open problems in liquid film flows.

7.2.2 Electro-Hydrodynamic instability to Chaotic flows

In this thesis, most efforts have been spent on the linear dynamics of flow systems in an external electric field. Linear stability analysis has been a versatile method to study the incipient stage of system perturbed by disturbances. However, for liquid mixing in channels, it is of interest to see the mixing efficiency or formation of organized patterns after a long time, and the nonlinear full system should be investigated.

It should be acknowledged that direct numerical simulation of turbulence of multi-phase flow is a daunting task. Usually, the prevailing methods, such as finite volume method, level-set method, phase-field method etc., are used to simulate two-layer flow with an interface. Again, simulation of turbulent flows in the two-layer flow system at high-Reynolds number starting

from the Navier-Stokes equations is formidable. A possible way to bypass these difficulties is to utilize the large eddy simulation by modeling the small scale motions in conjunction with level set method or phase-field method. One of my future research is to carry out large eddy simulation in these systems. For the two problems in chapter 5 and chapter 6, direct numerical simulation of three-dimensional fully developed turbulent flows will be carried out in future. When the flow becomes unstable, we would expect to see: periodic flows \Rightarrow quasi-periodic flows \Rightarrow chaotic flows \Rightarrow fully developed turbulence as the strength of electric field increases. Since the flow is very much like the canonical Rayleigh-Bénard convection, it is of great interest to perform a comparison between the two systems, specifically at very large Rayleigh number. To perform the direct numerical simulation, the Chebyshev-Fourier spectral method would be utilized. The numerical code has been developed and tested for two-dimensional/three-dimensional Rayleigh-Bénard convection. To illustrate the numerical simulation method, computation of the two-dimensional Rayleigh-Bénard convection has been documented in the Appendix C.

7.2.3 Non-Newtonian flows

In this thesis, all the liquids considered have been assumed to be Newtonian. In many practical cases, the liquids are non-Newtonian, such as shear-thinning fluids, or viscoelastic fluids. In these fluids, the non-Newtonian effect would be significantly important. For non-Newtonian fluids, there have been some preliminary studies on the linear stability of canonical flows: such as plane Couette flow, Poiseuille flow, Hagen-Poiseuille flow and Taylor-Couette flow in which the normal mode analysis as well as the non-modal theory have been implemented[134, 135]. Nevertheless, it should be indicated that these studies did not provide sufficient numerical simulations to give direct evidences that the transition ‘does’ occur in plane-Couette flow and Hagen-Poiseuille flow which are linearly stable. It should be emphasized here that the non-modal theory predicts that the energy of perturbation can be

significantly amplified but will eventually decay! Hence, direct numerical simulation should be carried out to demonstrate that the transition can be triggered by optimal disturbances and can be sustained by the nonlinear mechanism. However, due to the complicated governing equations of non-Newtonian flows, there is now a lack of study of direct numerical simulations of non-Newtonian flows in these systems. To perform the numerical simulation, it would be convenient to construct a solenoidal basis from the Petrov-Galerkin method which provides high numerical accuracy[136]. In a different way, I have developed a solenoidal basis from the eigenmodes of the linearized Navier-Stokes equations and derive an ordinary differential-integral system.

Beyond direct numerical simulation, in multi-field systems, such as electrohydrodynamic systems, the study of linear stability of non-Newtonian flows in an electric field is very limited. In particular, the control of instability in a micro channel with complex geometries is of great interest and the global stability analysis should be carried out. For such complex problems, the finite element method or spectral element method will be used. Finite element method is very easy to be implemented in open source software *Freefem++* and I have been working on the software for nearly a half year.

APPENDIX A

Chebyshev collocation method

In this thesis, the eigenvalue problem is resolved by the Chebyshev collocation method. For a function f in a domain $y \in [-1, 1]$, it can be approximated by the Chebyshev polynomials:

$$f = \sum_0^N a_m T_m(y), \quad (\text{A.1})$$

where T_m is the Chebyshev polynomial

$$T_m(y) = \cos(m \cos^{-1}(y)). \quad (\text{A.2})$$

The first order derivative of f , now can be expressed as

$$\frac{df}{dy} = \sum_0^N a_m \frac{dT_m}{dy}, \quad (\text{A.3})$$

where $\frac{dT_m}{dy} = m \frac{\sin(m \cos^{-1}(y))}{\sin(\cos^{-1}(y))}$.

The N-dimensional subspace expanded by the Chebyshev functions, i.e $\{T_0, T_1, \dots, T_N\}$, is complete, therefore, the derivative of f can also be approximated by

$$\frac{df}{dy} = \sum_0^N b_m T_m. \quad (\text{A.4})$$

Obviously, there is

$$\sum_0^N b_m T_m = \sum_0^N a_m \frac{dT_m}{dy}. \quad (\text{A.5})$$

Now, collocation of f at $y = y_j$ gives

$$\sum_0^N b_m T_m(y_j) = \sum_0^N a_m \frac{dT_m}{dy} \Big|_{y=y_j}. \quad (\text{A.6})$$

Discretization of the problem on these collocation points gives

$$\mathbf{F} = \mathcal{T} \mathbf{a}, \quad (\text{A.7})$$

where $\mathbf{a} = [a_0, a_1, \dots, a_N]^T$, $\mathbf{F} = [f(y_0), f(y_1), \dots, f(y_N)]^T$ and \mathcal{T} is a matrix $\mathcal{T}_{ij} = T_i(y_j)$.

Now, we can obtain:

$$\mathbf{b} = (\mathcal{T}')^{-1} \mathcal{T} \mathbf{a}. \quad (\text{A.8})$$

Now, the function f is unknown, thereby the coefficients a_m serve as the unknowns in the discretized problem. Furthermore, setting $\mathbf{D} = (\mathcal{T}')^{-1} \mathcal{T}$ which is the discrete differentiation matrix. Hence, for the first order derivative of f and in discrete form, there is $\mathbf{F}' = \mathcal{T} \mathbf{D} \mathbf{a}$. Moreover, for the n -th derivative of f and in the discrete form, there is $\mathbf{F}^{(n)} = \mathcal{T} \mathbf{D}^n \mathbf{a}$. In the eigenvalue problem, $\omega \mathcal{A} \mathbf{x} = \mathcal{B} \mathbf{x}$, the unknown coefficients serve as the eigenvector \mathbf{x} .

In the computation of the eigenvalue problem, if we set $f(y_j)$, i.e the grid points, as the unknowns \mathbf{x} , it is necessary to construct the discrete differentiation matrix. Using the Lagrange interpolation, the function f can be expressed as:

$$f = \sum_0^N p_m(y) f(y_m), \quad (\text{A.9})$$

where $p_m(y)$ is the interpolation polynomials,

$$p_m = \prod_{j=0, j \neq m}^N \frac{y - y_j}{y_m - y_j}. \quad (\text{A.10})$$

Here, $y_j = \cos(\theta)$ and $\theta = \frac{j\pi}{N}$ is the Chebyshev collocation points.

For the first order derivative of f , now, can be expressed as

$$f' = \sum_0^N \frac{dp_m(y)}{dy} f(y_m). \quad (\text{A.11})$$

The discrete from of $\frac{dp_m}{dy}$ represents the discrete differentiation matrix D .

For instance, if there is only two points in the domain $[-1, 1]$, the discrete differentiation matrix D is

$$D = \begin{bmatrix} \frac{1}{2} & -\frac{1}{2} \\ \frac{1}{2} & -\frac{1}{2} \end{bmatrix}. \quad (\text{A.12})$$

If there is three points in the domain, i.e $y_j = 1, 0, -1$, the discrete differentiation matrix reads

$$D = \begin{bmatrix} \frac{3}{2} & -2 & \frac{1}{2} \\ \frac{1}{2} & 0 & -\frac{1}{2} \\ -\frac{1}{2} & 2 & -\frac{3}{2} \end{bmatrix}. \quad (\text{A.13})$$

Generally, when there is $N+1$ points in the domain $y \in [-1, 1]$, the components in the discrete differentiation matrix are

$$\begin{cases} D_{11} = \frac{2N^2 + 1}{6}, & D_{N+1, N+1} = -\frac{2N^2 + 1}{6}, \\ D_{jj} = -\frac{y_j}{2(1 - y_j^2)}, & j = 2, \dots, N, \\ D_{ij} = \frac{c_i (-1)^{i+j}}{c_j y_i - y_j}, & i \neq j, \quad i, j = 1, \dots, N+1, \end{cases} \quad (\text{A.14})$$

in which $c_j = 2$ if $i = 1, N+1$. Otherwise, $c_j = 1$.

APPENDIX B

Direct numerical simulation: thin films

We briefly present here the key points of the algorithm for the simulation of the spatio-temporal evolution of thin films based on the reduced models. Here, the Benny type equation is taken as an example:

$$h_t + h^2 h_x + \epsilon \left[\frac{h^3}{6} (-\cot \alpha h_x + \epsilon^2 We h_{xxx}) + \frac{2Re}{5} h^6 h_x \right]_x = 0. \quad (\text{B.1})$$

Making the transformation: $t \rightarrow \epsilon t$ and $x \rightarrow \epsilon x$, the Benney equation is restated as:

$$h_t + h^2 h_x + \left[\frac{h^3}{6} (-\cot \alpha h_x + We h_{xxx}) + \frac{2Re}{5} h^6 h_x \right]_x = 0. \quad (\text{B.2})$$

An initial condition of the problem is $h(x, 0) = h_0$.

B.1 Periodic domain

When the problem is solved with periodic boundary conditions:

$$h(0, t) = h(L, t), \quad h_x(0, t) = h_x(L, t), \quad h_{xx}(0, t) = h_{xx}(L, t), \quad h_{xxx}(0, t) = h_{xxx}(L, t), \quad (\text{B.3})$$

where L is the length of the computational domain, it is convenient to calculate the derivatives of h , h_x , h_{xx} , h_{xxx} in the Fourier domain. Now, we write:

$$h(x, t) = \sum_{-N/2}^{N/2} \exp(ij \frac{2\pi}{L} x) \hat{h}_j \quad (\text{B.4})$$

where $\hat{h}_{-j} = \hat{h}_j^*$ is the Fourier amplitude. Now, we would like to set the grid points at $x = x_j$, $h(x_j)$ as the unknowns and we are going to construct the discrete differentiation matrix. In discrete matrix form

$$\mathbf{h} = \mathbb{A} \hat{\mathbf{h}}, \quad (\text{B.5})$$

where $\mathbf{h} = [h(x_0), h(x_2), \dots, h(x_N)]^T$, $\hat{\mathbf{h}} = [\hat{h}_{-N/2}, \dots, \hat{h}_{N/2}]^T$ and $\mathbb{A}_{mn} = \exp(in \frac{2\pi}{L} x_m)$. The derivative of h can be expressed as $h' = \sum_{-N/2}^{N/2} ij \frac{2\pi}{L} \exp(ij \frac{2\pi}{L} x) \hat{h}_j$. Hence, in discrete form: $\mathbf{h}' = \mathbb{A} \mathbb{C} \hat{\mathbf{h}}$ where \mathbb{C} is a diagonal matrix and $\mathbb{C} = \text{diag}(i \frac{2\pi}{L} \mathbf{k})$ with $\mathbf{k} = [-N/2, -N/2 + 1, \dots, 0, \dots, N/2 - 1, N/2]^T$. Using the Fourier transform $\hat{h}_j = \sum_0^N \exp(-ij \frac{2\pi}{L} x_k) h(x_k)$, and finally, the derivative h' , in the discrete form, \mathbf{h}' is related to the grid function \mathbf{h} by

$$\mathbf{h}' = \mathbb{A} \mathbb{C} \mathbb{B} \mathbf{h}, \quad (\text{B.6})$$

where $\mathbb{B}_{mn} = \exp(-im \frac{2\pi}{L} x_n)$ and therefore the discrete differentiation matrix $\mathbb{D} = \mathbb{A} \mathbb{C} \mathbb{B}$.

Hence, the discretized Benney equation can be expressed as:

$$\mathbf{h}_t + \mathbb{D} \frac{\mathbf{h}^3}{3} + \mathbb{D} \left[\frac{\mathbf{h}^3}{6} (-\cot \alpha \mathbb{D} \mathbf{h} + W e \mathbb{D}^3 \mathbf{h} + \frac{2Re}{5} \mathbf{h}^6 \mathbb{D} \mathbf{h}) \right] = 0. \quad (\text{B.7})$$

Then, the time-evolution problem can be solved by an implicit Gear's method.

Indeed, the problem can be solved by the fast Fourier method. First, we compute the Fourier amplitudes by the Fourier transform. Second, the derivatives of h are calculated in the Fourier space. Third, the derivatives of h in the physical space are computed by the inverse Fourier

transform.

B.2 non-Periodic domain

When the non-periodic problem is considered, the Fourier method is not applicable. The Crank-Nicolson method is used here:

$$\frac{h^{n+1} - h^n}{\Delta t} + \frac{1}{2}\mathcal{N}(h^n) + \frac{1}{2}\mathcal{N}(h^{n+1}) = 0, \quad (\text{B.8})$$

where $\mathcal{N}(h) = h^2 h_x + \frac{h^3}{6}(-\cot \alpha h_{xx} + We h_{xxx}) + \frac{2Re}{5} h^6 h_{xx} + \frac{h^2 h_x}{2}(-\cot \alpha h_x + We h_{xx}) + \frac{12Re}{5} h^5 h_x^2$. Boundary conditions of the non-periodic problem, usually can be $h(0, t) = 1$, $h_x(0, t) = 0$ and the film is free at $x = L$: $h_x = h_{xxx} = 0$. However, previous studies on the boundary conditions are not inconsistency and some researchers proposed that the flow rate q is given at the inlet.

Here, we apply the finite difference method to approximate the derivatives:

$$\partial_x h_j = \frac{h_{j+1} - h_{j-1}}{2\Delta x} + O(\Delta x^2), \quad (\text{B.9})$$

$$\partial_{xx} h_j = \frac{h_{j+1} - 2h_j + h_{j-1}}{\Delta x^2} + O(\Delta x^2), \quad (\text{B.10})$$

$$\partial_{xxx} h_j = \frac{h_{j+2} - 2h_{j+1} + 2h_{j-1} - h_{j-2}}{2\Delta x^3} + O(\Delta x^2), \quad (\text{B.11})$$

$$\partial_{xxxx} h_j = \frac{h_{j+2} - 4h_{j+1} + 6h_j - 4h_{j-1} + h_{j-2}}{\Delta x^4} + O(\Delta x^2). \quad (\text{B.12})$$

For $j = 1, N + 1$ (left first node and right end node), the central difference schemes for the first order and second order derivatives are not applicable. For higher order terms h_{xxx} , h_{xxxx} , the central difference schemes are also not applicable at $j = 2, N$. Hence, we use a forward or

backward differential scheme of second order accuracy at these points:

$$\partial_x h|_{x=x_1} = \frac{-3h_1 + 4h_2 - 3h_3}{2\Delta x} + O(\Delta x^2), \quad (\text{B.13})$$

$$\partial_x h|_{x=x_{N+1}} = \frac{3h_{N+1} - 4h_N + h_{N-1}}{2\Delta x} + O(\Delta x^2), \quad (\text{B.14})$$

$$\partial_{xx} h|_{x=x_1} = \frac{2h_1 - 5h_2 + 4h_3 - h_4}{\Delta x^2} + O(\Delta x^2), \quad (\text{B.15})$$

$$\partial_{xx} h|_{x=x_{N+1}} = \frac{2h_{N+1} - 5h_N + 4h_{N-1} - h_{N-2}}{\Delta x^2} + O(\Delta x^2), \quad (\text{B.16})$$

$$\partial_{xxx} h|_{x=x_1} = \frac{-5h_1 + 18h_2 - 24h_3 + 14h_4 - 3h_5}{2\Delta x^3} + O(\Delta x^2), \quad (\text{B.17})$$

$$\partial_{xxx} h|_{x=x_2} = \frac{-5h_2 + 18h_3 - 24h_4 + 14h_5 - 3h_6}{2\Delta x^3} + O(\Delta x^2), \quad (\text{B.18})$$

$$\partial_{xxx} h|_{x=x_N} = \frac{5h_N - 18h_{N-1} + 24h_{N-2} - 14h_{N-3} + 3h_{N-4}}{2\Delta x^3} + O(\Delta x^2), \quad (\text{B.19})$$

$$\partial_{xxx} h|_{x=x_{N+1}} = \frac{5h_{N+1} - 18h_N + 24h_{N-1} - 14h_{N-2} + 3h_{N-3}}{2\Delta x^3} + O(\Delta x^2), \quad (\text{B.20})$$

$$\partial_{xxxx} h|_{x=x_1} = \frac{3h_1 - 14h_2 + 26h_3 - 24h_4 + 11h_5 - 2h_6}{\Delta x^4} + O(\Delta x^2), \quad (\text{B.21})$$

$$\partial_{xxxx} h|_{x=x_2} = \frac{3h_2 - 14h_3 + 26h_4 - 24h_5 + 11h_6 - 2h_7}{\Delta x^4} + O(\Delta x^2), \quad (\text{B.22})$$

$$\partial_{xxxx} h|_{x=x_N} = \frac{3h_N - 14h_{N-1} + 26h_{N-2} - 24h_{N-3} + 11h_{N-4} - 2h_{N-5}}{\Delta x^4} + O(\Delta x^2), \quad (\text{B.23})$$

$$\partial_{xxxx} h|_{x=x_{N+1}} = \frac{3h_{N+1} - 14h_N + 26h_{N-1} - 24h_{N-2} + 11h_{N-3} - 2h_{N-4}}{\Delta x^4} + O(\Delta x^2). \quad (\text{B.24})$$

The nonlinear equation (B.8) is then solved by the Newton iteration method.

APPENDIX C

Direct numerical simulation: two-dimensional Rayleigh-Bénard convection

Here, the direct numerical simulation of two-dimensional Rayleigh-Bénard convection is briefly presented. Below are the governing equations of the problem:

$$u_x + v_y = 0, \quad (\text{C.1})$$

$$\frac{1}{Pr}(u_t + uu_x + vv_y) = -p_x + u_{xx} + v_{yy}, \quad (\text{C.2})$$

$$\frac{1}{Pr}(v_t + uv_x + vv_y) = -p_y + v_{xx} + v_{yy} + Ra\theta, \quad (\text{C.3})$$

$$\theta_t + J = \theta_{xx} + \theta_{yy}, \quad (\text{C.4})$$

where Ra is the Rayleigh number and Pr is the Prandtl number. The convective term $J = u\theta_x + v\theta_y$. There is no slip at $y = 0, 1$ and the temperature is specified as

$$\theta(x, 0, t) = 1, \quad \theta(x, 1, t) = 0. \quad (\text{C.5})$$

Periodic boundary conditions are applied in x direction.

Below, we are going to formulate the problem from the pressure Poisson equation. Using the

continuity equation, we obtain the pressure Poisson equation,

$$p_{xx} + p_{yy} = Ra\theta_y - \frac{1}{Pr}(G_x + H_y), \quad (C.6)$$

where $G = uu_x + vu_y$ and $H = uv_x + vv_y$ and $N = G_x + H_y = u_x^2 + v_y^2 + 2u_yv_x$. For simulation of shear flows, special attention should be paid to the nonlinear terms when the Reynolds number is high. In such a case, it is suggested using the skew-symmetric form $\mathbf{u} \cdot \nabla \mathbf{u} = \frac{1}{2} \mathbf{u} \cdot \nabla \mathbf{u} + \frac{1}{2} \nabla \cdot (\mathbf{u} \mathbf{u})$ to address the numerical instability.

Since the pressure Poisson equation is second order, proper boundary conditions should be imposed. From the derivation of the Poisson equation, it implies:

$$\frac{1}{Pr} \frac{\partial f}{\partial t} = \nabla^2 f, \quad (C.7)$$

where $f = \nabla \cdot \mathbf{u}$. For the sake of mass conservation, it is to impose: $f \equiv 0$ for all the time. For, $f \equiv 0$, there should be

$$f(x, y, 0) = 0, \quad f|_{\partial V} = 0, \quad (C.8)$$

where ∂V is the boundaries of the computational domain. It implies that, an initially solenoidal velocity field should be provided and the continuity equation should be imposed at all the boundaries of the computational domain:

$$v_y = 0, \quad \text{at } y = 0, 1. \quad (C.9)$$

Furthermore, if p is a solution of the pressure Poisson equation then $p + c$ is also a solution where c is a constant number. Hence, to remove the singularity of the Poisson equation, we need to fix the phase of pressure. Numerical simulation by our numerical method shows that $\|\nabla \cdot \mathbf{u}\|_2$ is around 10^{-13} for small Rayleigh number, e.g $Ra = 2000$, while it exponentially increases with Ra , e.g $\|\nabla \cdot \mathbf{u}\|_2 \approx O(10^{-8})$ for $Ra = 10^4$ during the simulation with 64×31

grids. For even larger Rayleigh numbers, the solenoidal condition of velocity may not exactly satisfied, but our numerical simulation shows that $\|\nabla \cdot \mathbf{u}\|_2 < 10^{-4}$ for $Ra = 10^7$ with 128×61 grids. It is also found that the finer grids is the smaller $\|\nabla \cdot \mathbf{u}\|_2$. It should be pointed out that summation of $\nabla \cdot \mathbf{u}$ at the grid points (x, y) should be zero. Else, the numerical method is not correct since there is dilation which contradicts with the assumption of incompressible liquids.

To study the spatio-time evolution problem, implicit scheme for all the linear terms and explicit scheme for the nonlinear terms are applied. Now, we make a Fourier transform of equations (C.2)-(C.4) and the pressure Poisson equation with respect to x :

$$\frac{1}{Pr} \left(\frac{\hat{u}_k^{n+1} - \hat{u}_k^n}{\Delta t} + \hat{G}_k^n \right) = -ikp_k^{n+1} + (\mathcal{D}^2 - k^2)\hat{u}_k^{n+1}, \quad (\text{C.10})$$

$$\frac{1}{Pr} \left(\frac{\hat{v}_k^{n+1} - \hat{v}_k^n}{\Delta t} + \hat{H}_k^n \right) = -\mathcal{D}p_k^{n+1} + (\mathcal{D}^2 - k^2)\hat{v}_k^{n+1} + Ra\hat{\theta}_k^{n+1}, \quad (\text{C.11})$$

$$\frac{\theta_k^{n+1} - \theta_k^n}{\Delta t} + \hat{J}_k^n = (\mathcal{D}^2 - k^2)\hat{\theta}_k^{n+1}, \quad (\text{C.12})$$

$$(\mathcal{D}^2 - k^2)\hat{p}_k^{n+1} = Ra\mathcal{D}\hat{\theta}_y^{n+1} - \frac{1}{Pr}\hat{N}_k^n, \quad (\text{C.13})$$

where $\mathcal{D} = \frac{d}{dy}$. Here, the \mathcal{D} is the Chebyshev differentiation matrix after transforming the physical domain $[0, 1]$ into the Chebyshev domain $[-1, 1]$. Hence, the numerical method has the spectral accuracy in space. Note that, the dealiasing by the 2/3 rule should be implemented which is very important for numerical stability. After solving the Fourier amplitudes $[\hat{u}, \hat{v}, \hat{p}, \hat{\theta}]_k^{n+1}$, we apply the inverse Fourier transform to obtain $[u, v, p, \theta]^{n+1}$ in the physical space. A case study of $Ra = 10^4$, $Pr = 1$ is shown in Figure C.1. Here, we have verified our code by comparing with that by Clever and Busse[133] as seen in Table C.1.

	$Pr = 0.71, Ra = 2500$	$Pr = 0.71, Ra = 5000$	$Pr = 0.71, Ra = 10^4$
Clever and Busse[133]	$Nu = 1.475$	$Nu = 2.116$	$Nu = 2.661$
Present work	$Nu = 1.472$	$Nu = 2.110$	$Nu = 2.655$

Table C.1: Comparison of Nusselt number.

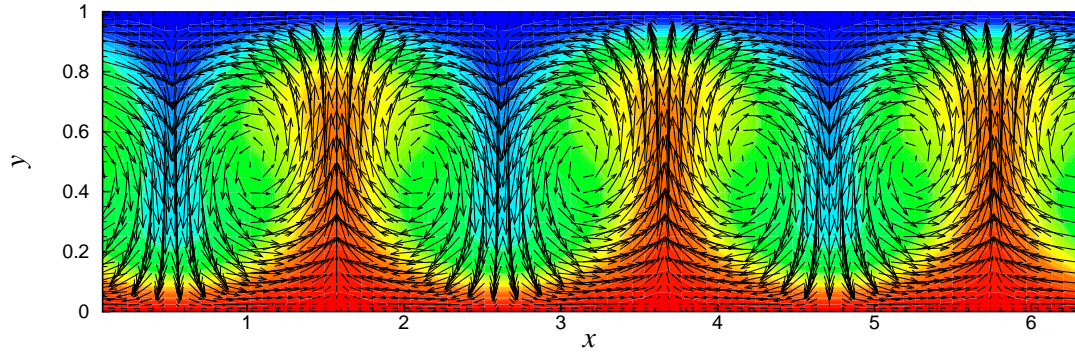


Figure C.1: The velocity field and temperature field of a two-dimensional Rayleigh-Bénard convection for $Ra = 10^4$ and $Pr = 1$ at $t = 10$.

A case of large Rayleigh number $Ra = 10^7$ has also been tested. Note that, the governing equations should be rescaled to reduce the numerical stiffness. Results are shown in Figure C.2.

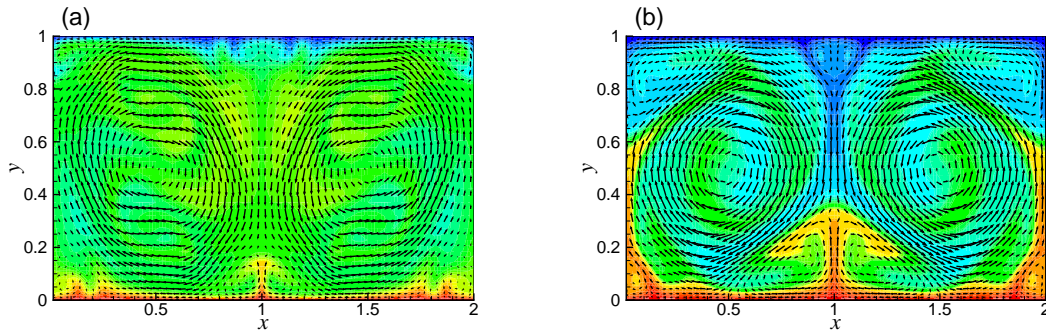


Figure C.2: The velocity field and temperature field of a two-dimensional Rayleigh-Bénard convection for $Ra = 10^7$ and $Pr = 1$. (a) $t = 20$; (b) $t = 25$.

Here, we show the steps of the 2/3 dealiasing rule by taking the nonlinear term $(u_x)^2$ as an example. The steps are summarized as follows:

- (i) suppose we have \hat{u}_k in the Fourier space;
- (ii) calculate u_x in the Fourier space: $ik\hat{u}_k$;
- (iii) dealiasing: for all $|k| > \frac{2}{3}\frac{N}{2}$, set $\hat{u}_k = 0$;
- (iv) use inverse fast Fourier transform to calculate u_x in the physical space and calculate $(u_x)^2$;
- (v) calculate \hat{u}_x^2 in the Fourier space.

Publications

Papers arising from this thesis

- [1] Ding Z, Xie J, Wong TN and Liu R, “Dynamics of liquid films on vertical fibres in a radial electric field”, *J. Fluid Mech.* **752**, 66, 2014.
- [2] Ding Z, Wong TN and Li H, “Stability of two immiscible leaky-dielectric liquids subjected to a radial electric field in an annulus duct,” *Phys. Fluids*, **25**, 124103, 2013.
- [3] Ding Z and Wong TN, “Electrohydrodynamic instability in an annular liquid layer with radial conductivity gradients”, *Phys. Rev. E* **89**, 033010, 2014.
- [4] Ding Z and Wong TN, “Electrohydrodynamic instability of miscible core-annular flows with electrical conductivity stratification, *J. Fluid Mech.* **764**, 488, 2015.
- [5] Ding Z and Wong TN, “Electric field enhances mixing in micro circular pipes”, *Procedia Engineering* **126**, 39, 2015.

Other related works published during the PhD program

- [6] Ding Z, Wong TN, Liu R and Liu Q, “Viscous liquid films on a porous vertical cylinder: Dynamics and stability,” *Phys. Fluids*, **25**, 064101, 2013.
- [7] Ding Z and Wong TN, “Stability of a localized heated falling film with insoluble surfactants,” *Int. J. Heat Mass Trans.*, **67**, 627, 2013.
- [8] Ding Z and Wong TN, “Falling liquid films on a slippery substrate with Marangoni effects”, *Int. J. Heat Mass Trans.* **90**, 689, 2015.

References

- [1] Drazin P. and Reid W., *Hydrodynamic Stability*, Cambridge University Press, ISBN 0-521-52541-1, 2004.
- [2] Trefethen N., *Hydrodynamic Stability Without Eigenvalues*, *Science*, **261**, 578, 1993.
- [3] Schmid P. and Henningson D. *Stability and Transition in Shear Flows*, Springer, New York, ISBN 0-387-98985-4, 2001.
- [4] Nagata M. *Three-dimensional finite-amplitude solutions in plane Couette flow: bifurcation from infinity*, *J. Fluid Mech.* **217**, 519, 1990.
- [5] Waleffe F., *Exact coherent structures in channel flow*, *J. Fluid Mech.* **435**, 93-, 2001.
- [6] Bottaro A., Corbett P. and Luchini P. *The effect of base flow variation on flow stability*, *J. Fluid Mech.*, **476**, 293, 2003.
- [7] Guy Ben-Dov, *Optimal Disturbances and Secondary Instabilities in Shear Flows*, Doctor thesis in Israel Institute of Technology, HaiFa, 2006.
- [8] Theofilis V. *Global linear instability*, *Annu Rev Fluid Mech.*, **43**, 319, 2011.
- [9] Batchelor G.K., Moffatt H. K. and Worster M. G., *Perspectives in Fluid Dynamics: A Collective Introduction to Current Research*, Cambridge University Press, ISBN:9-780-52153-1696, 2002.
- [10] Kapitza P., *Wave flow of thin viscous fluid layers*, *Zh. Eksp. Teor. Fiz.* **18**, 3, 1948.

- [11] Kapitza P. and Kapiza S., *Wave flow of thin viscous fluid layers of liquid*, *Zh. Eksp. Teor. Fiz.* **19**, 105, 1965.
- [12] Park C. and Nosoko T. *Three-dimensional wave dynamics on a falling film and associated mass transfer*, *AIChE J.* **49**, 2715, 2003.
- [13] Benney D., *Long Waves On Liquid Films*, *J. Math. Phys.* **45**, 150, 1966.
- [14] Joo S., Davis S. and Bankoff S. *Long-wave instabilities of heated falling films two-dimensional theory of uniform layers*, *J. Fluid Mech.* **230**, 117, 1991.
- [15] Scheid B., Oron A., Colinet P., Thiele U. and Legros J., *Nonlinear evolution of nonuniformly heated falling liquid films*, *Phys. Fluids* **14**, 4130, 2002.
- [16] Thiele U., Goyeau B. and Velarde M., *Stability analysis of thin film flow along a heated porous wall*, *Phys. Fluids* **21**, 014103, 2009.
- [17] Oron A., Davis S. and Bankhoff S. *Long-scale evolution of thin liquid films*, *Rev. Mod. Phys.* **69**, 931, 1997.
- [18] Pumir A., Manneville P. and Pomeau Y., *On solitary waves running down an inclined plane* *J. Fluid Mech.* **135**, 27, 1983.
- [19] Ooshida T. *Surface equation of falling film flows with moderate Reynolds number and large but finite Weber number*, *Phys. Fluids* **11**, 3247, 1999.
- [20] Shkadov V., *Wave flow regimes of a thin layer of viscous fluid subject to gravity*, *Izv. AN SSSR. Mekhanika Zhidkosti i Gaza.* **2**, 43, 1967.
- [21] Floryan J., Davis S. and Kelly R. *Instability of a liquid film flowing down a slightly inclined plane*, *Phys. Fluids* **30**, 983, 1987.
- [22] Chang H.-C., Demekhin E.A., Kopelevitch D.I. *Nonlinear evolution of waves on a vertically falling film*, *J. Fluid Mech.* **250**, 433, 1993.

- [23] Kalliadasis S., Demekhin E., Ruyer-Quil C. and Velarde M., *Thermocapillary instability and wave formation on a film flowing down a uniformly heated plane*, *J. Fluid Mech.* **492**, 303, 2003.
- [24] V. Shkadov, A. N. Beloglazkin, and S. V. Gerasimov, *Solitary waves in a viscous liquid film flowing down a thin vertical cylinder*, *Mosc. Univ. Mech. Bull.* **63**, 122, 2008.
- [25] Ding Z., Wong T., Liu R. and Liu Q., *Viscous liquid films on a porous vertical cylinder: Dynamics and stability*, *Phys. Fluids* **25**, 064101, 2013.
- [26] Ruyer-Quil C. and Manneville P., *Improved modeling of flows down inclined planes*, *Eur. Phys. J. B* **15**, 357, 2000.
- [27] Ruyer-Quil C. and Manneville P., *Further accuracy and convergence results on the modeling of flows down inclined planes by weighted-residual approximations*, *Phys. Fluids* **14**, 170, 2002.
- [28] Ruyer-Quil C., Trevelyan P., Giorgiutti-Dauphiné F., Duprat C. and Kalliadasis S., *Modelling film flows down a fibre*, *J. Fluid Mech.* **603**, 431, 2008.
- [29] Scheid B., Ruyer-Quil C., Thiele U., Kabov O., Legros J. and Colinet P., *Validity domain of the Benney equation including the Marangoni effect for closed and open flows*, *J. Fluid Mech.* **527**, 303, 2005.
- [30] Ruyer-Quil C., Scheid B., Kalliadasis S., Velarde M. and Zeytounian R., *Thermocapillary long waves in a liquid film flow. Part 1. Low dimensional formulation*, *J. Fluid Mech.* **538**, 199, 2005.
- [31] Trevelyan P., Scheid B., Ruyer-Quil C. and Kalliadasis S., *Heated falling films*, *J. Fluid Mech.* **592**, 295, 2007.

- [32] Ding Z. and Wong T.N. *Falling liquid films on a slippery substrate with Marangoni effects*, *Int. J. Heat Mass Trans.* **90**, 689, 2015.
- [33] Kalliadasis S., Ruyer-Quil C., Scheid B. and Velarde M., *Falling Liquid Films*, Springer London (2012).
- [34] Magarvey R.H. and Outhouse L.E., *Note on the break-up of a charged liquid jet*, *J. Fluid Mech.* **13**, 151, 1962.
- [35] Niamlang S. and Sirivat A., *Electric field assisted transdermal drug delivery from salicylic acid-loaded polyacrylamide hydrogels*, *Drug Delivery* **16**, 378, 2010.
- [36] Rayleigh L., *On the equilibrium of liquid conducting masses charged with electricity*, *Phil. Mag.* **14**, 184, 1882.
- [37] Griffiths D, *Introduction to electrodynamics, Third Edition*, Prentice Hall, 1999.
- [38] Darhuber A. and Troian S., *Principles of microfluidic actuation by modulation of surface stresses*, *Annu. Rev. Fluid Mech.* **37**, 425, 2005.
- [39] Brinkmann M. and Lipowsky R., *Wetting morphologies on substrates with striped surface domains*, *J. Appl. Phys.* **92**, 4296, 2002.
- [40] Klingner A. and Mugele F., *Electrowetting-induced morphological transitions of fluid microstructures*, *J. Appl. Phys.* **95**, 2918-2920, 2004.
- [41] Mugele F. and Baret Jean-Christophe, *Electrowetting: from basics to application*, *J. Phys.: Condens. Matter* **17**, 705-774, 2005.
- [42] Torza S., Cox R. and Mason S., *Electrohydrodynamic Deformation and Burst of Liquid Drops*, *Proc. R. Soc. Lond. A* **269**, 295-319, 1971.
- [43] Harris M. and Basaran O., *Capillary electrohydrostatics of conducting drops hanging from a nozzle in an electric field*, *J. Colloid and Interface Sci.* **161**, 389, 1993.

- [44] Notz P. and Basaran O. *Dynamics of Drop Formation in an Electric Field*, *J. Colloid and Interface Sci.* **161**, 218, 1999.
- [45] Reznik S., Yarin A., THERON A. and Zussman E., *Transient and steady shapes of droplets attached to a surface in a strong electric field*, *J. Fluid Mech.* **516**, 349, 2004.
- [46] González A. and Castellanos A., *Nonlinear electrohydrodynamic waves on films falling down an inclined plane*, *Phys. Rev. E* **53**, 3573, 1996.
- [47] González A. and Castellanos A., *Nonlinear dynamics of a falling vertical film subjected to a normal electric field*, IEEE Annual Report of 1997 Conference on Electrical Insulation and Dielectric Phenomena, Minneapolis, MN, *IEEE Dielectrics and Insulation Society*, **2**, 714, 1997.
- [48] Mukhopadhyay A. and Dandapat B., *Nonlinear stability of conducting viscous film flowing down an inclined plane at moderate Reynolds number in the presence of a uniform normal electric field*, *J. Phys. D: Appl. Phys.* **38** 138, 2005.
- [49] Tseluiko D. and Papageorgiou D.T., *Wave evolution on electrified falling films*, *J. Fluid Mech.* **556** 361, 2006.
- [50] Uma B. and Usha R., *A thin conducting viscous film on an inclined plane in the presence of a uniform normal electric field: Bifurcation scenarios*, *Phys. Fluids* **20** 032102, 2008.
- [51] Uma B. and Usha R., *Electrified film on a porous inclined plane: Dynamics and stability*, *Phys. Rev. E* **82**, 016305, 2010.
- [52] Uma B. and Usha R., *Contaminated electrified thin film over a substrate: dynamics and stability*, *Int J. Adv. Eng. Sci. Appl. Math.* **4**, 241-249, 2012.

- [53] Tseluiko D. and Papageorgiou D.T., *Nonlinear dynamics of electrified thin liquid films*, *SIAM J. Appl. Math.* **67**, 130-1329, 2007.
- [54] Rayleigh L., *On the Capillary Phenomenon of Jets*, *Proc. R. Soc. Lond.* **29**, 71, 1879.
- [55] Basset A., *Waves and jets in a viscous liquid*, *Am. J. Maths* **16**, 93, 1894.
- [56] Taylor G. I., *Electrically driven jets*, *Proc. R. Soc. Lond. A* **313**, 453, 1969.
- [57] Saville D.A., *Stability of electrically charged viscous cylinders*, *Phys. Fluids* **14**, 1095, 1971.
- [58] Cloupeau M. and Prunet-Foch B., *Electrostatic spraying of liquids in cone-jet mode*, *J. Electrostatics* **22**, 135, 1989.
- [59] Son P.H. and Ohba K., *Instability of a perfectly conducting liquid jet in Electrohydrodynamic spraying: perturbation analysis and experimental verification*, *J. Phys. Soc. Japan* **67**, 825, 1998.
- [60] Collins R. Harris M. and Basaran O., *Breakup of electrified jets*, *J. Fluid Mech.* **588**, 75, 2007.
- [61] Eggers J., *Nonlinear dynamics and breakup of free-surface flows*, *Rev. Mod. Phys.* **69**, 865, 1997.
- [62] Wang Q. and Papageorgiou D.T., *Dynamics of a viscous thread surrounded by another viscous fluid in a cylindrical tube under the action of a radial electric field: breakup and touchdown singularities*, *J. Fluid Mech.* **683**, 27, 2011.
- [63] Conroy D., Matar O., Craster R. and Papageorgiou D.T., *Breakup of an electrified, perfectly conducting, viscous thread in an AC field*, *Phys. Rev. E* **83**, 066314, 2011.
- [64] Ding Z., Xie J., Wong T.N. and Liu R., *Dynamics of liquid films on vertical fibres in a radial electric field*, *J. Fluid Mech.* **752**, 66, 2014.

- [65] Melcher J.R. and Schwarz, W.J., *Interfacial relaxation overstability in a tangential electric field*, *Phys. Fluids* **11**, 2604, 1968.
- [66] Setiawan E.R. and Heister S.D., *Nonlinear modeling of an infinite electrified jet*, *J. Electrostatics* **42**, 243, 1997.
- [67] El-Sayed M.F., *Electro-aerodynamic instability of a thin dielectric liquid sheet sprayed with an air stream*, *Phys. Rev. E* **60**, 7588, 1999.
- [68] Tilley B.S., Petropoulos P.G. and Papageorgiou D.T., *Dynamics and rupture of planar electrified liquid sheets*, *Phys. Fluids* **13**, 3547, 2001.
- [69] Savettaseranee K., Papageorgiou D., Petropoulos P. and Tilley B., *The effect of electric fields on the rupture of thin viscous films by van der Waals forces*, *Langmuir* **21**, 12290, 2005.
- [70] Papageorgiou D.T. and Vanden-Broeck J., *Large-amplitude capillary waves in electrified fluid sheets*, *J. Fluid Mech.* **508**, 71, 2004.
- [71] Schäffer E., Thurn-Albrecht T., Russell T. and Steiner U., *Electrically induced structure formation and pattern transfer*, *Nature* **403**, 874, 2000.
- [72] Morariu M., Voicu N., Schäffer E. Lin Z. Russell T. and Steiner U., *Hierarchical structure formation and pattern replication induced by an electric field*, *Nat. Mater.* **2**, 48-52, 2003.
- [73] Verma R., Sharma A., Kargupta K. and Bhaumik J., *Electric Field Induced Instability and Pattern Formation in Thin Liquid Films*, *Langmuir* **21**, 3710, 2005.
- [74] Wu N., Pease III L. and Russel W., *Electric-Field-Induced Patterns In Thin Polymer Films:Weakly Nonlinear and Fully Nonlinear Evolution*, *Langmuir* **21**, 12290, 2005.

- [75] Tseluiko D. and Blyth M., *Effect of inertia on electrified film flow over a wavy wall*, *J. Eng. Math.* **65**, 229, 2009.
- [76] Yeo L. and Chang H.C., *Electrowetting films on parallel line electrodes*, *Phys. Rev. E* **73**, 011605, 2006.
- [77] Taylor G., *Studies in electrohydrodynamics. I. The circulation produced in a drop by an electric field*, *Proc. R. Soc. Lond. A* **291**, 159, 1966.
- [78] Saville D., *Electrohydrodynamics: The Taylor-Melcher Leaky Dielectric Model*, *Annu. Rev. Fluids* **29**, 27, 1997.
- [79] Pereira A. and Kalliadasis S., *On the transport equation for an interfacial quantity*, *Eur. Phys. J. Appl. Phys.* **44**, 211, 2008.
- [80] Melcher J. and Smith C., *Electrohydrodynamic charge relaxation and interfacial perpendicular-field instability*, *Phys. Fluids* **12**, 778, 1969.
- [81] Ozen O., Aubry N., Papageorgiou D.T. and Petropoulos P.G., *Monodisperse Drop Formation in Square Microchannels*, *Phys. Rev. Lett.* **96**, 144501, 2006.
- [82] Abdella K. and Rasmussen H., *Electrohydrodynamic instability of two superposed fluids in normal electric fields*, *J. Comp. and Appl. Math.* **78**, 33, 1997.
- [83] Shankar V. and Sharma A., *Instability of the interface between thin fluid films subjected to electric fields*, *J. Colloid and Interface Sci.* **274**, 294, 2004.
- [84] Ozen O., Aubry N., Papageorgiou D.T. and Petropoulos P.G., *Electrohydrodynamic linear stability of two immiscible fluids in channel flow*, *Electrochimica Acta* **51**, 5316, 2006.

- [85] Li F., Ozen O., Aubry N., Papageorgiou D.T., and Petropoulos P.G., *Linear stability of a two-fluid interface for electrohydrodynamic mixing in a channel*, *J. Fluid Mech.* **583**, 347, 2007.
- [86] Uguz A., Aubry N., *Quantifying the linear stability of a flowing electrified two-fluid layer in a channel for fast electric times for normal and parallel electric fields*, *Phys. Fluids* **20**, 092103, 2008.
- [87] Artana G., Romat H. and Touchard G., *Theoretical analysis of linear stability of electrified jets flowing at high velocity inside a coaxial electrode*, *J. Electrostatics* **43**, 83, 1998.
- [88] Burcham C. and Saville D., *Electrohydrodynamic stability: Taylor-Melcher theory for a liquid bridge suspended in a dielectric gas*, *J. Fluid Mech.* **452**, 163, 2002.
- [89] Li F., Yin X. and Yin X., *Instability of a viscous coflowing jet in a radial electric field*, *J. Fluid Mech.* **596**, 285, 2008.
- [90] López-Herrera J., Riesco-Chueca P. and Gañón-Calvo A., *Linear stability analysis of axisymmetric perturbations in imperfectly conducting liquid jets*, *Phys. Fluids* **17**, 034106, 2005.
- [91] Wang Q., *Breakup of a poorly conducting liquid thread subject to a radial electric field at zero Reynolds number*, *Phys. Fluids* **24**, 102102, 2012.
- [92] Wray A., Matar O. and Papageorgiou D.T., *Non-linear waves in electrified viscous film flow down a vertical cylinder*, *J. Appl. Math.* **77**, 430, 2012.
- [93] Wray A., Papageorgiou D.T. and Matar O., *Electrified coating flows on vertical fibres: enhancement or suppression of interfacial dynamics*, *J. Fluid Mech.* **735**, 427, 2013.

- [94] Wray A., Papageorgiou D.T. and Matar O., *Electrostatically controlled large-amplitude, non-axisymmetric waves in thin film flows down a cylinder*, *J. Fluid Mech.* **736**, R2, 2013.
- [95] Preziosi L., Chen K.P. and Joseph D.D., *Lubricated pipelining: Stability of core-annular flow*, *J. Fluid Mech.* **201**, 323, 1989.
- [96] Joseph D.D., Bai R., Chen K.P. and Renardy Y.Y., *Core-Annular Flows*, *Annu. Rev. Fluid Mech.* **29**, 65, 1997.
- [97] Selvam B., Merk S., Govindarajan R. and Meiburg E., *Stability of miscible core-annular flows with viscosity stratification*, *J. Fluid Mech.* **592**, 23, 2007.
- [98] Dijkstra H.A., *The coupling of interfacial instabilities and the stabilization of two-layer annular flows*, *Phys. Fluids A* **4**, 1915, 1992.
- [99] Ding Z., Wong T. and Li H., *Stability of two immiscible leaky-dielectric liquids subjected to a radial electric field in an annulus duct*, *Phys. Fluids* **25**, 124103, 2013.
- [100] Lin H., Storey B.D., Oddy M.H., Chen C.H. and Santiago J.G., *Instability of electrokinetic microchannel flows with conductivity gradients*, *Phys. Fluids* **16**, 1922, 2004.
- [101] Baygents J. and Baldessari F., *Electrohydrodynamic instability in a thin fluid layer with an electrical conductivity gradient*, *Phys. Fluids* **10**, 301, 1998.
- [102] Hoburg J., Melcher J., *Electrohydrodynamic mixing and instability induced by colinear fields and conductivity gradients*, *Phys. Fluids* **20**, 903-911, 1977.
- [103] Hoburg J., *Internal electrohydrodynamic instability of liquids with colinear fields and conductivity gradients*, *J. Fluid Mech.* **84**, 291-303, 1978.
- [104] Melcher J., *Continuum Electromechanics*, MIT, Cambridge, MA, 1981.

- [105] Chang M., Ruo A. and Chen F., *Electrohydrodynamic instability in a horizontal fluid layer with electrical conductivity gradient subject to a weak shear flow*, *J. Fluid Mech.* **634**, 191, 2009.
- [106] Ruo A., Chang M., and Chen F., *Effect of rotation on the electrohydrodynamic instability of a fluid layer with an electrical conductivity gradient*, *Physics Fluids* **22**, 024102, 2010.
- [107] Carriere P. and Monkewitz P., *Convective versus absolute instability in mixed Reyleigh-Bénard-Poiseuille convection*, *J. Fluid Mech.* **384**, 243, 1999.
- [108] Clever R., and Busse F., *Three-dimensional convection in a horizontal fluid layer subjected to a constant shear*, *J. Fluid Mech.* **234**, 511, 1999.
- [109] Ding Z., and Wong T.N., *Electrohydrodynamic instability in an annular liquid layer with radial conductivity gradients*, *Phys. Rev. E* **89**, 033010, 2014.
- [110] Chen C., Lin H., Lele S. and Santiago J., *onvective and absolute electrokinetic instability with conductivity gradients*, *J. Fluid Mech.* **524**, 263, 2005.
- [111] Storey B., Lin H. and Santiago J.G. *Electrokinetic instabilities in thin microchannels*, *Phys. Fluids* **17**, 018103, 2005.
- [112] Santos J. and Storey B., Lele S. and Santiago J., *Instability of electro-osmotic channel flow with streamwise conductivity gradients.*, *Phys. Rev. E* **78**, 046316, 2008.
- [113] Felderhof B., *Dynamics of free liquid films*, *J. Chem. Phys.* **49**, 44, 1968.
- [114] Gallez D. and Coakly G., *Interfacial instability at cell membranes*, *Prog. Biophys. Molec. Biol.* **48** 155, 1986.

- [115] Georgiou E., Papageorgiou D., Maldarelli C. and Rumschitzki D., *The double layer-capillary stability of an annular electrolyte film surrounding a dielectric-fluid core*, *J. Fluid Mech.* **226**, 149, 1991.
- [116] Conroy D., Craster R., Matar O. and Papageorgiou D., *Dynamics and stability of an annular electrolyte film*, *J. Fluid Mech.* **656**, 481-506, 2010.
- [117] Conroy D., Matar O., Craster R. and Papageorgiou D., *Dynamics and stability of an annular electrolyte film*, *Phys. Fluids* **23**, 022103, 2011.
- [118] Lin H., *Electrokinetic instability in microchannel flows: A review*, *Mechanics Research Communications* **36**, 33, 2009.
- [119] Ding Z., and Wong T.N., *Electrohydrodynamic instability of miscible core-annular flows with electrical conductivity stratification*, *J. Fluid Mech.* **764**, 488, 2015.
- [120] Takashima M. *Electrohydrodynamic instability in a dielectric fluid between two coaxial cylinders*, *Q. J. Mech. Appl. Math.* **33**, 93, 1980.
- [121] Shivakumaraa I., Leeb J., Vajraveluc K. and Akkanagammaa M. *Electrothermal convection in a rotating dielectric fluid layer: Effect of velocity and temperature boundary conditions*, *Int. J. Heat Mass Trans.* **55**, 2984, 2012.
- [122] Yoshikawa H. N., Tadie Fogaing M., Crumeyrolle O. and Mutabazi I. *Dielectrophoretic Rayleigh-Bénard convection under microgravity conditions*, *Phys. Rev. E* **87**, 043003, 2013.
- [123] Tsai P.-C. *The Route to Chaos and Turbulence in Annular Electroconvection*, Ph.D thesis, 2007.
- [124] Craster R. and Matar O. *On viscous beads flowing down a vertical fibre*, *J. Fluid Mech.* **553**, 85, 2007.

- [125] Lister J.R., Rallison J.M., King A.A., Cummings L.J. and Jensen O.E., Capillary drainage of an annular film: the dynamics of collars and lobes, *J. Fluid Mech.* **552**, 311-343, 2006.
- [126] Ding Z. and Liu Q. *Stability of liquid films on a porous vertical cylinder*, *Phys. Rev. E* **84**, 046307, 2011.
- [127] Kliakhandler I., Davis S. and Bankhoff S., *Viscous beads on vertical fibre*, *J. Fluid Mech.* **429**, 381, 2001.
- [128] Birikh R., Briskman V., Velarde V. and Legros J.C. *Liquid interfacial systems: Oscillations and Instability*, CRC Press, New York, 2003.
- [129] Khorrami, M. *A Chebyshev spectral collocation method using a staggered grid for the stability of cylindrical flows*, *Int. J. Numer. Meth. Fluids* **12**, 825, 1991.
- [130] Govindarajan, R. *Effect of miscibility on the linear instability of two-fluid channel flow*, *Int. J. Multiphase Flow* **30**, 1177, 2004.
- [131] Govindarajan R., L'vov V. and Procaccia I. *Retardation of the onset of turbulence by minor viscosity contrasts*, *Phys. Rev. Lett.* **87**, 174501, 2001.
- [132] Talon L. and Meiburg E. *Plane Poiseuille flow of miscible layers with different viscosities: instabilities in the Stokes flow regime*, *J. Fluid Mech.* **686**, 484, 2011.
- [133] Clever R. and Busse F., *Transition to time-dependent convection*, *J. Fluid Mech.* **65**, 625, 1974.
- [134] Liu R. and Liu Q. *Non-modal instability in plane Couette flow of a power-law fluid*, *J. Fluid Mech.* **676**, 145, 2011.
- [135] Liu R. and Liu Q. *Nonmodal stability in Hagen-Poiseuille flow of a shear thinning fluid*, *Phys. Rev. E* **85**, 066318, 2012.

- [136] López Carranza S., Jenny M. and Nouar C. *Instability of streaks in pipe flow of shear-thinning fluids*, *Phys. Rev. E* **88**, 023005, 2013.